Investigation of Sanding around Water Injector Wells in Unconsolidated and Weakly-Consolidated Sand Reservoir under Water Hammer Pressure Pulsing

by

Mahshid Jafar Pour

A thesis submitted in partial fulfillment of the requirements for the degree of

Doctor of Philosophy

in

PETROLEUM ENGINEERING

Department of Civil and Environmental Engineering

University of Alberta

Abstract

This research is focused on massive sand production around injector wells immediately after well shut-in events. Sand production in some water injector wells has been reported to be catastrophic, massive and always occurring after an unplanned shut-in. High pore pressures around injectors, numerous cycles of injection and shut-in, the strength-weakening effect of water and water hammer (WH) induced pressure pulses make the conditions around wellbore susceptible to sandstone degradation and sand production. WH is a general term describing the generation, propagation and damping of pressure waves in pipes. It occurs due to sudden velocity changes occurring upon quick shutting down of the well. There are several examples of massive sand production and even complete injectivity losses. Progressive failure and liquefaction are among the theories to explain massive sanding. However, no numerical modeling has been performed to verify the underlying responsible mechanism. A dynamic analysis together with a suitable constitutive model can help us understand the mechanism, and hence take the necessary precautions to prevent catastrophic sand production conditions.

The relevance of the research is not restricted to injection wells. Production wells also deal with WH waves during sudden shut-ins. Sudden sanding can be expected in producers particularly at high water cuts for which low compressibility of the water column in the wellbore ensures low attenuation of the WH pressure pulses.

In this research a 2D axsisymmetric, single-phase fluid, sequentially coupled dynamic code is developed, capable of modeling pore pressure waves propagating within saturated porous media. The code ignores cyclic behavior and the effect of fatigue. It is used to study the sanding potential because of dynamic WH waves in a small-scale synthetic case study. The model

simulates a layer of both weakly-consolidated and unconsolidated reservoir with the WH waves applied as a boundary condition. The modeling results indicate progressive failure as the underlying mechanism for massive sanding. The stress paths and dominant factors affecting failure and potential sand production are also discussed. The fast changes of stress conditions and failure progression confirms the need for a dynamic analysis.

Preface

The research conducted for this thesis was a part of a research program funded by NSERC through a Collaborative Research Development program supported by BP.

Part of of Chapter 2 is based on the following publication:

Rahmati, H., Jafarpour, M., Azadbakht, S., Nouri, A., Vaziri, H., Chan, D., and Xiao, Y., 2012. Review of Sand Production Prediction Models, Journal of Petroleum Engineering, Vol 2013, Article ID 86498.

A slightly different version of Chapter 3 was previously published in:

Jafarpour, M., Rahmati, H., Azadbakht, S., Nouri, A., Chan D., Vaziri, H., 2012. Determination of mobilized strength properties of degrading sandstone, J. of Soils and Foundations, Vol 52, Issue 4, pp. 658-667.

A version of Chapter 4 was previously published in:

Jafar Pour, M., Nouri, A., Chan, D., 2016. Numerical modelling of waterhammer pressure pulse propagation in sand reservoirs, J of Petroleum Science and Engineering, Vol 137, pp. 42-54.

TO MY PARENTS

ACKNOWLEDGEMENTS

This page is intentionally left blank

TABLE OF CONTENTS

LIST OF TABLES

LIST OF FIGURES

Chapter 1: Introduction

1.1 Background

Seventy percent of the world oil and gas are contained in weakly consolidated reservoirs. Oil extraction using deep wells in these weakly cemented materials is prone to sand production. Material degradation and loss of sandstone strength are necessary conditions for sanding. Drilling operations, fatigue caused by several cycles of shut-in and injection, generation of high pore pressures, operational conditions and strength-weakening effect of water gradually lead to sandstone degradation around the perforations. High pressure gradients along perforations also facilitate the detachment of sand particles. In addition, fluid flow is responsible for the transportation and production of de-bonded sand particles or detached sand clumps into the wellbore.

Sand production is the source of several problems in the oil industry. These problems include but are not limited to the following: plugging the perforations or production liner, wellbore instability, failure of sand control completions (Willson et al., 2002), lower wellbore productivity/injectivity, filling the well with sand after a massive sanding, environmental effects, additional cost for remedial and clean-up operations, and erosion of pipelines and surface facilities. Prevention of sanding by sand control completions such as gravel packing is costly and leads to lower well productivity/injectivity. Therefore, there is always a cost benefit if sand management and modeling is implemented early during the design stage of well completions.

A sizable portion of oil reserves are recovered by waterflood requiring water injection wells. Beside petroleum production wells, water injector wells can also

be prone to sand production. However, the problem for injector wells remains unnoticed or is ignored until it is too late, mainly because the flow direction obscures sanding. Sand production in injector wells occurs during the shut-in period when cross-flow, backflow, water hammer (WH) and well interference lead to sanding (Santarelli et al., 2011). There are several examples of massive sand production and even complete loss of injectivity in the Norwegian North Sea (Santarelli et al., 1998; Santarelli et al., 2000), Indonesia (Papamichos, 2006) and Buzzard field in the UK (Santarelli et al., 2011) for injector wells. The Norwegian Sea well serves as a good example for the severity of sanding in injector wells, where the injectivity of the well decreased from 8000 m^3/d to 0 m^3/d in just half an hour when the injection was resumed following a quick wellbore shut-in. All of these problems could have been prevented if a comprehensive sand assessment had been performed and the wellbore had not been shut-in quickly.

The focus of this work is the dynamic response of sand formations to WH pressure pulsing that has been alluded to in the literature as a major factor in massive sand production, primarily in water injection wells. WH is a general term describing the generation, propagation, reflection and damping of pressure waves through liquids in pipes (Jardine et al., 1993). A realistic investigation of WH pulsing effects requires a dynamic analysis. Sudden changes in the flow velocity lead to liquid depressurization at one end of the well and extra pressure at the other end. WH pressure pulses hit the reservoir formation like seismic waves following the shut-in and may lead to sand liquefaction and massive sanding (Santarelli et al., 2000).

1.2 Objective

The primary objective of this research is to numerically investigate the importance of WH pressure pulsing on the sanding potential and mechanism in water injection wells. The goal is to assess if the WH pressure pulsing can lead to

massive sand failure and investigate the conditions that may lead to massive sanding. Some speculate that dynamic liquefaction due to WH is the culprit mechanism for massive sanding after sudden shut-ins, but no measurements or simulation studies have verified this. Massive failure could also be due to progressive failure when near well-bore failure leads to additional failure progressing through the reservoir.

Since no commercial simulator is available to realistically mimic pore pressure pulses (such as WH waves) in porous media, the secondary objective is to develop a numerical model capable of simulating fluid dynamics in porous media. The model must take into account the effect of fluid acceleration and the results are validated against experimental data.

1.3 Hypothesis

The hypothesis is that the WH pressure pulsing can lead to massive sandstone degradation through two possible mechanisms: (1) the high pore pressures during WH propagations leads to low mean effective stresses and liquefaction, and (2) the zone surrounding the wellbore may undergo failure due to sudden changes in pore pressure and stress, the failure zone may then expand as a result of stress redistribution and wave propagation through a progressive failure process. When the failure process is self-enhancing, and different parts of the material fail at different times, it is called progressive failure.

The counter argument against the liquefaction hypothesis is the great depth of the reservoirs that have experienced massive sanding after the sudden well shut-in. The high depth of the reservoirs formation should indicate lower porosities, i.e. dense sandstone and high stresses lessening the liquefaction potential.

1.4 Research Motivation

Sanding is a widespread problem in weakly-consolidated sandstone reservoirs, which comprise more than seventy percent of the hydrocarbon reservoirs. Water injection is expected to be the secondary recovery method of choice for a considerable number of these resources. To design optimum completion, it is necessary to estimate the rate and volume of the potential sand that will be produced in the life span of a wellbore. However, the existing models require further development to accurately predict sanding for field-scale problems. Sanding in injector wells is usually ignored until it is too late, e.g. in Norwegian North Sea (Santarelli et al., 1998; Santarelli et al., 2000), Indonesia (Papamichos, 2006) and Buzzard field in the UK (Santarelli et al., 2011). The problem in injectors is often regarded as the case with sudden and massive sand production. The Norwegian Sea well serves as a good example where the injectivity of the well decreased from 8000 m^3/d to 0 m^3/d in just half an hour after a shut-in (Santarelli et al., 2000).

Because of the fast and massive nature of the produced sand, researchers (Santarelli et al., 2011; Santarelli et al., 1998; Santarelli et al. 2000; Han et al., 2003; Hayatdavoudi, 2005) speculated that dynamic WH waves, generated after an abrupt shut-in, are the main culprit, and liquefaction could be the governing mechanism. Progressive failure can be a potential mechanism too. However, little research has been conducted to verify which the dominant mechanism. Numerical study of the former hypothesis requires the implementation of an appropriate constitutive model in a dynamic hydro-mechanical model to capture the excess pore pressure generation observed in liquefaction. The model should provide a safe shut-in and start-up window to minimize the sanding in injection wells as well as production wells with high water-cut.

1.5 Methodology and Scope

The methodology consists of developing a suitable model to simulate pressure pulsing propagation in the porous media and capture sand liquefaction around water injector wells. The model includes the following important features:

- Axisymmetric condition is assumed for a single injection well analysis to limit the model size;
- The geomechanical modeling platform is Itasca's FLAC software. Dynamic load in the Civil Engineering context (e.g. earthquake engineering) is usually conducted by specifying the stress or displacement as the boundary condition. However, the dynamic load in this research consists of WH pressure pulses and the corresponding normal stress pulses on the well face. The dynamic option of FLAC only solves for solid dynamics. The fluid flow is still calculated using Darcy's law, hence ignoring the pore fluid acceleration. Therefore, FLAC cannot simulate the pore pressure waves. A CFD code, capable of solving dynamic fluid flow in porous media, is developed in MATLAB and the two software are sequentially coupled using an undrained split methodology;
- The simulation steps involve drilling a wellbore, applying the mud pressure, and installing the casing; a static injection period leads to the dynamic simulation involving several cycles of WH pressure pulses. The applied WH waves are based on the measured data available for a well in an Alaskan field;
- The study involves the utilization of different constitutive models for weakly-consolidated sandstone and unconsolidated sand and comparison of the results. The conditions under which sudden failure is triggered and the extent of failure is studied. The area of failure is identified and related to the potential amount of sand production around the injection well.

Finally, the conditions under which a dynamic analysis is necessary are specified;

- A parametric study is conducted to investigate the effect of rock parameters, WH wave properties and operating conditions on the model response in terms of sand failure and sanding potential.

For the feasibility of the study, some simplifications are necessary. The code is developed for 2D axisymmetric conditions. Single-phase flow is considered, as the waves only affect the vicinity of the injector well which is mostly water saturated. The reservoir is assumed homogenous.

The effect of fatigue due to cyclic loading is outside the scope of this work. However, it is anticipated that the fatigue should have a significant effect on the sand failure and the generation of excess pore pressure when WH pulses hit the well. Moreover, it is assumed that static constitutive models are still suitable in the simulation of dynamic conditions.

1.6 Thesis Layout

Chapter 2 presents a literature review on the modeling of sand production and the sanding cases in the context of water injection wells, particularly those that are suspected to occur due to liquefaction. The chapter also introduces the essential theory and background for the stated problem.

Chapter 3 discusses the behavior of sandstone and its degradation under shear yielding. A bilinear hardening/softening Mohr-Coulomb model is presented and calibrated for two different types of sandstone and validated with experimental data. The same model is used for the model presented in Chapter 5. Also, Fracture Energy Regularization is applied to eliminate mesh dependency during softening.

Chapter 4 covers the mathematical formulation of porous media dynamics. The governing equations are presented and extended to elastoplastic conditions. The equations presented by De la Cruz and Spanos (1989) are adopted under isothermal conditions and solved using the Finite Difference Method. The results are also compared with those obtained from Biot's theory (Biot, 1956). A new form of artificial viscosity is presented for the numerical stability. The numerical solutions are validated using a shock-tube experiment and some simple models are simulated to examine the propagation of the pressure waves through an elastic medium. The flow equations are then coupled with the FLAC dynamic module. Both undrained and drained splits are investigated and it is concluded that the undrained split coupling is more robust and stable.

Chapter 5 investigates the failure and sanding potential for a synthetic model that is based on the case study reported by Santarelli et al. (2000). Axisymmetric condition is assumed for a single injection well in the reservoir. WH waves are applied as the boundary condition following a sudden shut-in for a dynamic analysis. Different constitutive models are used and the dynamic response of the medium is investigated. Both weakly-consolidated sandstone and cohesionless sand are simulated. Finally, a parametric study is performed to study the effect of sand properties (e.g. friction angle, dilation angle, permeability and porosity), operational parameters (e.g. injection pressure and wave amplitude) on the model response.

Chapter 6 presents a summary and conclusion of the findings as well as the recommendations for further advancement of this research.

Chapter 2: Literature Review

2.1 Introduction

To investigate numerical modeling of sanding under dynamic effect of WH pressure pulsing, several topics have to be considered including modeling sand production, WH waves, dynamic analysis, progressive failure and liquefaction. In this chapter a summary of previous numerical studies on sanding are mentioned and some theories are introduced regarding the phenomenon under investigation. This chapter introduces a review of the current sanding models and how they lack the ability to capture dynamic effects. Then it briefs a review of soil response under dynamic loading. The chapter ends with a discussion on WH pressure pulsing as a result of sudden shut-in.

2.2 Sanding Models[1]

Over the time, numerous approaches have been adopted to predict and understand the sand production phenomenon using physical model testing, analytical and empirical relationships, and numerical modeling. Routine laboratory tests can only predict the onset of sand production (Xiao and Vaziri, 2011). They are also time-consuming and expensive. In addition, because of the small size of the sample plugs, the results are usually influenced by boundary effects. Analytical

---

[1] This section is based on the following publication: Rahmati, H., Jafarpour, M., Azadbakht, S., Nouri, A., Vaziri, H., Chan, D., and Xiao, Y., 2012. Review of Sand Production Prediction Models, Journal of Petroleum Engineering, Vol 2013, Article ID 86498.

models are fast and easy to use but they are only good for the onset of sand predictions and have some restrictions. Most of them are only valid for certain limited assumptions, which are not usually the case in complicated field-scale problems. Numerical models are by far the most powerful tools for predicting and managing sand production. They can be combined with analytical correlations to obtain the results more efficiently. Experimental results are also utilized to calibrate or verify numerical models. Yet, numerical models have their own limitations and extensive efforts have been made to improve them.

The many numerical sand models reported in the literature can be divided into two groups: continuum-based models and discontinuum-based models. Discrete element method (DEM) is a good tool to mimic sand production, especially to understand the mechanism of sanding in the grain-scale level. However, it cannot be used for large-scale problems because of the large computational time required. The calibration of the model is also very difficult and involves several uncertainties as it is not possible to create a model with the exact particle arrangement as the real sandstone. It is also not possible to measure micro properties of sandstone directly. They are obtained in such a way that the set of properties predicts the desired sand behaviour. Therefore, continuum-based models are more popular especially for field-scale problems. Table 2-1 summarizes all the continuum-based numerical works in the literature.

An important issue about the current sand models is that almost all of them are for producer wells. There are a number of issues that are common between water injectors and producers, including erosion. However, injectors face other potential problems such as WH, well-to-well backflow, inter-layer crossflow during shut-ins, thermal fractures, and gravel loss into fracture systems (Sadrpanah, 2005).

Only a few researchers (Yi, 2001; Vaziri et al., 2008; Azadbakht et al., 2012) performed numerical studies to predict sanding in injectors. Sanding mechanisms

in injectors have not been investigated thoroughly and may be quite different due to, for instance, the effects of WH waves. The situation in these wells is often described as cases with high sand production within a short duration. A few papers (Santarelli et al., 2011, 1998, 2000; Hayatdavoudi, 2005) tried to explain the sanding problems in injectors and stated that sand liquefaction due to WH, the process by which spontaneous loss of shear strength occurs under undrained condition, is a likely mechanism for massive sand production. Progressive failure, where different elements undergo failure at different time, is also likely to cause massive sanding. Nevertheless, no work has been published which investigates possible mechanisms and the conditions leading to massive sanding.

Table 2-1 Summary of the numerical works on sand production in the literature

Model	Geometry & Solution Method	Yield	Hard. /Soft.	Coupling	Onset of Sanding	$\dfrac{\partial \varphi}{\partial t} =$	Permeability Change	Other Features
(Morita et al., 1989; Morita et al., 1998; Burton et al., 1998)	3D; FE (SAND3D software)	Kinematic model with a cap	yes (flow friction)	Iteratively coupled	plastic strain limit	0	0	1.Only the onset of sanding. 2.Burton applied it for gas reservoirs
(Vardoulakis et al., 1996)	1D; FD	N/A	N/A	Fluid flow & erosion are coupled.		$k\dfrac{\dot{m}}{\rho_s} =$ $\lambda(1-\varphi)c\|q_i\|$ And with sand deposition: $=\lambda(1-\varphi)(c-\dfrac{c^2}{c_{cr}})\|q_i/q_0\|^n$	$\dfrac{k}{k_0} = \varphi^3/(1-\varphi^2)$ (Carman -Kozeny)	1.Only hydro-mechanical effects; Equilibrium eqn is not solved. 2.Sand deposition is neglected in modeling.
(Skjærstein et al., 1997)	1D; FD	N/A	N/A	Fluid flow & erosion are coupled.		$\dfrac{\dot{m}}{\rho_s} = \lambda c(\varphi - \dfrac{\varphi}{\varphi_{cr}})q_x$	$\dfrac{1}{k} = B\varphi + A$ (found experimentally)	Forcheimer's law was used instead of Darcy's law to account for turbulancy.
(Papamichos and Stavropoulou, 1998)	2D Axial symmetry & 3D; FE; Newoton-Paphson (NR) iterations	MC	yes	Fully-coupled		$\dfrac{\dot{m}}{\rho_s} = \lambda(1-\varphi)c\sqrt{q_iq_i}$ No crit. porosity	$\dfrac{k}{k_0} = \varphi^3/\bar{\rho}(1-\varphi^2)$ $\bar{\rho} = \rho_f + c(\rho_s - \rho_f)$	Tension cut-off: function of both plastic strain & porosity ; by the factor $(1-\varphi)/(1-\varphi_i)$.
(Papamichos et al., 2001)	2D Axial symmetry; FEM; NR iterations	MC	yes	Fully-coupled		$\dfrac{\dot{m}}{\rho_s} = \lambda(1-\varphi)\|q_i\|$	Carman -Kozeny	Tension cut-off & Young mod changed by the factor $(1-\varphi)/(1-\varphi_i)$.

11

(Yi, 2001)	2D axial symmetry; FD	MC	no		yielding	$\eta \dfrac{\dot{m}}{\rho_s} - \lambda_d v c_s$ $\dfrac{\dot{m}}{\rho_s} = \lambda(1 - \varphi - \dfrac{m_d}{\rho_s})v^2$ $\dfrac{\dot{m}_d}{\rho_s} = \lambda_d v c_s + (1 - \eta)\dfrac{\dot{m}}{\rho_s}$	$\dfrac{k}{k_0}$ $= \gamma \dfrac{\varphi^3(1 - \varphi_0^2)}{\varphi_0^3(1 - \varphi^2)}\dfrac{1}{1 + \beta n}$	Sand deposition in porous media is considered.
(Vaziri et al., 2002)	2D axial symmetry; FE; fully-implicit	Modified MC with tensile failure	yes	Fully-coupled	Tensile failure (zero effective stress)	0 (sand is remained in place as a liquefied zone)	$\dfrac{k}{k_0}$ $= \exp[-2.88$ $\times 10^{-3}(\sigma_i' - \sigma_0')]$	Zero stiffness, compressibility & high k for the liquefied tensile zone.
(Wang and Xue, 2002)	FE; Crank-Nicholson for time integration	MC	no	Fully-coupled	ε^p $= .02$ $+ .008J_1$	$\dfrac{\dot{m}}{\rho_s} + (1 - \varphi)\varepsilon_v$ $\dfrac{\dot{m}}{\rho_s} = \lambda(1 - \varphi)\Omega\sqrt{q_i q_i}$	Kozeny-Poiseuille law & Carman - Kozeny	
(Chin and Ramos, 2002)	2D & 3D; FE; explicit; NR iteration	Drucker-Prager	no	Coupled	yielding	$(1 - \varphi)\nabla \cdot v_s$	Power law with porosity (exponent=5.6)	
(Nouri et al., 2003)	2D plane strain; FD	Bilinear MC	yes	Fully-coupled	Tensile failure or shear-failed element falls in tension	N/A (sudden element removal)	N/A	Capillary is considered as a residual cohesion.
(Wang et al. 2005)	2D; FE	Drucker-Prager	no	Fully-coupled		λ a function of plastic strain	$k = k_0 \exp[A$ $\dfrac{\varphi - \varphi_0}{\varphi_{max} - \varphi_0}]$	Cohesion & friction drop linearly with porosity.
(Servant et al., 2006)	2D; FE	MC	no	Iteratively coupled	Yielding & seepage	Based on filtration theory		Constant viscosity for the slurry.
(Detournay et al., 2006)	2D; FD	MC	yes	Iteratively coupled	Tension or $q>q_{cr}$	$\dfrac{S_L}{V_L}\dfrac{\dot{m}}{\rho_s}$	$\dfrac{k}{k_0} = \dfrac{\varphi^3(1 - \varphi_0^2)}{\varphi_0^3(1 - \varphi^2)}$	Bulk mod. changed by φ_0/φ

					$q_{cr} = ak(1 - \varphi)(c_r - \sigma'_t tan\phi) /(\mu R_p)$	$\frac{\dot{m}}{\rho_s} = \lambda(1 - \varphi)(q - q_{cr})$		
(Nouri et al., 2006b)	2D axial symmetry; FD	Bilinear MC	yes	Iteratively coupled	Tensile failure or a shear-failed element falls in tension	element removal if produced, else: $\dot{\varepsilon}_v(1 - \varphi)$	$k = C\varphi^3/\gamma_f(1 - \varphi^2)$	
(Nouri et al., 2006a)	FE; NR iterations	MC	yes	Fully-coupled	Tension	N/A (sudden element removal)	N/A	Adaptive mesh is used.
(Nouri et al., 2007; Vaziri et al., 2008)	2D plane strain & axial symmetry; FD	Bilinear MC	yes	Iteratively coupled	Complete degradation and tensile *mean* effective stress		Applied but not reported how. Vaziri (2008)	WH pulsing is included in the model; stiffness changes with sanding (Vaziri et al., 2008)
(Detournay-Piette, 2008)	2D plane strain; FD	Double-yield	yes	Iteratively coupled	Same as 2006			Only cap yielding is considered.
(Nouri et al., 2009)	All the features are the same as (Nouri et al., 2007) but fracture energy regularization is applied to remove mesh dependency and the calibration of hardening/softening behavior is discussed thoroughly.							
(Kim et al., 2011)	3D; FD	MC	yes		Calculated from force balance on the element	N/A (sudden element removal)	N/A	No calibration parameter to match the experiment is used and yet a good match is observed.
(Wang et al., 2011)	2D; FE (ELFEN software)	Soft rock model	yes	Fully-coupled			K changes as a function of dilation or volumetric strain: $k = \exp(A\varepsilon_v)$	1.adaptive mesh; 2.Arbitrary Largrangian Eulerian formulation; 3.Fracture Energy Regularization

The importance of WH is amplified by the fact that the produced flow rates due to WH are higher than crossflows and backflows (Santarelli et al., 2011). In 2006, Hayatdavoudi investigated the WH effects in three production wells in sandstone reservoirs that had experienced loss of production. They observed, at least in three deep wells with highly consolidated reservoir rocks, that not only did they lose fluid production, but they also produced a great deal of pulverized, highly angular rock fragments. The situation exacerbates for weakly consolidated sandstones.

Wang et al. (2008) measured high frequency WH pulses (above 17 Hz) in an Alaska oil field. Therefore, WH is a short transient event requiring a dynamic approach in modeling. Only Vaziri et al. (2008) and Azadbakht et al. (2012) performed a simulation study of WH effect on sanding. However, the authors took a quasi-static approach. Hence, the accelerations of fluid in porous media and solid particles were ignored. Solving for dynamic fluid considers the pore fluid acceleration and any possible turbulence in the fluid flow. Previously, Skjærstein et al. (1997) used Forcheimer's law instead of Darcy's law to account for fluid turbulence around the wellbore. Yet, this approach also ignores pore fluid acceleration. In fact, the only research in which a dynamic numerical model for sanding is mentioned, though not applied, is for modeling unstable responses in CHOPS (Wang et al., 2011).

To capture a more realistic model than those currently available, it is necessary to take a dynamic approach. To investigate the hypotheses for massive sanding it is necessary to utilize a constitutive model capable of predicting excess pore pressure generation during liquefaction.

Despite numerous efforts in modeling sand production, field case studies show that the ability to predict the quantity and rate of sand production has not been achieved yet. Considering the works reported in the literature, there are still many areas for improvement:

1. No dynamic analysis has been conducted in sanding for those cases with intense WH pulses generated after fast shut-ins in injection wells and high water-cut production wells.

2. The main mechanism is not identified. Although liquefaction is speculated as the main mechanism in sudden and massive sand production in injection wells, it has not been investigated in the current models yet. Progressive failure is another likely mechanism.

3. Critical-state based constitutive models are recognized to predict sand behaviour more precisely. Most of these models are capped to capture compression yielding, which is necessary to capture the compactive sanding response and slit-mode of failure around wellbore (Detournay, C., 2008). Sand tendency to compaction when combined under undrained conditions are expected to lead to liquefaction when WH pressure pulses hit the reservoir.

4. Fatigue and cyclic effect of loading and unloading due to drilling, injection, and WH effect are not included in the current sanding models.

There are other deficiencies in the current models which can be improved. However, addressing all of them is beyond the scope of this work. The main focus of this work is the first two points: modeling the dynamic effect of the WH pressure pulses, investigating the culprit mechanism for massive sanding in injector wellbores and identifying the potential for massive sand production i.e. progressive failure and liquefaction.

2.3 Dynamic Analysis

Dynamic analysis is necessary to capture the response of a medium under dynamic loading. The difference between dynamic and static analysis is the incorporation of the inertia effect in dynamic analysis. Oscillating, fast changing, and impact forces are all considered as dynamic loads. Soil behavior under dynamic loads can be very different from the same under static loads. These differences include, but are not limited to, inclusion of acceleration and damping in the formulation and shear modulus degradation.

After FEM discretization, the equilibrium equation for a dynamic analysis will be in the form of:

$$\underline{M}\ddot{u} + \underline{C}\dot{u} + \underline{K}u - \underline{Q}p = f, \tag{2-1}$$

where $\underline{M}$ is the mass matrix, $\underline{C}$ is the damping matrix, $\underline{K}$ is the stiffness matrix, $\underline{Q}$ is the pressure coefficient matrix, and u, p and f represent the displacement, pore pressure, and force vectors, respectively.

2.3.1 Damping

Damping refers to the gradual decrease of amplitude with time due to environment energy absorbing through mechanisms such as grain-to-grain friction and interface slippage (Das and Ramana, 2011). A suitable model for soil under dynamic loading would capture the hysteresis curves and energy-absorbing characteristics of the soil (FLAC user manual, 2008). In soils and rocks, natural damping is hysteretic, i.e. damping is independent of the applied frequency (Wegel and Walther, 1935; Gemant and Jackson, 1937). For geological materials and for structures, damping commonly falls in the range of 2-5% and 2-10% of the critical damping, respectively (Biggs and Biggs, 1964). A system is critically damped when damping ratio equals one and the system returns to a steady-state

quickly without oscillating. The damping ratio of a soil sample can be measured by a "resonant column test" (Jefferies and Been, 2006).

There are various damping models available in numerical models: Raleigh damping, hysteretic damping, viscous damping, and artificial viscosity. Hysteretic damping is the most realistic representation of soils in which the plastic deformation is independent of the applied load frequency (Gemant et al., 1937; Wege et al., 1935; Bear, 2010). Hysteretic damping is not effective at low strain cycles; therefore, it should be combined with small (about 0.2%) stiffness-proportional Raleigh damping (FLAC user manual, 2008). Artificial viscosity is also used in fluid dynamics especially to damp numerical overshoots behind a shock front and to diffuse the shock front over a number of zones as the shock progresses (Wilkins, 1980). Artificial viscosity does not damp shear waves.

2.3.2 Sand Behavior under Dynamic Loads

Laboratory research has been conducted to measure soil behavior under dynamic loads. Some of the experiments have been specifically proposed to measure the properties of dynamically loaded soils. Figure 2-1 shows damping ratio obtained from previous experimental studies. Other studies show that sand Young's modulus is approximately the same under static and transient loads (Casagrande and Shannon, 1949).
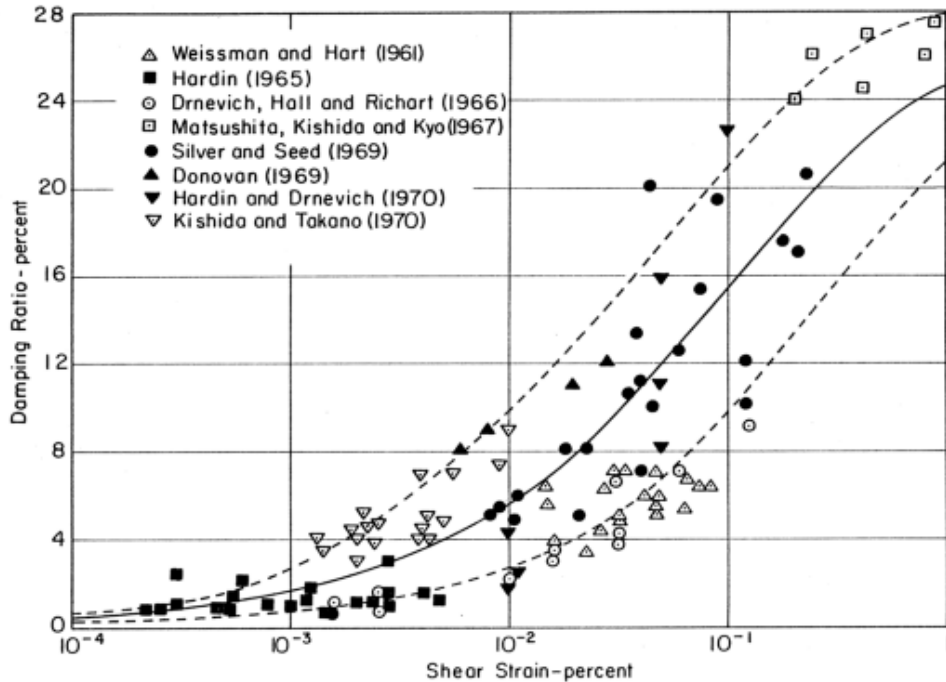
Figure 2-1 Dependence of damping ratio on shear strain for sands (Seed et al., 1984)

2.3.3 Dynamic Formulation

A dynamic analysis involves modeling the mechanical deformation as well as the transient fluid flow and pore pressure distribution considering the acceleration terms. Biot (1956) described the dynamic governing equations in saturated porous media for low frequency waves. The basic principles are conservation of mass and conservation of momentum. Spanos and De la Cruz (1989) extended the formulation by adding thermodynamics and treating porosity as a primary variable. A detailed formulation and numerical solution are presented in Chapter 4.

2.4 Water hammer (WH)

WH is a general term describing pressure wave generation and propagation through liquids in pipes and pipe networks (Jardine et al., 1993). The classic

analysis of WH shows that if flow is stopped suddenly (e.g. a valve is closed) a positive pulse is generated. This positive pulse will travel to the end of the conduit and reflect as a positive pulse if the end of the conduit is closed. If the end empties into a large reservoir the positive pulse will reflect as a negative pulse (McStravick et al., 1992). A typical WH wave is measured in Alaska field (Wang et al., 2008).

2.4.1 Wave Magnitude and Attenuation

The velocity and the magnitude of the initial pressure pulse created depend on the fluid inside the pipe, geometry, stiffness of the pipe material, and frictional effects. The rock quality at the wellbore-reservoir interface affects the amplitude of the reflected waves as energy dissipates faster in a well with higher Productivity Index (PI) (Sadrpanah et al., 2005).

The magnitude of initial WH amplitude can be estimated using:

$$\Delta p_{max} = \rho c \Delta v \tag{2-2}$$

Where ρ is density, Δv is change in fluid velocity, and c is the speed with which the pressure-pulse wave is transmitted along a pipe and is calculated using:

$$c^2 = \frac{\left(\frac{K}{\rho}\right)}{1 + \left(\frac{K}{E}\right)\left(\frac{D}{l}\right)} \tag{2-3}$$

where K is the bulk modulus of elasticity of fluid, E is the elastic modulus of the pipe, D is the inner diameter of the pipe, and l is the thickness of the pipe.

The basic equations for formulating WH are Newton's second law and continuity equation:

$$g\frac{\partial H}{\partial x}+v\frac{\partial v}{\partial x}+\frac{\partial v}{\partial t}+f_f\frac{v|v|}{2D}=0 \tag{2-4}$$

$$\frac{c^2}{g}\frac{\partial v}{\partial x}+v\frac{\partial H}{\partial x}+vsin\theta+\frac{\partial H}{\partial t}=0 \tag{2-5}$$

where f_f is the friction factor, H is the head, v is fluid velocity, and θ is the angle that pipe makes with horizon. These equations can be solved by the characteristic method (Streeter et al., 1998).

Figure 2-2 illustrates that a pulse attenuates considerably during the travel towards longer lengths.

Some measurements at three different depths in a well in Alaska show that only 10% of the wave amplitude generated at the surface is observed at a depth of 1356 m. The frequency however is doubled at higher depths and the wave is no longer a smooth sinusoidal shape at that depth but is in more erratic shock wave form.
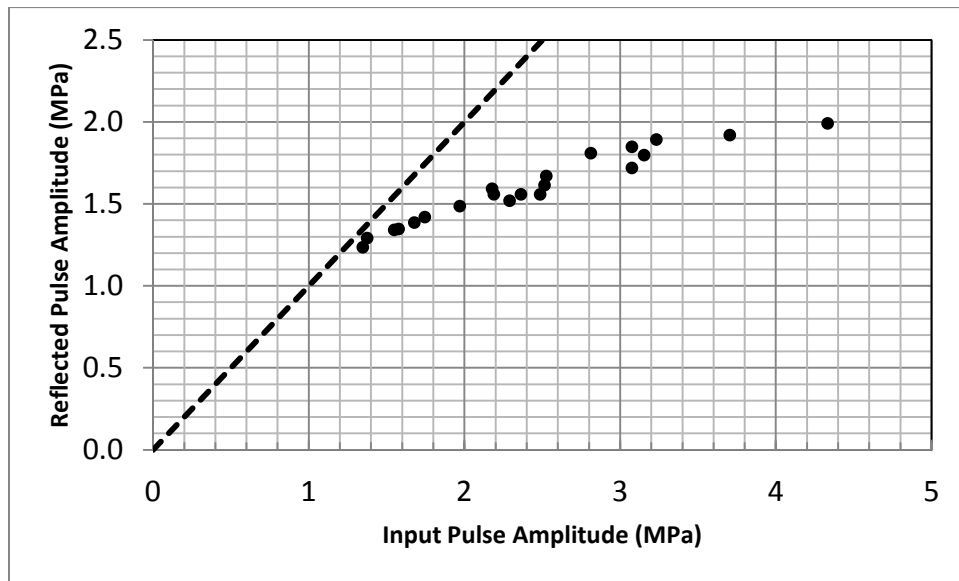
Figure 2-2 Wave attenuation (after McStravick et al., 1992)

Wang et al. (2008) measured the WH wave effects in an Alaska field by downhole memory pressure gauges. The repeatability of the wave generation is

tested by measuring them twice. They found out that WH waves may have frequencies as high as 17 Hz. Hence, WH is a short transient event and its modeling requires a dynamic approach.

2.4.2 WH in Production Wells

Little research in the literature addresses WH effects in producers while most express concern on the impact in injection wells. Hayatdavoudi (2006) investigated sanding and production loss of three high-pressure oil and gas wells in consolidated reservoirs with thin seals and explained peak pressure of WH wave as the primary reason of well sanding. He reported that at least three deep wells with highly consolidated reservoir rocks lost production and produced a great deal of pulverized, highly angular rock fragments.

The aftermath of WH pressure pulsing was as follows: (a) fracture propagation into the water zone below the perforations, (b) increased water saturation in the producing zone, (c) rock strength loss, (d) pulverization of sand, (e) sand production, and of course (f) production loss. The highly angular and orthogonal shapes of the produced sand are indicative of fracture extension, and the sheared surfaces with ripple marks are indicative of the cyclic rock grain slips. Cavitation of trapped gas under high cyclic stress waves may also occur. Hayatdavoudi (2006) also reported a highly fluctuating gas production immediately after the sudden shut-in of the well. The well lost its production after this event.

The author concluded that the instantaneous emergency shut-in of a producer appears to cause a WH effect in the form of strong cyclic peak pressure, which travels down the tubing into the perforations. This extra pressure builds up cyclically in the reservoir rock near the well bore until it is attenuated with time. WH waves detrimentally changed the cyclic effective stresses around the perforations.

The pressure rise due to WH changes the stress around the perforations. As a result, the reservoir rock may fail due to the cyclic WH of the fluid mixture in the well. Therefore, fracture is created in the reservoir, and the grains pulverize. The sets of fractures facilitate water flow towards the perforation and increase both water saturation and water cut. The increased water saturation and pressure build-up within the capillaries weaken the rock strength by as much as 50 percent. The increased water saturation increases the angle of internal friction due to the lubricating effect of water film on the surfaces of rock grains and at the grain contact points. This caused the well to sand up and hurt production (Hayatdavoudi, 2006).

Experiments on the produced grains confirm the presence of highly angular rock fragments and tensile fracture as a result of cyclic stress waves (see Figure 2-3). Since wave damping depends on the fluid compressibility, only producers with high water cuts are vulnerable to detrimental effects of WH.

2.4.3 WH in Injectors

Strictly speaking, WH is an upstream problem while the same term has been largely used in injector wells. The reason might be that a similar mechanism to that of WH is responsible for producing waves in injectors. Once the injection well is shut down, there will be a negative wave travelling down the wellbore. When the wave hits the reservoir, it results in backflow from the reservoir to the wellbore which in turn leads to a high pressure wave. This process continues until all the wave energy is damped. Figure 2-4 shows typical WH pressure pulses measured with downhole gauges in an Alaska field at a depth of 760 m .
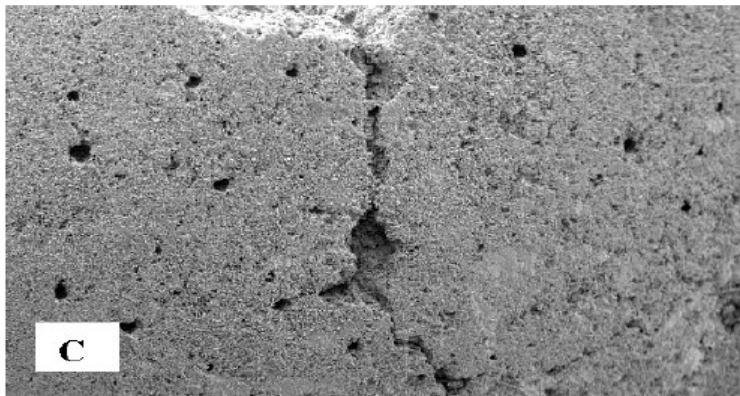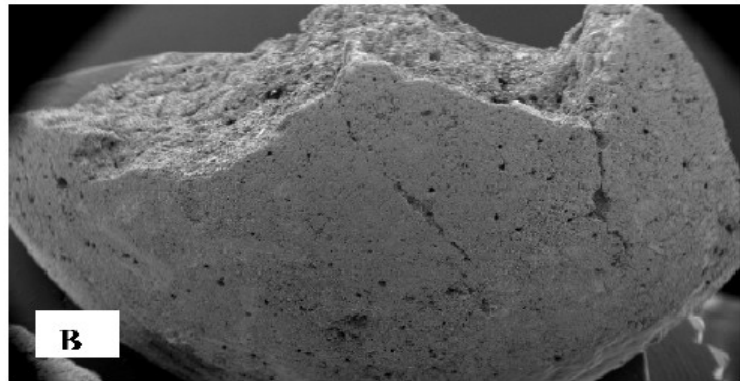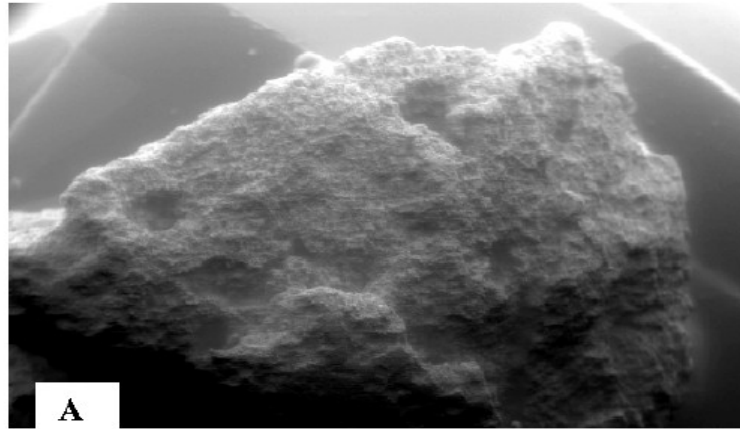
Figure 2-3 Characteristics of rock failure under the action of cyclic stress waves. A) Gas cavitation molds, B) Highly angular and broken grains, and C) Orthogonal set of tensile fracture (Hayatdavoudi, 2006).
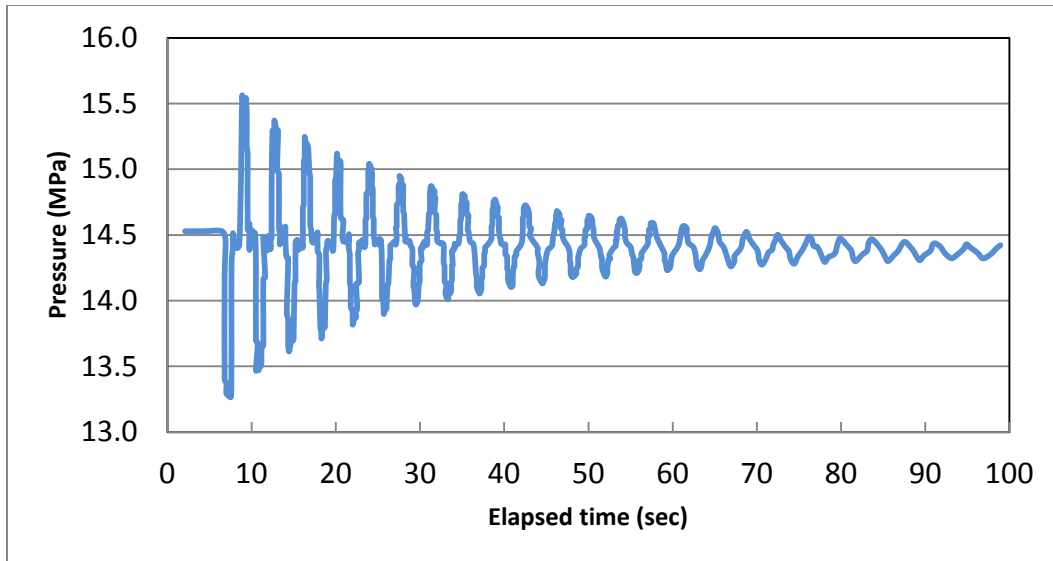
Figure 2-4 WH pressure pulses recorded with downhole gauges in an Alaska field (Wang et al., 2008)

WH waves could be generated in a well due to sudden shut-in caused by pump malfunctions, sudden shut-in on emergency cases by blow-out preventer (BOP), velocity changes due to step-rate-testing (SRT), shut-in by a pressure build-up test, and sudden changes in flow rate during the injection/production. They may also be generated during drilling operations by a kick, tripping out, pulling the string, casing, or even screens (Hayatdavoudi, 2005). WH effects resulting from the shutting-in of water injection wells are an often ignored issue in petroleum production operations, but they have considerable impact on injection well performance and longevity (Wang et al., 2008). It is also more dominant in injectors compared to producers (Sadrpanah et al., 2005; Wang et al., 2008) probably due to lower water compressibility compared to hydrocarbons and less damping of the waves.

The WH effect hits the reservoir formation like seismic waves during the shut-in and may lead to liquefaction of the sand (Santarelli et al., 2000). As a result,

24

sudden shut-in of the well should be avoided; however, there are always emergency cases.

2.5 Progressive Failure

Progressive failure is defined as the process where failure of one element leads to failure of adjacent elements. It refers to non-uniform mobilization of shear strength along a potential failure zone (Morgenstern, 1977) where the self-propagating failure zone develops due to the redistribution of stresses after initial failure.

It is expected that near-wellbore area undergoes failure as a results of drilling, different cycles of injection and shut-in, cohesion-weakening effect of water and WH waves. Stress redistribution and continuous effect of WH waves can lead to failure of additional elements and a growing failure zone. Therefore, progressive failure is a possible mechanism for sudden massive sanding where initial failure around perforations triggers a more global failure.

2.6 Liquefaction

Liquefaction is defined as the process by which temporary and spontaneous loss of shear strength occurs in soils under undrained condition. It is usually associated with medium-to-fine grain cohesionless soils (Das and Ramana, 2011). It is the reduction in the contact forces between particles, and not pore pressure increase, that is responsible for decrease in the effective stress (Dinesh et al., 2004). During straining, gravity loads are transferred from the soil to the pore fluid (Das and Ramana, 2011). As a result, pore pressure increases. Even though straining may be evident for days before the failure, the transition to high excess pore pressures is normally very rapid (Jefferies and Been, 2006). That is why a dynamic approach seems reasonable for modeling liquefaction.

There are two types of liquefaction reported in the literature (Robertson, 1994):

1. Static Liquefaction (Flow Liquefaction): under undrained conditions
2. Cyclic Softening

   a) Cyclic liquefaction: Cyclic shear stresses exceed the initial static shear stress and cause a shear stress reversal. A condition of zero effective stress may be achieved.

   b) Cyclic mobility (limited liquefaction): Deformations accumulate during each cycle of shear stress, but cyclic loads do not yield a shear stress reversal. During static liquefaction under undrained conditions, pore pressure increases such that $P' = 0$. However, this is not the condition for dynamic loading due to the rapid cycles. Figure 2-5 and Figure 2-6 compare the stress paths for different types of liquefactions. Cyclic mobility is typical of dense soils where dilation causes an increase in void ratio and a decrease in pore pressure.

Liquefaction mostly occurs at shallow depths and not at reservoir depths. Also sandstone has less void ratio than that of sand, and based on these factors cyclic mobility seems to be more likely than cyclic liquefaction. However, cyclic mobility cannot justify the production of a large amount of sand as the strength increases after some cycles. It is probable that the increase in void ratio due to sand production around the wellbore at some later stage leaves very soft porous sandstone in place, which has the potential of cyclic liquefaction. At the same time, it is possible that other factors are contributing to massive sand production.
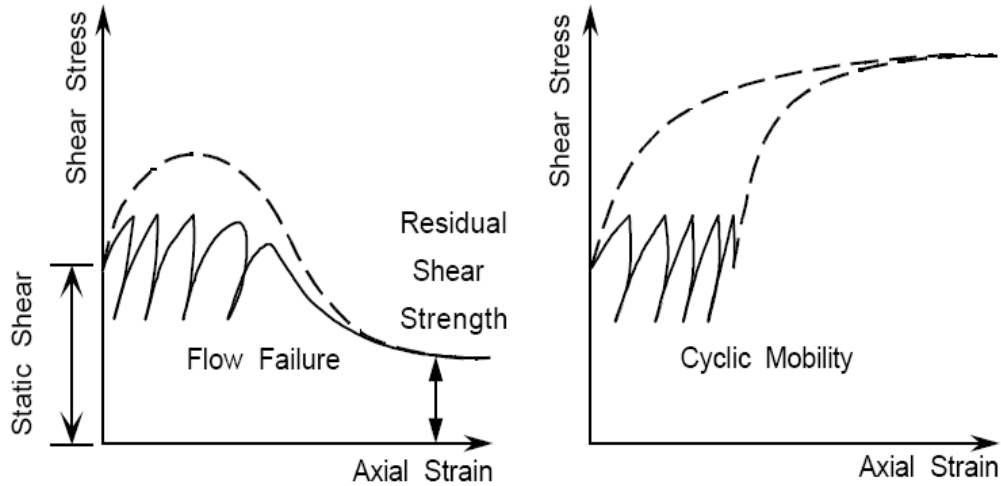
Figure 2-5 Response of contractive (left) and dilative (right) sand under liquefaction (Rauch, 1997)
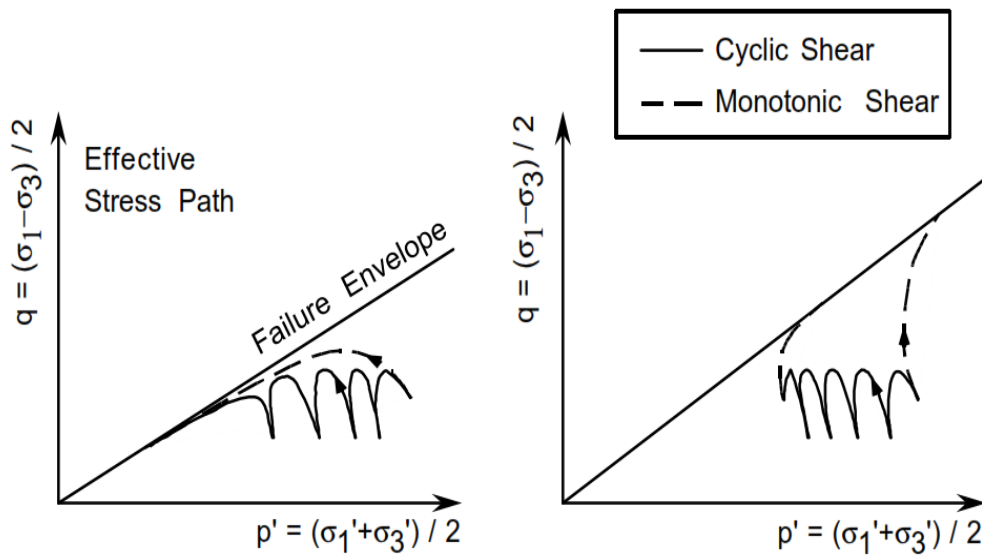
Figure 2-6 Response of contractive (left) and dilative (right) sand under liquefaction in a q-p plot (Rauch, 1997)

Santarelli et al. (2000) took the first steps in proposing liquefaction as the most likely mechanism for catastrophic sanding around injectors. They documented a well undergoing massive sand production in a field in the Norwegian Sea operated by Statoil.

There are a few factors that can be concurrent in injector wells that may lead to liquefaction e.g. water degrading effect on the cementation, presence of a stiff strong cap rock (so that the vertical stress is reduced in the sandstone layer due to the arching effect), previous sand production leading to higher porosity and a tendency to compact, and full degradation of the rock around the wellbore due to drilling and several cycles of injection and shut-in. When WH waves hit the reservoir after quick shut-ins, they expose the degraded sandstone around the wellbore to dynamic loading.

Since no investigation has been performed on liquefaction in wellbores with sand production problems, it is therefore difficult to confirm its role in massive sand production. One may argue that high sandstone density (more tendency to dilate than to compact), high permeability, and cementation around the grains and high depths (thus high stresses) make the conditions of liquefaction unlikely. Under these conditions, one would expect other mechanisms for massive sanding.

2.7 Summary

Although Sand production has been addressed by many researchers, there are still some areas that require further investigation, including the phenomena of massive sand production. There are several factors that lead to massive sand production in injectors such as sandstone degradation due to drilling and several cycles of injection and shut-in, loss of cohesion due to the presence of water, cross-flow, and WH waves. The focus of this study will be the effect of WH waves on massive sanding around injector wells.

The fast nature of pore pressure pulses requires a dynamic analysis where acceleration terms are not ignored. Both liquefaction and progressive failure are among the proposed mechanisms for massive sanding. However, the conditions in reservoirs are not in favor of liquefaction. Lack of sufficient measurements in such incidents makes it hard to defend one mechanism against the other. A

numerical study under dynamic analysis will deepen our understanding of the behavior of near-wellbore reservoir exposed to WH waves and the main parameters triggering and affecting the extent of massive sand production.

2.8 Nomenclature

c Speed of wave in the pipe

$\underline{C}$:   Damping matrix

D Inner diameter of the pipe

E Elastic modulus of the pipe

f Force vector

f_f Friction factor

H Head

k Permeability

K bulk modulus of elasticity of fluid

$\underline{K}$ Stiffness matrix

l Pipe thickness

$\dot{m}$ Rate of mass/sand production

$\underline{M}$ Mass matrix

p Pore pressure

29

q flow rate

t Time

S_L Surface area

$\underline{Q}$ Pressure coefficient matrix

 u   Displacement

v   Fluid velocity

V_L Volume

ε^P Plastic strain

ε_v Volumetric strain

θ Angle of pipe with horizon

λ Sand production coefficient; a calibration parameter

ρ Density

σ_t Tensile stress

φ Porosity

Chapter 3: Elastoplastic Behavior of Sandstone[2]

3.1 Introduction

Sand production is a two-stage process. The first stage involves sandstone degradation due to the stress concentration induced by creating and completing the wellbore. The degraded sand particles may then be dislodged by the seepage forces during the petroleum production or, in the case of injection wells, during the back flow and cross flow following the well shut-in. Hence, capturing the sandstone degradation by accurately describing the hardening/softening behavior normally observed in sandstone is essential in the sanding simulation. Yet, as discussed in Chapter 1, most sanding models have been based on simple constitutive models that do not adequately capture the sandstone degradation. One reason for this is the complexity involved in the calibration of advanced constitutive models that capture the plastic hardening and softening.

This chapter presents a detailed approach to calibrate a bilinear Mohr-Coulomb model for simulating the degrading behavior of sandstones. The procedure is demonstrated by calibrating the model for two sets of triaxial testing data on two different sandstones, namely TB and Castlegate sandstones. The same constitutive model will be used in Chapter 5 to simulate the degradation of weakly-consolidated sandstone in a dynamic analysis.

---

[2] This chapter is based on the following publication: Jafarpour, M., Rahmati, H., Azadbakht, S., Nouri, A., Chan D., Vaziri, H., 2012. Determination of mobilized strength properties of degrading sandstone, J. of Soils and Foundations, Vol 52, Issue 4, pp. 658-667.

Sandstone is a granular material with cementation that shows frictional and dilatancy behavior. Sulem et al. (1999) showed that sand behavior can be modeled using the friction hardening and cohesion softening concept using the Mohr-Coulomb model. Sulem's work assumes uniform deformation in triaxial tests and produces questionable results by neglecting localization of deformation. Later, Nouri et al. (2009) adopted the same approach for calibration, but used a bilinear Mohr-Coulomb yield surface instead of a linear one to capture a more accurate behavior at high effective confining stresses.

This chapter presents a few modifications and simplifications that are incorporated into Sulem's work (1999) to ensure the calibration procedure is easy to implement, objective, and efficient in mimicking the rock behavior. Bilinear Mohr-Coulomb yield surface is used, which was also adopted by Nouri et al. (2009). Emphasis is given here to simulating the softening behavior of the material. Sulem's work is based on uniform deformation in a triaxial test, an assumption which is questionable in the softening regime where localization occurs. Hence, the approach proposed by Vermeer and de Borst (1984) is adopted for modeling the softening regime. They calibrated the softening regime using an exponential function with a tuning parameter to match the experimental data. Fracture energy regularization is also employed to enhance the Mohr-Coulomb model. In addition, an oriented mesh with an inclination equal to the expected rock failure angle is used. This special mesh design limits the localized deformation to only one element size so that the shear band thickness is produced numerically. The model calibration is applied to different sandstones (Castlegate and TB sandstone). Back-analysis of the results is then conducted to ensure the calibrated formulation can predict the experimental results. The chapter ends with the results of mesh sensitivity analysis and a comparison of the results of an oriented mesh with those of a regular mesh.

3.2 Theory and Formulation

3.2.1 Elastic Properties

Stress-dependent elasticity is commonly observed in sandstone and more generally in granular materials. For simplicity and due to a lack of unloading data, however, elastic parameters are assumed to depend on the confining stresses but not on the plastic strain. Due to a lack of unloading data, however, the error in the selection of the initial yield point is inevitable. Elastic properties are determined at 50% of the peak stress (see Figure 3-1) as recommended by Schanz et al. (1999). The Poisson's ratio can be calculated using the definition of $-\frac{\varepsilon_r}{\varepsilon_z}$, and the Young modulus is calculated by:

$$E = \frac{q}{\varepsilon_z} \qquad\qquad\qquad (3\text{-}1)$$

where v is the Poisson's ratio, ε_i is strain in the i direction, E is Young's modulus, and q is the shear stress.

Sulem et al. (1999) emphasized the significance of calibration of the elastic moduli since they not only affect the elastic calculations but also influence the calculation of the plastic strains considerably.
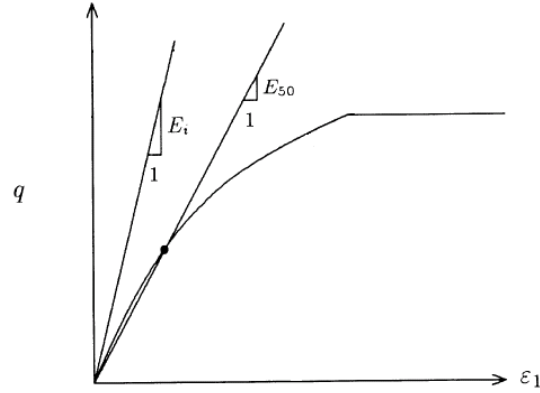
Figure 3-1 . Secant stiffness modulus at 50% of the peak loading, E50 (Schanz et al., 1999)

3.2.2 Yield Surface

The yield function implemented is a bilinear Mohr-Coulomb model which was also used by Nouri et al. (2009). Figure 3-2 shows the yield surface in a T - P plot where T is the square root of the second invariant of the deviatoric stress tensor and P is the mean effective stress. For a triaxial test conditions, they are simplified as:

$$P = \frac{\sigma_{ii}{}'}{3} = \frac{\sigma_z' + 2\sigma_r'}{3} \tag{3-2}$$

$$T = \sqrt{J_2} = \sqrt{\frac{1}{2} S_{ij} S_{ji}} = \frac{|\sigma_z - \sigma_r|}{\sqrt{3}} \tag{3-3}$$

The yield surface equation is bilinear with each line described by:

$$F = T - \mu(q + P) = 0 \tag{3-4}$$

where μ is the friction coefficient. It has the following relationship with the mobilized friction angle for the axisymmetric state of stress:

$$\mu = \frac{2\sqrt{3}\sin\varphi}{3 - \sin\varphi}$$

(3-5)
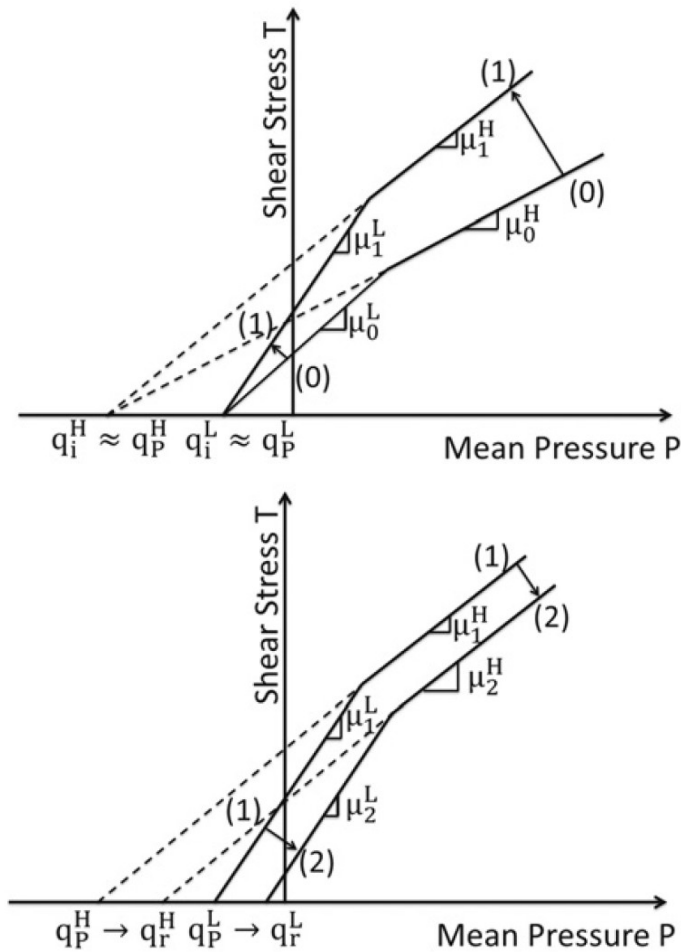
Figure 3-2 Friction hardening (top) and cohesion softening (bottom) of the bilinear Mohr-Coulomb model (Jafarpour et al., 2012)

q is the tension cut-off which can be related to the mobilized cohesion, C, by the following relation:

$$q = C/\tan\varphi$$

(3-6)

The behavior of sandstone is schematically demonstrated in Figure 3-2, where Line (0) shows the initial yield surface. Once a stress state reaches Line (0),

plastic deformation begins. Further loading increases the friction coefficient or the slope of the line up to the peak yield surface (Line (1)). This is shown by the upward arrows from Line (0) to Line (1). Up to this point, the tension cut-off is approximately constant both for the low and high effective confining stresses ($q_i{}^L \approx q_P^L$ and $q_i^H \approx q_P^H$). Additional deformation after the peak results in the softening of the material and shrinkage of the yield surface. This is demonstrated in Figure 3-2 (bottom) by the downward arrows from Line (1) to Line (2). During softening, tension cut-off shrinks to the residual value (q_r), and it is equal to zero for fully degraded sandstone, as depicted in Figure 3-2 (bottom). However, the friction coefficient remains constant. That is, the line is lowered to the residual state with the same slope as that of the peak. Line (2) is the new yield surface during softening when the residual tension cut-off gradually decreases to zero leading to the development of shear bands.

3.2.3 Friction Hardening

Plotting the initial yield points and peak stress points for all the tests in the T - P space gives the yield functions at initial yielding and at peak strength. The plot gives an indication in dividing the data into two lines: low effective confining stress (LECS) and high effective confining stress (HECS). The data are fitted using a bilinear curve whose slopes give the friction coefficient at LECS and HECS.

In measuring plasticity, the hardening parameter rate is defined as:

$$\dot{h}_p = \sqrt{\frac{(\dot{\varepsilon}_z^{ps})^2 + (\dot{\varepsilon}_r^{ps})^2 - \dot{\varepsilon}_r^{ps}\dot{\varepsilon}_z^{ps}}{3}} \tag{3-7}$$

where $\dot{\varepsilon}_i^{ps}$ is the plastic shear strain rate in the i direction. The hardening parameter, h_p, is the cumulative summation of the hardening parameter rates.

Sulem et al. (1999) suggested that the friction angle in the hardening phase can be related to the hardening parameter using the following formulation:

$$\varphi = \begin{cases} \sin^{-1}\left(y_0 + \dfrac{(m_1 - m_2 h_p)h_p}{1 + m_0 h_p}\right) & 0 \le h_p \le h_p^P \\ \varphi^P & h_p \ge h_p^P \end{cases} \tag{3-8}$$

To calculate this friction angle one has to obtain q and μ from the peak yield stress. The value of q may change from the initial to peak yield stress, especially at HECS, but the change is found to be insignificant. Assuming q is constant from the initial yield point up to the peak point, the friction coefficient can be calculated based on the T and P values from the triaxial tests. The friction coefficient is also a function of the mean stress. Sulem et al. (1999) assumed the friction coefficient is a function of the plastic shear strain and a linear function of the mean stress. In this work, two lines are calibrated (one for LECS and another one for HECS) instead of considering the mean stress in the formulation.

3.2.4 Cohesion Softening

In the softening regime, the friction coefficient is assumed to remain constant and equal to the value at the peak strength. However, a decrease in the tension cut-off (Sulem, 1999) results in a decrease in cohesion. The formulation proposed by Sulem et al. (1999) is used in simulating tests on sandstone, which produced poor results. The reason is primarily attributed to the localized deformation in the post-peak regime, which was assumed to be uniform in Sulem's approach. Hence, the method proposed by Vermeer and de Borst (1984) is utilized to describe the cohesion behavior for the softening part. The following functional form is used:

$$c^* = c^P \exp\left[-\left(\frac{h_p - h_p^P}{h_c}\right)^2\right] \tag{3-9}$$

where c^* is the softened cohesion, c^P is the mobilized cohesion at peak, h_p^P is the hardening parameter at peak strength, and h_c is a calibration parameter.

3.2.5 Mobilized Dilation Angle

Plastic volumetric strains, also known as shear dilation, develop as a result of plastic shear strain. Shear dependency is defined by the dilation angle:

$$\sin \psi = \frac{\dot{\varepsilon}_v^p}{-2\dot{\varepsilon}_z^p + \dot{\varepsilon}_v^p} = \frac{d\varepsilon_v^p}{d(-2\varepsilon_z^p + \varepsilon_v^p)} \tag{3-10}$$

where ψ is dilation angle, $\dot{\varepsilon}_v^p$ is rate of volumetric plastic strain, and $\dot{\varepsilon}_v^p$ is rate of axial plastic strain.

Equation (3-10) can be used to calibrate the dilation angle directly from triaxial testing data. Another approach is to use Rowe's dilatancy formula. Rowe (1972) correlated the mobilized dilation angle to the mobilized friction angle:

$$\sin \psi = \frac{\sin \varphi - \sin \varphi_{cv}}{1 - \sin \varphi \sin \varphi_{cv}} \tag{3-11}$$

where φ_{cv} is the constant volume friction angle (Rowe, 1972), which can be calculated from the dilation angle and friction angle at the peak strength in Rowe's formula.

3.3 Calibration of Experimental Data

The results of 16 triaxial tests on sandstone core samples from a petroleum reservoir, referred to as TB here, are utilized. The samples were taken from different depths and at different temperatures and orientations with respect to the bedding plane.

Four out of the 16 tests were selected for this calibration task. All samples for these four tests were from the same depth, with the core plug axis being perpendicular to the bedding plane, and the tests were carried out at a temperature of 21.11º C (70º F).

As for the Castlegate sandstone, conventional triaxial compression testing results were available for six samples. The stress-strain responses are shown in Figure 3-3 and Figure 3-4. Each curve shows the response at a different confining stress. The figures show show the average radial strains measured at two points 90º apart on the outer surface and at mid-height of the samples. Both TB and Castlegate sandstones were used in the calibration as disussed next.

Figure 3-5 shows the best-fit envelopes for the initial yield and peak yield on a T vs. P' scale. The selection of initial yield is based on deviation from straigth line due to a lack of unloading data.
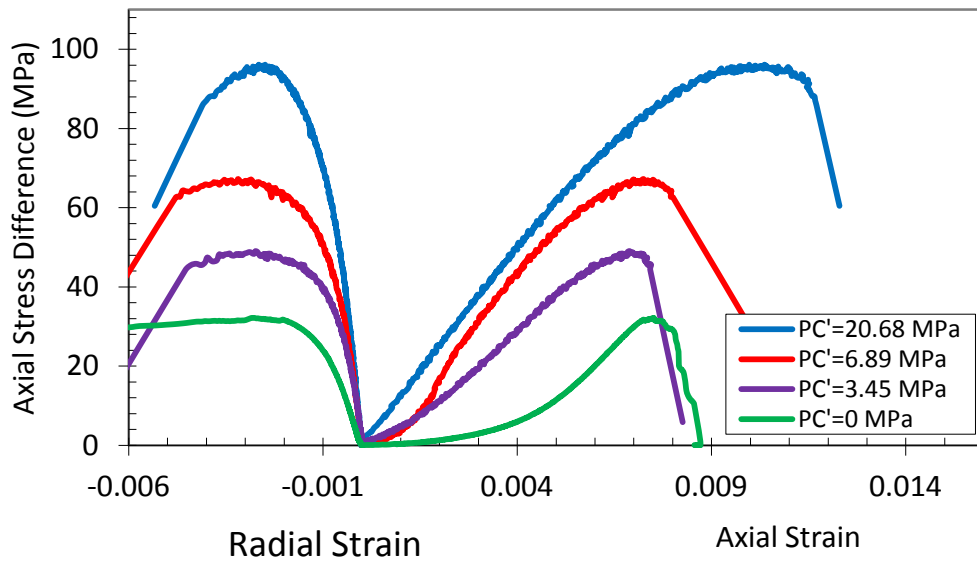
Figure 3-3 Experimental triaxial data for TB at different effective confining stresses (ECS)
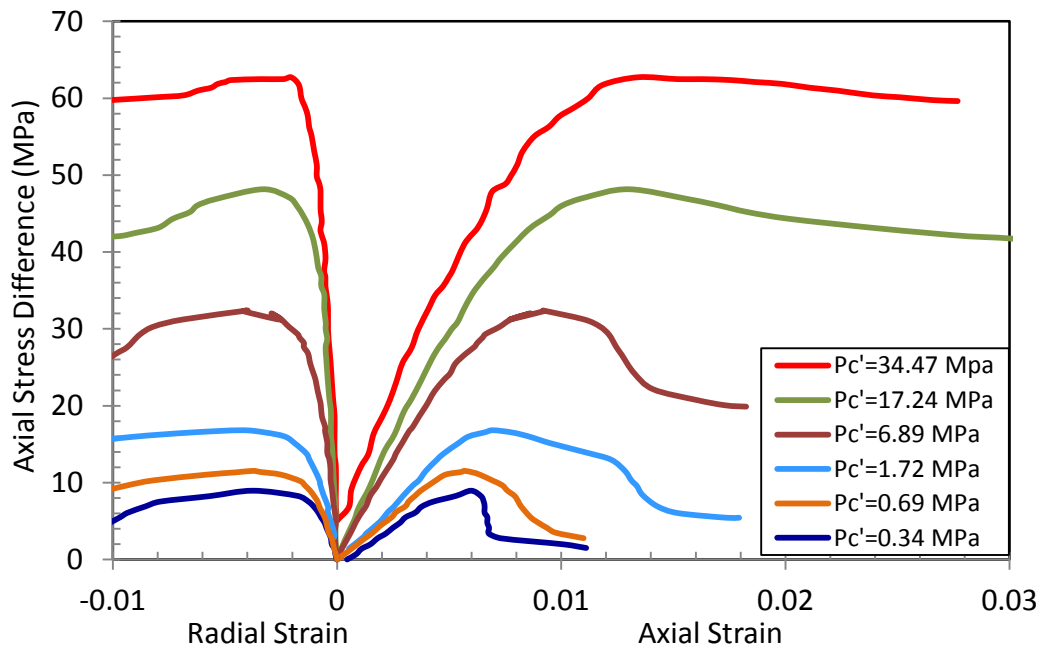
Figure 3-4 Experimental triaxial data on Castlegate at different ECS's

40
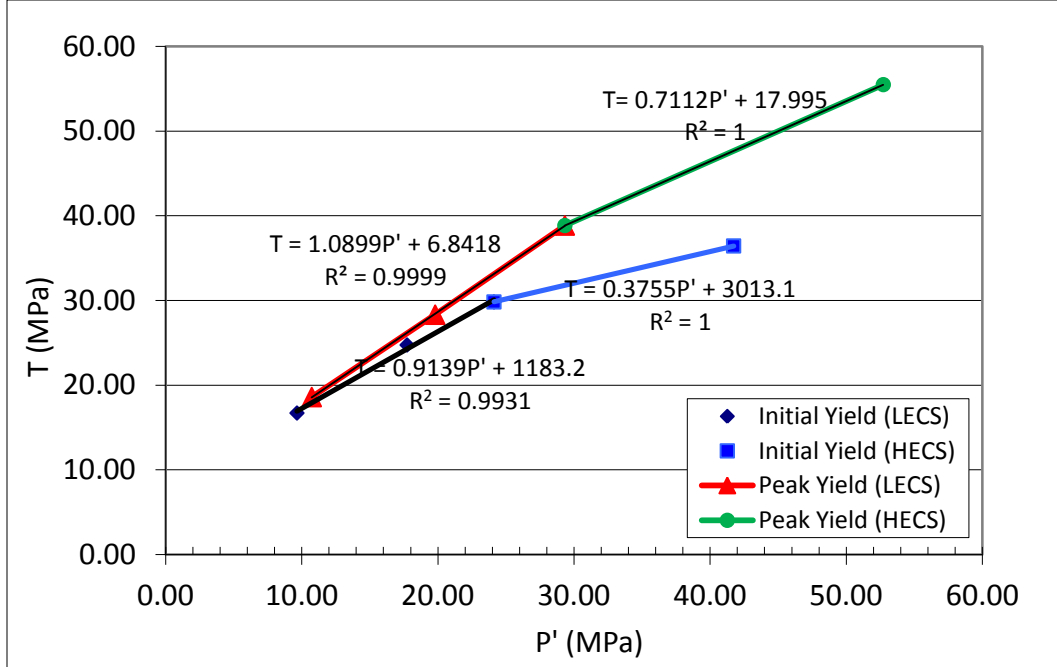
Figure 3-5 Failure envelope at initial and peak yield based on triaxial tests on TB

3.3.1 Friction Hardening

As stated above, experimental data indicate a nearly constant q in the pre-peak phase. q is evaluated from the yield envelope at the peak strength. Next, the pre-peak triaxial data are used in Eqs. (3-4) and (3-7) to plot the friction coefficient versus the hardening parameter for LECS and HECS. A correlation is found based on the best fitting curve of Eq. (3-8) For TB at LECS:

$$\mu = \begin{cases} 1.06 + \dfrac{(258 - 1823h_p)h_p}{1 + 3203h_p} & 0 \leq h_p \leq 0.002 \\ 1.12 & h_p \geq 0.002 \end{cases} \tag{3-12}$$

and at HECS:

$$\mu = \begin{cases} 0.65 + \dfrac{(168 - 6543h_p)h_p}{1 + 680h_p} & 0 \leq h_p \leq 0.003 \\ 0.8 & h_p \geq 0.003 \end{cases} \tag{3-13}$$

41

Figure 3-6 shows the friction angle versus hardening parameter calculated from Eq. (3-5), (3-12) and (3-13) for TB sandstone.

In the same way, for Castlegate at LECs:

$$\mu = \begin{cases} 0.819 + \dfrac{(300 - 9060h_p)h_p}{1 + 1580h_p} & 0 \le h_p \le 0.0025 \\ 0.96 & h_p \ge 0.0025 \end{cases} \tag{3-14}$$

and at HEC:

$$\mu = \begin{cases} 0.418 + \dfrac{(80 - 31614h_p)h_p}{1 + 665h_p} & 0 \le h_p \le 0.0011 \\ 0.446 & h_p \ge 0.0011 \end{cases} \tag{3-15}$$
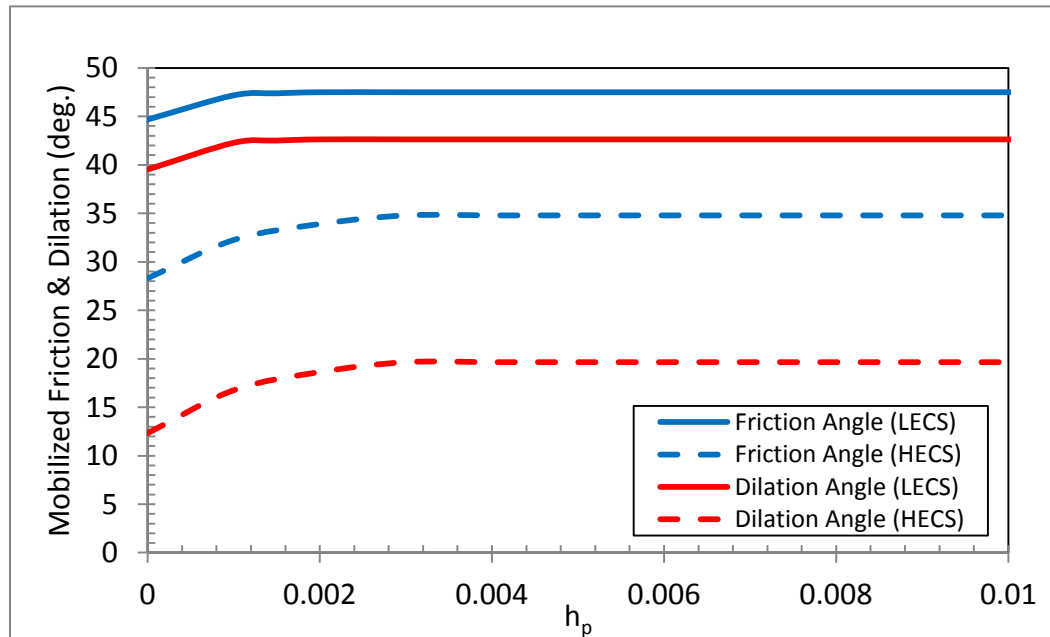
Figure 3-6 Friction and dilation angles of TB vs. hardening parameter

Figure 3-7 shows the friction angle versus hardening parameter calculated from Eqs (3-5), (3-14) and (3-15) for Castlegate sandstone.
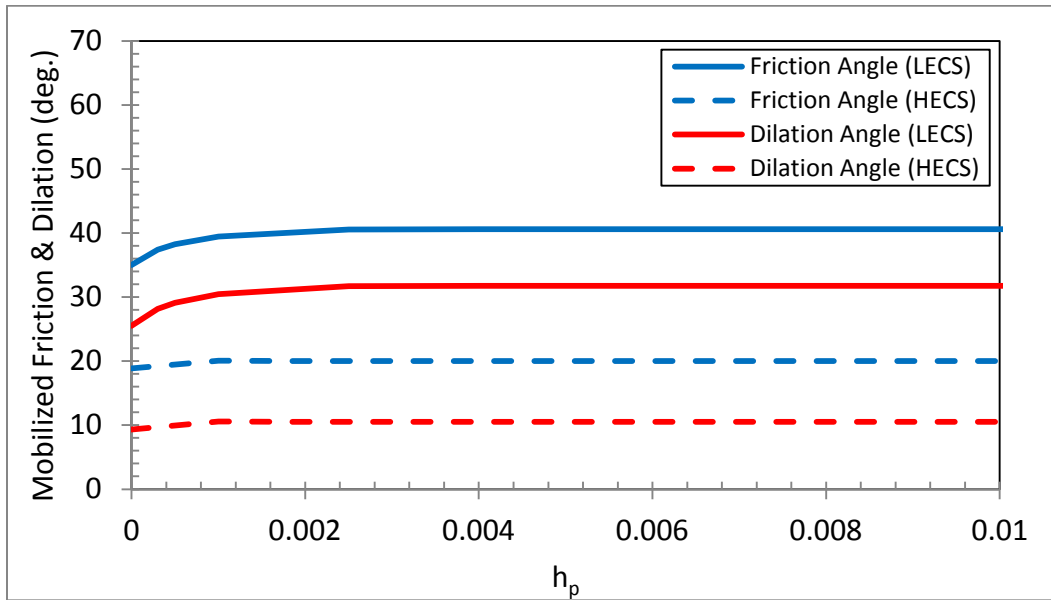
Figure 3-7 Friction and dilation angles of Castlegate vs. hardening parameter

3.3.2 Cohesion Softening

For the post-peak regime, it is assumed that the friction angle remains constant at peak-strength. The constant friction angle was used along with cohesion from Eq. (3-9) in a series of numerical simulations. Several values were tried for the calibration parameter h_c. In the end, values of 0.05 and 0.1 for the calibration parameter were found to give the best match at LECS and HECS for TB. The mobilized cohesion is shown in Figure 3-8.
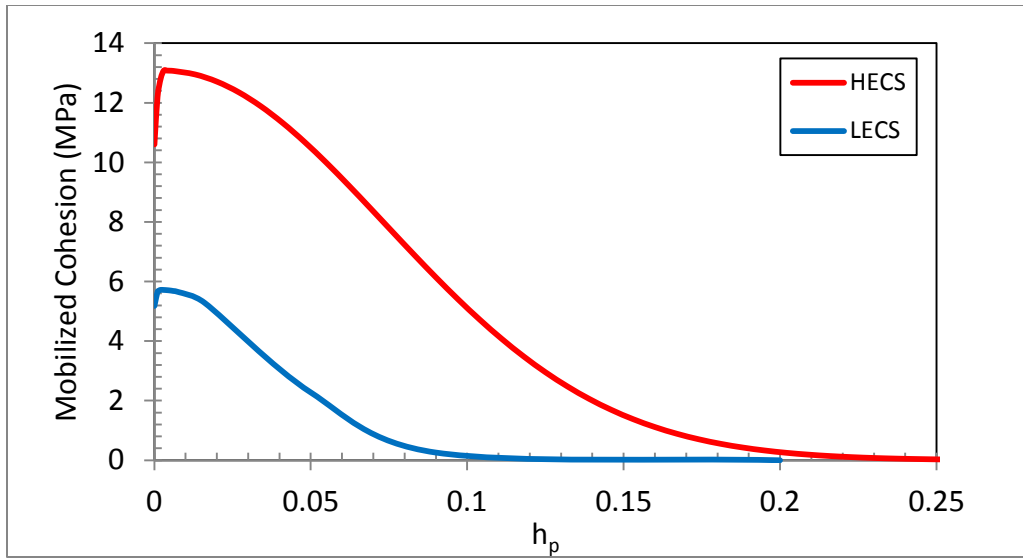
Figure 3-8 Mobilized cohesion vs. hardening parameter for TB

In the same way, values of 0.15 and 0.2 for the calibration parameter are found to give the best match at LECS and HECS for Castlegate, respectively. The mobilized cohesion for this sandstone is shown in Figure 3-9.
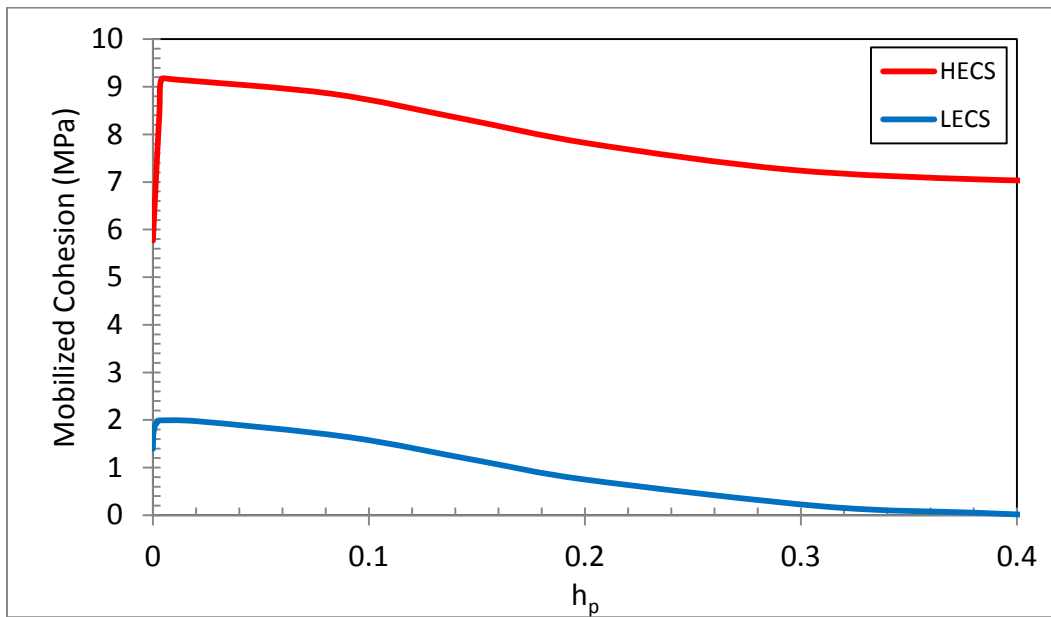
Figure 3-9 Mobilized cohesion vs. hardening parameter for Castlegate

3.3.3 Mobilized Dilation Angle

The dilation angle at the peak strength is calculated using Eq. (3-10), which is then used along with the friction angle at the peak strength to calculate $\sin \varphi_{cv}$ in Eq. (3-11). Applying this procedure, the average values of 0.12 at LECS and 0.29 at HECS are used for $\sin \varphi_{cv}$ for TB, while 0.19 at LECS and 0.17 at HECS are used for Castlegate. The relationships for the friction angle as a function of the hardening parameter are already known; therefore, equations for the dilation angle as a function of hardening parameter can easily be established at LECS and HECS. Since the friction angle is assumed constant in the softening regime, Eq. (3-11) predicts constant dilation angle after the peak.

Figure 3-6 and

Figure 3-7 show the calculated dilation angle for TB and Castlegate, respectively.

3.4 Numerical Modeling of Sand Softening Behaviour

Simulation of the post-peak response of geomaterials using continuum-based models has been observed to produce results that are spuriously dependent on the numerical mesh design. The continuum model must be modified by a regularization method to reduce or eliminate mesh dependency (Crook et al., 2003). Regularization can be carried out by incorporating a characteristic length scale into the formulation. The characteristic length depends on the material, and it is usually related to the grain sizes of the granular material. Methods such as Cosserat continuum, gradient plasticity, and non-local models have been used to address the mesh-dependency problem. However, the Cosserat method is effective as a regularization method when frictional slip is prevailing (Sluys, 1992). Gradient plasticity regularization is applicable as long as the shear band is thicker than the element size, thus requiring a very fine mesh in many cases. Non-local models are computationally intensive when modeling field-scale

45

applications. Fracture energy regularization developed by Pietruszcak and Mroz (1981) and Bazant and Oh (1983) among others is applied here. This method also has its limitation: the characteristic length of the element must be larger than the material characteristic length. However, this is of little consequence for field applications (Crook et al., 2003).

3.4.1 Fracture Energy Regularization

During the hardening phase, the deformations are nearly uniform. As a result, the whole sample deforms uniformly independent of the mesh design. However, in the softening regime, deformation concentrates in the shear bands. When numerically solving the equations for the softening regime, the shear band resolves itself into the smallest possible thickness, which is one row of elements. The energy released for this localized deformation depends on the size of the shear band (i.e., the size of that one row of deforming elements). The larger the elements, the higher the energy release rate. This difference in energy release for different mesh sizes results in the mesh-dependency. This mesh dependency is not observed in the hardening regime because the whole sample deforms uniformly; hence, the same energy is used to deform the sample for different mesh sizes. But once the deformations are localized, the behavior will be different.

Figure 3-10 shows the mesh dependency normally observed in the softening regime for TB sandstone. For brevity, only the results of TB sandstone are presented in this part. There are several methods to regularize the continuum to reduce this mesh dependency. One way is to use fracture energy regularization in which one has to include a material characteristic length, l_c^m. The finest acceptable mesh is when $l_c^e = l_c^m$, where l_c^e is the characteristic length of the element defined as the diameter of the sphere (circle) having equal volume (area) to the element under consideration.
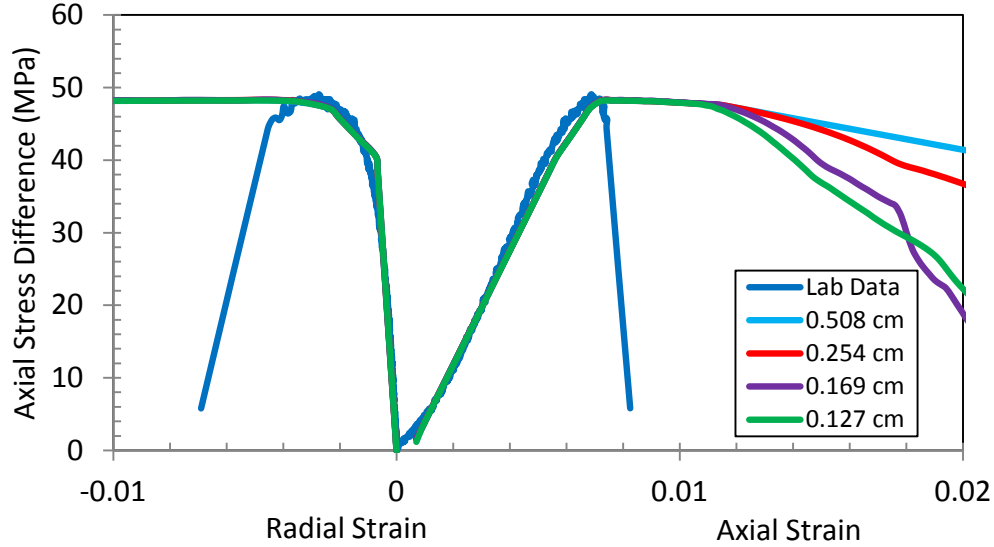
Figure 3-10 Mesh-size dependency in the softening regime (legend shows mesh size)

To use larger element sizes, one needs to change the hardening parameter such that it yields the same fracture energy (Crook et al., 2003):

$$h_p^e = h_p^m (\frac{l_c^m}{l_c^e})^n \qquad (3\text{-}16)$$

where h_p^m is the material hardening parameter, h_p^e is the modified hardening parameter, and *n* is a material constant equal to unity when the energy release rate for the fracture growth is constant. The value of *n=0.6* is calibrated in this work.

Eq. (3-16) makes the energy release (area under the stress-strain curve) in the softening region the same for different element sizes.

3.4.2 Shear Band Thickness

Previous research suggested that the shear band thickness, t_s, should be 10 to 20 times the mean grain size, d_{50}, of the material (Desrues and Hamad, 1989; Oda and Kazama 1998; Viggiani et al., 2001; Yoshida et al., 1994). Marcher and Vermeer (2001) assembled all the data and correlated them using two lines:

$t_s = 10d_{50}$ and $t_s = 20d_{50}$. They then concluded that most data coincide with the line $t_s = 10d_{50}$. They also reported that the data falling on this line were obtained by more reliable measurement techniques such as thin-slice and X-ray methods. Hence, we assume the shear band thickness is about 10 times the mean grain size.

3.4.3 Characteristic Length

The mesh size is selected so that the same experimental shear band thickness is produced numerically. It is important to accurately reproduce the thickness of the shear band to avoid, or at least to reduce, the mesh dependency of the results in the softening phase. In other words, the size of the elements is selected such that the actual size of the shear band is reproduced numerically. The material characteristic length, l_c^m, has been reported to be equivalent to the shear band thickness (Nouri et al., 2009). However, this assumption is only valid as long as the shear band is produced within one row of elements. Figure 3-11 shows a linear dependency of the numerically produced shear band thickness on the material characteristic length for a common rectangular element. Shear band would be approximately 4.73 times the characteristic length for rectangular shaped elements. Hence, for a rectangular element:

$$l_c^m = \frac{t_s}{4.734} = \frac{10d_{50}}{4.734} = 2.11d_{50} \tag{3-17}$$
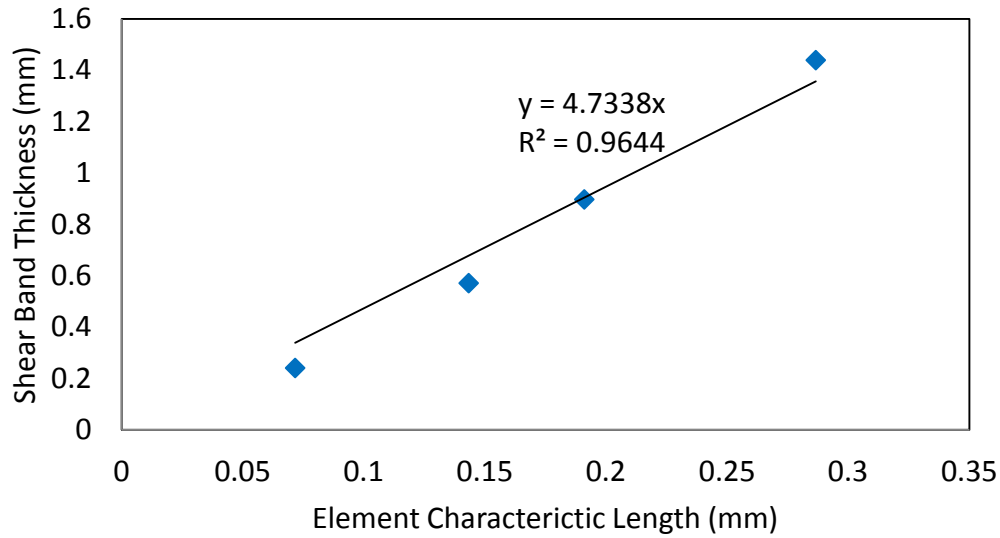
Figure 3-11 Dependency of numerically produced shear band thickness on the characteristic length

Since this value is only an average value between a limited number of tests and since localization usually occurs diagonally with an inclination of the failure angle, the shear band will still be slightly thicker than the real physical size (Figure 3-12 a and b). Therefore, oriented mesh geometry is used to reduce the size of the shear band to one row of elements only (Figure 3-12 c). Several numerical experiments demonstrate that if the angle of oriented mesh is the same as that of the failure angle, i.e. $45 + (\frac{\varphi+\psi}{4})$, the shear band will be limited to one element row, and the material characteristic length will be the same as the shear band thickness (Figure 3-12 c). If the effect of the mesh shape was not considered in the characteristic length, we would have had different results even with regularization.
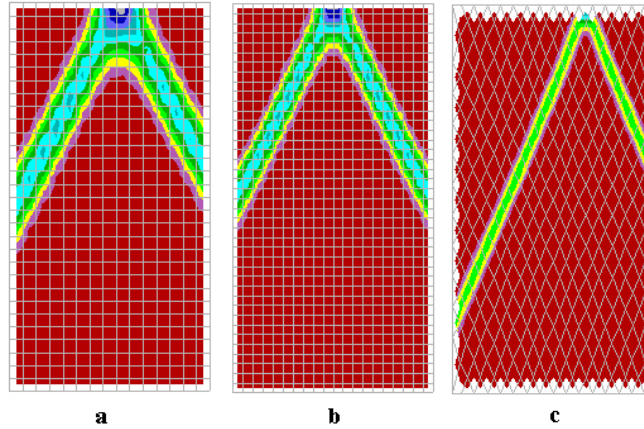
Figure 3-12 Plastic strain contours for different mesh designs: a) coarse mesh, b) fine mesh and c) oriented mesh

The oriented mesh is considered to be the base case here, and all the other simulations are compared with this base case. A plane strain model with regular rectangular mesh (both coarse and fine) is simulated and compared with the base case. An axisymmetric model is also performed and compared with the base case.

In field-scale simulations it is impossible to predict the failure zone and align the mesh with that, especially when the failure occurs at different angles such as breakouts around a wellbore. The purpose here is to match the rectangular mesh results with the oriented one as much as possible.

3.5 Back-Analysis of Triaxial Tests

Back-analyses of the tests are performed using FLAC software. Various approaches are taken to capture the stress-strain behavior of the reservoir rock. It is common to simulate triaxial experiments using an axisymmetric configuration; however, an axisymmetric configuration does not allow localization of deformation. A plane strain configuration is used to capture localization. The results are later compared with those from using an axisymmetric configuration. Fracture energy regularization is applied to remove mesh dependency.

50

3.5.1 Mesh Size

The triaxial samples are 1 in. (2.54 cm) in diameter and 2 in. (5.08 cm) in length. Mesh sizes of 0.2 in. (0.508 cm), 0.1 in. (0.254 cm), 0.067 in. (0.169 cm), and 0.05 in. (0.127 cm) are used for the rectangular mesh. The mean average grain size of TB is 0.0055 in. (0.14 mm). Hence, the characteristic length would be approximately 0.0116 in. (0.2957 mm) and 0.055 in. (1.4 mm) for the rectangular and oriented mesh, respectively.

3.5.2 Boundary Conditions

The bottom boundary of the finite element mesh is fixed in the z (vertical) direction. The radial and axial loads are applied on the boundaries, and then a small velocity in the vertical direction is applied on the top boundary as directed by the experimental procedure.

In the laboratory experiments, two steel platens are used at the top and bottom of the rock samples. Axial loads are directly applied on the platens. The surfaces between the steel and the rock are usually lubricated to avoid end effects. As a result, the platens are assumed to be frictionless.

3.5.3 Back-Simulation Results

As described previously, plane strain conditions with oriented mesh are used in the simulation. The elastoplastic material properties are calculated as presented in Section 3.3. Tables of cohesion, friction, and dilation angle versus hardening parameter are used as the input data in the model. The results are presented in Figure 3-13 and Figure 3-14.
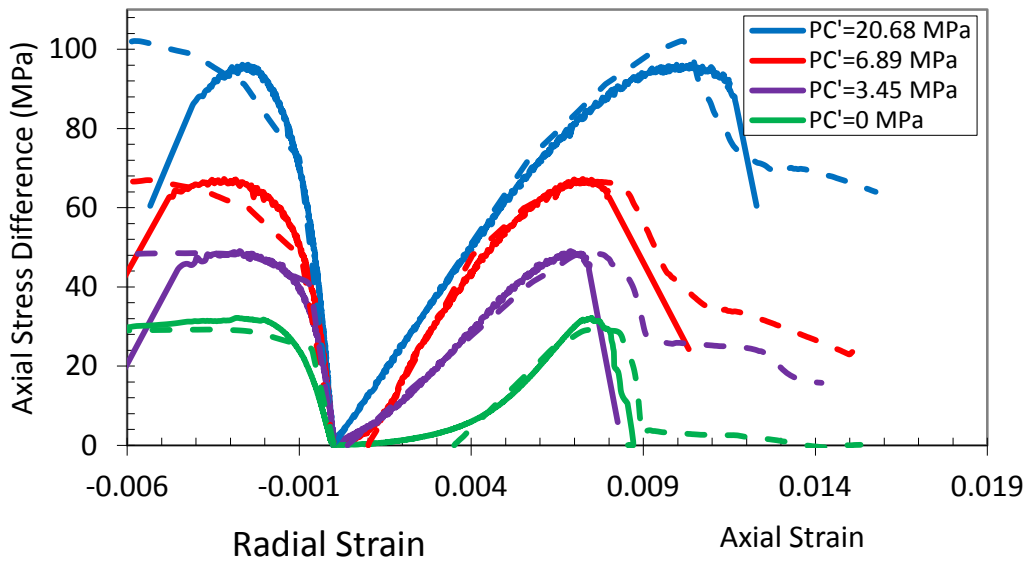
Figure 3-13 Comparison of simulated results with triaxial experiments for TB sandstone (simulated results are shown with dash lines)

It should be noted that radial displacement measurements are not uniform along the sample after the onset of localization. In other words, radial displacements at different heights and radial angles are different. Two experimental radial strain measurements are located at mid-height 90º apart to compare the experimental radial displacements with numerical calculations. Hence, obtaining a match for the radial strains is not carried out in this calibration. Actually, the radial displacements for plane strain conditions are the maximum displacements possible. Accurate calculation of radial strain requires a 3-D analysis, and even then it is difficult to compare radial strain with the laboratory measurements taken at only two measurement points.

LECS   HECS
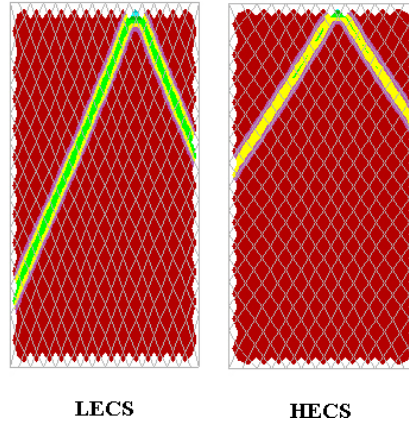
Figure 3-14 Plastic strain contours showing the formation of shear band

In addition to TB, the calibration and simulation method is applied to six Castlegate tests as well. The results are shown in Figure 3-15.
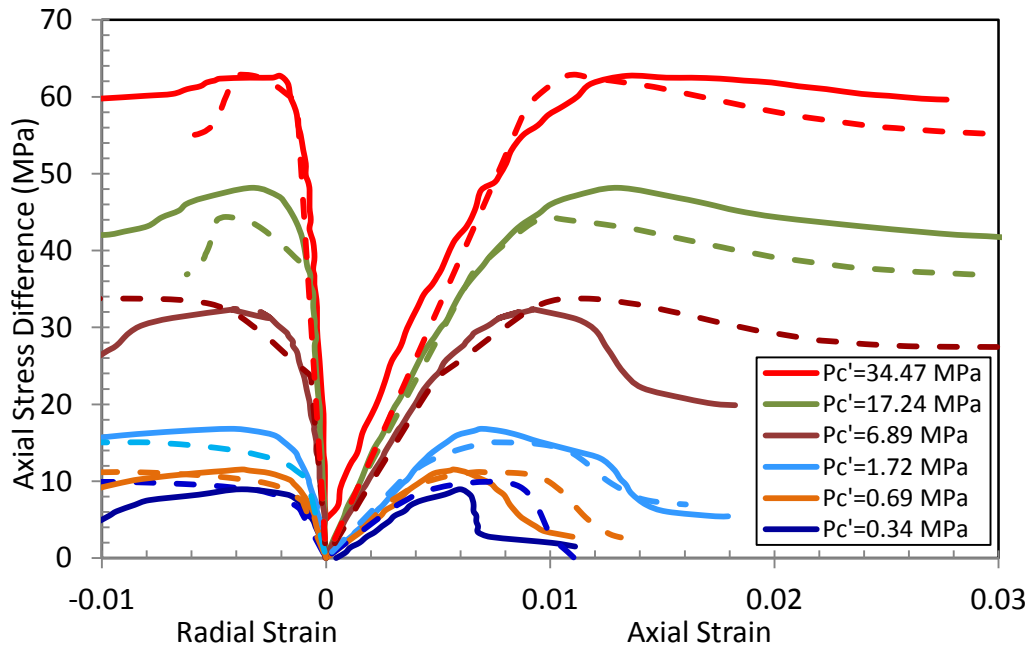
Figure 3-15 Comparison between simulation and triaxial test results for Castlegate sandstone (simulated results are shown with dash lines)

3.5.4 Effect of Mesh Design

Regular coarse mesh and fine mesh with fracture energy regularization are also simulated using the calibrated data and are compared with the base case (i.e., oriented mesh). Plane strain is assumed in all the models. The results are shown in Figure 3-16 for 3.45 MPa (500 psi) effective confining stress.
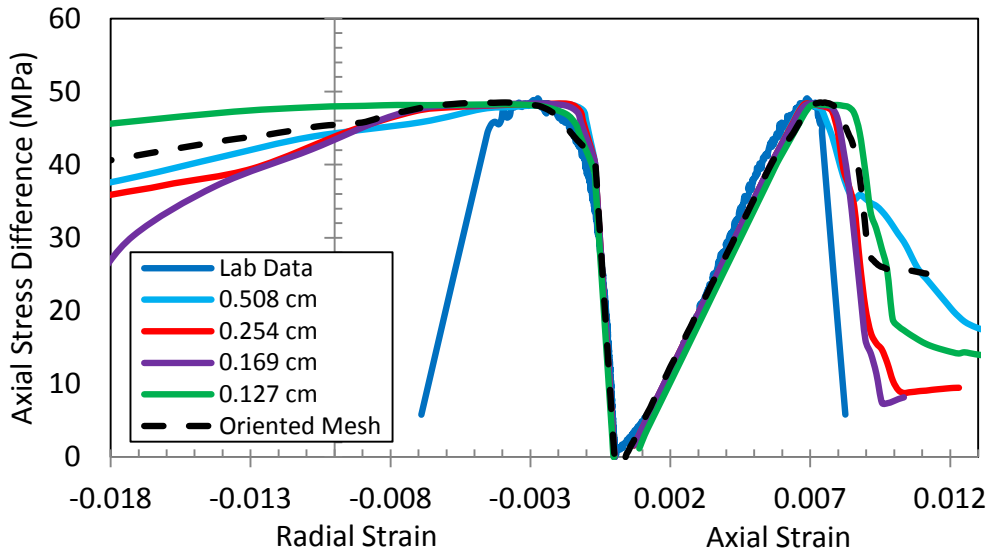
Figure 3-16 Comparison between simulations and experimental observations for different mesh designs (confining stress=3.45 MPa, legend shows mesh size)

Compared to Figure 3-10, not only is the mesh dependency largely reduced, but also the results are closer to the experimental data.

Selecting the characteristic length equal to the shear band thickness regardless of the mesh shape does not result in good matches. Figure 3-17 demonstrated the results for such a case.

Differences in the softening part of each simulation are expected. As shown in the figures, the results are highly dependent on the mesh design and the choice of characteristic length. Utilization of the fracture energy regularization method with

the angular mesh ensured objective calibration. For simpler simulations, such as a triaxial test, it is most favorable to apply oriented mesh and to select the elements size equal to the shear band size so that the actual shear band thickness can be captured. However, in more complicated applications it is very difficult, if not impossible, to align the mesh with the shear band as it requires preknowledge of the shear band location and thickness. In general, as long as the material characteristic length is selected based on the mesh size and shape the results will be adequately well.
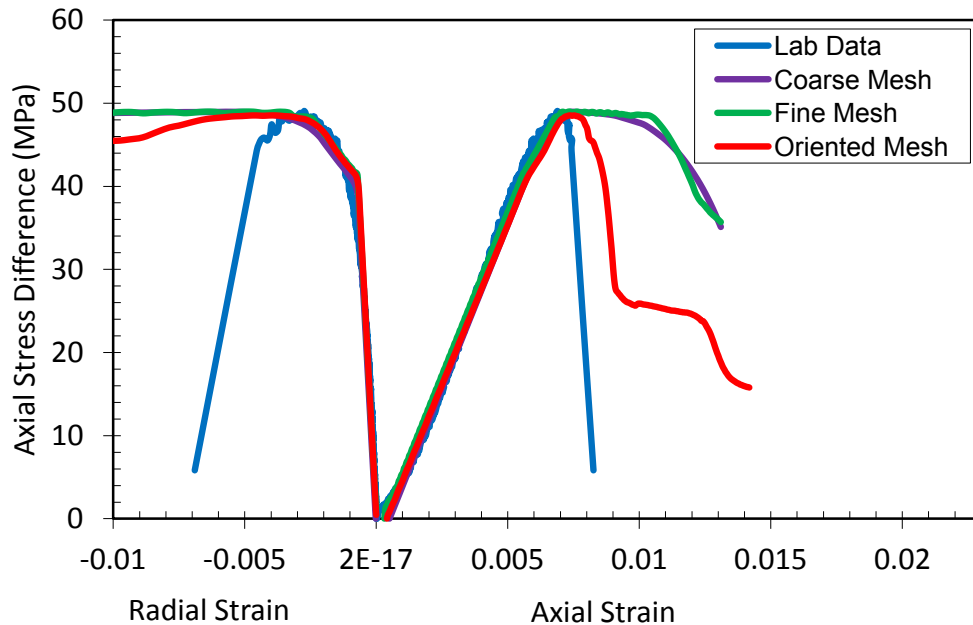
Figure 3-17 Comparison of simulations and experimental observations for different mesh designs without proper selection of characteristic length (confining stress=3.45 MPa)

3.5.5 Axisymmetric Model

The triaxial tests were cylindrical, but the plane strain simulations are rectangular. The difference in the configuration and assumption of plane strain had an impact on the simulation results. Simulation of triaxial experiments is usually carried out using an axisymmetric assumption. However, this assumption does not allow

localization, which is commonly seen in the post-peak regime, to occur. Note that a cylinder with a cutting plane is no longer axisymmetric. Figure 3-18 demonstrates the axisymmetric mesh of one-half sample section.
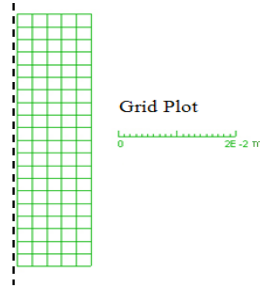
Figure 3-18 Axisymmetric mesh

The simulation results for 3.45 MPa confining stress are shown in Figure 3-19. This model predicts better radial strains as the radial strains in the axisymmetric model are somehow the average strains. Since the axisymmetric model cannot capture localization of deformation, the displacements are completely different from those of the plane strain models. Figure 3-20 shows the displacements in the plane strain and the axisymmetric models. The modeling approach is, therefore, seen to have a high impact on the calibration and the numerical response.
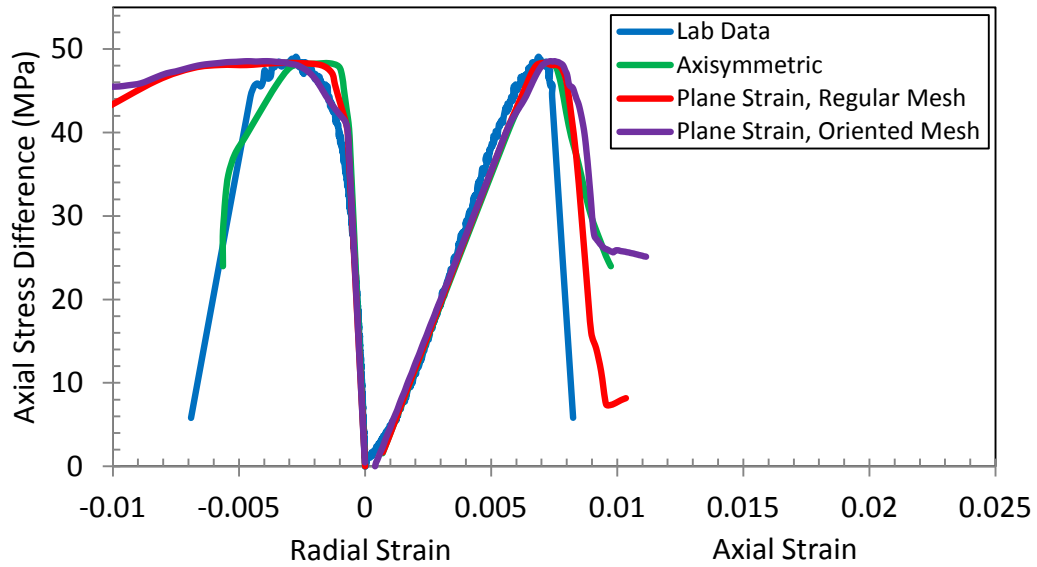
Figure 3-19 Comparing results of the axisymmetric with plane strain model (confining stress=3.45 MPa)

(a)   (b)
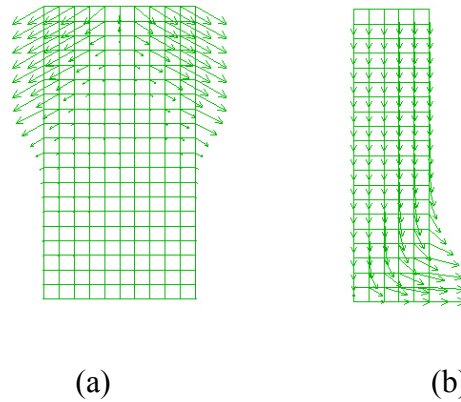
Figure 3-20 Comparison of displacement between (a) a plane strain and (b) an axisymmetric model for the same mesh size (confining stress=3.45 MPa)

3.6 Conclusions

This chapter presented a detailed approach for calibrating a Mohr–Coulomb model for simulating the degrading behavior of sandstones. The procedure is demonstrated by calibrating the model for two sets of triaxial testing data. The

calibrations and back-simulation of TB and Castlegate sandstones show the following:

- The bilinear Mohr–Coulomb model with friction-hardening/cohesion-softening is capable of reproducing sandstone behavior.

- The friction hardening formula offered by Sulem et al. (1999) along with constant tension cut-off is found to be adequate in the strain-hardening phase.

- The cohesion softening formula along with constant friction angle as offered by Vermeer and De Borst (1984) combined with a plane strain modeling of triaxial tests with angular mesh is found to simulate the softening phase reasonably well.

- The oriented mesh inclined at the failure angle results in the formation of shear band in one element row. This is most favorable in shear band simulations if the elements size is selected equal to the shear band size so that the actual shear band thickness can be captured.

- The fracture energy regularization method is found to be capable of reducing mesh dependency. However, the appropriate choice of characteristic length is essential.

- To have effective regularization, it is important to consider the shape of the mesh in the calculations of the characteristic length. The characteristic length for each mesh can be chosen in such a way that simulation produces the shear band thickness numerically.

- Although axisymmetric assumption yields the best match for stress–strain curve when deformations are uniform, it does not allow capturing shear band formation and development in the softening phase. A Plane strain model is a better choice and is the only way to model shear bands in 2D simulations.

3.7 Nomenclature

ECS   Effective confining stress

HECS High effective confining stress

LECS Low effective confining stress

C Cohesion

c^P Peak cohesion

c^* Mobilized cohesion in the softening regime

d_{50} Average grain size

E Young modulus

e_r Radial strain

e_z Axial strain

$\dot{e}_1^p$ Plastic axial strain rate

$\dot{e}_v^p$ Plastic volumetric strain rate

F Yield function

h_p Hardening parameter

$\dot{h}_p$ Hardening parameter rate

hp^P Peak hardening parameter

J_2 Second invariant of the deviatoric stress

k_n Normal stiffness between steel platens and rock sample

k_s Shear stiffness between steel platens and rock sample

P Mean stress

q Tension cut-off

q^i Initial yield tension cut-off

q^P Peak tension cut-off

q_r Residual tension cut-off

S_{ij} Deviatoric stress

T Square root of the second invariant of the deviatoric stress

t_s Shear band thickness

μ Friction coefficient

μ^H Friction coefficient at HECS

μ^L Friction coefficient at LECS

υ Poisson's ratio

σ'_r Effective axial stress

σ'_z Effective radial stress

φ Friction angle

φ_{cv} Constant volume friction angle

ψ Dilation angle

Chapter 4: Numerical Modeling of Pressure Pulse Propagation in Porous Media[3]

4.1 Introduction

As explained in Chapter 2, WH waves are fast transient phenomena which are best described if they are modelled dynamically. To the best knowledge of the author, none of the available sanding models have considered dynamic approach to simulate the transient behaviour of WH phenomenon. This is mainly because there is no commercial software available that considers the fluid flow dynamics in porous media. Instead, the available commercial software only solves Darcy's law which is valid for steady-state flow regimes.

In this chapter, first the dynamic formulations of saturated porous media are presented. Afterwards, the partial differential equations (PDE) are discretized and solved for elastic conditions. The proposed model solves the momentum balance of fluid and solid phases coupled with the fluid mass balance equation in the prediction of dynamic fluid flow and mechanical deformation in porous media. The model is a two-dimensional, elastic, axisymmetric, single-phase and sequentially-coupled model. To ensure stability, artificial viscosity is extended to tensor form and applied. The numerical model is validated against experimental data for a step wave in a shock tube. Good agreement between model calculations and measured data has been obtained. The equations are then extended for

---

[3] A version of this chapter is published as Jafar Pour, M., Nouri, A., Chan, D., 2016. Numerical modelling of waterhammer pressure pulse propagation in sand reservoirs, J of Petroleum Science and Engineering, Vol 137, pp. 42-54.

elastoplastic conditions and the fluid flow part of the equations is sequentially coupled with the dynamic module of FLAC. Finally, comparison between the sequentially coupled FLAC-MATLAB code vs. the fully coupled MATLAB code is made and the best method of coupling dynamic fluid flow with dynamic solid deformation is presented.

4.2 Literature Review

Coupling of fluid flow with geomechanics is necessary when analysing the propagation of pore pressure waves in porous media. Biot (1941) proposed the theory of poroelasticity which ignores the acceleration terms and wave effects. By wave, we mean any discontinuity or jump in the field properties such as pressure, temperature, or stress (Hill, 1962). Later, Biot extended his formulations to the elastic waves in saturated porous media for low frequency waves (Biot, 1956a) and high frequency waves (Biot, 1956b). A wave with low frequency is defined as a wave whose wavelength is less than the pore scale for which Poiseuille flow is valid (Sivrikoz, 2009). Different mathematical modeling is required at high frequencies since certain parameters such as permeability and tortuosity are frequency dependent. The critical frequency above which frequency is considered high can be calculated using Chiavassa and Lombard's equation (2011):

$$f = \frac{\mu n}{2\pi(1-\tau)k\rho_f} \tag{4-1}$$

where μ is viscosity, n is porosity, τ is tortuosity, k is permeability, and ρ_f is fluid density.

Biot's formulations have been used in various applications from the study of the effects of earthquake shear waves on saturated sand response (Cheng, 1986; Desai and Galagoda, 1989) to the ultrasonic wave travelling in human bones (Lakes et al., 1986). The applications, however, focused on stress waves and ignored the

effect of pore pressure waves in the fluid flow mainly because they are mostly damped and are of importance only around the source. Another reason is that Biot's theory predicts two compressional waves in porous media while the second wave was not observed experimentally in porous media until 1980 (Plona, 1980) and later by van der Grinten (van der Grinten et al., 1985) in soil. An example of a Pore pressure wave is WH waves around an injector wellbore, the effects of which can be detrimental to the stability of wellbore and is suspected to induce sudden massive sand production because of sand liquefaction (Santarelli et al., 2000, 2011; Hayatdavoudi, 2005). The exposure of the reservoir to WH amplitudes that can move the stress conditions towards near-zero mean effective stress (or liquefaction conditions) poses a potential risk to the stability of the wellbore.

Verruijt (2010) presented an analytical solution to Biot's 1D dynamic formulation for a shock pore pressure wave and showed that two p-wave will be generated as a result of a shock wave. He also verified the results with numercal simulations and obtained a reasonable match. The simulation results, however, showed numerical oscillations when the shock waves were calculated. He discussed two special cases using analytical models under dynamic pore pressure waves for a 1D problem: 1) pressure waves in undrained environment and 2) pressure waves in porous media where solid matrix is rigid so that there is no solid deformation.

Verruijt' solutions predict nearly the same velocities for the fluid and solid phases ($w \sim v$) under undrained conditions and elastic solid. It also predicts the wave propagation at the velocity of c_1 given by:

$$c_1 = \sqrt{\frac{K_u + \frac{4}{3}G}{\rho}}$$

(4-2)

where K_u is the undrained bulk modulus, G is shear modulus, ρ is density and w and v are solid and fluid velocities, respectively.

During the second wave fluid and solid move out of phase with the velocity of:

$$c_2 = \sqrt{[\frac{1-\alpha+S_p/m_v}{\alpha-n+\tau+(1+\tau)S_p/m_v}]\frac{n}{\rho_f S_p}} \qquad (4\text{-}3)$$

where $S_p = nC_f + (\alpha - n)C_s$ is the storativity, $m_v = \frac{1}{K+\frac{4}{3}G}$ is one-dimensional compressibility of porous medium, α is Biot's coefficient, C_f is fluid compressibility, C_s is solid compressibility and τ, n and ρ_f have been defined earlier. Since the fluid and solid move out of phase, this wave is highly damped due to friction. In a rigid solid matrix ($w=0$) the wave is highly damped and only observed near the source. The second wave speed for very high frequencies is

$$c_2 = \sqrt{n/[(1+\tau)\rho_f S_p]}, \qquad (4\text{-}4)$$

which is the same as the propagation wave velocity in fluids.

In a two-dimensional domain, the PDE set has three eigenvalues contributing to three waves including two compressional and one shear wave.

Chiavassaa and Lombard (2011) focused on the efficiency of solving Biot's equations. They quantified three types of waves: one fast compressional wave, one shear wave, and one slow compressional wave with velocities even slower than the shear wave. The velocities of these waves increase asymptotically towards the eigenvalues of the PDEs as the wave frequency increases. They solved the diffusive part of the equations for slow compressional wave analytically and combined several sophisticated numerical techniques, i.e. fourth order ADER scheme (Schwartzkopff et al., 2004), flux-conserving space-time

adaptive mesh refinement (Berger, LeVeque, 1998), and immersed interface method (Lombard, 2006), to achieve a smooth jump for wave propagation.

de la Cruz and Spanos (1989) solved the thermodynamics of porous media for low-frequency seismic waves. They used continuity and momentum balance equations and added thermal coupling to the poroelasticity equations and treated porosity as a primary variable. In their formulation, they related velocities and deformations to heat generation of the second order and compression to heat generation of the first order. They showed that the heat flow leads to wave attenuation. Their formulation has been used in the mathematical demonstration of the feasibility of the application of pore pressure pulsing as an Enhanced Oil Recovery (EOR) method (Spanos et al., 1999).

Sivrikoz (2009) simplified the equations presented by de la Cruz and Spanos for pore pressure and solid displacements as the main variables under isothermal conditions, and solved them for application of pore pressure pulsing as an EOR method. After some simplifications, the author showed that the equations are equivalent to mathematical wave operator $(\frac{1}{C^2}\frac{\partial^2}{\partial t^2} - \nabla^2)$ on porosity. Low-frequency pulses of fluid in a porous medium create a slow strain wave called the porosity dilation wave, which results from the interactions and deformations between the fluid and matrix in the porous media. The porosity dilation wave travels at velocities in the order of 5–150 m/sec and is characterized by a spreading front of elastic porosity changes. The method of solution adopts an elastic constitutive model to simplify the governing equations and is not applicable to elastoplastic cases.

The work presented in this chapter adopts the approach proposed by de la Cruz and Spanos (1989) for a saturated porous medium, ignoring the thermal effects by assuming isothermal conditions, assuming 2D axial symmetry, and developing a tensor form of artificial viscosity to damp the numerically-induced oscillations

and achieve smooth response for shock waves. An elastoplastic constitutive model is implemented to account for inelastic deformations. The state variables are chosen to be fluid velocity, solid velocity, pore pressure, porosity, and stresses. The model is validated against experimental data published by van der Grinten et al. (1985) and van der Grinten et al. (1987). The results are also compared with those of Biot's formulation. The explicit finite difference method is used to solve the governing equations by employing a sequential coupling scheme combined with the velocity–stress method (Virieux, 1986).

Finally, the fluid flow part of the equations is sequentially coupled with the dynamic module of FLAC. Comparison between the sequentially-coupled code versus the fully-coupled code is made and an acceptable method of coupling dynamic fluid flow code with dynamic solid deformation software is presented.

4.3 Governing Equations for Elastic Conditions

de la Cruz and Spanos derived the governing equations for elastic solids by substituting stresses with displacements in Hook's law. The following equations are derived for isothermal conditions.

4.3.1 Fluid Mass Balance

The derivation of mass balance is expressed in more detail to emphasize the assumption of elasticity in describing the solid response. The next section will discuss changes required on the governing equations for a more general constitutive model for solid. The mass balance equation for fluid is:

$$\frac{\partial(n\rho_f)}{\partial t} + \text{Div}(n\rho_f \boldsymbol{v}) = 0 \tag{4-5}$$

where n is the porosity, ρ_f is the fluid density, and $\boldsymbol{v}$ is the fluid velocity vector. This equation is Eulerian while the solid momentum equation is usually expressed

in the Lagrangian framework. Due to the solid deformation, the change in mass will not be equal to the change in $n\rho_f$. Hence, material derivative is introduced in Eq. (4-6).

$$\frac{\partial()}{\partial t} = \frac{d()}{dt} - \boldsymbol{w}.\,\mathrm{Grad}() \tag{4-6}$$

where $\boldsymbol{w}$ is the solid velocity vector. The mass balance equation for the fluid can be rewritten as:

$$\frac{d(n\rho_f)}{dt} - \boldsymbol{w}.\,\mathrm{Grad}(n\rho_f) + \mathrm{Div}(n\rho_f \boldsymbol{v}) = 0 \tag{4-7}$$

Also since divergence is a linear operator, it satisfies the product rule. Therefore, for any vector $\boldsymbol{F}$ and scalar a, one can write:

$$\mathrm{Div}(a.\,\boldsymbol{F}) = \mathrm{Grad}(a).\,\boldsymbol{F} + a\mathrm{Div}(\boldsymbol{F}) \tag{4-8}$$

Now if $a = n\rho_f$ and $\boldsymbol{F} = \boldsymbol{w}$, it yields:

$$\boldsymbol{w}.\,\mathrm{Grad}(n\rho_f) = \mathrm{Div}(n\rho_f \boldsymbol{w}) - n\rho_f \mathrm{Div}(\boldsymbol{w}) \tag{4-9}$$

Replacing $\boldsymbol{w}.\,\mathrm{Grad}(n\rho_f)$ in the mass balance equation:

$$\frac{d(n\rho_f)}{dt} + n\rho_f \mathrm{Div}(\boldsymbol{w}) + \mathrm{Div}(n\rho_f(\boldsymbol{v} - \boldsymbol{w})) = 0 \tag{4-10}$$

Fluid compressibility is defined:

$$C_f = \frac{\partial \rho_f}{\rho_f \partial p_T} = \left(\frac{\frac{\partial \rho_f}{\partial t}}{\rho_f \frac{\partial p}{\partial t}} \right)_T \tag{4-11}$$

Under isothermal conditions:

$$\frac{d(n\rho_f)}{dt} = \left(n\frac{d\rho_f}{dp}\frac{dp}{dt} + \rho_f\frac{dn}{dt}\right) = (n\rho_f C_f\frac{dp}{dt} + \rho_f\frac{dn}{dt}) \tag{4-12}$$

The porosity change proposed here depends on the solid and fluid compressibilities and is valid only for elastic behaviour:

$$\frac{dn}{dt} = (\alpha - n)C_s\frac{dp}{dt} + (\alpha - n)\text{Div}(\boldsymbol{w}) \tag{4-13}$$

Elastoplastic conditions are discussed in Section 4.4. Substituting this into Eq. (4-10) one gets:

$$\rho_f(nC_f + (\alpha - n)C_s)\frac{dp}{dt} + \rho_f\alpha\text{Div}(\boldsymbol{w}) + \text{Div}\left(n\rho_f(\boldsymbol{v} - \boldsymbol{w})\right) = 0 \tag{4-14}$$

Defining storativity as: $S_p = nC_f + (\alpha - n)C_s$, mass balance equations yields:

$$S_p\frac{dp}{dt} + \alpha\text{Div}(\boldsymbol{w}) + \frac{1}{\rho_f}\text{Div}(n\rho_f(\boldsymbol{v} - \boldsymbol{w})) = 0 \tag{4-15}$$

Verruijt (2010) derived the same equation by combining solid and fluid mass balance equations.

Using Eq. (4-8) one gets:

$$\text{Div}(n\rho_f(\boldsymbol{v} - \boldsymbol{w})) = (\boldsymbol{v} - \boldsymbol{w}).\text{Grad}(n\rho_f) + n\rho_f\text{Div}(\boldsymbol{v} - \boldsymbol{w}) \tag{4-16}$$

$$\text{Grad}(n\rho_f) = n\text{Grad}(\rho_f) + \rho_f\text{Grad}(n) = n\frac{\partial\rho_f}{\partial p}\text{Grad}(p) + \rho_f\text{Grad}(n)$$
$$= \rho_f(nC_f\text{Grad}(p) + \text{Grad}(n)) \tag{4-17}$$

Substituting into Eq. (4-10) and combining with Eq. (4-12), mass balance equation will be obtained:

$$S_p \frac{dp}{dt} + \alpha \text{Div}(\boldsymbol{w}) + (\boldsymbol{v} - \boldsymbol{w}).\left(nC_f \text{Grad}(p) + \text{Grad}(n)\right) + n\text{Div}(\boldsymbol{v} - \boldsymbol{w})$$
$$= 0$$

(4-18)

Note that the change in porosity is based on elastic theory. For elastoplastic conditions, Eq. (4-30) is derived in the Section 4.4.

4.3.2 Equation of Motion for Solid-Fluid System

Assuming that stresses in the fluid and solid are related by $\boldsymbol{\sigma}^f \boldsymbol{n} - p\boldsymbol{n} = \boldsymbol{\sigma}^s \boldsymbol{n}$, where $\boldsymbol{n}$ is the normal unit vector, one obtains (de la Cruz and Spanos, 1989):

$$(1-n)\rho_s \frac{\partial \boldsymbol{w}}{\partial t} + n\rho_f \frac{\partial \boldsymbol{v}}{\partial t} = \text{Div}(\boldsymbol{\sigma}) + \rho \boldsymbol{g} - K_s \text{Grad}(n),$$

(4-19)

Stress in the fluid can be defined in terms of fluid velocities as:

$$\text{Grad}(\boldsymbol{\sigma}^f) = \left(\mu + \lambda_f\right)\text{Grad}\left(Div(\boldsymbol{v})\right) + \mu \text{Grad}^2(\boldsymbol{v})$$

(4-20)

where subscripts s and f denote the solid and fluid phases and $\lambda_f = -\frac{2}{3}\mu$ since shear stresses for fluid are assumed to be zero. Stress is then replaced by effective stress through $\boldsymbol{\sigma}' = \boldsymbol{\sigma} - \alpha p \boldsymbol{I}$, where $\boldsymbol{I}$ is the identity matrix.

4.3.3 Momentum Balance for Fluid

The equation of motion for fluid is presented in differential form as (de la Cruz and Spanos, 1989):

$$n\rho_f \frac{\partial \boldsymbol{v}}{\partial t} = -n\text{Grad}(p) - \frac{n^2 \mu}{k}(\boldsymbol{v} - \boldsymbol{w}) + n\mu \text{Div}\left(\text{Grad}(\boldsymbol{v})\right) + n(\mu$$
$$+ \lambda_f)\text{Grad}\left(\text{Div}(\boldsymbol{v})\right) + \rho_f \boldsymbol{g} + \rho_{12} \frac{\partial(\boldsymbol{v} - \boldsymbol{w})}{\partial t}$$

(4-21)

The added mass, ρ_{12}, comes from the tortuous path that the fluid follows to pass through the porous medium. The narrowing-widening nature of porous media

makes the fluid more accelerated. In other words, it is equivalent to an increase in the fluid mass. This added mass depends on the tortuosity or connectivity of pores.

Replacing λ_f, one obtains:

$$
\begin{aligned}
n\rho_f \frac{\partial \boldsymbol{v}}{\partial t} = &-n\mathrm{Grad}(p) - \frac{n^2 \mu}{k}(\boldsymbol{v} - \boldsymbol{w}) + n\mu[\mathrm{Div}\big(\mathrm{Grad}(\boldsymbol{v})\big) \\
&+ \frac{1}{3}\mathrm{Grad}\big(\mathrm{Div}(\boldsymbol{v})\big)] + \rho_f \boldsymbol{g} + \rho_{12}\frac{\partial(\boldsymbol{v} - \boldsymbol{w})}{\partial t}
\end{aligned}
\tag{4-22}
$$

As Eq. (4-22) shows, the fluid momentum balance reduces to Darcy's law under negligible compressibility and no dynamic effect (Verruijt, 2010). A convection term, $(\mathrm{Div}(\boldsymbol{v}))\boldsymbol{v}$, may appear in some formulations, but it is avoided here. Beck (1972) stated that this term is inappropriate since it increases the order of partial differential equation. It is also inconsistent with the slip boundary condition. In addition, this term is not an appropriate way to account for nonlinear drag arising from inertial effects since this term is zero for steady incompressible 1D flow regardless of the fluid velocity. The convection term can only be of importance for high-speed compressible fluid flow in highly porous medium. In general, this term will be small and can be ignored since solid structure may prohibit some motion and cause a change in momentum (Nield, D.A., and Bejan A, 2006).

4.3.4 Porosity Equation

de la Cruz and Spanos proposed the following equation for porosity. This equation is also valid for elastic conditions:

$$
\frac{\partial n}{\partial t} = \delta_s \mathrm{Div}(\boldsymbol{w}) - \delta_f \mathrm{Div}(\boldsymbol{v})
\tag{4-23}
$$

$$\begin{cases} \delta_s = \dfrac{C_f n_0 (1 - n_0)}{C_f n_0 + C_s (1 - n_0)} \\ \delta_f = \dfrac{C_s n_0 (1 - n_0)}{C_f n_0 + C_s (1 - n_0)} \end{cases}$$

4.3.5 Constitutive Law

Hook's law is used for elastic description of solid deformation.

$$\dot{\boldsymbol{\sigma}}' = \left(K_s - \frac{2}{3} G \right) \dot{\varepsilon} \boldsymbol{I} + 2G \dot{\boldsymbol{\varepsilon}} \tag{4-24}$$

where $\dot{\boldsymbol{\sigma}}'$ is the rate of change of effective stress, $\dot{\boldsymbol{\varepsilon}}$ is the rate of change of strain, K_s is the bulk modulus, G is the shear modulus, and $\boldsymbol{I}$ is the identity matrix defined before. Compressive stresses are assumed to be positive.

4.4 Mass Balance Equation for Elastoplastic Medium

For elastoplastic deformation of rock, one may expect that nearly all the porosity change will originate from bulk volumetric deformation. The assumption here is that the fluid volume change is negligible compared to that of the solid. The porosity of the rock can be calculated from:

$$n = 1 - \frac{1 - n_0}{1 + \varepsilon_v} \tag{4-25}$$

where n_0 is the initial porosity and ε_v is the volumetric strain. Taking differentiation, yields:

$$dn = \frac{1 - n_0}{(1 + \varepsilon_v)^2} d\varepsilon_v \tag{4-26}$$

Therefore, the rate of change of porosity with respect to time is:

$$\frac{dn}{dt} = \frac{1 - n_0}{(1 + \varepsilon_v)^2} \text{Div}(\boldsymbol{w})$$

(4-27)

where $d\varepsilon_v = \text{Div}(\boldsymbol{w})$. Mass balance equation is derived by combining Eq. (4-10) and Eq. (4-12):

$$n\rho_f C_f \frac{dp}{dt} + \rho_f \frac{dn}{dt} + n\rho_f \text{Div}(\boldsymbol{w}) + \text{Div}\big(n\rho_f(\boldsymbol{v} - \boldsymbol{w})\big) = 0$$

(4-28)

Substituting Eq. (4-16), (4-17) and (4-27) into Eq. (4-28), yields:

$$\rho_f(nC_f)\frac{dp}{dt} + \rho_f \frac{1 - n_0}{(1 + \varepsilon_v)^2}\text{Div}(\boldsymbol{w}) + n\rho_f \text{Div}(\boldsymbol{w}) + n\rho_f \text{Div}(\boldsymbol{v} - \boldsymbol{w})$$
$$+ (\boldsymbol{v} - \boldsymbol{w}).\rho_f(nC_f \text{Grad}(p) + \text{Grad}(n)) = 0$$

(4-29)

Dividing by ρ_f and simplifying the equation, one obtains Eq. (4-30) for the fluid mass balance:

$$(nC_f)\frac{dp}{dt} + \frac{1 - n_0}{(1 + \varepsilon_v)^2}\text{Div}(\boldsymbol{w}) + n\text{Div}(v) + (\boldsymbol{v} - \boldsymbol{w}).(nC_f \text{Grad}(p)$$
$$+ \text{Grad}(n)) = 0$$

(4-30)

4.5 Comparison with Biot's Theory

Biot's theory neglects some physics that govern the transport phenomenon in saturated porous media. One questionable assumption in Biot's theory is that porosity change is ignored. This porosity change leads to a porosity diffusion wave which can play a significant role in multi-phase saturated porous medium by enhancing the transport of the non-wetting phase (Spanos et al., 1999). The other difference is the fluid compressibility terms in fluid momentum balance, $n\mu[\text{Div}(\text{Grad}(\boldsymbol{v})) + \frac{1}{3}\text{Grad}(\text{Div}(\boldsymbol{v}))]$. The effect of these differences on the results is demonstrated in Figure 4-4 to Figure 4-6.

4.6 Axisymmetry

Since only one injector well will be modeled in this study, the equations are derived assuming axial symmetry in cylindrical coordinates. Therefore, the equations are extended to cylindrical coordinates under axisymmetry assumption. The assumption here is that horizontal stresses are isotropic. Furthermore, the assumption of axisymmetry, does not allow to capture the perforation geometry and direction as the model approximates the perforation tunnel with a ring opening in the casing. Under axisymmetric conditions, one can write:

$$\frac{\partial}{\partial\theta} = 0, \quad \sigma_{r\theta} = \sigma_{z\theta} = 0 \tag{4-31}$$

$$\dot{\varepsilon}_{rr} = \frac{\partial w_r}{\partial r}; \ \dot{\varepsilon}_{\theta\theta} = \frac{w_r}{r}; \ \dot{\varepsilon}_{zz} = \frac{\partial w_z}{\partial z} \tag{4-32}$$

$$Div(w) = \frac{\partial\varepsilon_v}{\partial t} = \dot{\varepsilon}_{rr} + \dot{\varepsilon}_{\theta\theta} + \dot{\varepsilon}_{zz} \tag{4-33}$$

Therefore, the equations can be rewritten as:

$$\rho_f \frac{\partial v_r}{\partial t} = -\frac{\partial p}{\partial r} - \frac{n\mu}{k_r}(v_r - w_r) + \mu\left[\frac{\partial^2 v_r}{\partial r^2} + \frac{1}{r}\frac{\partial v_r}{\partial r} + \frac{\partial^2 v_r}{\partial z^2} - \frac{v_r}{r^2}\right] + (\mu$$
$$+ \lambda_f)\left[\frac{\partial^2 v_r}{\partial r^2} + \frac{1}{r}\frac{\partial v_r}{\partial r} - \frac{v_r}{r^2} + \frac{\partial^2 v_r}{\partial r\partial z}\right] + \frac{\rho_{12}}{n}\frac{\partial(v_r - w_r)}{\partial t} \tag{4-34}$$

$$\rho_f \frac{\partial v_z}{\partial t} = -\frac{\partial p}{\partial z} - \frac{n\mu}{k_z}(v_z - w_z) + \mu\left[\frac{\partial^2 v_z}{\partial r^2} + \frac{1}{r}\frac{\partial v_z}{\partial r} + \frac{\partial^2 v_z}{\partial z^2}\right]$$
$$+ (\mu + \lambda_f)\left[\frac{\partial^2 v_r}{\partial r\partial z} + \frac{1}{r}\frac{\partial v_r}{\partial z} + \frac{\partial^2 v_z}{\partial z^2}\right] + \frac{\rho_{12}}{n}\frac{\partial(v_z - w_z)}{\partial t} \tag{4-35}$$
$$+ \rho_f g$$

where $\lambda_f = -2\mu/3$ assuming shear stress in liquids are zero.

$$n\rho_f \frac{\partial v_r}{\partial t} + (1-n)\rho_s\frac{\partial w_r}{\partial t} = \frac{\partial\sigma'_{rr}}{\partial r} + \frac{\partial\sigma_{rz}}{\partial z} + \propto\frac{\partial p}{\partial r} + \frac{\sigma'_{rr} - \sigma'_{\theta\theta}}{r} - K_s\frac{\partial n}{\partial r} \tag{4-36}$$

$$n\rho_f \frac{\partial v_z}{\partial t} + (1-n)\rho_s \frac{\partial w_z}{\partial t} = \frac{\partial \sigma_{rz}}{\partial r} + \frac{\partial \sigma'_{zz}}{\partial z} + \propto \frac{\partial p}{\partial z} + \frac{\sigma_{rz}}{r} - K_s \frac{\partial n}{\partial z} + \rho g \qquad (4\text{-}37)$$

$$S_p \frac{\partial p}{\partial t} = -\propto \frac{\partial \varepsilon_v}{\partial t} - \frac{\partial [n(v_r - w_r)]}{\partial r} - \frac{\partial [n(v_z - w_z)]}{\partial z} - \frac{n(v_r - w_r)}{r} \qquad (4\text{-}38)$$

$$\frac{dn}{dt} = (\alpha - n)[C_s \frac{dp}{dt} + \frac{\partial \varepsilon_v}{\partial t}] \qquad (4\text{-}39)$$

4.7 Convergence and Stability

Multi-dimensional numerical modeling of waves in porous media is tricky due to coexistence of both propagating fast compressional wave, shear wave, and a diffusive slow compressional wave (Chiavassaa and Lombard, 2011).

Sequential coupling of explicit dynamic equations is conditionally stable. The time step necessary for convergence must be smaller than the required time for waves to pass each element. For a 2-D system, this condition can be expressed as:

$$\frac{u_x \Delta x}{\Delta t} + \frac{u_y \Delta y}{\Delta t} \le C_{max} \qquad (4\text{-}40)$$

where u_i is the wave velocity in i direction.

This is called the CFL condition (Courant, Friedrichs and Lewy, 1967), which is a very limiting constraint on the time step. For some PDEs, attempts are made to avoid this condition by solving the equation implicitly. However, the CFL condition arises for hyperbolic PDEs regardless of using an implicit method when waves are involved and when emphasis is on the transient behaviour with time, not the steady-state solution. The value of C_{max} depends on the method of solving the equations, whether implicit or explicit.

In addition, there are more implications with this condition, e.g. when the size of element is reduced due to compression by wave. Therefore, CFL only predicts an upper bound for the time step. In many cases, it is extremely hard, if not

impossible, to theoretically predict the highest CFL number. In this study, it is found heuristically that the coefficient of $0.8 \times n$ puts the solution on the safe stable window:

$$\Delta t < \frac{\min (\Delta L)}{2c_1} \times 0.8 \times n \tag{4-41}$$

The speed of the wave, c_1, is given by Eq. (4-2).

Running the simulation with coarse mesh is also problematic. Chiavassaa and Lombard (2011) related this to the small wavelength of the slow compressional wave. One has to use coarse grid appropriate for the fast wave where slow wave is poorly discretized or use a fine grid and increase the computational cost. The authors tackled this time restriction by solving the diffusive part for the slow compressional wave analytically. The authors also noted that the previous works were not able to answer the difficulty of handling numerical instability due to the viscous effects.

In this study, an extended form of artificial viscosity damping is derived to damp numerically-induced oscillations, as described in Section 4.7.1.

4.7.1 Artificial Viscosity Damping

In fluid dynamics, artificial viscosity is very common to damp the unrealistic oscillations resulting in a smooth response for modeling shock waves. Artificial viscosity makes it possible for the wave to be modeled as a viscous dissipation over a thin space, instead of a jump with infinitesimally small thickness. In reality, the thickness of the waves is at the molecules levels.

Artificial viscosity damping has evolved over the years. The first representation is a scalar form in terms of the velocity rate. It includes the Von Neumann term, q_1 and the Landshhoff term, q_2, which are given by Wilkins, (1980):

$$q_1 = -\text{sign}(\dot{\varepsilon}_v)c_0{}^2\rho L^2 \dot{\varepsilon}_v{}^2$$

$$(4\text{-}42)$$

$$q_2 = -\text{sign}(\dot{\varepsilon}_v)c_L\rho La\dot{\varepsilon}_v$$

where L is the element size, $\dot{\varepsilon}_v$ is the rate of volumetric strain, c_0 and c_L are constant values equal to 2 and 1 respectively, and a is the speed of sound which is equal to $\sqrt{(K_s + \frac{4}{3}G)/\rho}$ (Wilkins. 1980). q_1 is the von Neumann term which damps the oscillations behind the front and spreads the wave over the mesh. q_2 is the Landshhoff term which diffuses the shock front over an increased number of zones as the shock wave progresses (FLAC user manual, 2008). The minus sign of volumetric strain ensures that damping always occur in the opposite direction of the strain.

This damping is a scalar value which is used in calculation of stress gradients. For a 2D axisymmetric case, the tensor form of artificial viscosity is adopted here based on the original scalar form:

$$q_{r1} = -sign(\dot{\varepsilon}_{rr})c_0{}^2\rho\Delta r^2 \dot{\varepsilon}_{rr}{}^2$$

$$q_{r2} = -sign(\dot{\varepsilon}_{rr})c_L\rho\Delta ra\dot{\varepsilon}_{rr} \qquad\qquad (4\text{-}43)$$

$$q_{z1} = -sign(\dot{\varepsilon}_{zz})c_0{}^2\rho\Delta z^2 \dot{\varepsilon}_{zz}{}^2$$

$$q_{z2} = -sign(\dot{\varepsilon}_{zz})c_L\rho\Delta za\dot{\varepsilon}_{zz} \qquad\qquad (4\text{-}44)$$

$$q_{\theta 1} = -sign(\dot{\varepsilon}_{\theta\theta})c_0{}^2\rho r^2 \dot{\varepsilon}_{\theta\theta}{}^2$$

$$\qquad\qquad (4\text{-}45)$$

$$q_{\theta 2} = -sign(\dot{\varepsilon}_{\theta\theta})c_L\rho ra\dot{\varepsilon}_{\theta\theta}$$

$$q_{rz1} = -sign(\dot{\varepsilon}_{rz})c_0{}^2\rho \left(w_{zi+1,j} - w_{zi-1,j} + w_{ri,j+1} - w_{ri,j-1}\right)^2 /4$$

$$(4\text{-}46)$$

$$q_{rz2} = -sign(\dot{\varepsilon}_{rz})c_L\rho a(w_{zi+1,j} - w_{zi-1,j} + w_{ri,j+1} - w_{ri,j-1})/2$$

Comparing the smoothness of the results for the discussed artificial viscosities, this tensor form is more effective in damping numerical oscillations of 2D problems.

4.8 Discretization and Solution Method

To solve the equations, finite difference discretization is applied with second order approximation in space and first order backward approximation in time given by Eq. (4-47) and Eq. (4-48).

$$\frac{\partial f}{\partial x} = \frac{f_{x+\Delta x} - f_{x-\Delta x}}{2\Delta x} + O(\Delta x^2) \tag{4-47}$$

$$\frac{\partial f}{\partial t} = \frac{f^{t+\Delta t} - f^t}{\Delta t} + O(\Delta t) \tag{4-48}$$

The explicit time marching scheme is used because of the complexity and nonlinearity of the equations. However, this method imposes conditional stability, and small time step with fine mesh is required to achieve stable solution.

To solve the equations, they are simplified and rearranged in the following order so that they can be solved sequentially. For simplicity, index notation is applied.

$$\frac{\partial v_i}{\partial t} = \frac{-1}{\left(\rho_f - \frac{\rho_{12}}{n}\right)}(p_{,i} + \frac{n\mu}{k}(v_i - w_i) - \mu\left(v_{i,jj} + \frac{1}{3}v_{j,ji}\right) + \frac{\rho_{12}}{n}\frac{\partial w_i}{\partial t}) \tag{4-49}$$

$$\frac{\partial w_i}{\partial t} = \frac{1}{\rho_s(1-n)}(-n\rho_f\frac{\partial v_i}{\partial t} + \sigma_{ij,j} + \rho g_i - K_s n_{,i}) \tag{4-50}$$

$$\frac{dp}{dt} = \frac{-1}{S_p} \left(\alpha \boldsymbol{w}_{i,i} + (\boldsymbol{v}_i - \boldsymbol{w}_i) \cdot \left(nC_f p_{,i} + n_{,i} \right) + n(\boldsymbol{v}_i - \boldsymbol{w}_i)_{,i} \right) \qquad \text{(4-51)}$$

$$\frac{dn}{dt} = (\alpha - n)C_s \frac{d\boldsymbol{p}}{d\boldsymbol{t}} + (\alpha - n)\boldsymbol{w}_{i,i} \qquad \text{(4-52)}$$

$$\dot{\varepsilon}_{ij} = \frac{1}{2} \left(\boldsymbol{w}_{i,j} + \boldsymbol{w}_{j,i} \right) \qquad \text{(4-53)}$$

$$\dot{\sigma}_{ij}{}' = - \left(K_s - \frac{2}{3}G \right) \dot{\boldsymbol{\varepsilon}}_{ij}\delta_{ij} - 2G\dot{\boldsymbol{\varepsilon}}_{ij} \qquad \text{(4-54)}$$

First, fluid velocity is calculated explicitly from the fluid momentum balance. Then the new values for fluid velocities (shown in bold) are used in the momentum balance to find solid velocities. The calculated values of velocities for both phases are used in the mass balance equation to solve for pore pressure. Finally, using the new values of pore pressure and solid velocities, strains rates are calculated and porosity and stresses are updated. The algorithm is shown in Figure 4-1.
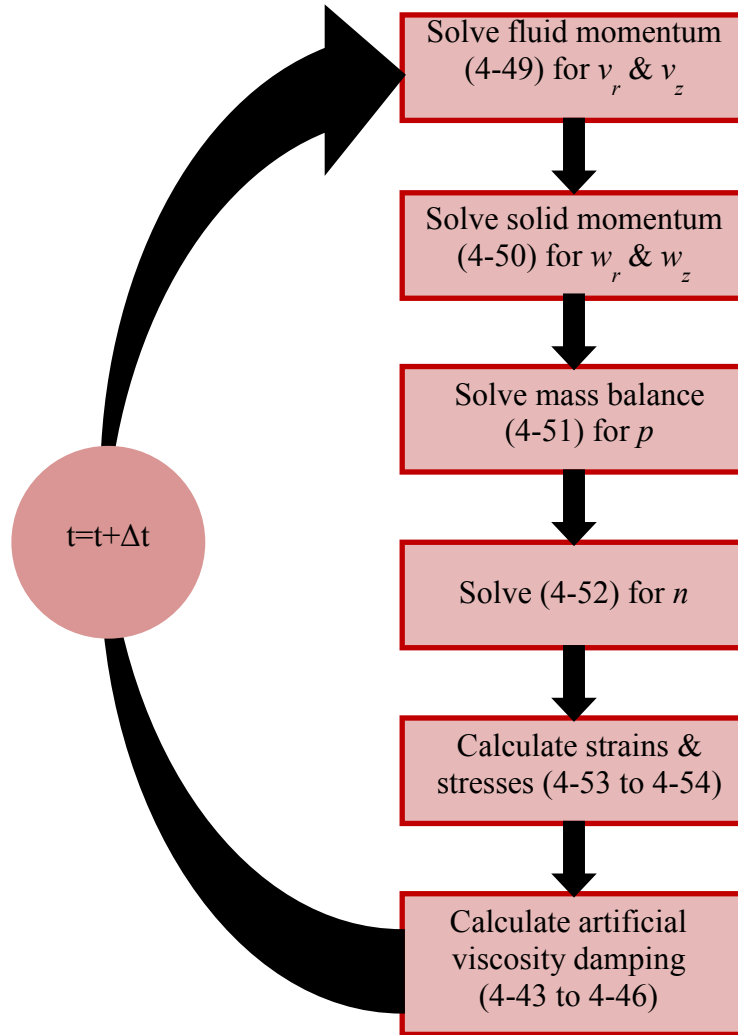
Figure 4-1 Algorithm for PDE solution

4.9 Validation against Experimental Data

van der Grinten et al. (1985, 1987) conducted a shock tube study by applying single step-like pore pressure wave to a cylindrical sand sample and measuring the pore pressure at different locations from the top of the sample. There is a layer of water on top of the sample to ensure full saturation. Above that there is a plastic sheet separating the high pressure section from a low pressure part in the tube. To produce the shock wave, the sheet is burned and a plane wave hits the

water surface above the sample. This induces a step-like pore pressure increase. The schematic of the experiment is shown in Figure 4-2.

There is a thin water layer (1 mm) separating the sample from the shock tube preventing shear interaction between the wall and the sample. To measure pore pressure, the pressure gauges have been placed in the gap resulting in erroneous measurements caused by wave propagation in the water column. For instance, Wisse (1999) performed two similar tests: one with small (0.25 mm) and the other with large gap (3.5 mm). The author stated that over the entire frequency ranges the gap pressure and the porous sample pressure have the same order of magnitude. However, the results of the small gap measuremnts are closer to the theoretical predictions. North (2002) performed a 2D modelling of both water and porous media using Biot's theory and concluded good agreement between the results of the theoretical model and the measurements of the shock tube for tests with small gap. However, for large gap sizes between the sample and shock tube, the wave in the water has an impact on the amplitude of the measurements. No explanation of the gauge placement is provided by van der Grinten et al. (1985). However, in a later work they measured both pore pressures in the gap and in the sand sample using identical experimental set-up (van der Grinten et al., 1987). This newer experiment also included strain measurements. Hence, we use the later work which used the same type of soil as in their earlier work to validate the simulator developed here.

The soil properties are summarized in Table 4-1. The compressibility of sand grain is not reported in the experiment. A value of 2.35×10^{-11} 1/Pa, which is the average of grain compressibility values reported for Ottawa sand and quartz from Gulf of Mexico, is used in the modeling (Richardson et al., 2002). The sample is saturated with water whose properties are not measured. As such, typical water properties are assigned in the model as summarized in Table 4-2.
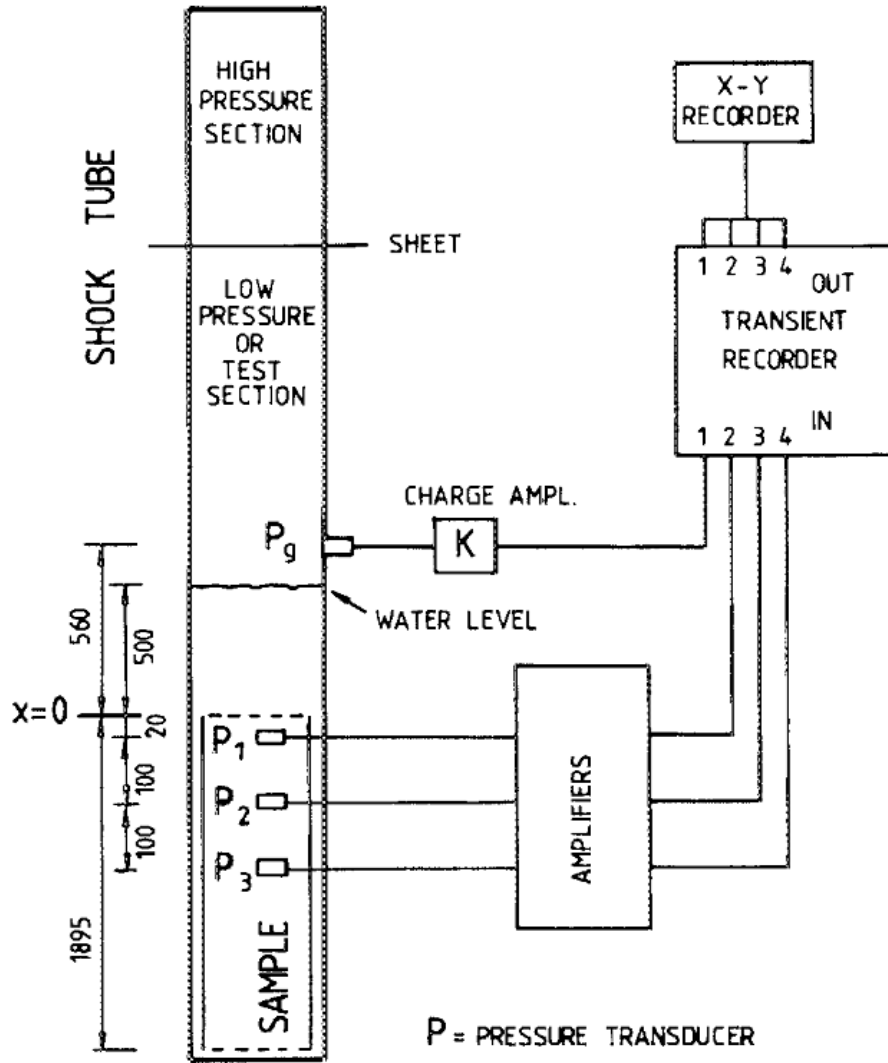
Figure 4-2 Shock tube experiment (van der Grinten et al. 1985)

Table 4-1 Properties of the porous sand (van der Grinten et al. 1985)

Property	Value
Sand Intrinsic density (kg/m^3)	2650
Bulk Modulus (GPa)	8.16
Shear Modulus (GPa)	1.3
Permeability (m^2)	5.62e-11
Porosity	0.3
Added mass	2.7

Table 4-2 Water properties used in the simulation

Property	Value
Density (kg/m^3)	1000
Viscosity (cP)	1
Bulk Modulus (GPa)	2.00

4.9.1 Comparison of Simulation and Experimental Results

Figure 4-3 shows the schematic of the model under 2D axisymmetric conditions. The sample size is 75 mm in diameter and 1.895 m in length. Very fine mesh is required for the convergence of the solutions and to capture the wave propagation through the sample. For this work, the radius and the length are divided into 10 and 400 equal elements, respectively, following a mesh sensitivity analysis. The time step is selected so that the waves travel the length of one element during one time step. The bottom of the model is assumed to be fixed in the vertical direction and the shock wave is applied from the top. This shock wave is represented by a combination of pore pressure and normal stress wave, i.e. zero effective stress normal to the top surface. The right boundary is allowed to move freely in the model in r direction; while in the experiment, water would prevent some (but not all) of the displacements.

Figure 4-4 shows two jumps in the pore pressure response. It is hypothesized that (1) the first jump is the result of an undrained wave where both phases move together while the sample is contracted under the shock load and (2) the second jump is due to deceleration of solid velocity while fluid phase is accelerating (see Figure 4-8).
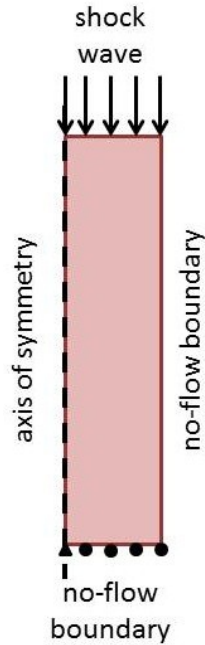
Figure 4-3 Schematic of the model geometry

Figure 4-4 to Figure 4-12 show the results of the numerical model, which indicate a reasonable agreement between the measured and calculated pore pressures at 120 and 220 mm from the top. Note that tortuosity (or added mass) is used as a calibration parameter to obtain a closer match, because among the measured properties tortuosity has the highest uncertainty. This parameter is characterized by electrical conductivity measurements as suggested by Brown (1980). However, this measurement method is valid as long as the pore structure can be assumed incompressible and would be erroneous when applied to a deformable porous media. The effect of tortuosity on the simulation results is presented in Figure 4-10.

Figure 4-4 to Figure 4-6 show noticeable differences between the predictions of Biot's theory and the formulation used in this work during the transient period. Biot's theory prediction for the amplitude of the undrained wave is nearly half of the real value. Note that changing the value of tortuosity does not improve the

84

results obtained by Biot's theory results since tortuosity has no effect on the speed of the first wave which is overestimated by Biot's theory. van der Grinten et al. (1985, 1987) mistakenly attributed the difference to the radial motion of the sample and, therefore, modified the constrained modulus, $K_s + \frac{4}{3}G$, to an effective constrained modulus (4.5 GPa instead of 9.9 GPa) in their analytical model. We will see that the radial motion of the sample is negligibly small. Also the rise of the second wave as predicted by Biot's theory is more abrupt than the predictions of de la Cruz and Spanos' theory and the experimental measurements.
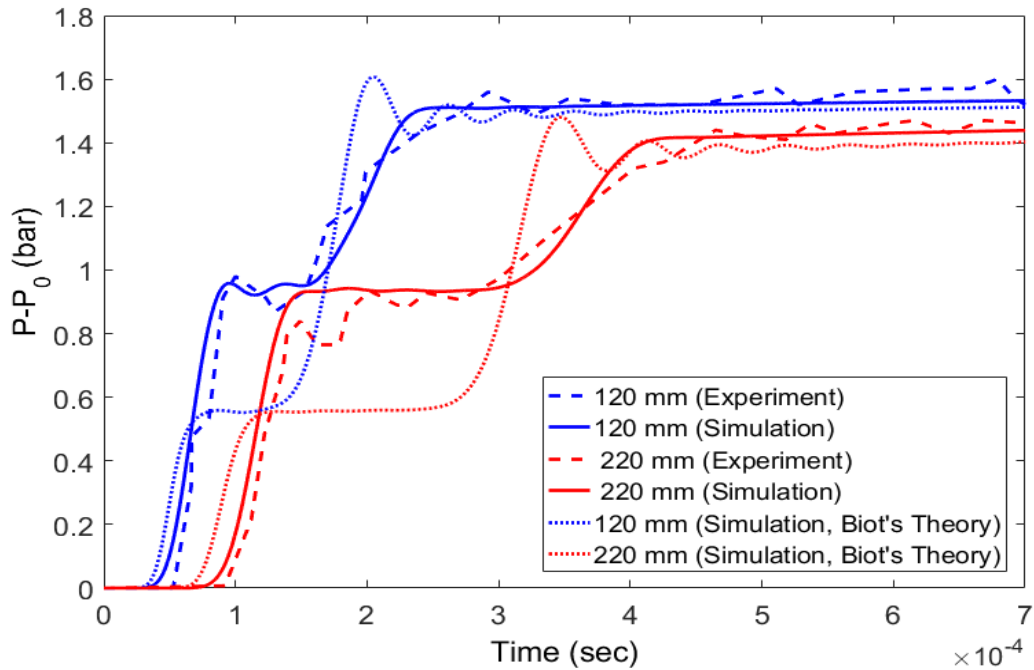
Figure 4-4 Comparison of pore pressure response for a shock wave

The strain gauges inserted on the wall of the sample are pressure-dependent because they are glued to the porous sample with epoxy resin whose bulk modulus is smaller than that of the sand. Therefore, the glue would be compressed with increasing pressures. This pressure dependency was calculated from separate experiments. Values of 3.5 and 5.0 microstrain/bar are reported for the pressure

sensitivity of these gauges (van der Grinten et al., 1987). Both the measured values and the corrected ones are shown in Figure 4-5 and Figure 4-6, assuming compressive strains to be positive. There is a difference in the transient regime but the trend is predicted correctly. This difference is more significant using Biot's theory.
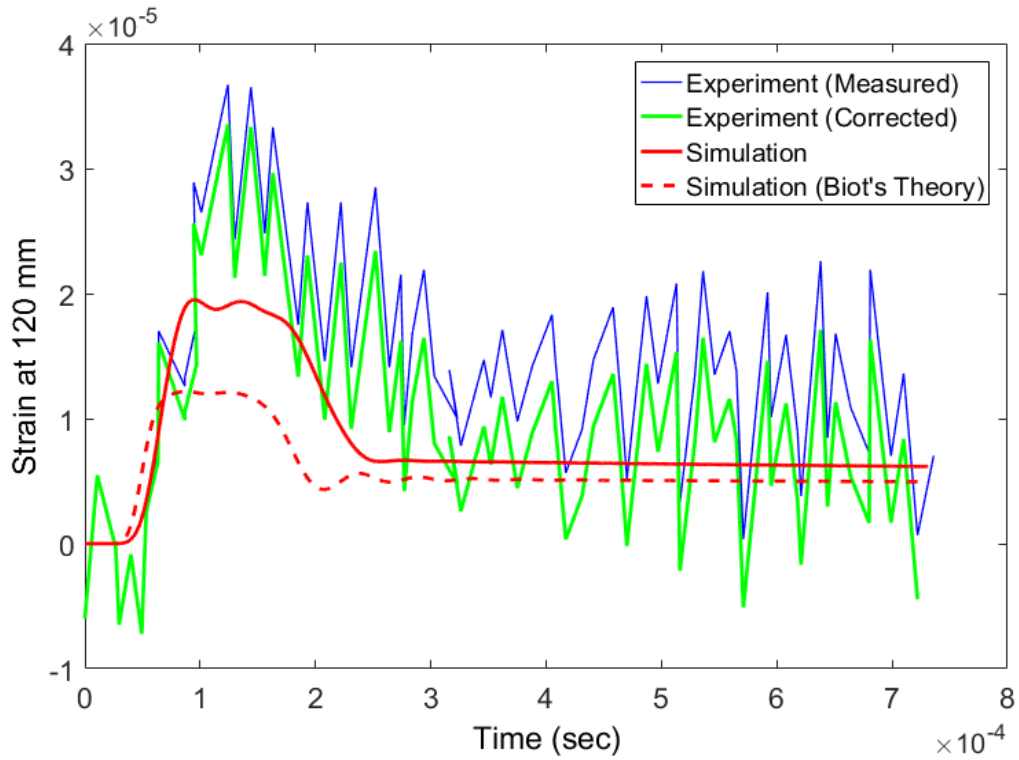
Figure 4-5 Comparison of axial strain response at 120 mm from the top of the sample
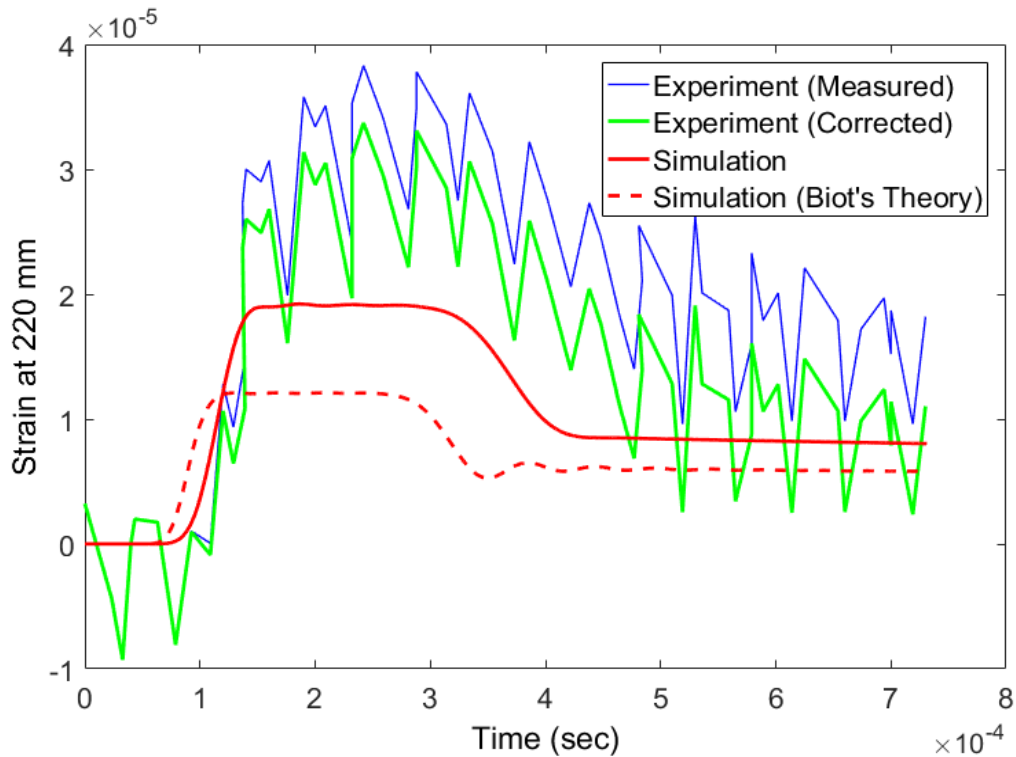
Figure 4-6 Comparison of axial strain response at 220 mm from the top of the sample

Figure 4-7 and Figure 4-8 show the axial velocity and acceleration of both phases at 220 mm from the top of the sample, respectively. The interesting point is that the solid and fluid phases move together in the beginning, resulting in undrained wave propagation due to undrained conditions (Verruijt, 2010). For the second wave, the phases move with opposite accelerations with larger differences in velocities. Therefore, the friction between the two phases leads to the damping of wave amplitude far from the source.

Simulation results indicate near zero values for radial acceleration and velocity. Therefore, it appears that the radial motion of the sample does not play a significant role in this experiment, which is contrary to the justification for wave speeds done by van der Grinten et al. (1985, 1987).
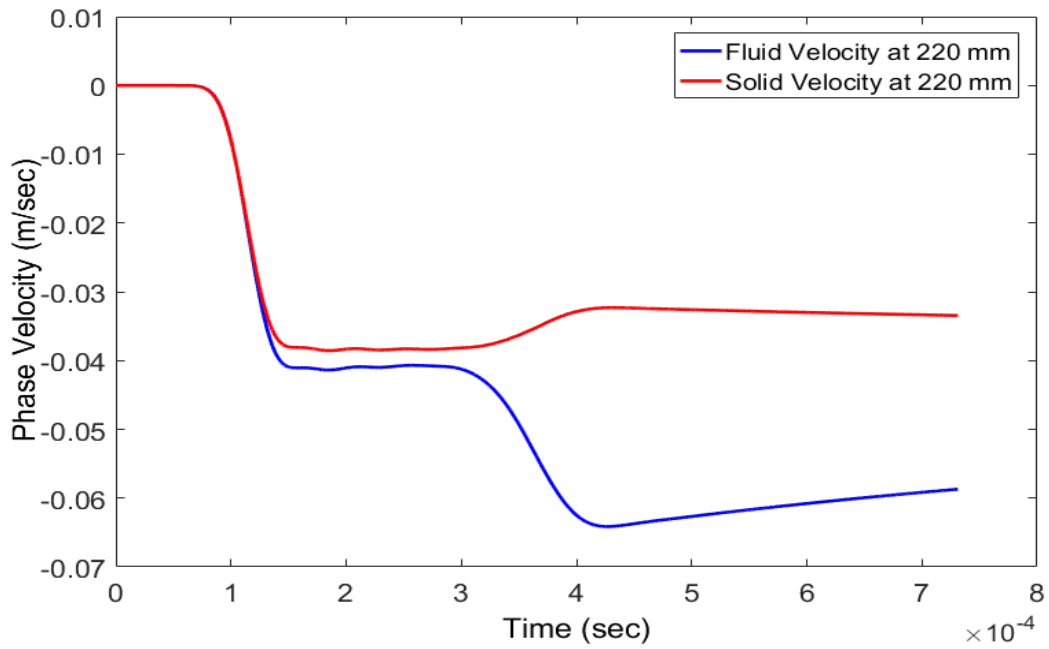
Figure 4-7 Simulated axial velocity response at 220 mm from the top of the sample
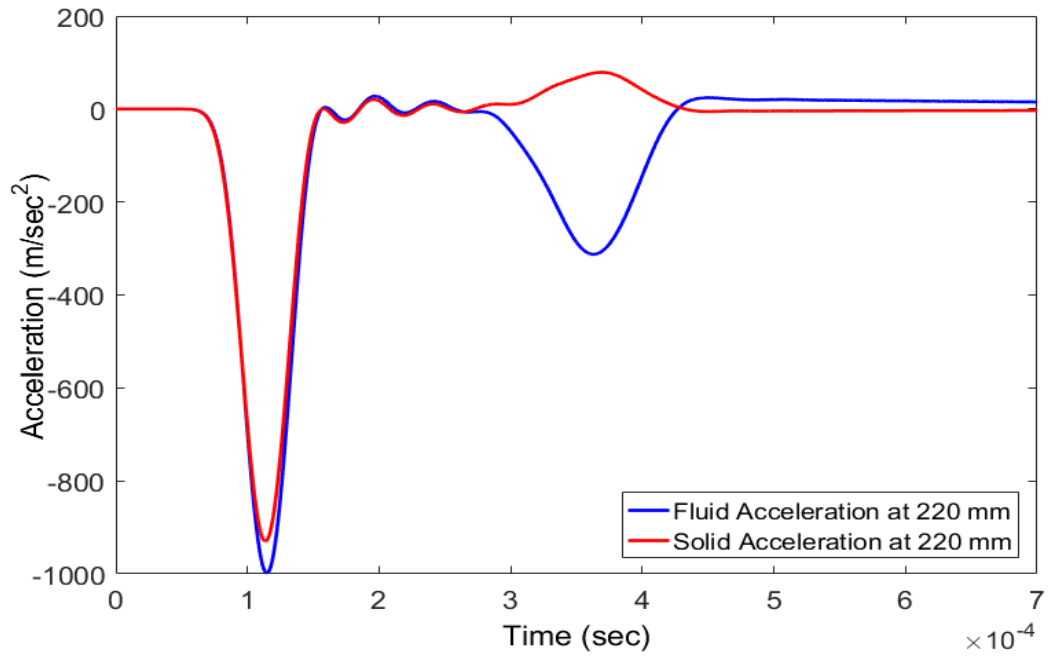
Figure 4-8 Simulated axial acceleration response at 220 mm from the top of the sample

It would be beneficial to look at the porosity changes during wave propagation. Figure 4-9 shows the time variation of normalized porosity as defined by $n_D = \frac{n-n_0}{n_0}$. The first drop in porosity is the result of the sample contraction due to the shock wave. The subsequent increase in porosity is the result of the second wave when the solid moves more slowly than the fluid, resulting in some expansion but not enough to cancel out all the initial contraction.
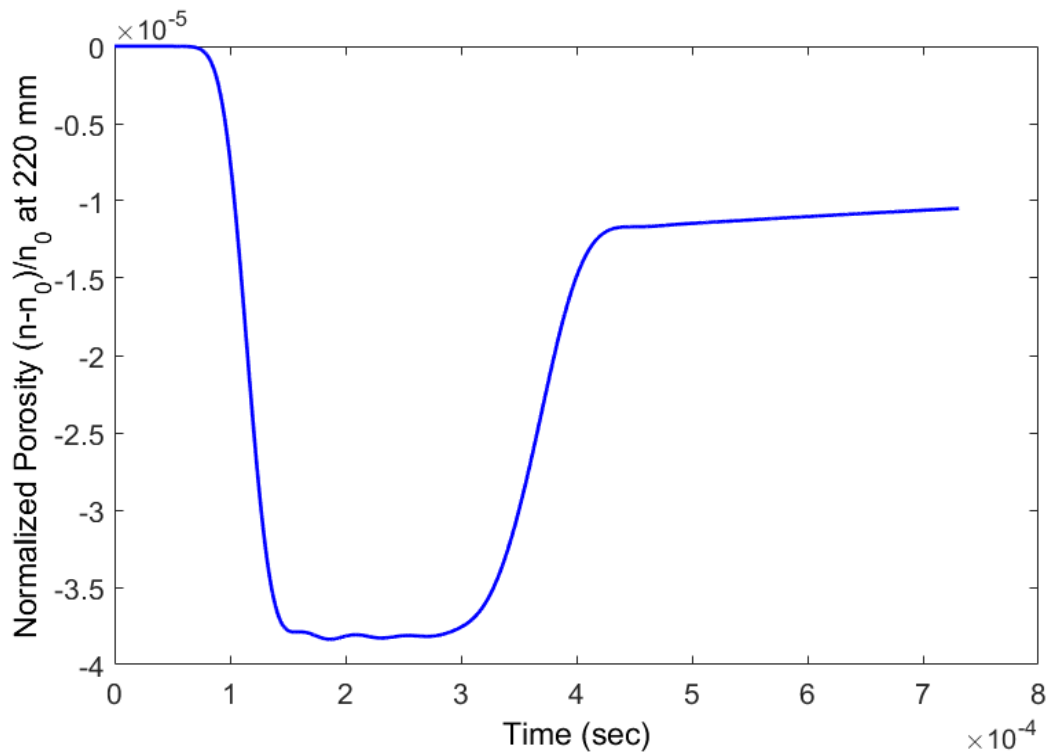
Figure 4-9 Simulated normalized porosity at 220 mm from the top of the sample

Figure 4-10 shows the effect of tortuosity on the numerical results. It affects the amplitude of the first wave and the speed of the second wave. Tortuosity or the narrowing–widening nature of porous media accelerates the fluid. This acceleration can generate a wave with a different amplitude.

89
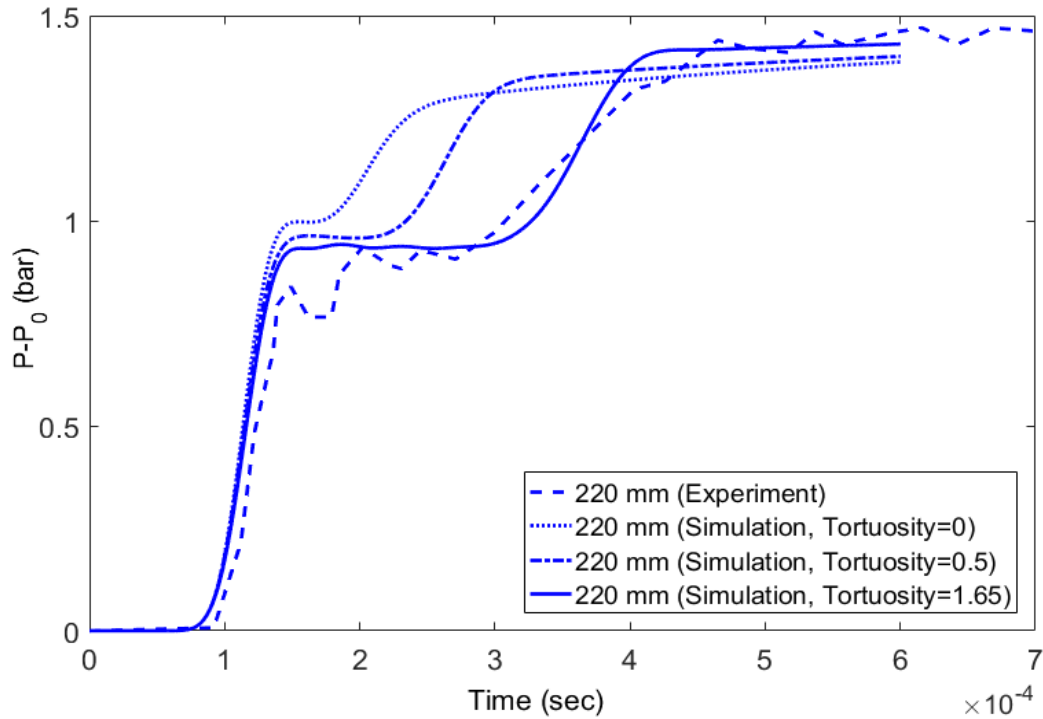
Figure 4-10 Effect of tortuosity

4.9.2 Wave Reflection in the Shock Tube

Eqs. (4-2) and (4-4) result in the analytical velocities of 2508 m/s and 732 m/s for the solid and fluid waves, respectively. Hence, the time for the solid and fluid waves to travel to the bottom end of the sample and return to point 2 (220 mm from top) is estimated to be 0.0014 sec and 0.0052 sec, respectively. Using the simulation results, the wave velocities are calculated as 1980 m/s for solid and 649.9 m/s for fluid waves. Therefore, the time needed for the reflected wave in the solid and fluid to reach Point 2 is estimated at 0.00184 and 0.0058, respectively. This assessment is in agreement with Figure 4-11 and Figure 4-12, which show the wave reflection in terms of pore pressure and porosity. The vertical lines represent the expected reflection times calculated from the wave velocities. It seems that there is a slowing factor as time increases. The figure

shows only the first wave reflection, and there are no pressure changes at the expected reflection times of the second wave. This wave is usually damped far from the source (Verruijt, 2010). In addition, the type of the boundary plays an important role in whether a wave is reflected or completely absorbed. The velocity of the first wave depends only on the moduli and the density of the medium. Density, especially that of the fluid, increases with higher pressure, resulting in a slightly slower wave. Thus, based on the first wave speed the reflections should occur slightly earlier.
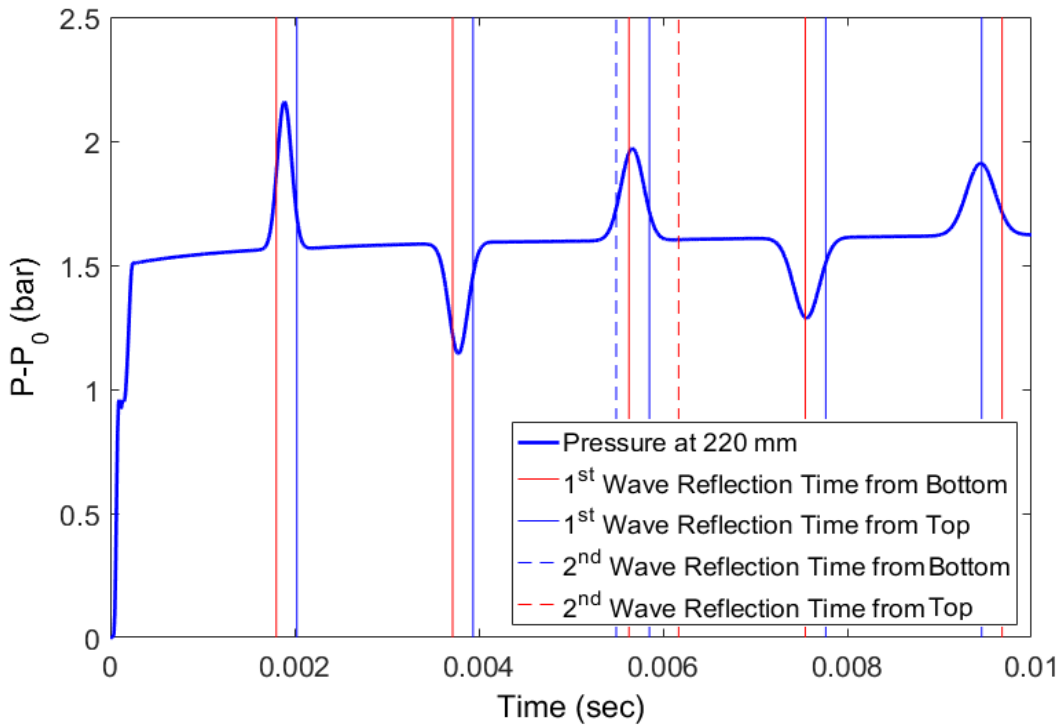
Figure 4-11 Pore pressure response due to the reflection of wave at 220 mm (P2) from the top of the sample

Figure 4-12 shows that the reflection of wave can also be observed by examining the porosity changes. The first drop in porosity is the result of the first undrained wave followed by an increase in porosity by the second wave to an approximately steady value. The later changes are due to the reflection of the first wave.

Figure 4-13 demonstrates the axial displacements through time. Initially, downward displacements are generated as the waves compress the soil sample. After a while, when the wave hits the boundary and is reflected, part of the compression is relieved.
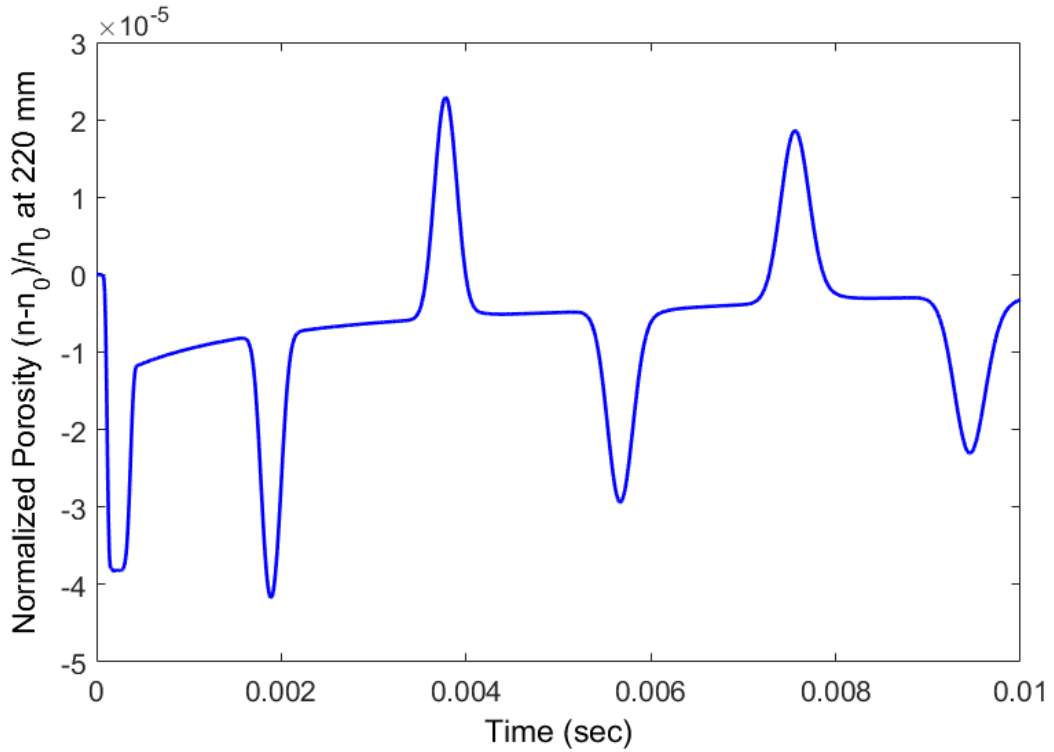
Figure 4-12 Porosity response due to the reflection of wave at 220 mm from the top of the sample
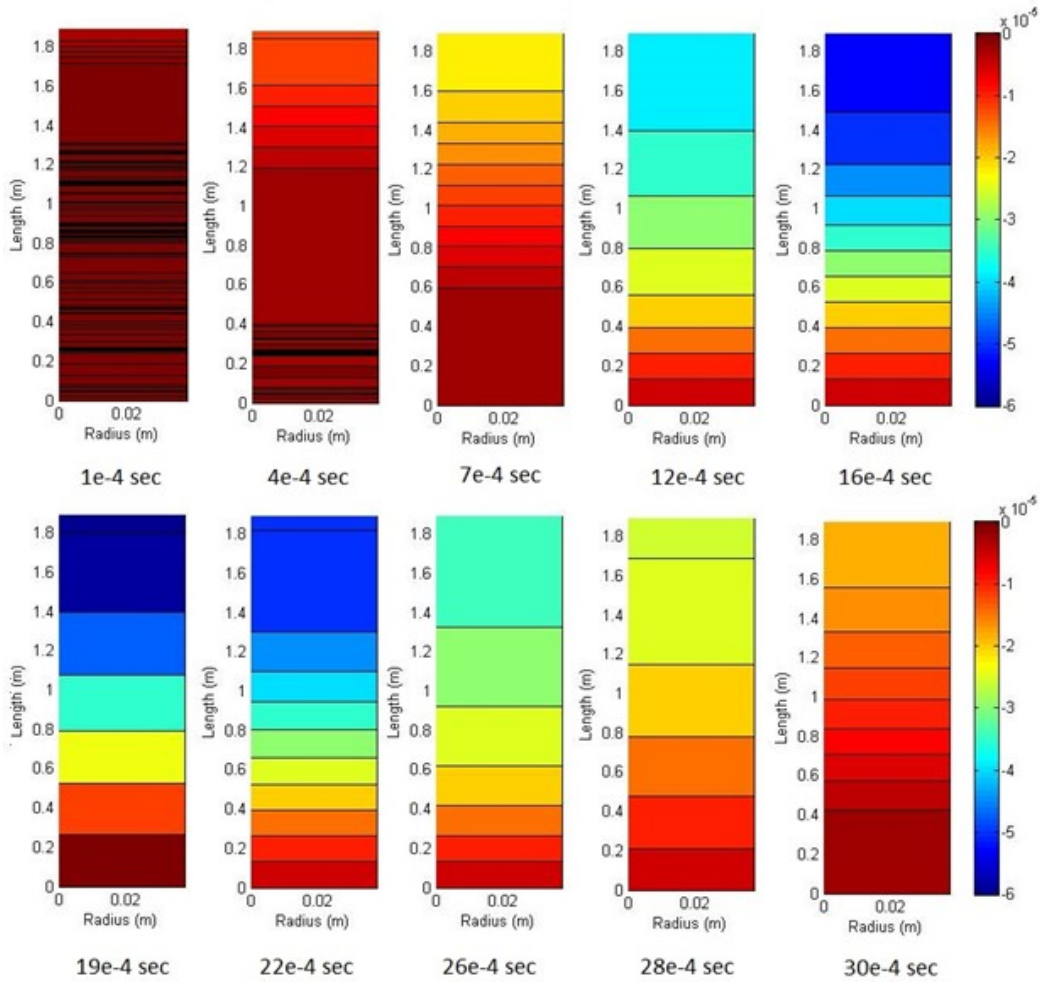
Figure 4-13 Contours of axial displacement

4.10 WH Pressure Propagation in Elastic Porous Media

The results of simulation of the propagation of a shock wave in a hypothetical reservoir are presented in this section. The rock deformation is assumed to be elastic obeying Hook's law. Elastoplastic conditions are discussed in Chapter 5. In this chapter, there is no attempt to incorporate failure or any possible liquefaction of the rock. The reservoir properties are zero tortuosity, 500 mDarcy permeability, bulk modulus of 218 MPa, and shear modulus of 131 MPa. The low moduli are to represent cohesionless sand at low effective stresses, which is the condition near an injector wellface. All the other properties are the same as those of the

93

experiment cited in Section 4.9. In situ reservoir pressure and vertical and horizontal stresses are selected to be 112, 120 and 115.6 MPa, respectively. The injection into the reservoir is applied from an openhole with the diameter of 10 cm with a pressure of 115.6 MPa. The right boundary fixed against displacement in the normal direction and the pore pressure is also fixed in the same boundary. The initial condition is considered to be steady-state injection, and axial symmetry is assumed. A drop wave with amplitude of 3.6 MPa is applied on the wellface. The total stress at the wellbore is also dropped simultaneously to the pressure drop so that the effective stress stays at $(1 - \alpha)p$, where α is Biot's coefficient. The schematic of the model is presented in Figure 4-14.
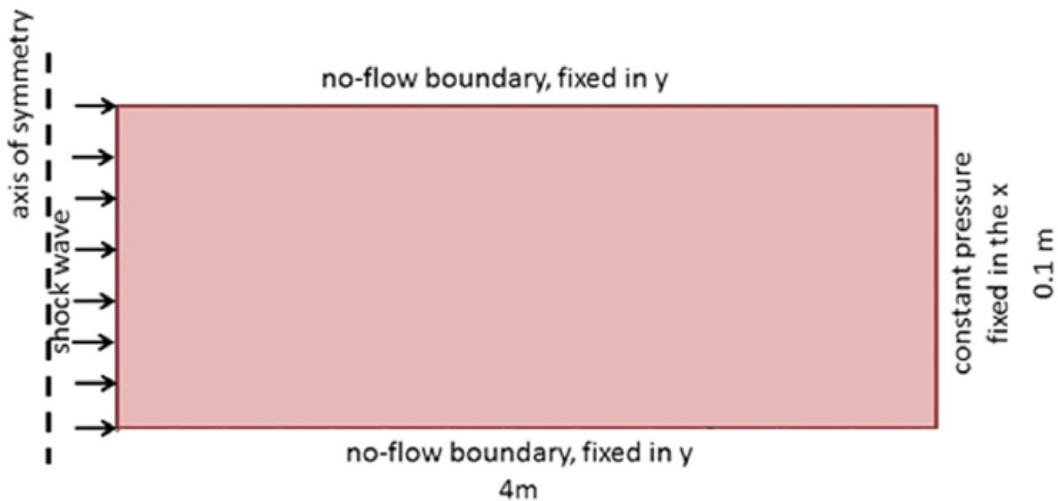
Figure 4-14 Model schematic

Figure 4-15 shows the pore pressure variation through time at three different locations. The two distinct pore pressure waves are characteristics of porous media, which are expected. However, the second wave is damped in most cases and its appearance depends on the properties of the medium. The predicted velocities show that the two phases are moving together, emphasizing that only the undrained wave occurs under these conditions.

For a cylindrical wave, there will be a geometric damping as the area exposed to the wave increases with radius. Hence the amplitude of the wave decreases with radius. In addition, for low permeabilities, the radius of drainage for Darcy flow cannot reach the wave front. Therefore, there will be a gradual increase of the pore pressure behind the wave front. If we use the properties of the shock tube example, there will be a two-wave response for the radial propagation of the wave.
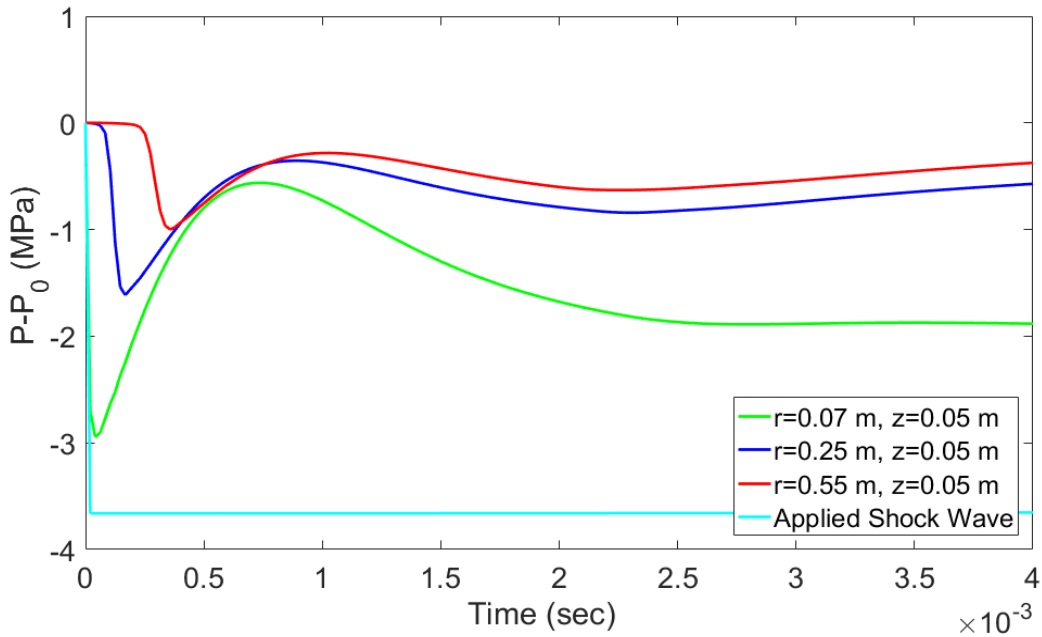
Figure 4-15 Pore pressure versus time at three locations

The results show that in this case only the areas near the well are affected by dynamics. Figure 4-15 shows that only one fifth of the applied wave is expected one meter away from the well. However, the nature of the wave is very quick and when the wellbore is exposed to subsequent multiple waves, e.g. for WH pressure pulsing, dynamic analysis is necessary to obtain a proper solution for the problem.

The changes in the effective stresses and shear stress are plotted in Figure 4-16 to Figure 4-19. Although pore pressures return to their original values when the waves are damped, effective radial stresses undergo a permanent change.
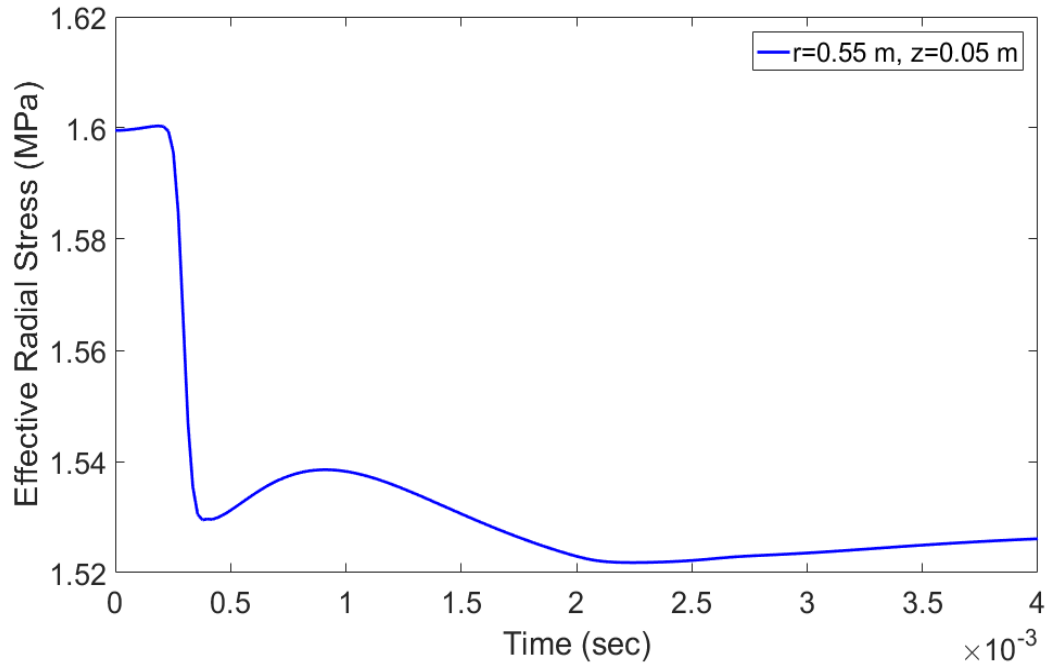
Figure 4-16 Effective radial stress at r=0.55 m and z=0.05 m
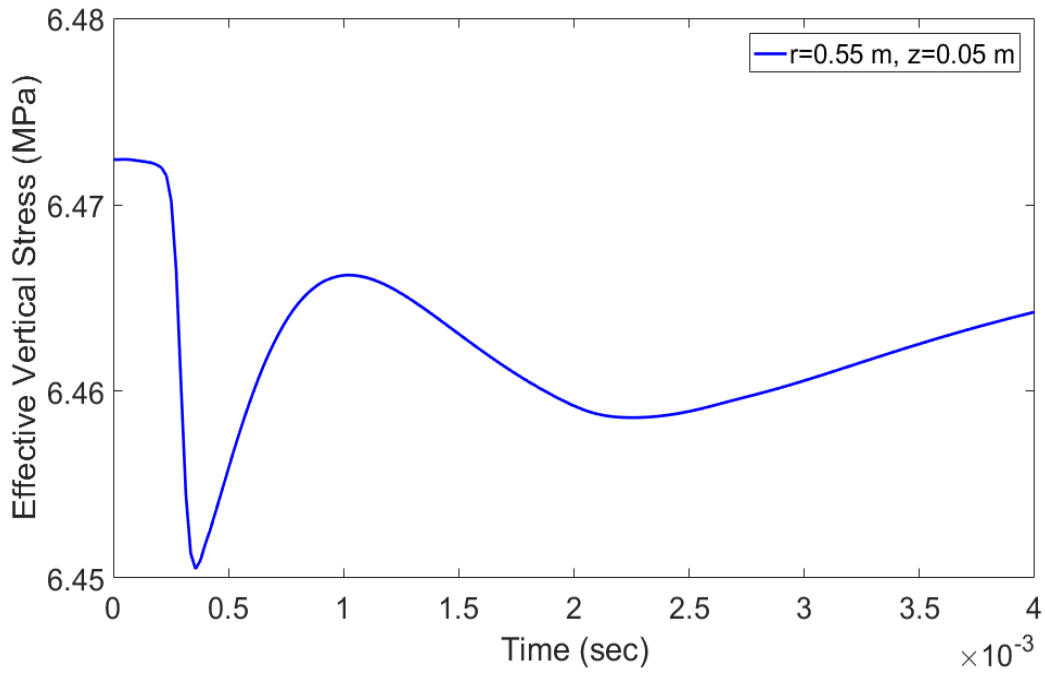
Figure 4-17 Effective vertical stress at r=0.55 m and z=0.05 m
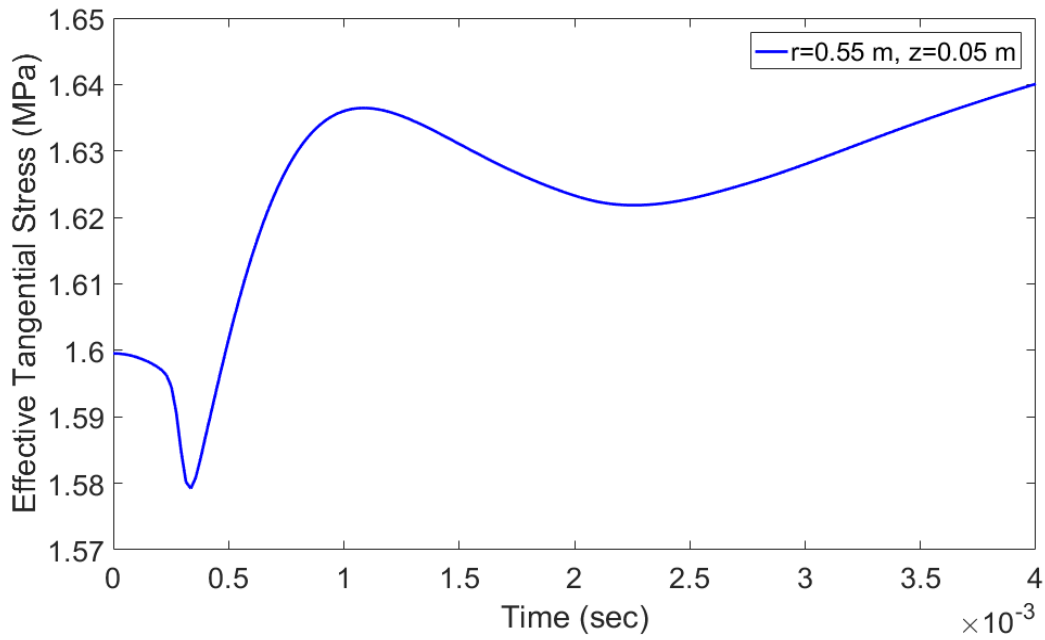
Figure 4-18 Effective tangential stress at r=0.55 m and z=0.05 m
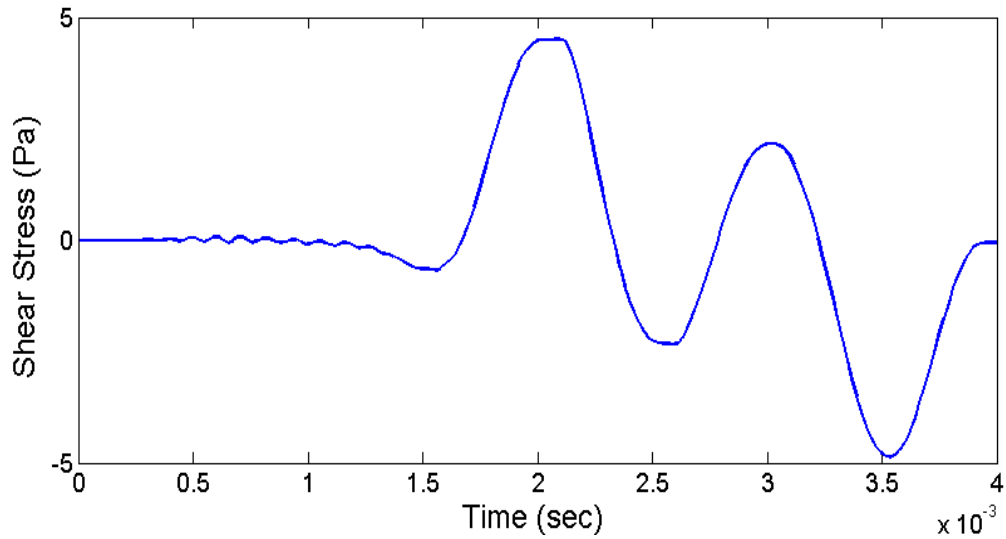
Figure 4-19 Shear stress at r=0.55 m and z=0.05 m

Since we are modelling a 2D problem, we should expect to observe the generation and travel of a shear wave in the model. A shear wave is a wave for which the direction of particle displacement is perpendicular to the wave travelling direction. Here we have a radial wave; under axisymmetric conditions, the shear wave must induce oscillating vertical displacements equivalent to ε_{rz}. Figure 4-20 shows the shear strain, which is small in values. This could be due to the fixed top and bottom boundaries and small reservoir thickness.
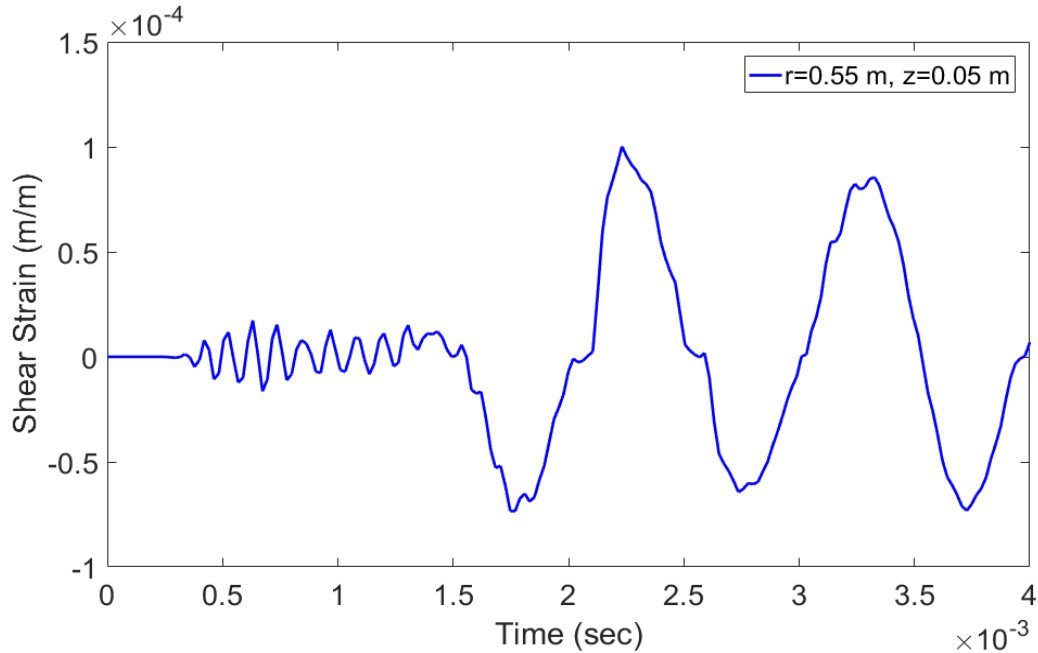
Figure 4-20 Shear strain at r=0.55 m and z=0.05 m

4.11 Coupling

Since elastoplastic solid deformation and its ability to liquefy are important in our application, it is a more appropriate choice to use more advanced constitutive models. For that, one needs to couple the fluid flow code in MATLAB with commercial software, the dynamic option in FLAC.

4.11.1 Coupling Schemes

There are different schemes of coupling fluid flow with geomechanics. Sequentially-coupled schemes are more popular since they are not as numerically-expensive as fully-coupled ones. Kim (Kim, 2010; Kim et al. 2011) investigated the stability, convergence, and accuracy of different sequentially-coupled algorithms. He divided the sequential methods into four categories: drained split and undrained split if the mechanical simulator is solved first (see Figure 4-21 and Figure 4-22) and fixed-strain and fixed-stress if the fluid flow simulator is solved

first. He concluded that undrained split and fixed-stress schemes are unconditionally stable, faster in convergence, and more accurate. In this work, the mechanical step is solved first; therefore, both drained split and undrained split coupling schemes are investigated to ensure Kim's conclusions are still valid for dynamic coupling.
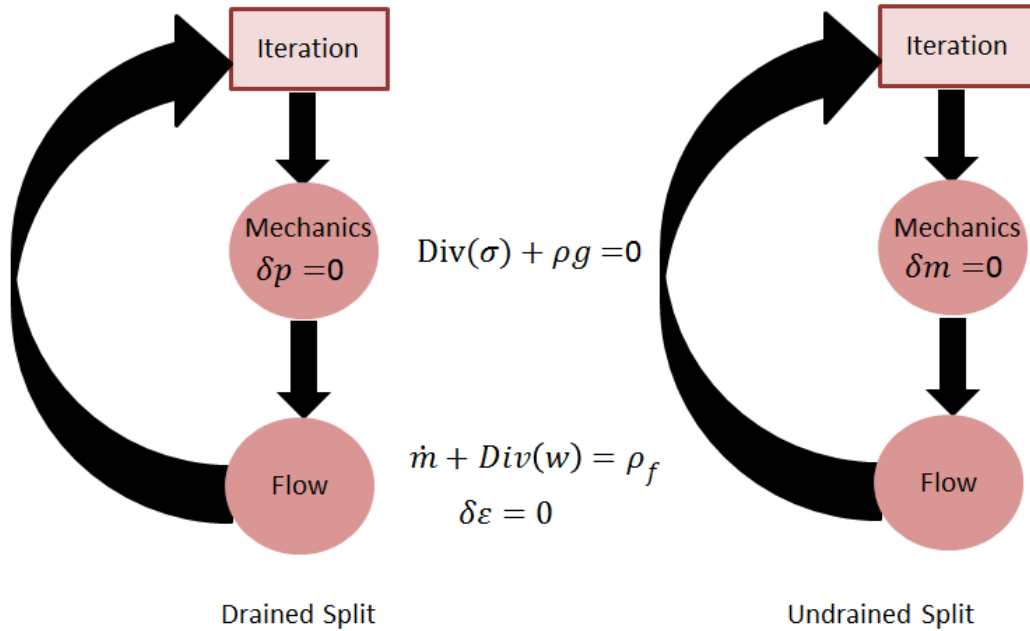
Figure 4-21 Different schemes of coupling fluid flow with geomechanics (Kim. 2010)

$$\begin{bmatrix} u^n \\ p^n \end{bmatrix} \xrightarrow{\text{mechanics}} \begin{bmatrix} u^{n+1} \\ p^n \end{bmatrix} \xrightarrow{\text{flow}} \begin{bmatrix} u^{n+1} \\ p^{n+1} \end{bmatrix} \qquad\qquad \begin{bmatrix} u^n \\ p^n \end{bmatrix} \xrightarrow{\text{mechanics}} \begin{bmatrix} u^{n+1} \\ p^* \end{bmatrix} \xrightarrow{\text{flow}} \begin{bmatrix} u^{n+1} \\ p^{n+1} \end{bmatrix}$$

Drained Split   Undrained Split
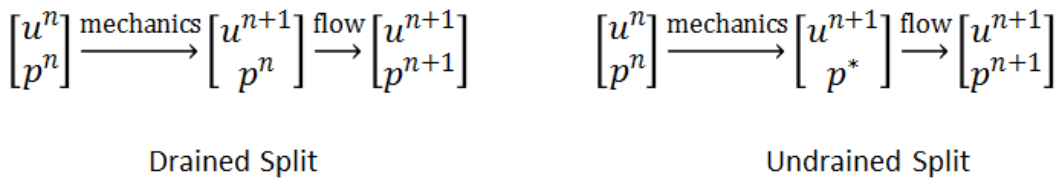
Figure 4-22 Different schemes of coupling fluid flow with geomechanics (Kim. 2010)

In the drained split, during the mechanical steps pore pressure remains constant, and then fluid flow is solved to update the pore pressure. In the undrained scheme, no fluid flow is allowed during the mechanical step (see Figure 4-21 and Figure 4-22). No fluid flow means pore pressure will change based on the volumetric strain

to an undrained (excess) pore pressure, p^*. This undrained pore pressure can be calculated by:

$$\delta p = \alpha \frac{\delta \varepsilon_v}{S_p} \tag{4-55}$$

$$p^* = p^n + \delta p \tag{4-56}$$

where n superscript shows the values at the last time step and $n + 1$ superscript represents the values at the new time step. Kim suggested calculating the pore pressure gradient using an intermediate time:

$$p^{n+\beta} = \beta p^* + (1 - \beta)p^n \tag{4-57}$$

where $n + \beta$ is a time between current time step, n, and the next time step, $n + 1$. He (Kim. 2010) concluded that this scheme is unconditionally stable for $\beta \geq 0.5$. He also showed that the drained scheme, even when stable, may not converge to the exact solution. All of his work was performed for quasi-static conditions and not dynamic conditions. Therefore, the same coupling schemes are investigated under dynamic conditions.

4.11.2 Coupling Fluid Dynamics with FLAC

The trick in coupling fluid dynamics code with FLAC is FLAC does not distinguish fluid acceleration from that of solid, and instead of Eq. (4-19), it solves the following equation in dynamic module:

$$\rho \frac{\partial w}{\partial t} = \text{Div}(\sigma) + \rho g, \tag{4-58}$$

To compensate for the difference in the accelerations, an additional acceleration is calculated by the difference between Eq. (4-58) and Eq. (4-19). Note that one cannot directly apply this acceleration, as the software considers it as a boundary

condition. Therefore, velocity on each node is updated at every step based on this acceleration.

$$a_{additional} = n\rho_f \left(\frac{\partial v}{\partial t} - \frac{\partial w}{\partial t} \right)$$
(4-59)

To verify the coupling algorithm, a shock tube example is solved to compare the results of the sequentially-coupled fluid dynamics and FLAC with fully-coupled code in MATLAB. Both drained and undrained schemes are applied and pore pressure is reported at three different locations: 2 mm, 12 mm, and 22 mm from the top of the sample.

In Fully-coupled approach the governing equations such as flow, mass balance and geomechanics are discretized and solved simultaneously at every time step. Sequentially-coupled approach is where either flow or mechanics is solved first to obtain an intermediate solution estimate. Solutions are then used in solving the other equation. The process can be iterated until the desired convergence tolerance is achieved. Loosely-coupled is done where coupling between flow and geomechanics is resolved only at certain time intervals (Klevtsov, 2017).

According to Figure 4-23, undrained response is closer to the fully-coupled response. In addition, the drained response converges to a different steady state solution. To conclude, the results are consistent with what Kim (Kim. 2010) reported for quasi-static conditions. Therefore, an undrained scheme is preferable both for quasi-static and dynamic coupling of fluid flow and geomechanics.

There are a number of possible reasons why the sequentially-coupled code is still different from fully-coupled code: the scalar version of artificial viscosity in FLAC vs. the tensor form in fully-coupled, the way additional acceleration is handled, and the truncation error introduced when exporting the values of variables from one code to another.
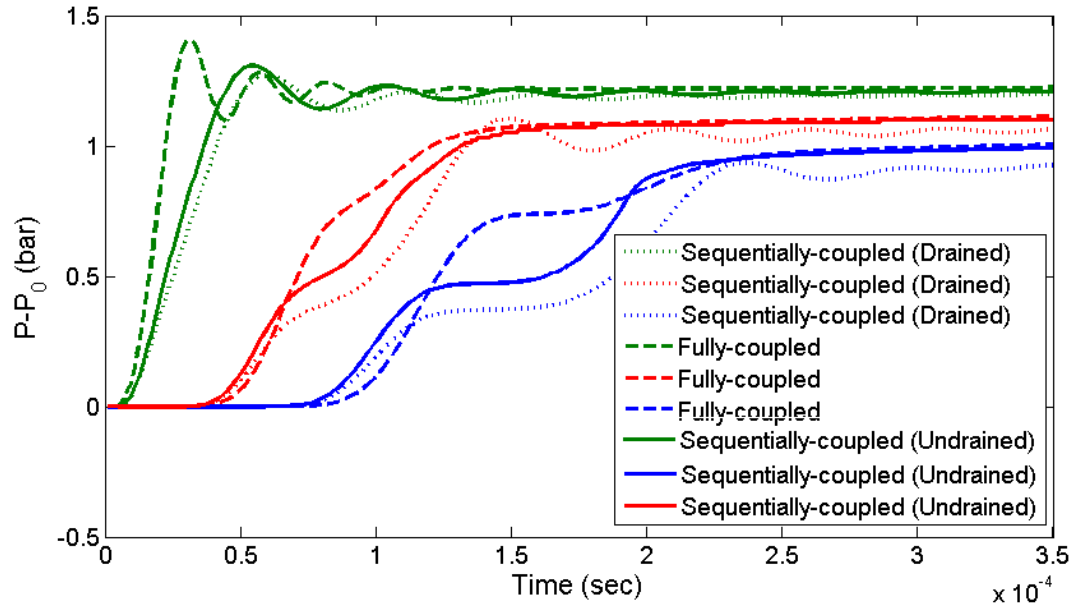
Figure 4-23 Comparison of coupling schemes for a shock tube example

Based on the results shown in Figure 4-23, undrained scheme of sequentially-coupling is closer to a fully-coupled case. In this work, the stable undrained scheme with $\beta = 0.5$ is adopted for coupling the dynamic codes. Figure 4-24 shows the final selected algorithm for coupling fluid dynamics code with FLAC Dynamics.
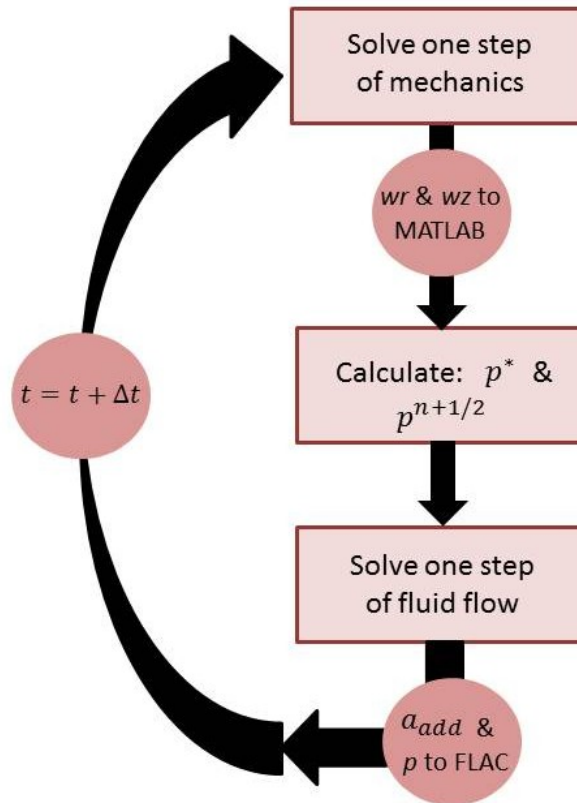
Figure 4-24 Coupling algorithm

Iterations are not implemented here mainly because the time steps are small enough for convergence and it reduces the numerical computations. As generally known, extremely fast phenomena if computed in all their time-dependent detail by solving Navier-Stokes are still beyond the practical reach of computational methods (Patankar, 1980). Two-way coupling of the code with geomechanics increases the time steps dramatically. Nevertheless, if the equations are solved without iterations during transient regimes in a small-scale model, a numerical response is still practical for short periods of time.

Appendix A shows the code developed in MATLAB for fully-coupled dynamics in porous media. Appendix B shows the MATLAB-FLAC code for sequentially-coupled scheme.

4.12 Conclusions

A two-dimensional mathematical formulation and numerical solution of dynamic wave propagation in saturated porous media is presented for low frequency waves with the emphasis on pore pressure waves. To predict the dynamic transient fluid flow accurately, de la Cruz and Spanos's approach is adopted. The formulation is modified in a displacement-stress format and the equations and the solution method are extended for elastoplastic solid behaviour. A new tensor form of artificial viscosity is proposed that is more efficient in damping numerically induced oscillations than the original Von Neumann and Landshhoff terms. The formulation is validated against experimental data and then compared with the formulation presented earlier by Biot. Biot's theory has been shown to be inaccurate in calculating wave propagation speed in deformable porous media and the amplitudes of pore pressure responses. However, it is sufficient in predicting the trends of pore pressure. Both theories predict two distinct waves as a result of a shock pore pressure wave: (1) undrained wave and (2) a wave which is highly damped due to opposite motion of the solid and the fluid. The presence of this wave depends on the porous media properties. Next, a reservoir response to WH pressure wave is simulated. Only near-wellbore areas could see the dynamic effect. In rocks with low permeability (compared to soil in the shock tube experiment), Darcy's flow cannot compensate for the pressure change as quickly as the wave propagates. Consequently, the pore pressure will return to the original values after the waves pass that specific location. In 2D problems, a shear wave is also generated as a result of the shock wave.

The fluid dynamic equations are then coupled with FLAC dynamic module to be able to use more complicated constitutive models. Different schemes of coupling are investigated: drained vs. undrained. The results show that similar to quasi-static conditions, an undrained scheme is the more appropriate choice in coupling

dynamic fluid and solid equations. It is more stable and converges to the correct answer for a steady state.

4.13 Nomenclature

C_f Fluid compressibility

C_m Porous medium compressibility

C_s Grain compressibility

k Permeability

K_s Bulk modulus

n Porosity

n_0 Initial Porosity

n_D Dimensionless Porosity

p Pore pressure

S_p Storativity of the porous medium

r Radial direction

t Time

v_r Fluid velocity in r direction

v_z Fluid velocity in z direction

w_r Solid velocity in r direction

w_z Solid velocity in z direction

z Vertical direction

α Biot's coefficient

δ_f Fluid dilatancy

δ_s Solid dilatancy

ε_v Volumetric strain

μ Fluid viscosity

ρ_f Fluid density

ρ_s Solid density

ρ_{12} Added mass density

σ_{ij} Stress component

$\overline{\sigma}$ Mean stress; $\overline{\sigma} = \sigma_{ii}/3$

Chapter 5: Dynamic Analysis of Near-Wellbore Sand Reservoir Response to WH Pressure Pulsing

5.1 Introduction

Chapter 4 described the development of a dynamic numerical tool and its validation to study the reservoir response to WH pressure pulses. In this chapter, the same tool is utilized to analyze the dynamic response of a synthetic sand reservoir using an elastoplastic model. A mesh sensitivity is performed to ensure the numerical results are independent of the selected grid size. Then the model is used to study sanding potential around an injector well. None of the sanding incidents reported in the literature provide enough data, such as material properties and operating conditions, for a meaningful comprehensive study with the results from the numerical simulation. The case study reported by Santarelli et al. (Santarelli et al. 1998; Santarelli et al. 2000), where the injector well was filled up with sand after an emergency shut-in, is selected for the construction of a numerical model since it provides a more comprehensive information on the wellbore and the reservoir compared to the other cases reported in the litarature.

A sensitivity analysis is performed to distinguish the sensitivity of the reservoir response to several constitutive and operational parameters. Different constitutive models are used in the model to assess their performance and compare their results.

5.2 Case Study: An Injection Well in Norwegian North Sea

There are several examples of massive sand production in the injector wells, which in some cases have led to a complete loss of injectivity. Examples include those in the Norwegian North Sea (Santarelli et al., 1998; Santarelli et al., 2000), Indonesia (Papamichos, 2006), and Buzzard field in UK (Santarelli et al., 2011). The Norwegian Sea well serves as a good example for the severity of sanding in an injector well, where the injectivity of the well decreased from 8000 m^3/d to 0 m^3/d in just half an hour.

An injector well in the Norwegian North Sea (Santarelli et al. 1998; Santarelli et al. 2000) is selected for this numerical study. This case is selected because the majority of the required properties and field operating conditions have been reported in the literature. Note that much key data for this case could not be found in the open literature and some assumptions are made. Therefore, the results and conclusions presented in this chapter should only be regarded as an exercise for the study of sanding potential in the injection wells and should not be regarded as firm conclusions for this case.

In this example, the reservoir properties and operational conditions that increase the possibility of liquefaction are:

- The sandstone was weakly consolidated (UCS= 2-10 MPa) and the strength was further reduced by 10 to 20% because of water.

- An 8,000 m^3/day injection flow rate indicates high injection pressure, which can substantially reduce effective stresses around the wellbore. Effective stresses are further reduced around the wellbore due to WH waves.

Therefore, Santarelli et al (2000) proposed liquefaction as the main mechanism based on the following evidence:

- A camera sent down the wellbore indicated that the perforations were filled with sand.

- The well was filled with 400 m of sand above the top perforation within only half an hour after the well shut-in. One explanation is that sand behaves as slurry otherwise the wellbore filling by sand should have stopped once the perforations had been covered.

- The slurry contained 60% sand by volume. The original porosity is not reported; however, 40% porosity (e=0.66) is considered a relatively high number for sandstone.

It is noted the above observations only implicitly suggest liquefaction as the main mechanism. In addition, such incidents were always accompanied by emergency shut-downs; and hence, affected by WH waves.

Alternatively, reservoir conditions, i.e. dense sandstone, higher stresses due to high depths and high permeability values, are not in favor of liquefaction. It is likely that a progressive failure where failure zone propagates quickly is the underlying reason of massive sand production. Sand production into the wellbore could redistribute the stresses leading to further failure, particularly in sand reservoirs where cavities are not stable.

5.2.1 Model Schematics

As discussed in Section 4.7, solving the dynamic equations for wave propagation in porous media is computationally demanding since the model requires very small time steps. Hence, a smaller model is used to investigate the potential sanding mechanisms.

There are limitations associated with the small-scale modeling: radial pressure/stress gradients can be affected, and the specification of boundary

conditions can be a challenge to set accurately. A single-layer model like what is used in this effort simplifies the effects of overburden and underburden layers into simple boundary conditions This model is 1 m in length and 0.3 m in height with a perforation of 0.02 m diameter. A schematic of the model is illustrated in Figure 5-1.
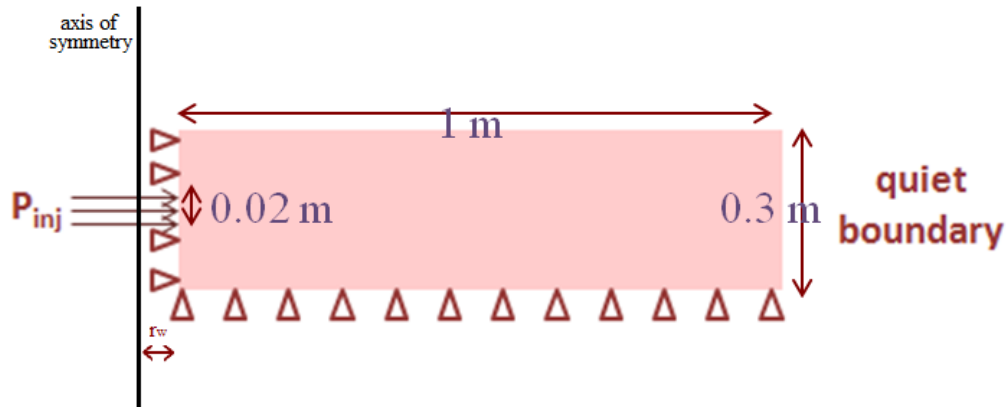
Figure 5-1 Model schematics

5.2.2 Initial and Boundary Conditions:

The initial conditions and in-situ stresses reported by Santarelli (Santarelli et al. 1998; Santarelli et al. 2000) are summarized in Table 5-1.

Table 5-1 In-situ conditions reported by Santarelli et al. (1998)

Initial Conditions	Value (MPa)
Vertical Stress	50.5
Horizontal Stress	39.4
Initial Pressure	27.6

The short radius of the model (1 m) will alter the radial pressure and stress gradients. In order to attain more realistic estimation for gradients, a longer model with 50-m radius (see Figure 5-2) is simulated for the initial steady-state injection before the sudden well shut-in. The horizontal stress and pore pressure at 1-m

distance from the well in the long model are used as the boundary conditions in the smaller model shown in Figure 5-1. The steady-state results from the long model are shown in Table 5-2.
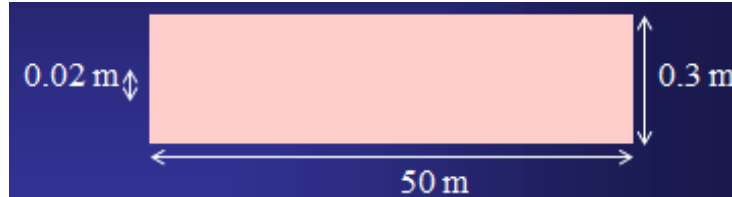
Figure 5-2 Longer model schematics for more realistic gradients

Table 5-2 Calculated boundary conditions at 1 m under steady state injection

Permeability (mDarcy)	Total Radial Stress (MPa)	Pore Pressure (MPa)
1000	40.15	29.07

The top and bottom of the model are fixed in the vertical direction. A fixed top boundary is representative of a rigid caprock, which does not move due to the arching phenomenon that allows the overburden stress redistribution. The wellbore is assumed to be cased and cemented and hence fixed in radial direction except for the perforation elements where WH waves will be applied after injection.

At the end of the steady-state solution, corresponding to the quick injection before shut-down, WH pressure pulses are applied at the perforation element and dynamic analysis is activated. Simultaneously, the right boundary condition is changed to a quiet boundary condition. A quiet boundary absorbs all the energy and acts as an infinitely large medium. It prevents the unrealistic wave reflection at the artificial boundary.

To ensure the validity of the stress and pressure distribution in the model, before the application of WH waves, the following steps are modeled quasi-statically:

- Initialization of in-situ conditions

- Wellbore drilling and applying mud pressure

- Casing installation and mud pressure removal

- Water injection until steady-state is achieved

The WH wave characterictics are not reported for the Norwegian Sea well. Wang et al. (2008) measured WH waves in an Alaskan field; a typical wave is shown earlier in Figure 2-2. They measured wave frequencies up to 17 HZ. Since Alaska measurements are made in an injection well, they are used in this research for generating the shape of the wave. Shallower waves (228 m) are smoother and easier to extract. Figure 5-3 shows that the wave shape can be approximated as a sinusoidal function.
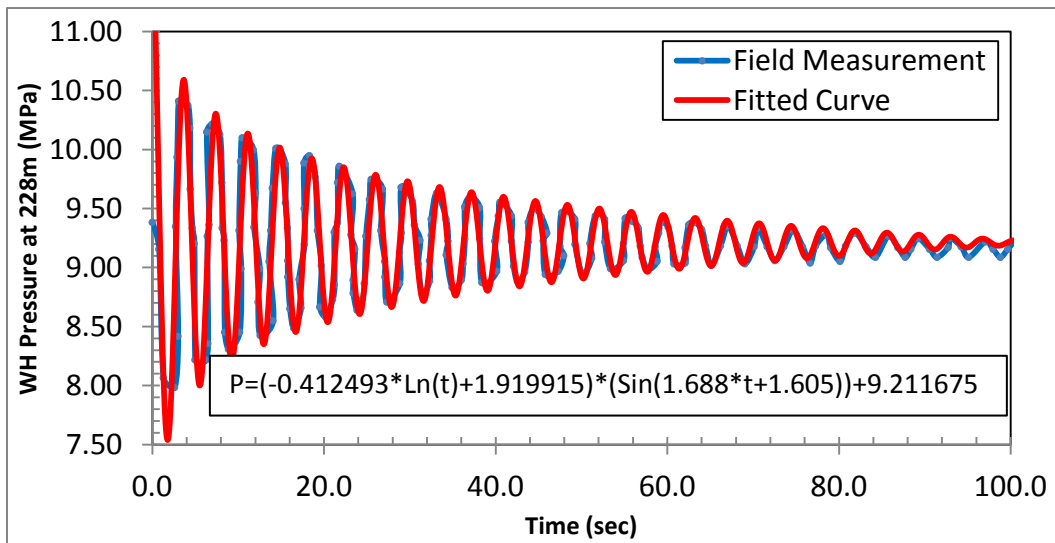
Figure 5-3 WH measurement in Alska Field at 228 m (Wang et al., 2008); and approximation using a sinusoidal function

In this study, the WH is assumed to have the maximum frequency meaured by Wang et al. (2008), i.e. 17 HZ, and an amplitude of 8 MPa in a sinusoidal pattern: $WH = 8Sin(2\pi \times 17t)$ MPa. There is a sensitivity analysis on the amplitude of the wave in Section 5.2.9. In general, the wave amplitude depends on the rate of

change in the flow velocity. This well had large injection rates, 8000 m^3/d, leading to significant WH amplitude following the emergency shut-in.

5.2.3 Flow Properties

Santarelli et al. (1998) reported a highly heterogeneous reservoir with sand permeability in the range between 0.1 to 5000 mDarcy. In this study, 1000 mDarcy is selected for the base model. No value for porosity is reported; therefore, a porosity of 22% is assumed. A sensitivity analysis is conducted on the permeability and porosity values to investigate the uncertainties. Since a water injector well is the focus of this study, water properties are considered for the fluid properties at 4°C.

5.2.4 Mesh Sensitivity

Three uniform grid sizes with square elements are compared for the mesh sensitivity analysis: 1.25 cm, 1.00 cm and 0.75 cm. Figure 5-4 shows the pressure response at four locations for these grid sizes. Pressure responses for the models with a grid size of 1.00 cm and 0.75 cm are sufficiently close. The results difference is within 1.5% for the element at r=5 cm and 0.8% for the element at r=15 cm. The same results differences for the models with 1.25 cm and 1.00 cm grid size are 5.8% and 2.9% for elements at r=5cma and r=1 cm, respectively. In addition, the run time is proportional to $N^{3/2}$ and N for FLAC and MATLAB, respectively, where N is the number of elements. To accelerate the numerical runs with the extremely small time steps (in the order of 10^{-6} sec), 1.00 cm grid size is used in this study.
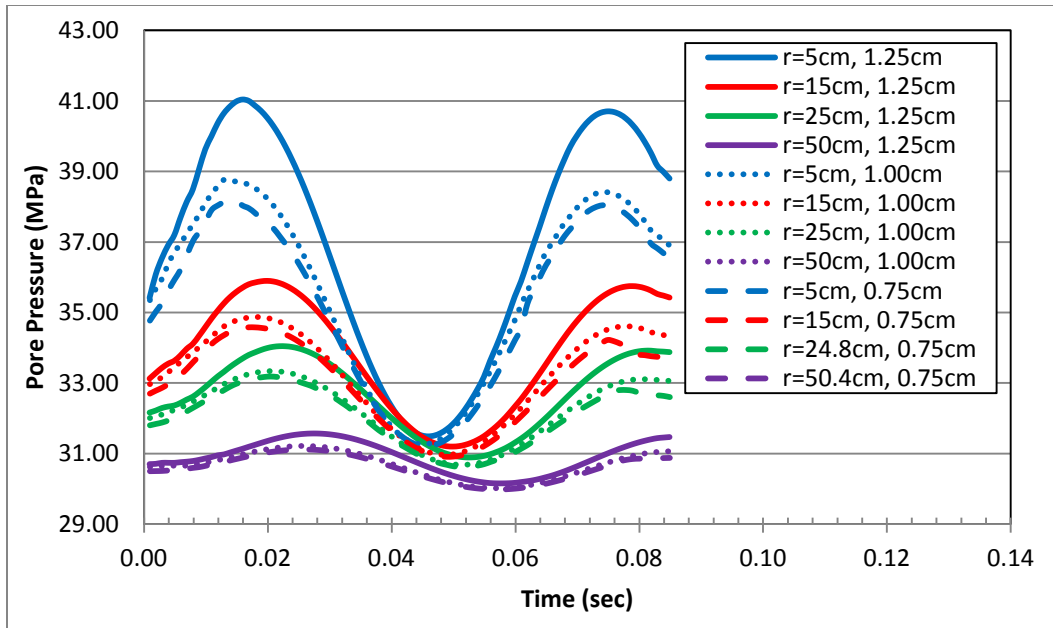
Figure 5-4 Impact of grid size on pressure response for an element at r=15cm

5.2.5 Rock Material Properties

Three sets of rock behaviour are considered:

1) elastic model

2) hardening/softening bilinear Mohr-Coulomb failure envelope discussed in Chapter 3

3) Martin model, a simple liquefaction-based model incorporated in FLAC (further details are discussed in Section 5.2.9)

Figure 5-5 shows the history points and their locations with respect to perforation elements..

115
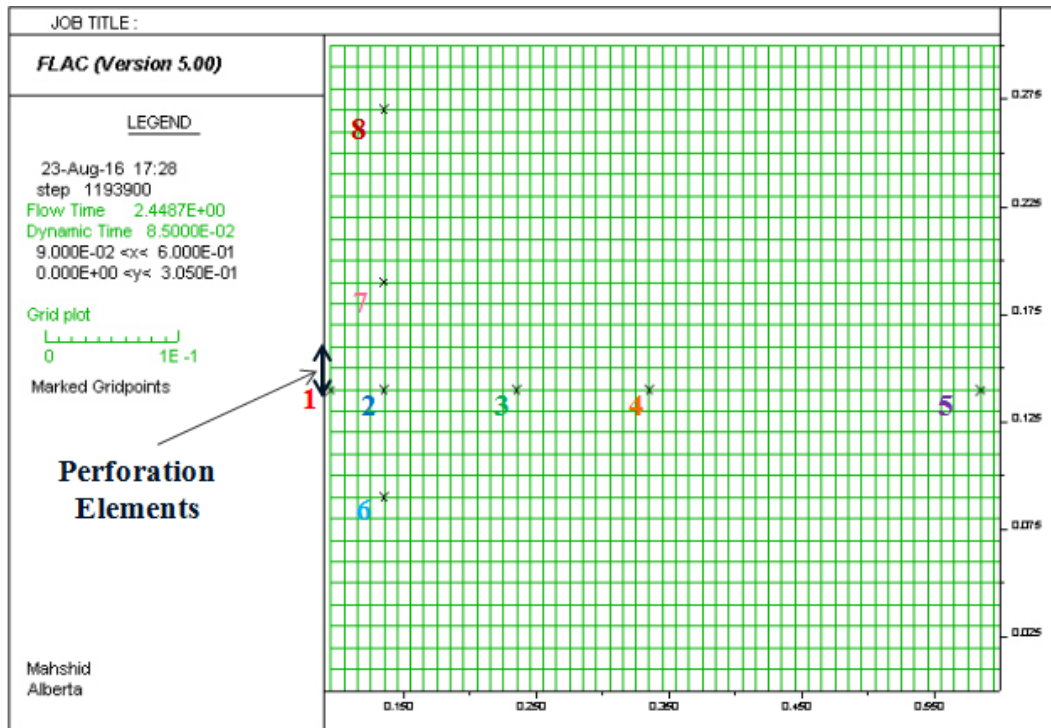
Figure 5-5 History points

5.2.6 Assumptions

There are certain assumptions or simplifications made for the numerical study in this work; where excluding them may lead to the elevation of the dynamic effect. These assumptions are summarized below:

- No sand production (material removal) is modeled. Sand production can potentially create a cavity, exposing a larger surface area to the high-amplitude WH waves. It also increases the porosity of the elements with higher deformability under the dynamic loads.
- The effect of fatigue and cyclic loadings are ignored in this study which may affect the pressure buildup due to multiple cycles of strain/pore pressure.

116

- A rigid caprock (top boundary fixed in vertical direction) is assumed to achieve numerically stable results. Application of stress at the top boundary of a cohesionless sand model leads to large failure zones in the model especially around perforation A thicker model would have alleviated the failure and model instability by redistributing the stress. The inclusion of the rigid caprock, represented by the fixed top boundary, allows the arching effect and vertical stress reduction at the perforation element. Further details are discussed in Sections 5.2.8.1.

- No permeability modification as a result of porosity change is devised in this study. Based on the sensitivity analysis presented in Section 5.2.10.6, the results are not sensitive to the permeability for highly permeable media.

- Three different constitutive models are applied in the analysis. The elastic model is used as a benchmark model. Then the model discussed in Chapter 3 is used to simulate the dynamic degradation of weakly-consolidated sandstone. Finally, a cohesionless sand model is simulated assuming sufficient sandstone degradation occurs due to drilling, different cycles of injection and shut-in, WH as well as presence of water. Martin model, a built-in constitutive model in FLAC for liquefaction studies, is used for modeling cohesionless sand. This model is discussed with further details in Section 5.2.9.

5.2.7 Elastic Model

The elastic model is used as a reference model against which the results of other models are compared. For this model, bulk and shear moduli are assumed to be 218 MPa and 131 MPa, respectively. These values represent elastic moduli of cohesionless sand at low effective stresses present near an injector wellface.

Figure 5-6 shows the pore pressure response generated by WH wave at different distances from the wellbore and at the perforation elevation. The results indicate significant damping of the pore pressure pulses with radial distance because of geometric damping, which causes the amplitude of waves to attenuate as distance from the perforation increases.
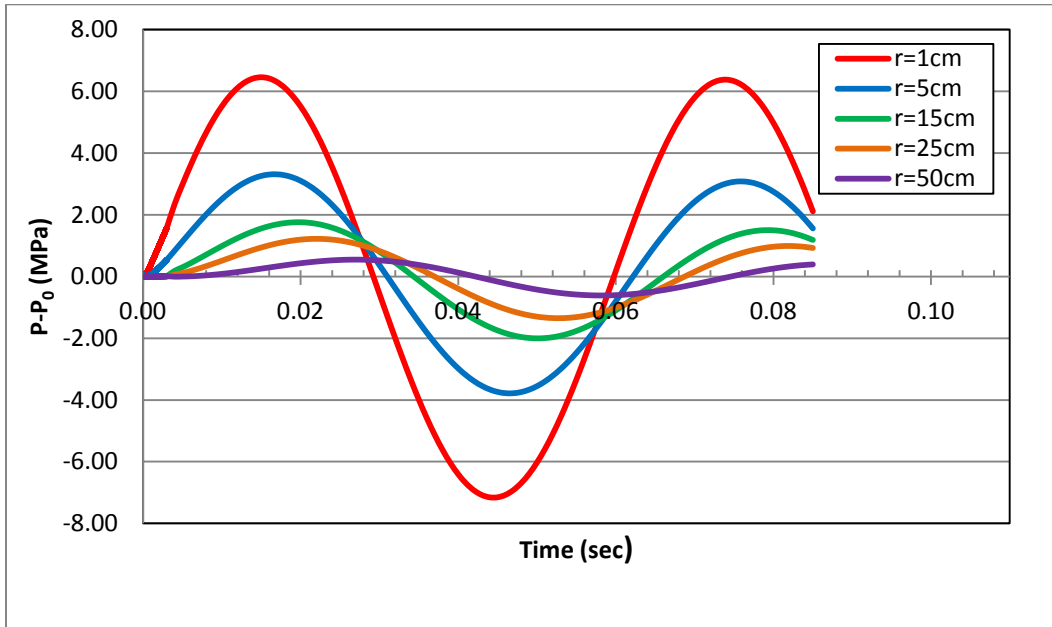
Figure 5-6 Change in pore pressure response to a sinusoidal wave at different radii

The curves of pressure change in Figure 5-6 appear to converge at about 0.03 sec and 0.06 sec, but they are not, as any two of them are intersecting at very close pore pressures and times. As Figure 5-6 shows, at t~0.03 sec the point at r=50 cm is experiencing its peak while the point at 1cm has nearly completed half a cycle. Points at r=1 cm, r=5 cm and r=15 cm are so close to each other that they experience very similar, although not exactly the same, phases at around 0.03 sec.

Upon exmining the pore pressure behaviour at early times, a fast low-amplitude wave is observed (see Figure 5-7). This is the first compressional wave which travels at a speed of ~2200 m/s. The pressure goes back to initial values because

118

the next wave is not as fast and cannot reach the points as quickly. This low-amplitude wave is not the primary focus in the rest of this chapter due to small amplitude and low effect on the stress path in comparison with the main sinusoidal wave. In other words, although the influence of high-velocity waves has already been included in all the reported results, characterization of their behaviour is outside the scope of this research.
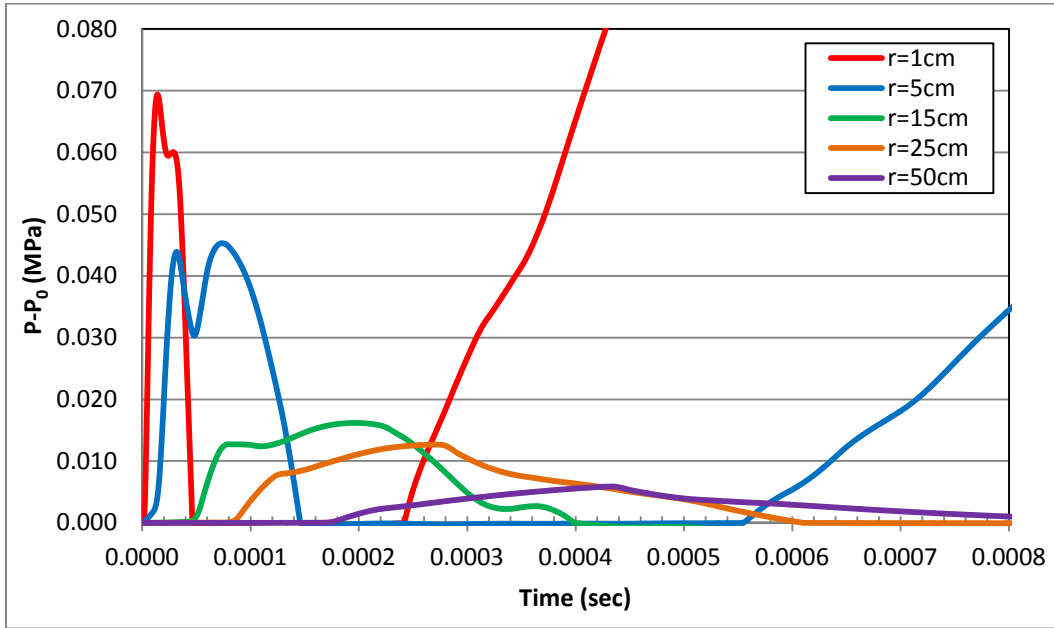
Figure 5-7 Changes to pore pressure as a result of sinusoidsl wave at very small times

The speed of the sinusoidal wave in the reservoir is calculated to be ~50 m/s, much slower than the waves speed discussed in Chapter 4. This slow wave has been characterized as porosity-diffusion wave (Davidson et al., 1999), or porosity-dilation wave (Sivrikoz, 2009), which is a wave that propagates through saturated porous media. Porosity-diffusion wave cannot exist without solid-liquid coupling and results from the simultaneous solid deformation and liquid-solid interaction. It is expected to have velocities of 5-150 m/s (Davidson et al., 1999). The wave was experimentally observed by Davidson et al. (1999) in a cylinderical sand pack at moderate frequencies (0.1-3 Hz). Any presence of gas will highly

dampen this wave. Figure 5-8 demonstrates the stress paths for the same elements at the perforation level and the same radial distances mentioned above. The stress paths indicate the mean effective stress reduces with an increase in the pore pressure. Also, shear stress reduces around the perforation. Furthermore, the WH pressure pulsing effect on shear stresses diminishes with distance.

Figure 5-9 depicts the pore pressures at radius of 5 cm and different depths. The reference point ($z=0$) is the perforation depth. The element at $z=0$ cm is the first one to see the peak pore pressure since it has the least radial distance from the source (perforation).
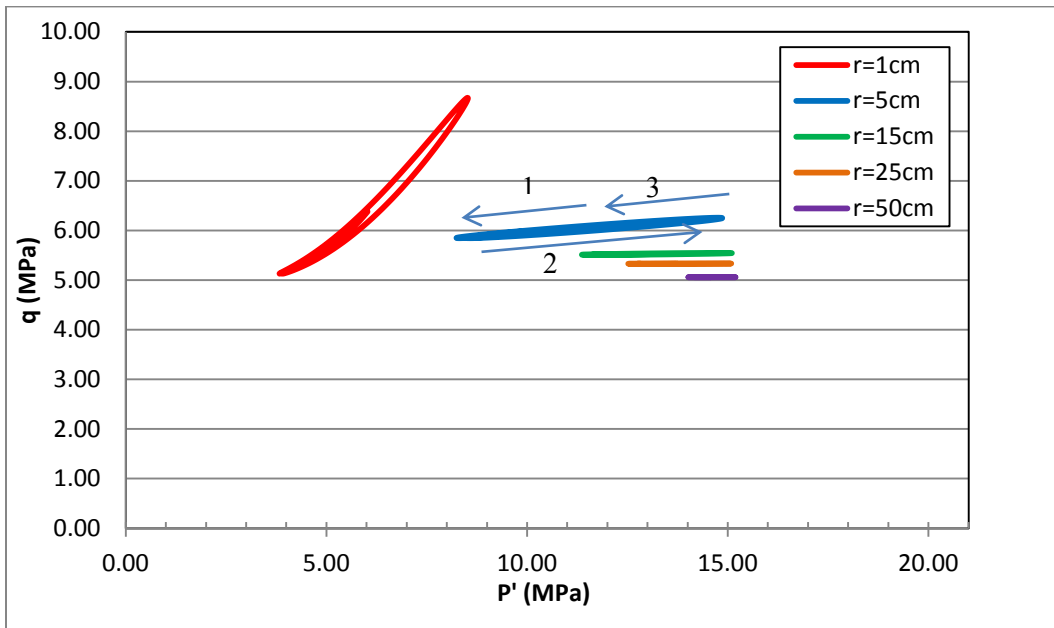
Figure 5-8 Stress paths for elements at different radii and perforation depth
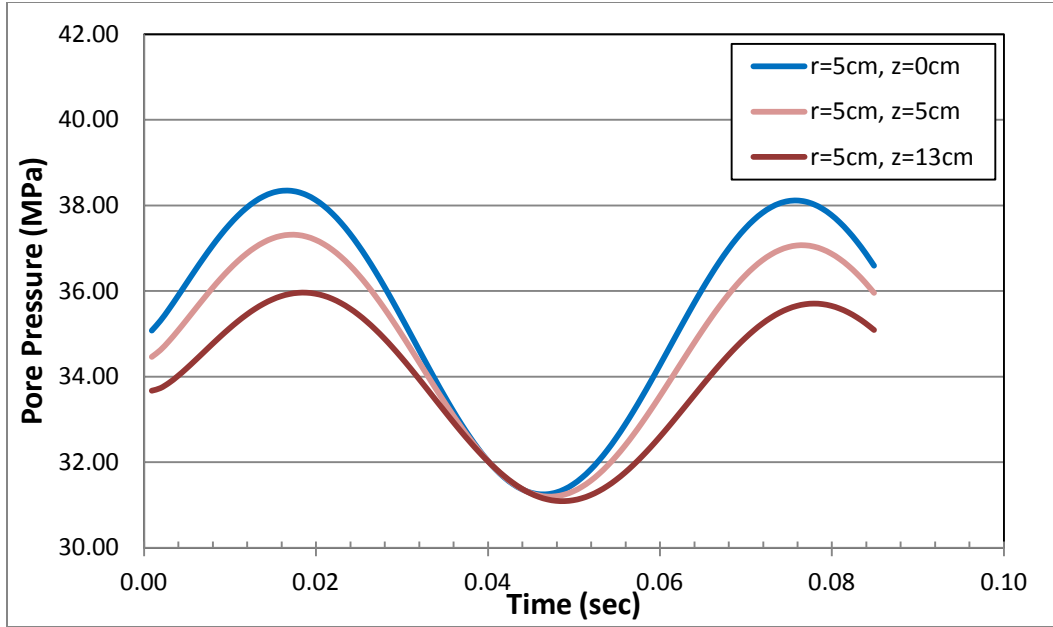
Figure 5-9 Pore pressure response to a sinusoidal wave at r=5cm and different depths with respect to perforation depth

5.2.8 Hardening/Softening Constitutive Model

The constitutive model developed and validated in Chapter 3 is used to study the dynamic degradation of weekly-consolidated sandstone. In the Norwegian Sea field, sandstone UCS is reported (Santarelli et al., 1998) to vary between 2 MPa and 10 MPa, and further reduced by up to 20% to 1.6 MPa to 8 MPa due to the injection of water incompatible with the formation rock.

In the absence of triaxial testing data, Salt Wash Sandstone (Rahmati et al., 2012) properties, calculated following the same procedure as in Chapter 3, are scaled down to obtain the properties for a sandstone with the UCS of 1.6 MPa. Assuming the same friction angle as that of Salt Wash (35 degrees at peak), the scaled-down peak cohesion will be 0.417 MPa. In other words, the shape of mobilized cohesion is the same as that of Salt Wash sandstone (see Figure 5-10) but scaled down to result in the 1.6-MPa UCS.

Negative dilation angles of -2 to -0.6 are assumed for the base case. Figure 5-11 demonstrates the mobilization of friction angles and dilation angles with hardening parameters (effective plastic strain). Similar to cohesion, the shape of mobilized dilation angles is the same as those of Salt Wash sandstone and only the values are scaled down.
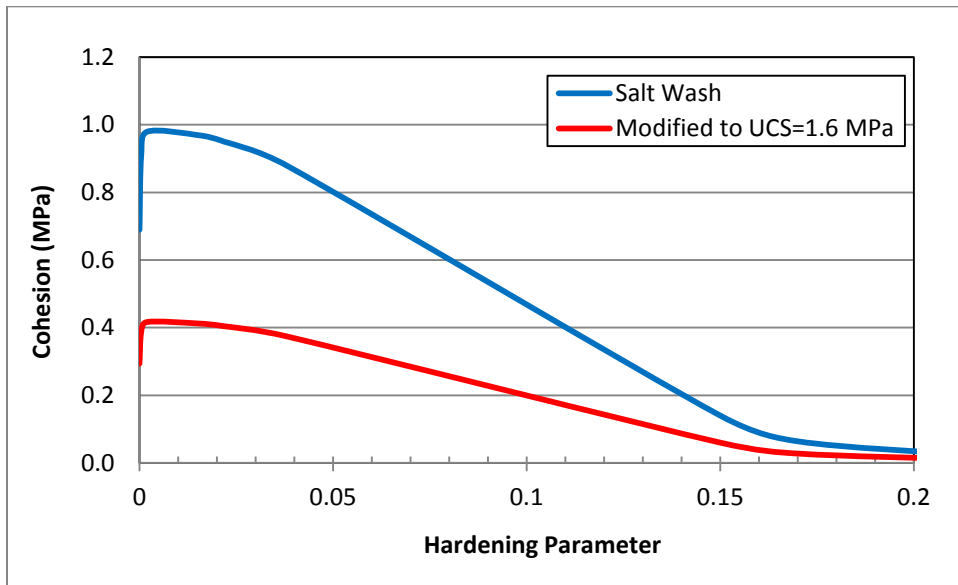
Figure 5-10 Mobilized cohesion
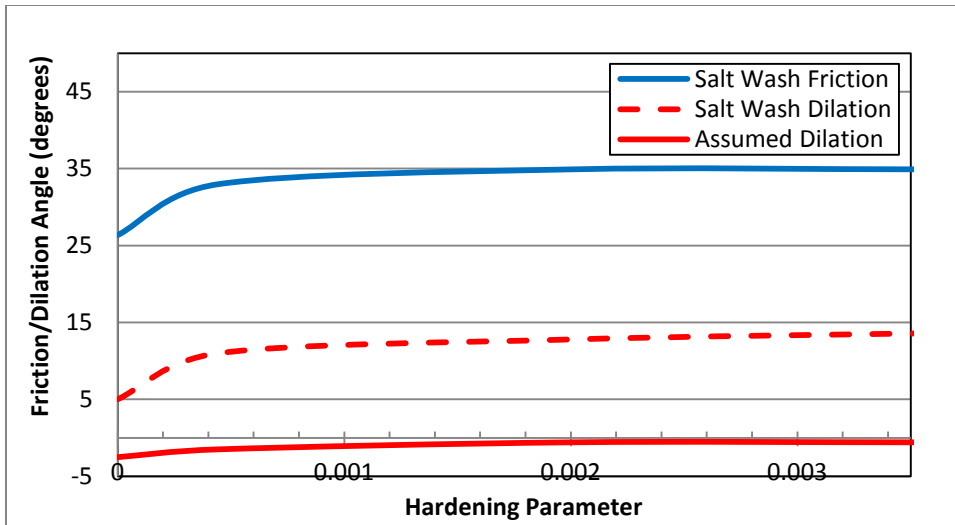
Figure 5-11 Mobilized friction and dilation angle

5.2.8.1 Simulation Results

The model is initiated following the simulation steps explained in Section 5.2.4, which are drilling, casing, and perforating the well, followed by water injection. At this point, simulation results indicate failure around the perforation, as shown in Figure 5-12, before any WH wave is applied which is similar to what Santarelli reported (Santarelli et al., 1998).
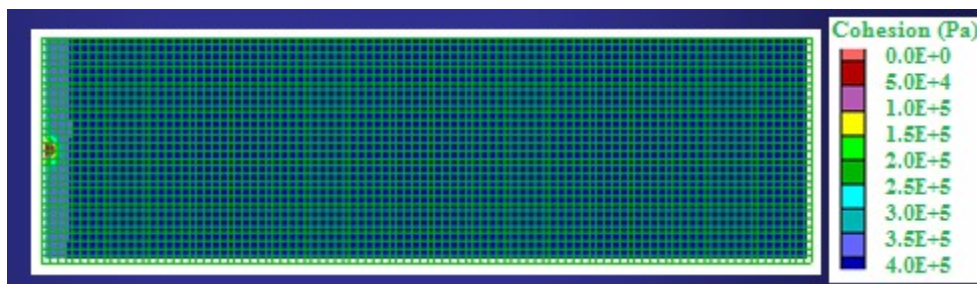
Figure 5-12 Failure around perforation before application of WH waves

WH waves are then applied as boundary conditions on the perforation with the frequency of 17 Hz and amplitude of 8 MPa as explained in Section 5.2.2. Two sets of runs are performed: one with the top boundary fixed in the vertical

direction (representing a rigid caprock) and the other with constant vertical stress ($\sigma_v = 50.5$ MPa) as the top boundary condition. The results are shown in Figure 5-13 to Figure 5-18.

Figure 5-13 illustrates that pore pressure response is almost identical for the two boundary conditions. This is because mechanical boundary conditions does not affect the fluid flow response, where porosity and permeability are not modified. Figure 5-14 shows the stress path for elements at different radial distances. The failure envelope is plotted for the element at r=2.5 cm after 0.085 sec.

The pressure anomaly at 0.04 sec is when the stress path for the perforation element passes through a zero mean effective stress (see Figure 5-14). This leads to a sudden volumetric change as demonstrated in Figure 5-15. This pressure anomaly is superposed on the WH wave as it transfers along the reservoir.
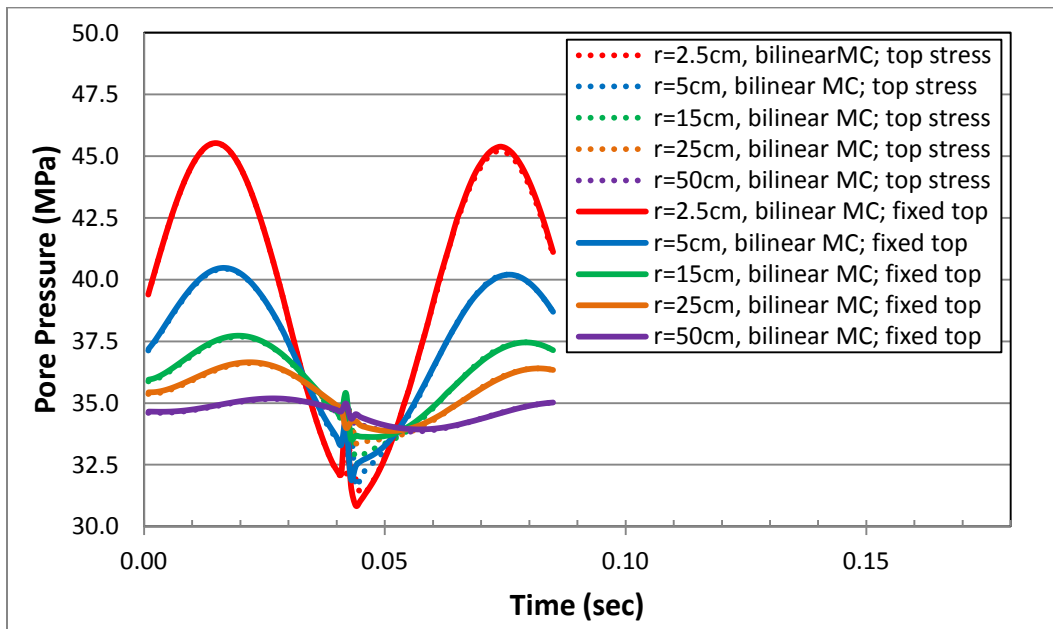
Figure 5-13 Pore pressure response for hardening/softening bilinear MC using different top boundary conditions
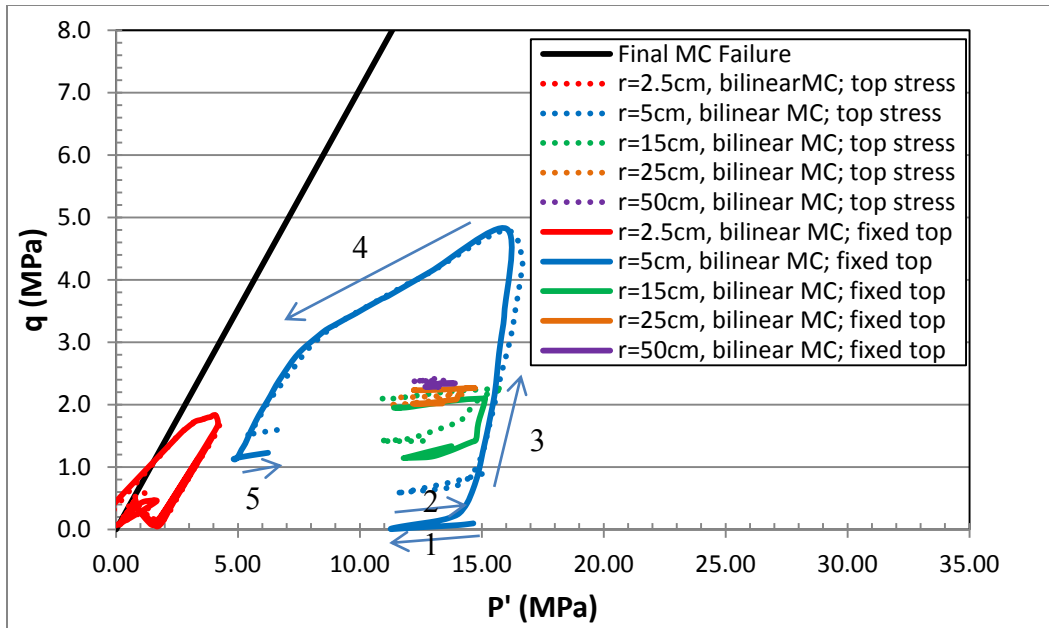
Figure 5-14 Stress path for hardening/softening bilinear MC using different top boundary conditions
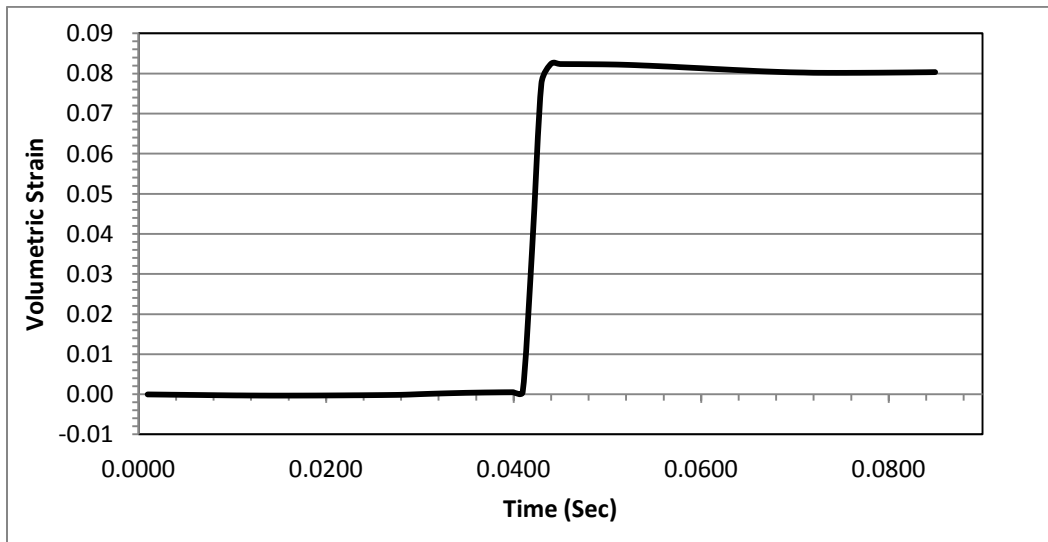
Figure 5-15 Volumetric strain change for the element at r=2.5 cm

The displacement vectors for both boundary conditions demonstrate sand tendency to be produced into the wellbore. This justifies the cases where mechanical failure of sand retention equipment are reported (Hayatdavoudi, 2005). In order to take sand production into consideration, and to investigate the

combined effect of wave propagation and sand production, further study is required which is out of the scope of this work.
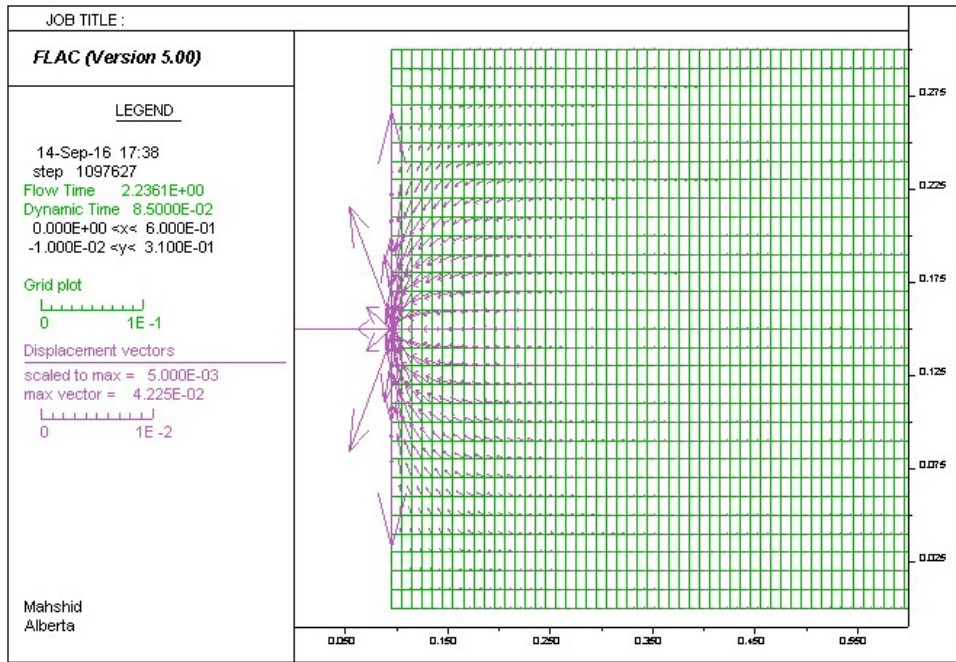
Figure 5-16 Displacement vectors for the bilinear MC model with fixed top boundary condition in the y direction
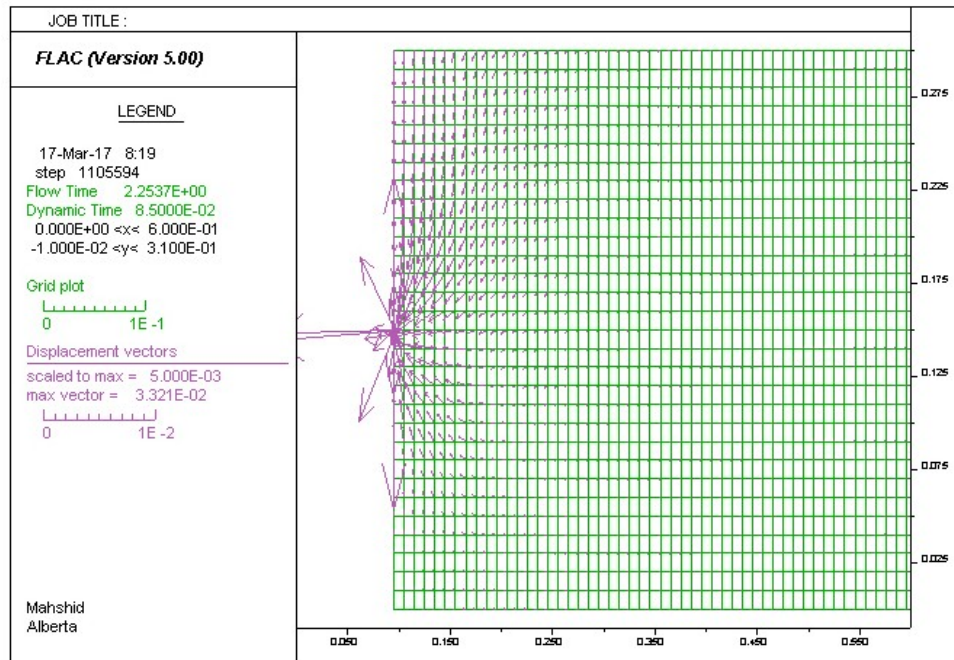
Figure 5-17 Displacement vectors for the bilinear MC model with constant vertical stress on the top boundary

To conclude, the top boundary condition only made a small difference on the stress path and displacement pattern. The downward displacement is more significant for the vertical stress case. However, sand degradation is larger for a fixed boundary in the vertical direction (see Figure 5-18). Therefore, the top boundary fixed in the vertical direction will be used in the follwoing sections for cohesionless sand.

Figure 5-12 and Figure 5-18 show the growth of degraded zone as a result of WH waves hitting reservoir for 0.085 sec. In a real reservoir, more failure is expected because of longer WH waves (as long as 100 sec) and fatigue due to multiple cycles of injection and shut-in. Therefore, in the next section a cohesionless sand reservoir is modeled to represent an extended failure zone around the injector.
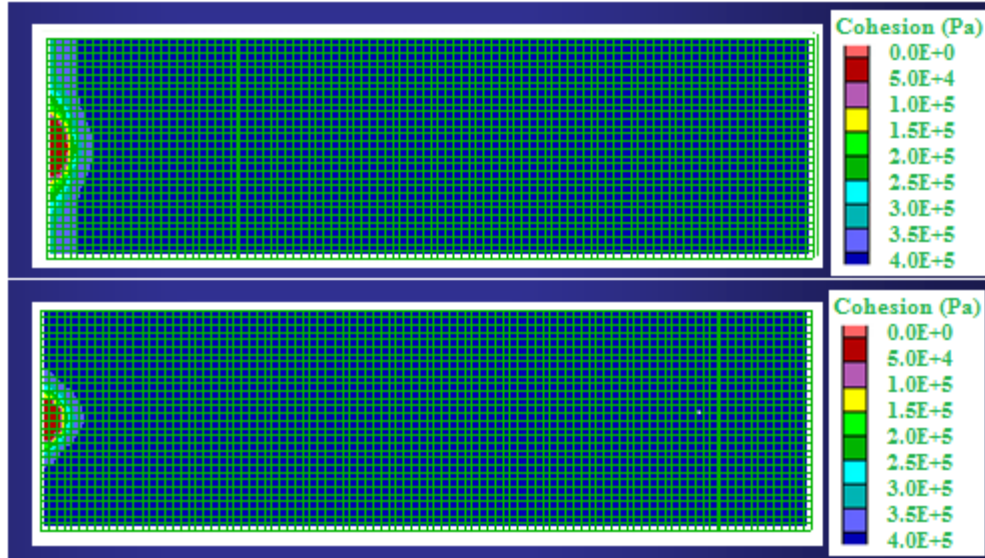
Figure 5-18 Dynamic degradation around perforation after 0.085 sec of WH waves for a fixed top boundary condition (top) and a constant stress top boundary condition (bottom)

5.2.9 Martin Model

FLAC software includes two simple empirical constitutive models to simulate generation of dynamic excess pore pressure observed in liquefaction. Both empirical relationships relate an irrecoverable decrease in volume, Δe_{vd}, to the cyclic shear strain. Martin et al. (1975) suggested the following equation:

$$\Delta e_{vd} = C_1(\gamma - C_2 e_{vd}) + \frac{C_3 e_{vd}{}^2}{\gamma + C_4 e_{vd}} \tag{5-1}$$

where γ is the engineering cyclic shear strain and C_1, C_2, C_3 and C_4 are calibration constants. Only three of these calibration parameters are independent: $C_3 = C_1 C_2 C_4$. Byrne (1991) proposed a simpler formulation:

$$\Delta e_{vd} = C_1 \gamma \exp\left(-C_2\left(\frac{e_{vd}}{\gamma}\right)\right) \quad \text{if } \gamma \geq C_3 \tag{5-2}$$

In many cases, $C_2 = 0.4/C_1$, and C_1 can be derived from relative density, D_r.

$$C_1 = 7600(D_r)^{-2.5} \hspace{6cm} (5\text{-}3)$$

The additional volumetric contraction causes an excess pore pressure because of the cyclic shear strain, mimicking the main physics of liquefaction. However, this additional pore pressure is not smooth and is only applied at the end of each cycle of shear strain. Also, the model uses a perfectly plastic Mohr-Coulomb yield surface that does not evolve. One possible solution is to use an appropriate mobilizing constitutive model until full-degradation occurs and then switch to this model with zero cohesion and residual parameters. The main drawback of this approach is that the strain cycles before full degradation are ignored.

Although excess pore pressure is generally associated with liquefaction, it is not considered as the direct cause of liquefaction. In constant volume experiments it is the decrease in contact forces between particles that is responsible for the decrease in effective stress (Dinesh et al., 2004). On the other hand, the effective stress does not necessarily have to be zero for a soil to liquefy. When a saturated cohesionless soil is subject to rapid static or cyclic loading, the tendency for the soil to compact causes the effective stress to decrease by transferring the loads from solid structures to the fluid, and the whole process leads to soil liquefaction (FLAC 7.0 user Manual).

Before simulating an injector well with Martin constitutive model, the shock tube experiment is simulated with Martin model. The first two waves are measured in the lab. After that, because of wave reflections, additional cycles of pressure can fail the soil. This example is used as a validation of the whole package when failure occurs, i.e. dynamic code, coupling with Flac, and Martin constitutive model.

The flow and elastic properties are reported in Table 4-1 and Table 4-2. For plastic properties, zero cohesion, 30 degrees friction angle together with $C_1 = 0.8$,

$C_2 = 0.79$, $C_3 = 0.45$ and $C_4 = 0.73$ are used. These calibration values are typical values for cohesionless sand suggested by Martin et al. (1975).

The results are plotted in Figures 5-19 to 5-20. Figures 5-19 shows the pore pressure and the wave reflection for two different points. The stress paths in Figure 5-20 show that failure initiates when the first pressure peak, or the first reflectin wave, reaches the element. This initial failure reduces the shear stress as the stress path moves on the failure envelope. Once pore pressure is decreased upon the arrival of the second reflected wave, the mean effective stress increases but shear streses remain low. Further pressure jumps (the third and fifth reflected waves) lead the stress path to zero mean effective stress.
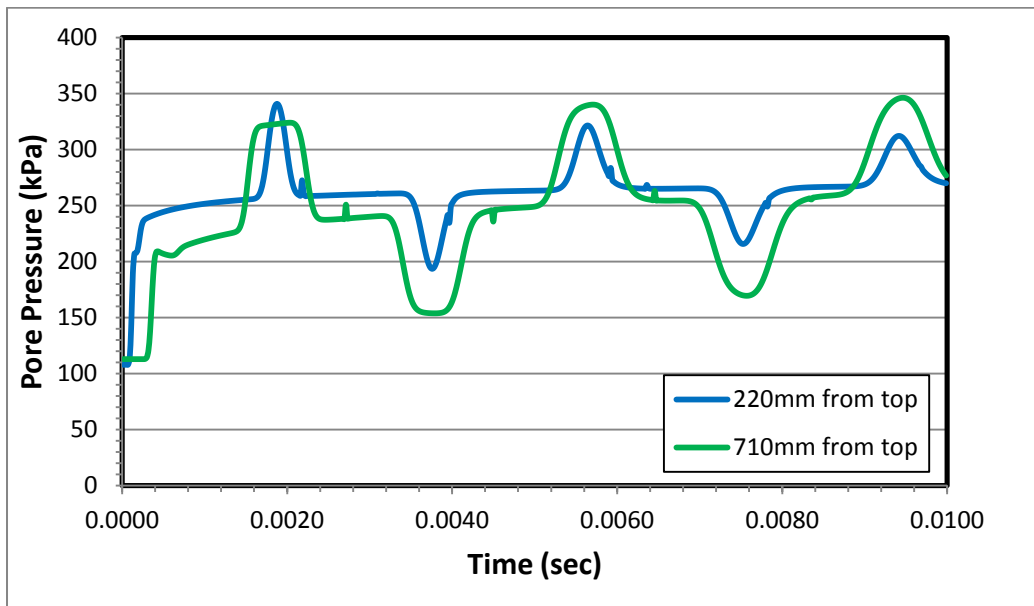
Figure 5-19 Pore pressure response to a shock wave in the shock tube experiment
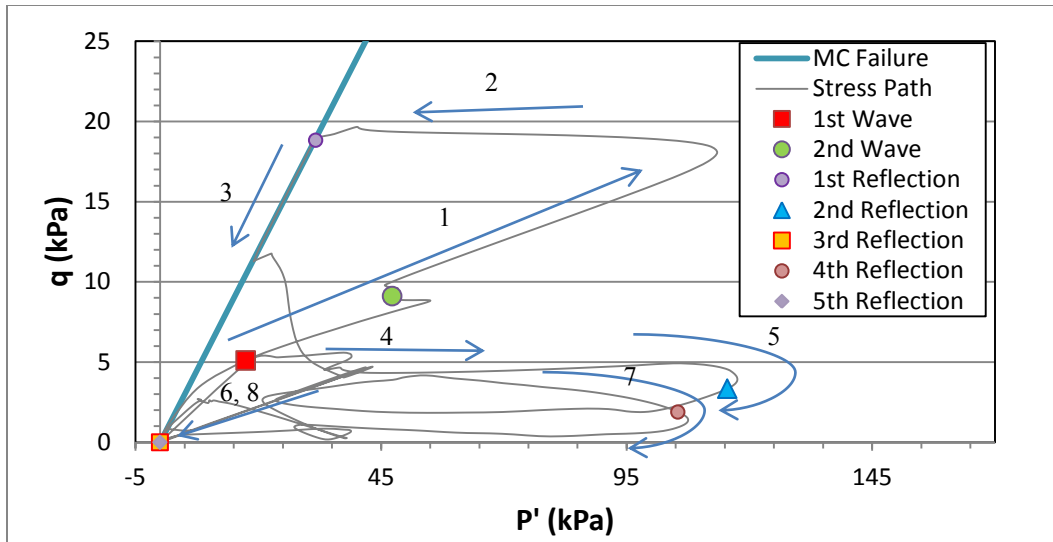
Figure 5-20 Stress path for a point 710 mm from the top

The results show that elastoplastic constitutive model together with coupled dynamic fluid flow and dynamic FLAC module is capable of modeling dynamic behavior beyond the elastic regime. The package can model the states of zero mean effective stress as a result of dynamic pore pressure/stress loading.

5.2.9.1 Simulation Results and Comparison with the Elastic Reference Model

The flow and elastic properties used in this section are similar to the values reported in Section 5.2.5.1. Cohesionless sand is assumed with the premise that sandstone is already fully-degraded because of drilling, water effect, several cycles of injection and shut-in, fatigue and dynamic effect of WH waves. Santarelli et al. (2000) confirmed that sandstone was at failure conditions before sudden shut-in of the well. Mohr-Coulomb properties are zero cohesion, 30 degrees friction angle, and -5 degrees dilation angle. The Martin liquefaction model has been used with $C_1 = 0.8$, $C_2 = 0.79$, $C_3 = 0.45$ and $C_4 = 0.73$. These are typical values for cohesionless sand suggested by Martin et al. (1975).

131

The results from the elastic and Martin models are compared in Figure 5-21 through Figure 5-26. Figure 5-21 shows the pore pressure propagation with radial distance and indicates slightly higher wave amplitudes compared to the elastic case. The reason can be attributed to the negative dilation and volumetric strain imposed by the Martin model. The observed spikes in the Martin model are due to failure of the perforation element where the stress path goes to a near-zero mean effective stress.
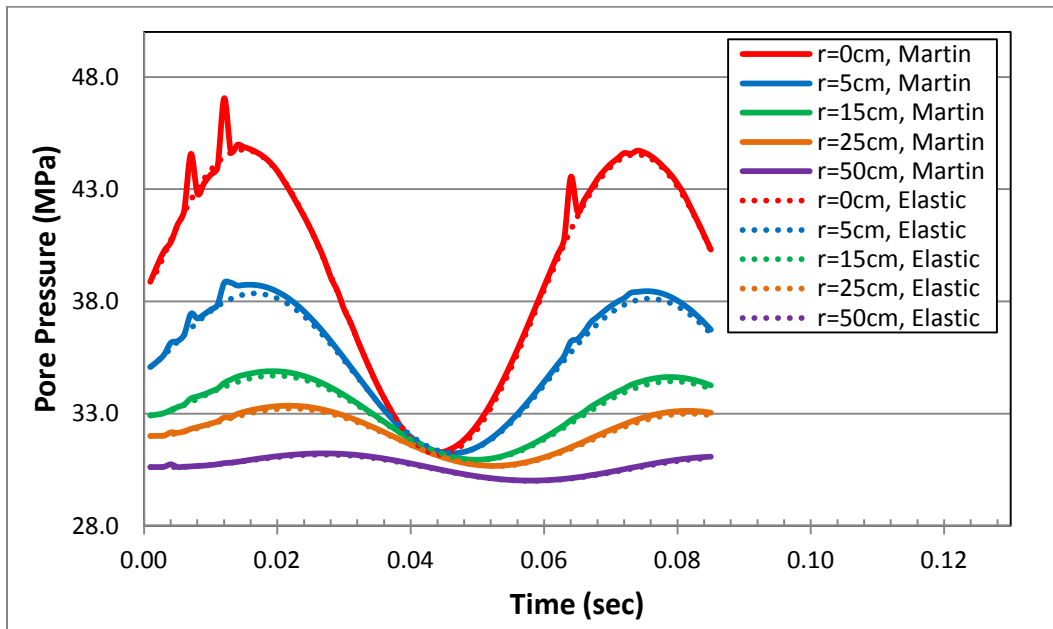
Figure 5-21 Pore pressure response to a sinusoidal wave at different radii and perforation depth

Although the pore pressure propagation in the Martin and elastic models are similar, the stress paths are quite different. According to Figure 5-22, the stress path for the perforation element is on the failure envelope moving towards a zero mean effective stress. The shear stress remains at near zero even when the pore pressure is decreasing in the cycle. With the second peak of pore pressure wave, the element is again at a zero mean effective stress. Note that sand production and element removal are not simulated in the model. Otherwise, the next elements

could have gone through the same stress path when forming a new boundary. Although the element 5cm farther away the perforation shows some initial shear stress reversal, it is not sufficient to reach near-zero mean effective conditions in this model.
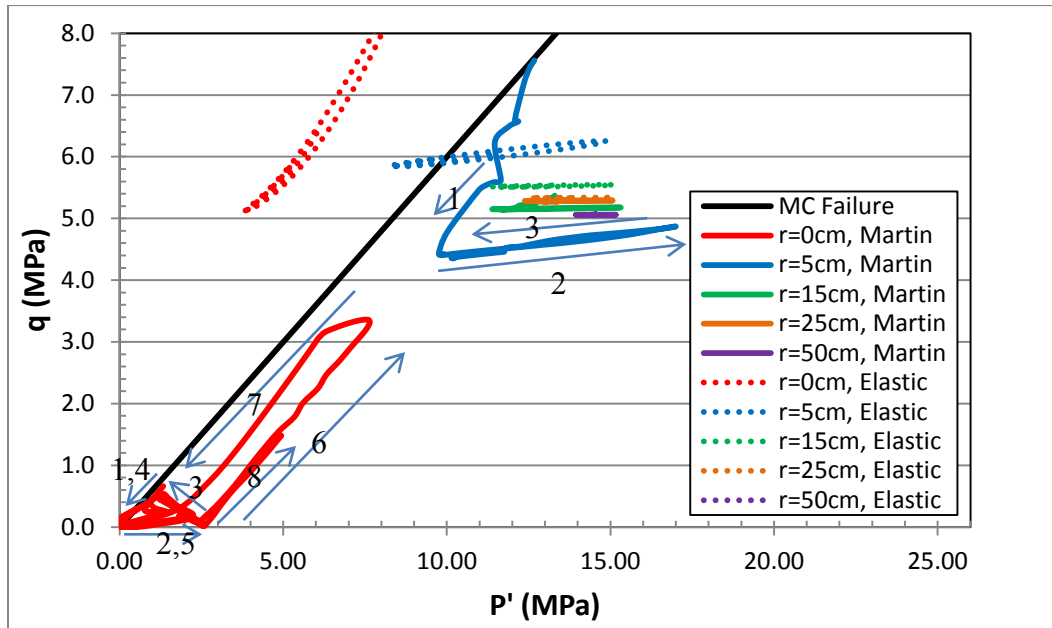
Figure 5-22 Stress path for elements at different radii using Martin model (the arrows shows the direction of stress path)

One main difference compared to the elastic behavior is the pressure spikes observed in the Martin model. The pressure anomaly corresponds to a zero mean effective stress on the stress path of the perforation element and its sudden volumetric change/contraction (see Figure 5-23 to Figure 5-24). The arrows show the direction of stress path, a double-headed arrow represents the stress path moves forward and backward. These pressure rises can be correlated to porosity changes and will be transferred to adjacent elements as secondary waves. They are also occurring at higher frequencies than WH waves.

Figure 5-25 shows the displacement vectors. The Martin model simulates sand tendency to contract toward the reservoir contrary to what the mobilized MC

constitutive model predicts. This is because of the additional contractive volume change incorporated in the Martin model. Another reason could be that the value of the dilation angle used in the sandstone model (see Figure 5-11) is larger than the constant value of -5 used for cohesionless sand for the Martin model.
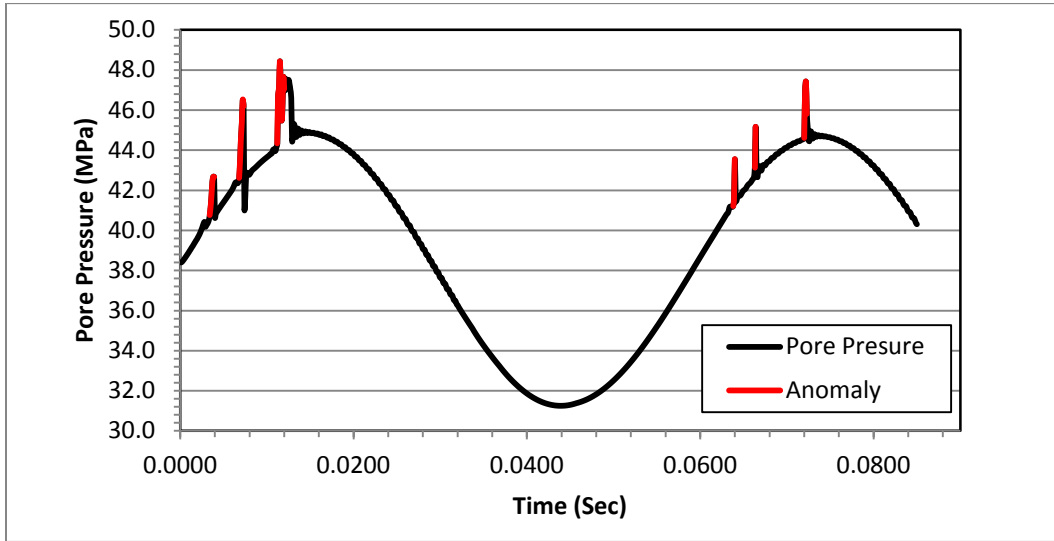
a
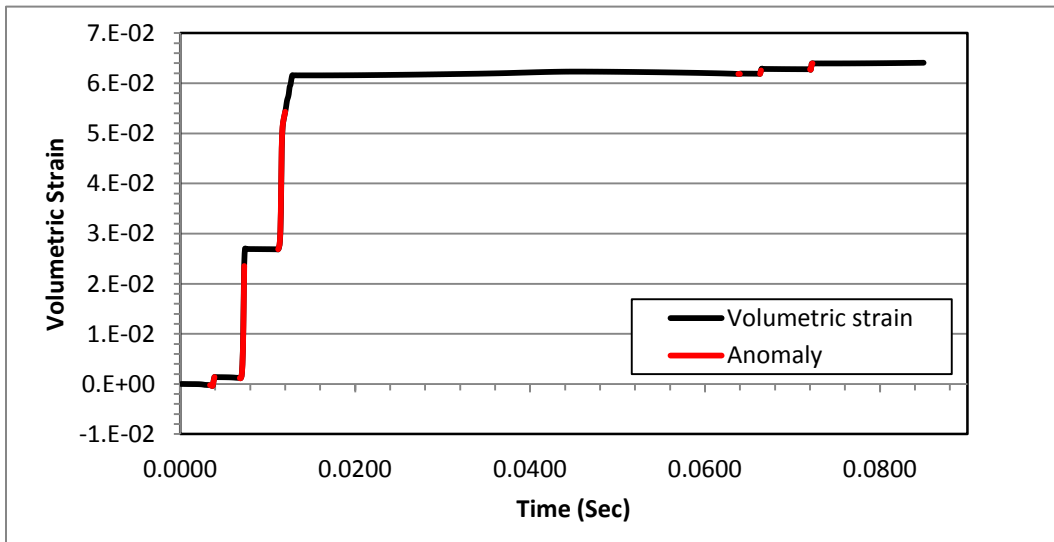
b

Figure 5-23 Pore pressure anomaly (a) corresponding to volume contraction (b)
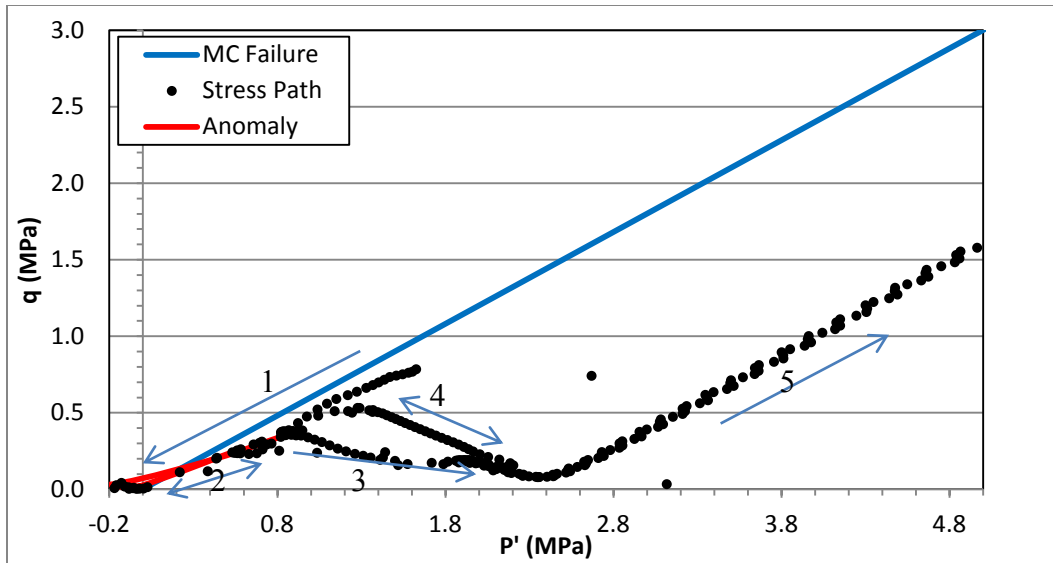
Figure 5-24 Zero mean effective stress during pressure spikes
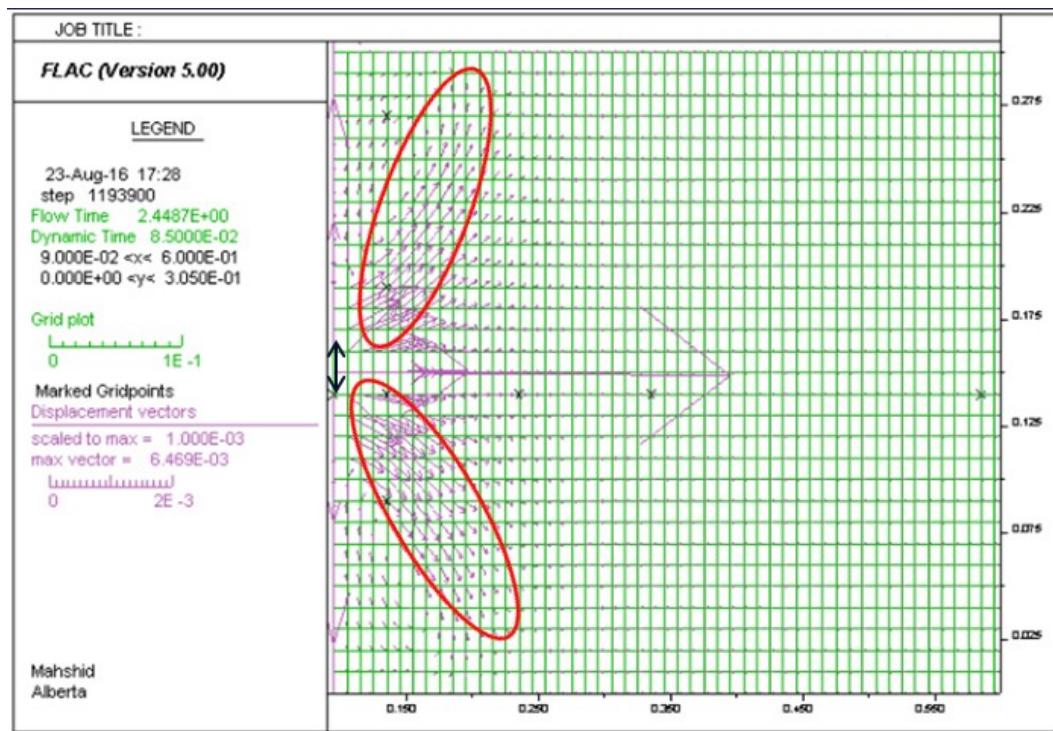
Figure 5-25 Displacements after 0.085 sec of WH

Failure occurs in two shear bands angular to the wellface. Figure 5-26 shows the stress paths for the elements in the shear band. The fact that the top and bottom

elements, located at z=±5 cm relative to the perforation element, are failing reduces the stress for the element at the perforation elevation (r=5 cm; z=0 cm) without its stress path even touching the yield envelope. After failure, the stress state moves back to elastic conditions when pore pressure is reduced.
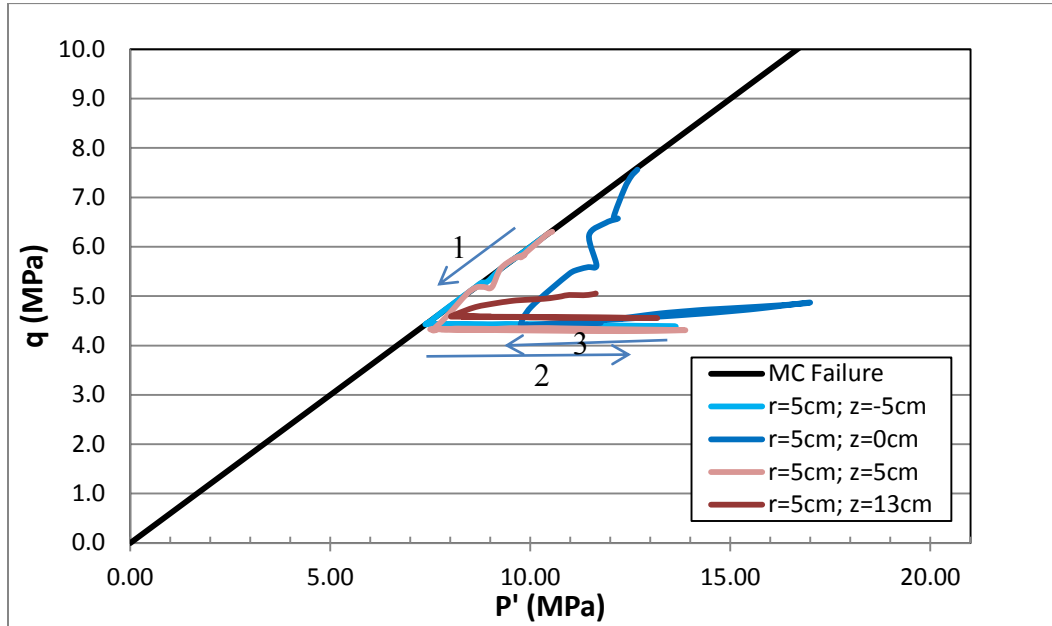
Figure 5-26 Stress paths for elements at different depths and radius of 5 cm

Based on the results, the stress path is similar to monotonic liquefaction shown in Figure 2-5 and Figure 2-6. However, this stress path is the same as material instability and failure. Note that the developed model is incapable of modeling cyclic fatigue and moving the stress conditions towards the failure envelope with each loading-unloading cycle. It is noted that the excess pore pressure included in the Martin model is very primitive. Figure 5-27 shows that the failure zone progresses through time very quickly. In other words, under the studied conditions and assumptions progressive failure is a more appropriate explanation of massive sand production than liquefaction.
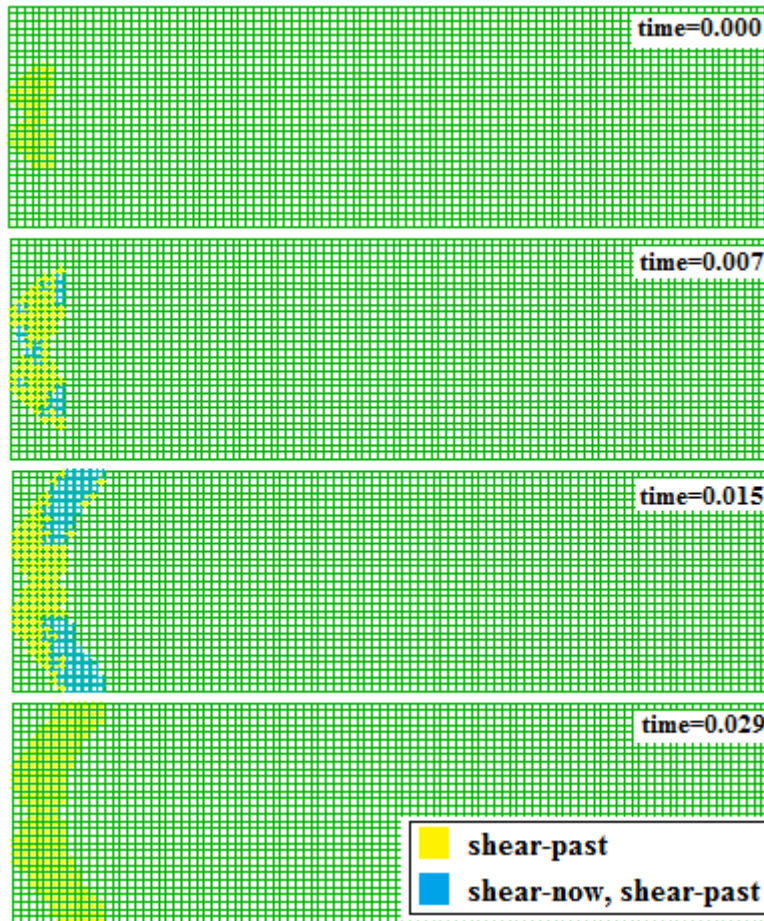
Figure 5-27 Progression of failure within a fraction of second

It is also noteworthy to mention that the boundary conditions could play a major role in the final displacement vectors. The top boundary fixed in a vertical direction is selected to represent a stiff caprock that allows the arching effect. However, this type of boundary may prevent the tendency for element compaction, which is expected during liquefaction.

A model with top vertical stress boundary condition at the reported stresses is not stable for cohesionless sand. This type of boundary was investigated before for weakly-consolidated sandstone in Section 5.2.8.1 using a mobilized Mohr-Coulomb (MC) constitutive model.

5.2.9.2 Sanding Estimation

Several assumptions/simplifications have been made in the sanding estimation in this work as listed below:

1) It has been assumed that failure is an indication of the potential of sanding.

2) For sanding to occur, fluid velocities should be larger than a critical velocity to be able to carry the sand particles into the injector during the back-flow and cross-flow. Detournay et al. (2006) proposed the critical velocity, q_{cr}, as:

$$q_{cr} = \frac{ak(1-n)(c_r - \sigma'_t tan\varphi)}{\mu R_p} \tag{5-4}$$

where a is the sanding coefiicient, k is the absolute permeability, n is porosity, c_r is the residual cohesion, σ'_t is the effective tangential stress, φ is the friction angle, μ is fluid viscosity and R_p is sand particle size.

Once an element on the boundary has failed, Eq. (5-4) is used, assuming a = 0.24 per Detournay's suggestion (2006), to see if flow rate can carry sand particles into the wellbore.

3) The elements that satisfy the conditions in (1) and (2) are not removed from the model, but is considered to be produced.

4) Once sand production occurs in an element, a new pseudo-boundary is formed, the same calculations are performed until there is no change in the pseudo-boundary.

5) Depending on the perforation density, the perforations area of the well may vary from the ring-shaped perforation area that is assumed in this study.

6) An actual injection well may be exposed to longer durations of WH waves. Hence, the sand around the well may potentially undergo a higher degradation.

7) Another potential factor is the cyclic pore pressure variations. The constitutive models used in this work do not account for the degrading effects of cyclic loading on the reservoir sand.

8) Sanding along the reservoir thickness may not be uniformly distributed due to lithology and strength variations.

Considering the above simplifications, the modeling effort here serves only as a semi-qualitative probe of some field observations in injection wells, which indicate a significant sand production in a short amount of time.

Following this procedure, the estimated sanding will be 13.16 kg after 0.085 sec for a reservoir with 30 cm thickness. This amount of sand will fill up the simulated well in this study by as much as 74% of the reservoir thickness with the formation porosity and 97% of the reservoir thickness with 40% porosity. The latter is consistent with the produced sand porosity as observed inside the North Sea well (Santarelli et al., 1998).

5.2.10 Sensitivity Analysis

Fast nature of massive sand production makes field measurements difficult; therefore, assuming some model parameters in the numerical analysis is inevitable. For this reason, and to investigate the main parameters affecting the underlying mechanism of massive sand production, sensitivity analyses have been performed on the parameters summarized in Table 5-3 by changing one parameter at a time while keeping the other parameters unchanged. In reality, however, the change of a parameter such as porosity, can influence other physical (e.g., permeability) and mechanical (e.g., strength and stiffness) properties. Martin Constitutive model is selected for the sensitivity analysis study.

Table 5-3 Summary of sensitivity analysis

	Dilation Angle	Friction Angle	Injection Pressure (MPa)	WH Amplitude (MPa)	Porosity (%)	Permeability (Darcy)
Reference Model	-5	30	39.4	8	22	1.0
Model 1-1	0	30	39.4	8	22	1.0
Model 1-2	+5	30	39.4	8	22	1.0
Model 2-1	-5	28	39.4	8	22	1.0
Model 2-2	-5	35	39.4	8	22	1.0
Model 3-1	-5	30	37.4	8	22	1.0
Model 3-2	-5	30	41.4	8	22	1.0
Model 4-1	-5	30	39.4	4	22	1.0
Model 4-2	-5	30	39.4	10	22	1.0
Model 5-1	-5	30	39.4	8	25	1.0
Model 5-2	-5	30	39.4	8	30	1.0
Model 6-1	-5	30	39.4	8	22	0.6
Model 6-2	-5	30	39.4	8	22	2.0

5.2.10.1 Effect of Dilation Angle

As Figure 5-28 and Figure 5-29 show, pore pressure is slightly higher in the model with negative dilation angles because a negative dilation angles favor compaction with yielding. Also, stress reversal for the element at r=5 cm is higher for the model with negative dilation angles. The secondary pressure spikes are only observed in models with negative dilation angles. As the stress paths in Figure 5-29 shows, these elements experience little to no failure with the exception of the element at r=0 cm. Therefore, the dilation angle, which controls plastic volumetric change, cannot affect the pore pressure.
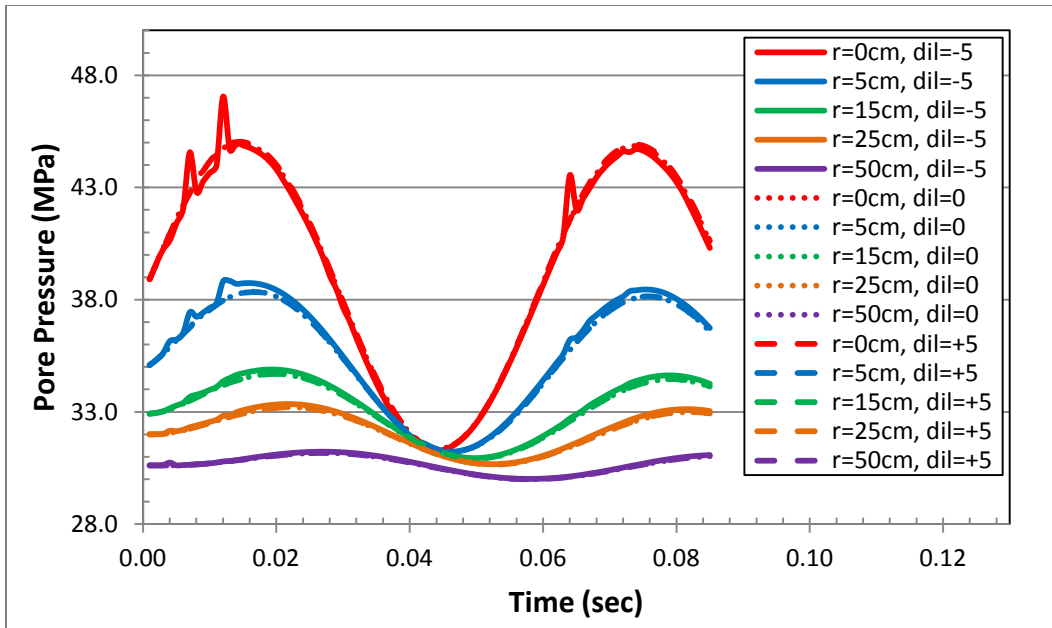
Figure 5-28 Pore pressure response for different dilation angles
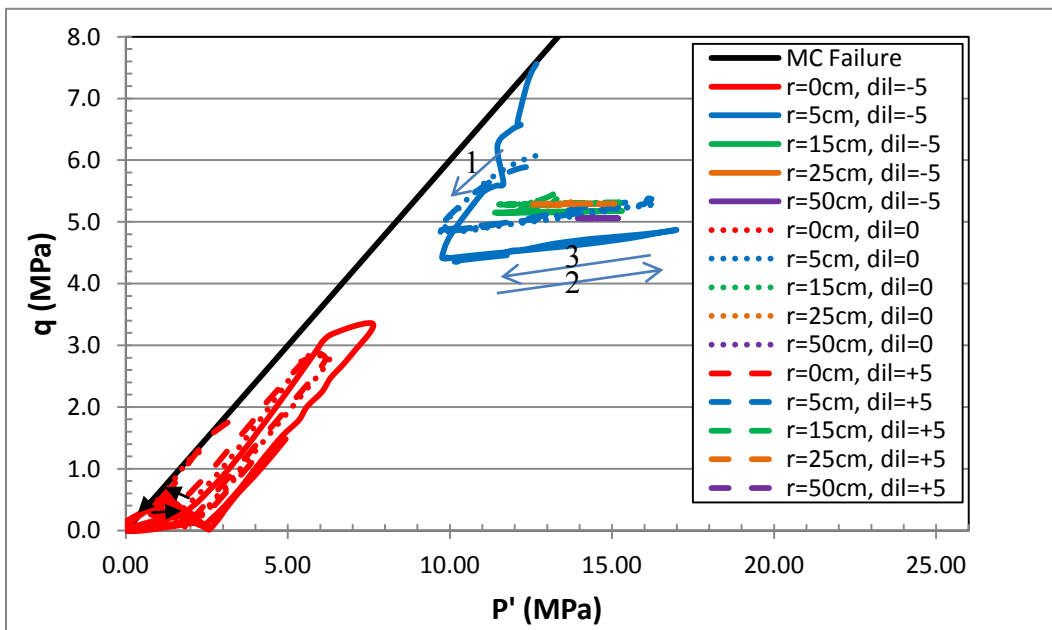
Figure 5-29 Stress paths for different dilation angles

141

5.2.10.2 Effect of Friction Angle

Figure 5-30 and Figure 5-31 show the effect of friction angle. A lower friction angle means elements may fail more easily under the same pressure wave amplitude. Failing and contraction (due to negative dilation angle) lead to the transfer of higher amplitude pressure waves, generated during plastic contraction, which in turn increases the potential for progressive failure. As a result, the element at r=5 cm shows a complete stress reversal due to the failure.
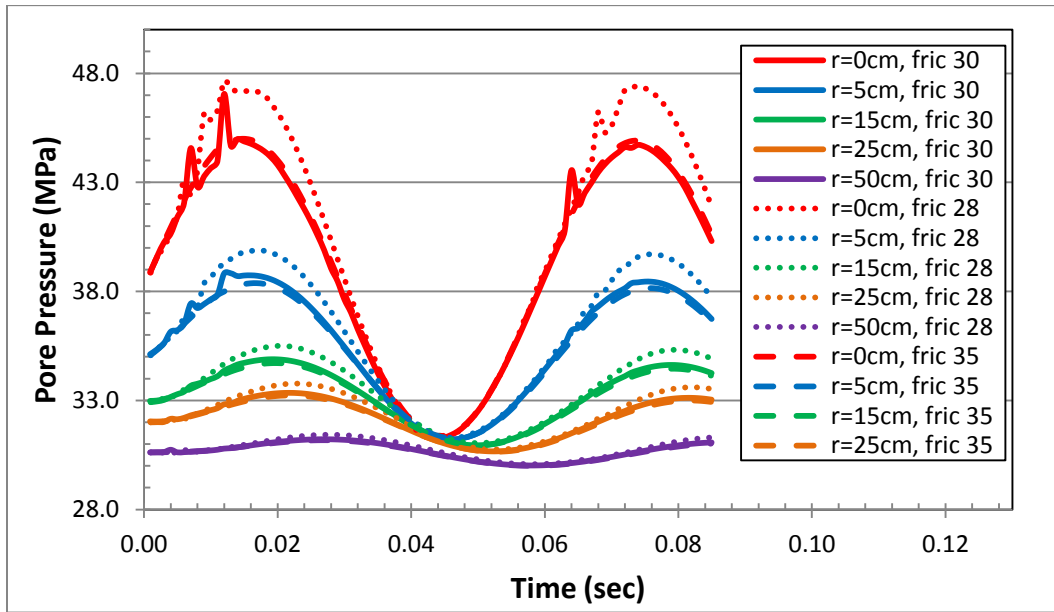
Figure 5-30 Pore pressure response for different friction angles
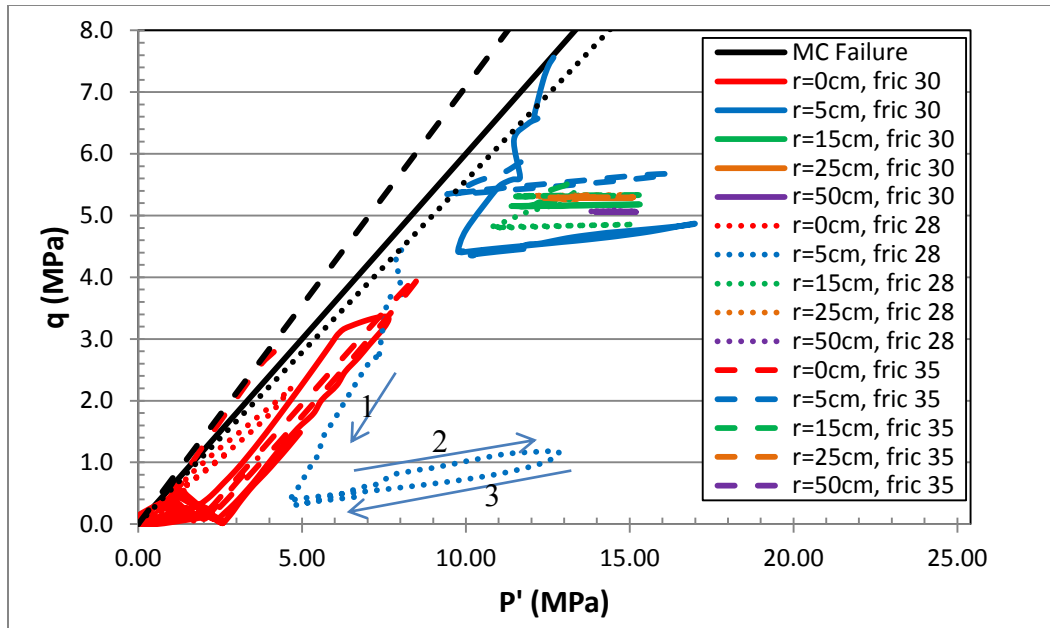
Figure 5-31 Stress paths for different friction angles

5.2.10.3 Effect of Injection Pressure

Higher injection pressure moves the stress path closer to the failure envelope by reducing the mean effective stress. Therefore, higher injection pressure leads to more failure and shear stress reversal. Figure 5-32 and Figure 5-33 depict the results.

Higher injection pressures result in higher injection rates into the reservoir. Since the WH amplitude is proportional to the magnitude of velocity change, an emergency shut-in will lead to a stronger WH pressure pulsing. However, as part of the sensitivity analysis only one parameter is varied at the time.
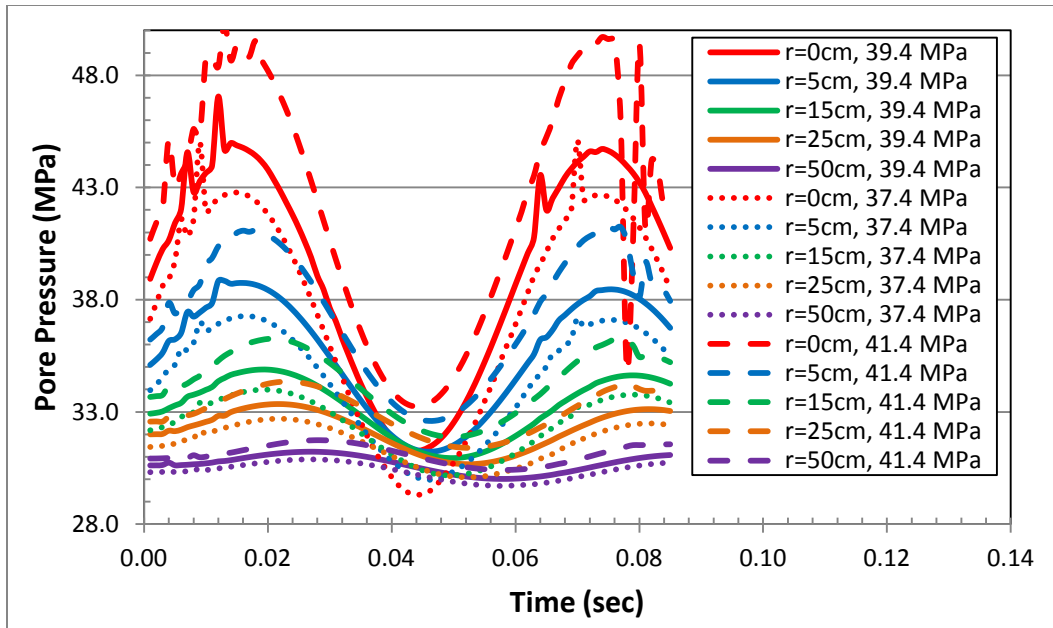
Figure 5-32 Pressure response for different injection pressure
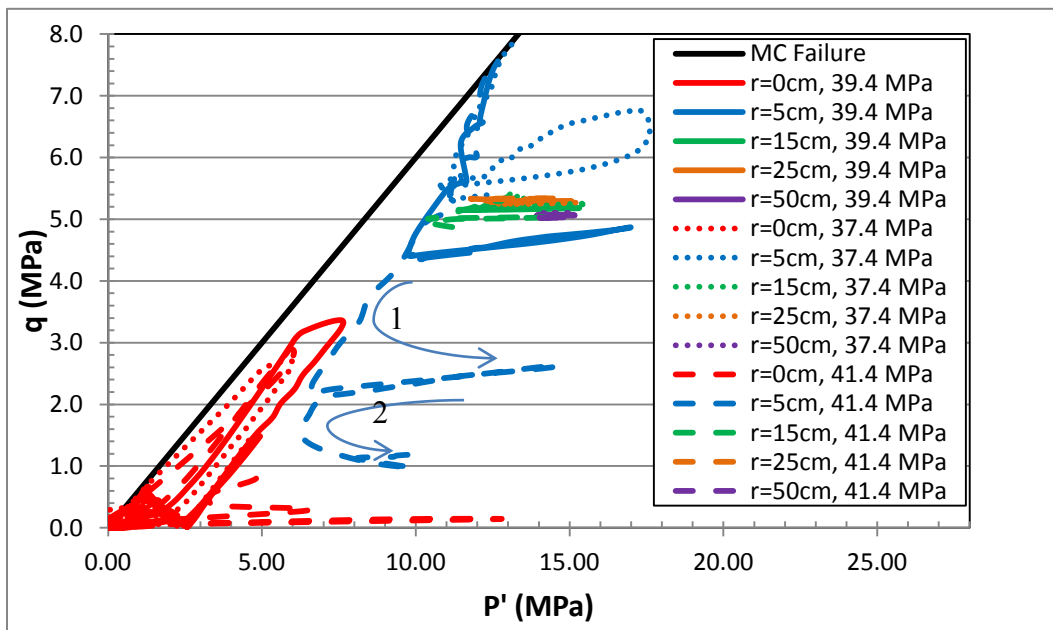
Figure 5-33 Stress paths for different injection pressures

144

5.2.10.4 Effect of WH Amplitude

Larger amplitudes of WH waves lead to more extensive failure and also a higher number of secondary pressure jumps as the mean effective stress is more susceptible to reaching near-zero values (see Figure 5-34 and Figure 5-35).
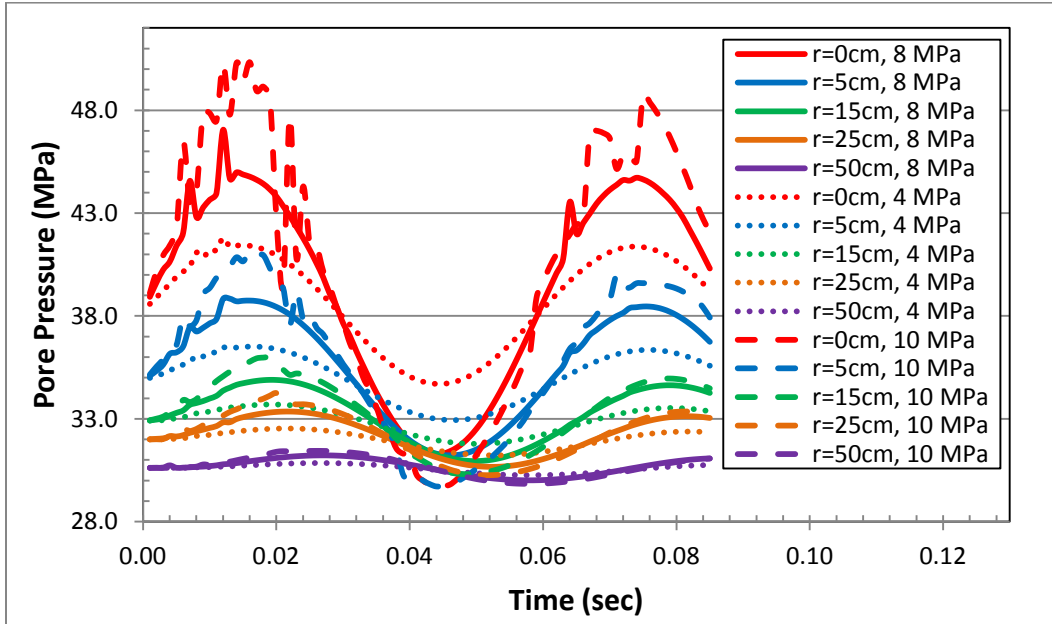
Figure 5-34 Pore pressure response for different WH amplitudes
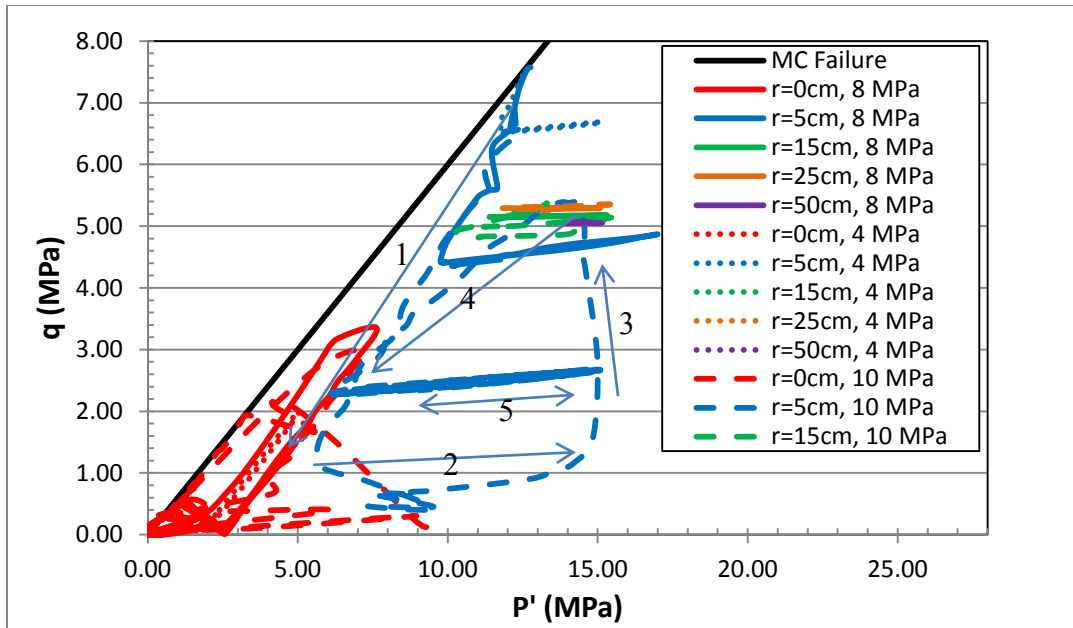
Figure 5-35 Stress paths for different WH amplitudes

5.2.10.5 Effect of Porosity

According to Figure 5-36, the wave amplitude is higher for a medium with a higher porosity, increasing the yield potential. The outcome is a higher likelihood for the complete stress reversal (see Figure 5-37) of farther elements from the well. In the absence of tortuosity, the fluid momentum equation, predicts higher fluid acceleration for higher porosity (see Eq. 4-49), which in turn increases solid acceleration in the momentum equation (Eq. 4-50).

The observed behavior is interesting because steady-state fluid flow (Darcy's law) is not highly sensitive to the porosity. However, under dynamic and transient conditions it plays an important role since the porosity appears in the acceleration term in the dynamic fluid flow equation (Eq. 4-21).

146
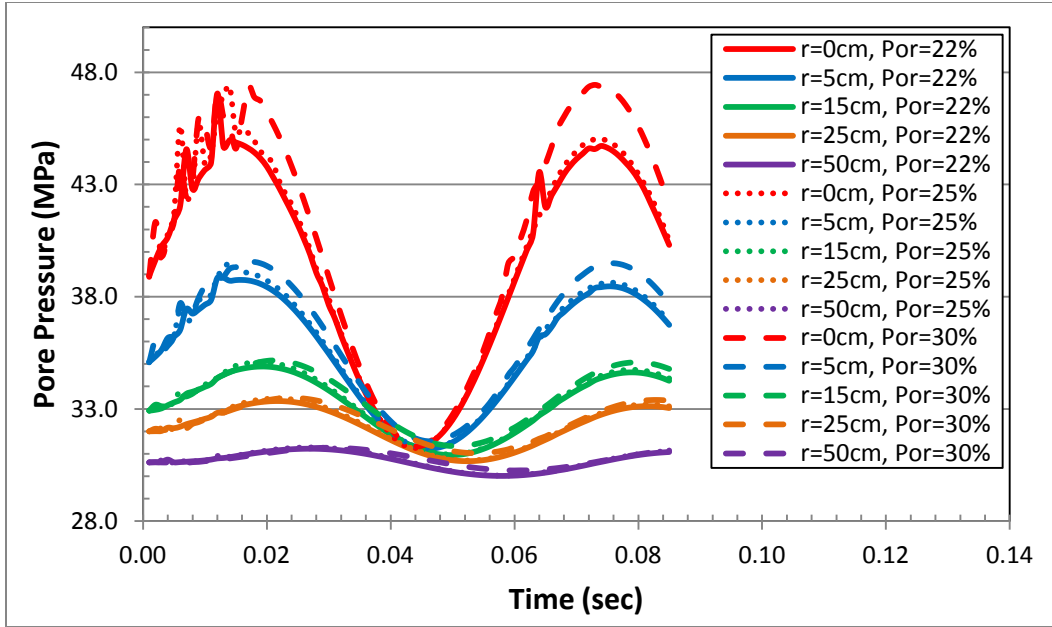
Figure 5-36 Pressure response for different porosities
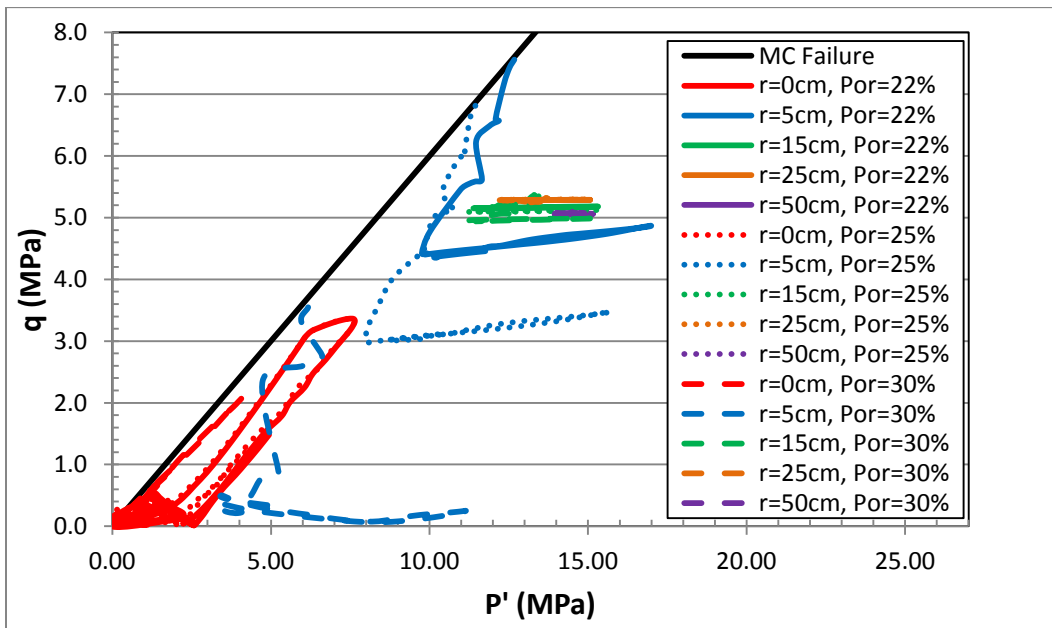
Figure 5-37 Stress paths for different porosities

5.2.10.6 Effect of Permeability

Figure 5-38 indicates an insignificant effect for the permeability in the permeability range used in the simulations. This is mainly because wave transfers

through compaction of the sand and fluid, and permeability does not affect it much if it is not a limiting factor, i.e. in case of very small permeabilities. Based on fluid momentum balance equation, permeability term is dominant for Darcy's flow regime and not the transient flow regime.
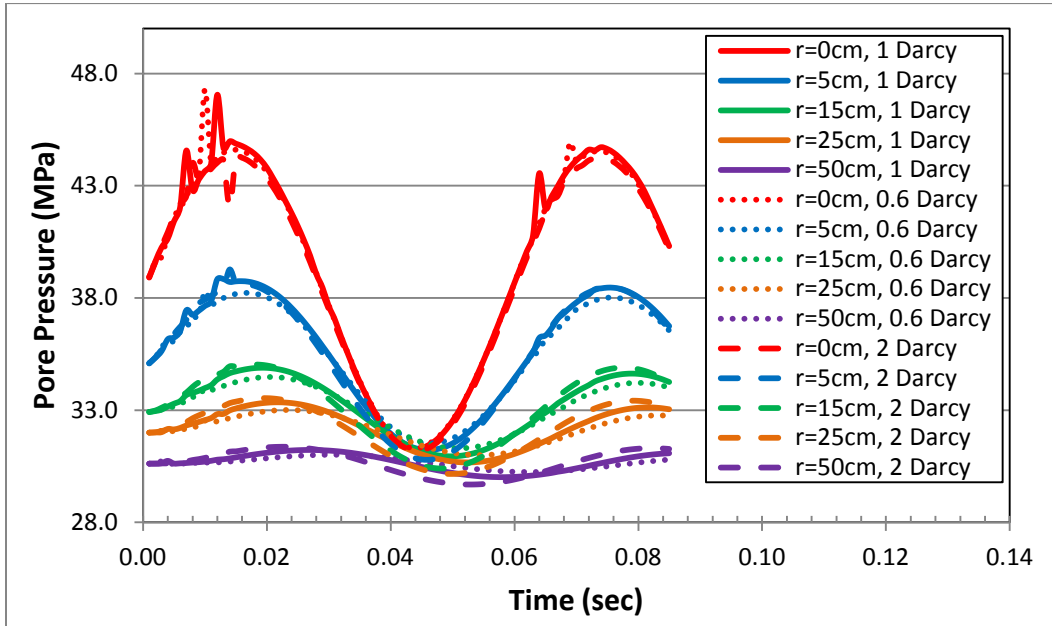
Figure 5-38 Pressure response for different permeabilities
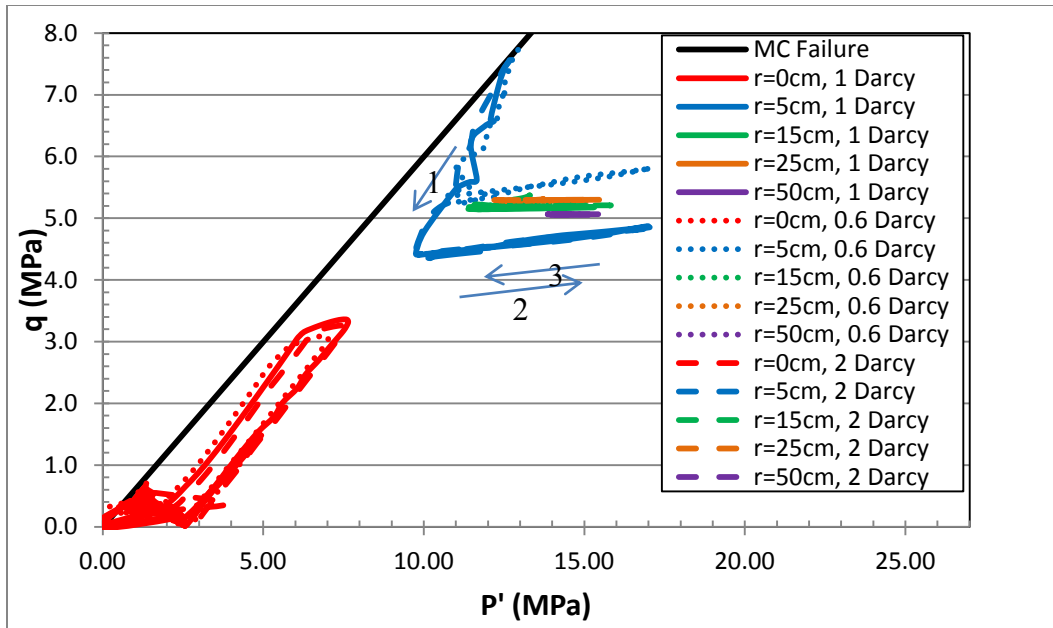
Figure 5-39 Stress paths for different permeabilities

5.3 Conclusions

A single injector well under WH wave is modeled dynamically. A weakly-consolidated sandstone is simulated to investigate the dynamic degradation of sandstone under WH effect. The following conclusions are drawn:

- The stress path moves toward low shear stress and low mean effective stress; however, it approaches near-zero conditions only for the perforation element which was already at failure conditions.
- Near-zero stress conditions of the perforation element generate an additional volume change and associated pore pressure change which is superposed on the WH wave and transferred along the reservoir.
- In case of a rigid cap rock (top boundary fixed in the vertical direction), more failure is observed around the perforation since arching and stress redistribution promote failure and stress reversal.

- The displacement vectors show a tendency for sand to be produced and push the sand retension equipment.

To investigate the liquefaction potential, Martin constitutive model is used for cohesionless sand. The premise stress changes caused by drilling, injection and shut-in cycles, fatigue and WH waves can lead to full degradation of sandstone. The following statements are concluded for this model:

- The estimated produced sand can fill the wellbore for the whole pay thickness, consistent with the observations in Norwegian field.
- Based on the displacement vectors and the stress paths diagrams, failure occurs at two shear bands angular to the wellface and propagates through time. Depending on the flow and mechanical properties, the shear stress may go to low near-zero values or possibly zero.
- Under the investigated conditions and assumptions, the stress path for the perforation element follows shear stress reversal (monotonic shear) on the yield envelope. Since cyclic fatigue is not included in the studied model, it is hard to distinguish liquefaction and simple material failure. It can only be concluded that progressive failure is an appropriate explanation of massive sand production.
- The fact that the top and bottom elements are failing reduces middle elements stresses. Hence, a stress reversal is observed in the middle elements although they have not touched the yield envelope.
- After failure, reduction in pore pressure moves back the stress state to elastic conditions and the behaviour becomes similar to an elastic stress path.
- The failure effect due to a WH pressure wave is more significant around the wellbore.
- Failure and sudden volumetric change of perforation elements (at near-zero mean effective stress) act as a high-frequency porosity wave and

propagates through the reservoir as a secondary wave superposed on the WH wave.

- The failure effect will be more significant for higher injection pressure, higher wave amplitude, negative dilation angle, higher porosity, and lower failure parameters such as lower friction angles. In such a case the elements beyond the perforation may undergo stress reversal. Without these extreme cases, only elements around the perforation are affected.

- The progressive failure and stress state changes occur in a fraction of second. Therefore, dynamic analysis is deemed necessary to simulate massive sand production realistically.

5.4 Nomenclature

a Sanding coefiicient

k Absolute permeability

n Porosity

C_i Constants for the Martin model, (i=1,..4)

c_r Residual cohesion

D_r Relative density

R_p Sand particle size

P' Mean effective stress; $P' = \frac{\sigma_1' + 2\sigma_3'}{3}$

q $\frac{\sigma_1 - \sigma_3}{2}$

q_{cr} Critical velocity for sanding

Δe_{vd} Additional irrecoverable volume change

γ Cyclic shear strain

μ Fluid viscosity

φ Friction angle

Chapter 6: Summary, Conclusions and Recommendations for Future Research

The primary aim of this research is to develop a numerical model that can predict sand behavior under dynamic effects of WH waves. In addition, investigationg the role of dynamic liquefaction in massive sand productions and the conditions that will lead to massive sand production are important. Below is the overall summary of the research project, conclusions of the findings, and future recommendations:

6.1 Summary

In Chapter 1 of the thesis, the general idea behind the research motivation was introduced. Research motivations are established thoroughly and project scope, objectives, and methodology adopted and applied have been stated.

In Chapter 2, a brief literature review was presented in order to shed more light on the concept under investigation, the general theory, and the background necessary to tackle such a complicated concept.

In Chapter 3, the degrading behavior of sandstone was discussed. A bilinear hardening/softening Mohr-Coulomb was developed. The model was calibrated for two different types of sandstone and validated with experimental triaxial data. Also, Fracture Energy Regularization was applied to eliminate mesh dependency during softening. This model was later used in Chapter 5 to study dynamic degradation of sandstone.

In Chapter 4, the mathematical formulation of porous media dynamics was established. The governing equations are presented and extended to elastoplastic conditions. Spanos and De la Cruz (1989) equations are adopted under isothermal condition and solved using Finite difference (FD) discretization. The equations are also compared with an earlier version presented by Biot (1956). A new tensor-form of artificial viscosity, required for stability, was presented. Numerical solution and discretization are validated using a shock-tube experiment and some simple models are simulated to give an idea of how pressure waves propagate through elastic reservoir. The dynamic flow equations are then coupled with FLAC dynamic module to use advanced elastoplastic constitutive models. Both undrained and drained coupling schemes are investigated. The results are then compared to the validated fully-coupled code.

In Chapter 5, a massive sanding case study in the Norwegian Sea was numerically investigated. Axisymmetric condition was assumed to model sand around a single injection well in the reservoir. It is important to recall the approximation of an actual perforation tunnel with an axisymmetric slit opening in the casing which can lead to an overestimation of the sand failure and sand production. WH waves are applied as the boundary conditions during sudden shut-downs under dynamic analysis. Different constitutive models are utilized to study the mechanism and stress paths under dynamic WH pressures. The first one, the Mohr-Coulomb hardening/softening model, was used to study dynamic degradation of weakly-consolidated sandstone and the effect of top boundary condition. The second one, the Martin model, is a simple liquefaction-based model. Finally, a parametric study was performed on rock properties, operational parameters, and wave properties.

Chapter 6 presents an overall summary of the research project, and a conclusion of the findings as well as future recommendations.

6.2 Contributions

The following are the academic contributions of this study:

- Results of numerical simulations using Biot's theory and de la Cruz and Spanos formulations are compared with measurements from a shock-tube experiment. It is demonstrated that Biot's formulation underestimates the magnitude of the first wave and overestimates the speed of the second wave.

- There is a hypothesis in the literature that liquefaction may occur during WH propagation in unconsolidated sand reservoirs. One of the objectives of this research is to find out through numerical simulations if dynamic liquefaction can be a mechanism for sanding in water injection wells. The results of numerical simulations for the cases studied in this research indicated only local stress reversal around the perforation, not a global phenomenon of liquefaction. As a result, it is concluded that, for the simulation cases in this research, the observed mechanism was progressive failure with time, not liquefaction. Progressive failure may be a more appropriate description of sudden massive sand production as a result of WH waves. The result of this research study can contribute to better understanding of reservoir behaviour under the WH propagation.

- All the previous numerical studies are either using Biot's theory, or are limited to elastic rock behavior. The research implemented the fundamentals of theoretical dynamics of porous media into practice in an innovative and unique fashion using a more advanced formulation and extended the simulation to the elasto-plastic reservoir rock response. The use of a new tensor-form artificial viscosity to achieve convergence is also a contribution in the finite difference numerical modeling in this field.

- Another novelty is applying an undrained coupling scheme in the dynamic porous solid-fluid flow calculations to obtain a faster numerical

convergence towards the solutions. The undrained scheme had been previously proven for static conditions, but not verified under dynamic conditions. Yet, the majority of geomechanics-fluid flow simulations use a drained coupling scheme.

The following are the industrial contribution of this study:

- A hardening/softening constitutive model and its calibration methodology is presented in this thesis. The model can predict sandstone behavior for applications where full sandstone degradation is important (e.g., in sand production analysis).
- The methodologies presented in this thesis can be used to (1) calculate the amplitude of the propagated WH waves in the reservoir; (2) estimate the stress conditions and potential failure during fast shut-ins in water injection wells; and (3) estimate the size of the zone around the wellbore within which the propagated WH may contribute towards sandstone degradation.

6.3 Conclusion

The following conclusions can be drawn from this research:

- A friction-hardening cohesion-softening the bilinear Mohr-Coulomb constitutive model is capable of modeling sandstone degradation under triaxial testing. The calibration procedure is also described.
- A fully-coupled dynamic fluid-solid code is developed. The code is two-dimensional and axisymmetric. Spanos and de la Cruz formulation is adopted and the equations are modified to be applicable to elastoplastic conditions.
- To achieve stability, scalar form of artificial viscosity is extended to a new tensor form.

- The code is validated against experimental shock-tube data. Two pressure waves are generated in a saturated porous medium as a result of a shock wave. The model is capable of predicting the waves' amplitude and speed.

- Dynamic fluid flow is sequentially-coupled with the FLAC dynamic module. Different coupling schemes are investigated. It is concluded that under dynamic conditions undrained split is the preferred coupling method. Compared to the more common undrained split, it is more stable and converges to the correct steady-state solution.

- The developed sequentially-coupled dynamic code is combined with the bilinear Mohr-Coulomb model and the Martin constitutive model to study massive sand production conditions, its mechanism, and the stress paths.

- Under the assumed conditions, the amount of produced sand predicted by the model can fill the simulated well past the perforation in a fraction of seconds after well shut-in. In reality, the perforation density may change the area of perforation. Also, the well was only exposed to about 1.5 cycles of WH. The results should, therefore, be seen in light of these assumptions.

- Failure and sudden volumetric change of perforation elements (at near-zero mean effective stress) act as a high-frequency porosity wave and propagates through the reservoir as a secondary wave superposed to the WH wave.

- The failure effect is more significant for higher injection pressure, higher wave amplitude, negative dilation angle, higher porosity, and lower failure parameters such as lower friction angle. In such a case the elements beyond the perforation may undergo stress reversal. Without these extreme cases, only elements around the perforation are affected.

- Under the studied conditions the stress path for perforation elements and the neighboring elements is similar to monotonic shear. The failure zone propagates quickly with time during WH wave dissipation. It is concluded

157

that under the investigated conditions, progressive failure is a more appropriate description of sudden massive sand production.

- In the case of a rigid cap rock (top boundary fixed in the vertical direction), more failure is observed around the perforation since arching and stress redistribution promote failure and stress reversal.

6.4 Future Recommendations

- There is a lack of measured and/or experimental data due to the fast nature of massive sand production; there are no comprehensive reports featuring all the necessary properties and conditions of this study. An experimental study will be of high value.

- Different cycles of loading and unloading during injection/shut-in cycles and WH waves are not considered in this study. Inclusion of an advanced constitutive model capable of modeling cyclic fatigue (such as bounding surface plasticity) is recommended.

- Although the current study does not confirm liquefaction as the underlying mechanism, it does not discredit it either. Using a more comprehensive liquefaction model will shed more light on the effect of liquefaction.

- Increasing the robustness of the numerical solution may allow element removal as a result of sand production. Having a moving interface is likely to result in more catastrophic progressive failure.

Bibliography

Bazant, Z. P., Oh, B. H., 1983. Crack band theory for fracture of concrete, Materials and Structures, RILEM, Paris, Vol 16, pp. 155-177.

Berger, M. J., LeVeque, R. J., 1998. Adaptive mesh refinement using wave-propagation algorithms for hyperbolic systems, SIAM J. Numer. Anal., Volume 35, Issue 6, pp. 2298-2316.

Biggs, J.M. and Biggs, J.M., 1964. Introduction to structural dynamics: McGraw-Hill.

Biot, M.A., 1956a. Theory of Propagation of Elastic Waves in a Fluid-Saturated Porous Solid I - Low-Frequency Range, Journal of the Acoustical Society of America Volume 28, Issue 2, pp. 168-178. doi: http://dx.doi.org/10.1121/1.1908239.

Biot, M.A., 1956b. Theory of Propagation of Elastic Waves in a Fluid-Saturated Porous Solid II - Higher Frequency Range, Journal of the Acoustical Society of America Volume 28, Issue 2, pp. 179-191. doi: http://dx.doi.org/10.1121/1.1908241.

Biot, M.A. 1941. General Theory of Three-Dimensional Consolidation, Journal of Applied Physics, Volume 12, Issue 2, pp. 155-164. doi: http://dx.doi.org/10.1063/1.1712886.

Brown, R.J.S., 1980. Connection between formation factor for electrical resistivity and fluid-solid coupling factor in Biot's equations for acoustic waves in fluid-filled porous media. Geophysics Volume 45, Issue 8, pp. 1269-1275. doi: 10.1190/1.1441123.

Casagrande, A., Shannon, W.L., 1949. Strength of soil under dynamic loads, Transactions, ASCE, Vol. 114, pp. 755-772.

Cheng, A. H. D., 1986. Effect of sediment on earthquake-induced reservoir hydro-dynamic response, J. Eng. Mech., Volume 112, Issue 7, pp. 654–665.

Chiavassaa, G., Lombard, B., 2011. Time domain numerical modeling of wave propagation in 2D heterogeneous porous media, J of Computational Physics.

Courant, R., Friedrichs, K.; Lewy, H., 1967. On the Partial difference equations of mathematical physics, IBM Journal of Research and Development Volume 11, Issue 2, pp. 215-234.

Crook, T, Willson S., Guo Yu J., Owen R. 2003. Computational modeling of localized deformation associated with borehole breakout in quasi-brittle materials, J. of Petroleum Science and engineering, Vol. 38, pp. 177-186.

Das, B.M. and Ramana, G.V., 2011. Principles of soil dynamics, 2nd edition. Stanford, CT: Cengage Learning.

Davidson B. C., Spanos, T. J. T., and Dusseault, M. B., 1999. Laboratory experiments on pressure pulse flow enhancement in porous media, In Proceedings of the 8th CIM Regina Petroleum Society Technical Meeting, Regina, Saskatchewan.

de la Cruz, V. and Spanos, T.J.T., 1989. Thermomechanical coupling during seismic wave propagation in a porous medium, Journal of Geophysical Research: Solid Earth, Volume 94, Issue B1, pp. 637-642. doi: 10.1029/JB094iB01p00637.

Desai, C. S., Galagoda, H. M., 1989. Earthquake analysis with generalized plasticity model for saturated soils, Earthq. Eng. Struct. Dyn., Volume 18, Issue 6, pp. 903–919.

Desrues, J., Hammad, W. 1989. Shear banding dependency on mean stress level in sand, International Workshop: Numerical methods for localization and bifurcation of granular bodies, Gdansk-Sobieszewo, pp. 57-67.

Detournay, C., 2008. Numerical Modeling of the Slit Mode of Cavity Evolution Associated With Sand Production, SPE Annual Technical Conference and Exhibition.

Dinesh, S., Sitharam, T. and Vinod, J., 2004. Dynamic properties and liquefaction behaviour of granular materials using discrete element method. Current science Vol 87, Issue 10, pp. 1379-1387.

Essam, I., Petrobel and Wally, A., 2007, Effect of water injection on sand production associated with oil production in sandstone reservoirs, SPE/IADC 108297.

FLAC user manual, version 6.0 2008., 4th edition. Minneapolis, Minnesota, USA: Itasca Consulting Group Inc.

Gemant, A. and Jackson, W., 1937. The measurement of internal friction in some solid dielectric materials. Philosophical Magazine Series 7, Vol. 23, Issue 157, pp. 960-983.

Han, G., Ioannidis, M., Dusseault M.B., 2003. Semi-analytical solutions for the effect of well shut-down on rock stability, J. of Canadian Petroleum Technology, Vol 42, No 12.

Hayatdavoudi, A., 2005. Formation Sand Liquefaction: A Mechanism for Explaining Fines Migration and Well Sanding. Journal of Energy Resources Technology, Vol 127, Issue 3, pp. 181-190.

Hayatdavoudi, A., 2006. Well Sanding and Lost Production Due to Cyclic Water Hammer, SPE Annual Technical Conference and Exhibition, San Antonio, Texas, USA, SPE-100928.

Hill, R., 1962. Acceleration waves in solids, Journal of the Mechanics and Physics of Solids Volume 10, Issue 1, pp. 1-16. doi: http://dx.doi.org/10.1016/0022-5096(62)90024-8.

Jafar Pour, M., Nouri, A., Chan, D., 2016. Numerical modelling of waterhammer pressure pulse propagation in sand reservoirs, J of Petroleum Science and Engineering, Vol 137, pp. 42-54.

Jafarpour, M., Rahmati, H., Azadbakht, S., Nouri, A., Chan D., Vaziri, H., 2012. Determination of mobilized strength properties of degrading sandstone, J. of Soils and Foundations, Vol 52, Issue 4, pp. 658-667.

Jardine, I.S., Johnson, B.A., White, B.D. and Stibbs, W., 1993. Hard or Soft Shut-in: Which Is the Best Approach? Presented at the SPE/IADC Drilling Conference.

Jefferies, M. and Been, K., 2006. Soil liquefaction: a critical state approach: Taylor & Francis.

Joseph, A., Ilozue, C.T., Osokogwu, U. and Ajienka, J.A., 2011. Effect of water-cut on sandstone strength and its implications in sand production prediction, SPE-150758.

Kim, J. 2010. Sequential Methods for Coupled Geomechanics and Multiphase Flow, PhD dissertation, Stanford University.

Kim, J., Tchelepi, H.A. and Juanes, R. 2011. Stability and convergence of sequential methods for coupled flow and geomechanics: Fixed-stress and fixed-strain splits, Computer Methods in Applied Mechanics and Engineering, Volume 200, pp. 1591-606. doi: http://dx.doi.org/10.1016/j.cma.2010.12.022.

Klevtsov, S., 2017. Linear solution techniques for reservoir simulation with fully coupled geomehanics, MSc Thesis, Stanford University.

Lakes, R., Yoon, H. S., Katz, J. L., 1986. Ultrasonic wave propagation and attenuation in wet bone, J. Biomed. Eng., Volume 8, Issue 2, pp.143–148.

Lombard, B., Piraux, J., 2006. Numerical modeling of elastic waves across imperfect contacts, SIAM J. Scient. Comput., Volume 28-1, pp. 172-205.

Marcher T., Vermeer P.A., 2001. Macromodelling of softening in non-cohesive soils, Continuous and Discontinuous Modelling of Cohesive-Frictional Materials, Springer, Vol 568, pp. 89-110.

McStravick, D.M., Rothers, D. and Blum, G., 1992. Laboratory Testing of Reflected Pressure Pulses in Small-Diameter Tubing, Offshore Technology Conference.

Mogenstern, N., 1977. Slope and excavations in heavily overconsolidated clays. Proc. of 9th Int. conf. on soil Mech. and Found. Eng., Tokyo, Vol 2, pp. 567-581.

North, R.E., 2002. Numerical modeling of pore pressure on a porous rock placed in a shock tube.

Nouri, A., Kuru, E., Vaziri, H., 2009. Elastoplastic Modelling of Sand Production Using Fracture Energy Regularization Method, J. of Canadian Petroleum Technology, Vol 48, Issue 4, pp. 64-71.

Oda, M., Kazama, H., 1998. Microstructure of shear bands and its relation to the mechanisms of dilatancy and failure of dense granular solids, Geotechnique, Vol 48, No. 4, pp. 465-481.

Papamichos, E., 2006. Sand Production: Physical and Experimental Evidence. Presented at the Geomechanical and Structural Issues in Energy Production, Aussois, France.

Patankar, S. 1980. Numerical Heat Transfer and Fluid Flow: Taylor & Francis.

Pietruszcak, S.T. and Mroz, Z,. 1981. Finite Element Analysis of Deformation of Strain Softening, International Journal of Numerical Methods in Engineering, Vol. 17, No. 3, pp. 327-334.

Plona, T. J., 1980. Observation of a second bulk compressional wave in a porous medium at ultrasonic frequencies: Applied Physics Letters, Volume 36, pp. 259-261.

Rahmati, H., Jafarpour, M., Azadbakht, S., Nouri, A., Vaziri, H., Chan, D., and Xiao, Y., 2012. Review of Sand Production Prediction Models, Journal of Petroleum Engineering, Vol 2013, Article ID 86498.

Rahmati, H., Nouri, A., Vaziri, H. et al., 2012. Validation of Predicted Cumulative Sand and Sand Rate Against Physical-Model Test. Journal of Canadian Petroleum Technology, Volume 51, Issue 5, SPE-157950-PA.

Rauch, A.F., 1997., EPOLLS: An Empirical Method for Predicating Surface Displacements Due to Liquefaction-Induced Lateral Spreading in Earthquakes. PhD dissertation, Virginia Polytechnic Institute and State University, Blacksburg, Virginia.

Robertson, P. K., 1994. Suggested Terminology for liquefaction, Proceeding of the 47th Canadian Geotechnical Conference, Canadian Geotechnical Society, Halifax, NS, pp. 277-286.

Rowe, P.W., 1972. Theoretical Meaning and Observed Values of Deformation Parameters for Soils, Proc. Roscoe Memorial Symp. on Stress-Strain Behaviour of Soils, Cambridge, Foulis, Henley-on-Thames, pp. 143-194.

Richardson, M.D., Williams, K.L., Briggs, K.B. et al., 2002. Dynamic measurement of sediment grain compressibility at atmospheric pressure: acoustic applications, Oceanic Engineering, IEEE Journal Volume 27, Issue 3, pp. 593-601. doi: 10.1109/JOE.2002.1040941.

Sadrpanah, R. H., Allam, L.R., Murra, D.J., 2005. Designing Effective Sand Control Systems to Overcome Problems in Water Injection Wells, SPE Europec/EAGE Annual Conference, Spain, SPE 93564.

Santarelli, F.J., Skomedal, E., Markestad, P., Berge, H.I. and Nasvig, H., 1998. Sand Production on Water Injectors: Just How Bad Can It Get?, SPE/ISRM Rock Mechanics in Petroleum Engineering, SPE-47329-MS.

Santarelli, F.J., Skomedal, E., Markestad, P., Berge, H.I. and Nasvig, H., 2000. Sand Production on Water Injectors: How Bad Can It Get?, SPE Drilling & Completion, Vol 15, Issue 2, SPE-64297-PA.

Santarelli, F.J., Sanfilippo, F., Embry, J., White, M. and Turnbull, J.B., 2011. The Sanding Mechanisms of Water Injectors and their Quantification in Terms of Sand Production: Example of the Buuzard Field (UKCS), SPE Annual Technical Conference and Exhibition.

Schanz T., Vermeer P.A., Bonnier P.G., 1999. The hardening soil model: formulation and verification, beyond 2000 in computational geotechnique.

Schwartzkopff, T., Dumbser, M., Munz, C., 2004. Fast high order ADER schemes for linear hyperbolic equations, J. Comput. Phys., Volume 197- 2, pp. 532-539.

Seed, H.B., Wong, R.T., Idriss, I.M. and Tokimatsu, K., 1984. Moduli and damping factors for dynamic analyses of cohesionless soils. UCB/EERC-84/14.

Seed, H. Bolton, and Idriss, I. M., 1970. Soil moduli and damping factors for dynamic response analyses. Springfield, Va: Reproduced by National Technical Information jService, U.S. Dept. of Commerce.

Sivrikoz, A., 2009. Enhanced Oil Recovery Modeling Using a Pressure Pulse-geomechanical Black Oil Simulator, PhD dissertation, University of Alberta, Dept. of Civil and Environmental Engineering.

Skjærstein, A., Stavropoulou, M., Vardoulakis, I. and Tronvoll, J., 1997. Hydrodynamic erosion; A potential mechanism of sand production in weak sandstones, International Journal of Rock Mechanics and Mining Sciences, Vol 34, Issues 3–4, pp. 292.e1-292.e18.

Sluys L.J., 1992. Wave propagation, localisation and dispersion in softening solids, PhD Thesis, Delf Inst. Tech.

Spanos, T., Davidson, B., Dusseault, M.B. et al., 1999. Pressure Pulsing At the Reservoir Scale: A New IOR Approach, Annual Technical Meeting, Jun 14 - 18, 1999,. 10.2118/99-11.

Streeter, V.L., Wylie, E.B. and Bedford, K.W., 1998. Fluid mechanics: WCB/McGraw Hill.

Sulem, J., Vardoulakis I., Papamichos E., Oulahna A., 1999. Elasto-plastic modeling of Red Wildmoor sandstone, Mechanics of Cohesive-Frictional Materials, Vol. 4, pp. 215-245.

van der Grinten, J.G.M., van Dongen, M.E.H. and van der Kogel, H., 1987. Strain and pore pressure propagation in a water-saturated porous medium, Journal of Applied Physics Volume 62, Issue 12, pp. 4682-4687. doi: http://dx.doi.org/10.1063/1.339018.

van der Grinten, J.G.M., van Dongen, M.E.H. and van der Kogel, H. 1985. A shock-tube technique for studying pore-pressure propagation in a dry and water-saturated porous medium. Journal of Applied Physics Volume 58, Issue 8,   pp. 2937-2942. doi: http://dx.doi.org/10.1063/1.335841.

Vaziri, H.H., Nouri, A., Hovem, K.A. and Wang, X., 2008. Computation of Sand Production in Water Injectors, SPE Production & Operations, Vol 23, Issue 4, pp. 518-524.

Vermeer, P.A., De Borst, R., 1984. Non-Associated Plasticity for Soils, Concrete and Rock, Heron 29 , pp. 1–62.

Verruijt, A., 2010. *An introduction to soil dynamics [electronic resource]*. Dordrecht; New York: Springer.

Viggiani, G., K̈untz, M., Desrues, J., 2001. An Experimental investigation of the relationships between grain size distribution and shear banding in sand, Continuous and Discontinuous Modeling of Cohesive Frictional Materials, Lecture Notes in Physics, Vol. 568, pp. 111-127.

Virieux, J. 1986. P-SV wave propagation in heterogeneous media: Velocity-stress finite-difference method. Geophysics Volume 51, Issue 4, pp. 889-901. doi: 10.1190/1.1442147.

Wang, J., Yale, D.P. and Dasari, G.R., 2011. Numerical Modeling of Massive Sand Production, SPE Annual Technical Conference and Exhibition.

Wang, X., Hovem, K.A., Moos, D. and Quan, Y., 2008. Water Hammer Effects on Water Injection Well Performance and Longevity, SPE International Symposium and Exhibition on Formation Damage Control, SPE-112282-MS.

Wegel, R.L. and Walther, H., 1935. Internal Dissipation in Solids for Small Cyclic Strains. J. of Applied Physics, Vol. 6 (4): 141-57.

Wilkins, M.L. 1980. Use of artificial viscosity in multidimensional fluid dynamic calculations. Journal of Computational Physics Volume 36, Issue 3, pp. 281-303. doi: http://dx.doi.org/10.1016/0021-9991(80)90161-8.

Willson, S.M., Moschovidis, Z.A., Cameron, J.R. and Palmer, I.D., 2002. New Model for Predicting the Rate of Sand Production, SPE/ISRM Rock Mechanics Conference.

Wisse, C.J., 1999. On Frequency Dependence of Acoustic Waves in Porous Cylinders, University of Technology.

Wu, B., Tan, C.P., 2005. Effect of water cut on sand production-an experimental study, SPE 92715.

Xiao, Y. and Vaziri, H.H. 2011. Import of strength degradation process in sand prediction and management, 45th U.S. Rock Mechanics/Geomechanics Symposium.

Yi, X., 2001. Water Injectivity Decline Caused by Sand Mobilization: Simulation and Prediction. Presented at the SPE Permian Basin Oil and Gas Recovery Conference.

Yoshida, T., Tatsuoka, F., Siddiquee, M. S. A., Kamegai, Y., Park, C. -S., 1994. Shear banding in sands observed in plane strain compression, in: Chambon, Desrues, Vardoulakis (Eds.), Loacalisation and Bifurcation Theory for Soils and Rocks, pp. 165-179

Appendix A: Fully-Coupled Dynamic Code Developed in MATLAB for Shock-Tube Example

```matlab
clear
clc
z_length=1.895;
r_length=.0375;   %ID=75mm
Nr=10; % number of nodes    %i index
Nz=401;                      %j index
N=Nr*Nz;
dr=r_length/Nr;
dz=z_length/Nz;
%Fluid properties
ro_f=1000; %kg/m3
muf=1*.001; %cp to kg/(m.Sec) water viscosity
mu=muf;%0;
ro_s=2650;
k0=5.6e-11 ; % m2
kr=k0*ones(Nr,Nz);
kz=k0*ones(Nr,Nz);
n0=0.3; %initial porosity
n=n0*ones(Nr,Nz);
tow=1.65; %Tortuosity
g=-9.8;
bu=ones(Nr,Nz)*8.16e9;
sh=ones(Nr,Nz)*1.3e9;
nu=(3*bu(1,1)-2*sh(1,1))/(2*(3*bu(1,1)+sh(1,1)));
mv=1/(bu(1,1)+4*sh(1,1)/3);
cf=.0005*1e-6; %m2/MN fluid compressibility to 1/Pa
cm=mv;
ro=ro_f*n0+(1-n0)*ro_s;
cs=2.35e-11; %1/Pa
alfa=1-cs/cm; %Biot Coeff
Sp=n0*cf+(alfa-n0)*cs;
cc1=sqrt(1/(ro*mv)+alfa^2/(ro*(Sp)));
cc2=sqrt((1-alfa+Sp/mv)*n0/(Sp*ro_f*(alfa-
n0+tow+(1+tow)*Sp/mv)));

ds=cf*n0*(1-n0)/(n0*cf+(1-n0)*cs);
df=cs*n0*(1-n0)/(n0*cf+(1-n0)*cs);
% wave properties
f=17;%0; %frequency 1/s   (f or w)
period=1/f; %sec
cc=sqrt(1/(ro*mv));   %p_wave speed
ccf=sqrt(1/(ro_f*cf));   %p_wave speed
Fdrr=zeros(Nr,Nz);
```

```matlab
Fdrr_past=Fdrr;
Fdzz=zeros(Nr,Nz);
Fdzz_past=Fdzz;

%mesh properties
dz=z_length/(Nz-1);
z=zeros(Nz,1);
r=zeros(Nr,1);
for jj=1:Nz
    z(jj)=(jj-1)*dz;
end
dr=r_length/(Nr-1);
for ii=1:Nr
    r(ii)=(ii-1)*dr;
end
rw=r(1);
re=r(Nr);
jj2=1;

dx1=r(2)-r(1);
dx2=z(2)-z(1);

dxmin=min(dx1,dx2);

dt1=dxmin/cc1;
dt2=dxmin/cc2;

dt=.4*n0*min(dt1,dt2);

t01=z_length/cc1;
t02=z_length/cc2;
t0=max(t01,t02);   %time the wave reaches the end
%2D in r and z directions
%%%%%%%%%%%%%%%%%%%%%%%%%%%%%%%%%%%%%%%%%%%%%%%%%%%%%%%%%%%%%%%%%%%%%
%%%%%%%%%
%initial conditions
wr_past=zeros(Nr,Nz);
wz_past=zeros(Nr,Nz);
wr=wr_past;
wz=wz_past;
p_past=zeros(Nr,Nz); %10*ones(N,1);
p=p_past;
vr=zeros(Nr,Nz);
vz=zeros(Nr,Nz);
ur=zeros(Nr,Nz);
uz=zeros(Nr,Nz);
vr_past=zeros(Nr,Nz);
vz_past=zeros(Nr,Nz);
n_past=n;

time=0;
jj=1;  %used for p_wave & history points
```

```matlab
srr=0*ones(Nr,Nz);
szz=0*ones(Nr,Nz);
stt=0*ones(Nr,Nz);
srz=0*ones(Nr,Nz);
srr_past=srr;
szz_past=szz; %initialized by weight in the IC
stt_past=stt;
srz_past=srz;
Ev=zeros(Nr,Nz);

%initialization
p0=zeros(Nz,1);
for j=1:Nz
    p0(j)=1.01e5+.48*abs(g)*ro_f+(z(Nz)-z(j))*ro_f*abs(g);% .5m
water on top
    p(:,j)=1.01e5+.48*abs(g)*ro_f+(z(Nz)-z(j))*ro_f*abs(g);%
    szz(:,j)=1.01e5+.48*abs(g)*ro_f+(z(Nz)-z(j))*(ro*abs(g))-
alfa.*p(:,j);
    szz_0(j)=1.01e5+.48*abs(g)*ro_f+(z(Nz)-z(j))*(ro*abs(g))-
alfa.*p0(j);
end
szz_past=szz;
p_past=p;

%history
Xp1=0.12;
Ip1=floor((z_length-Xp1)/dz);
Xp2=0.22;
Ip2=floor((z_length-Xp2)/dz);
jj=0;
t=zeros(100,1);
f1=zeros(100,1);
f2=zeros(100,1);
ezz1=zeros(100,1);
ezz2=zeros(100,1);
fporo=f;
Nr_mid=floor(Nr/2);
f1(1)=0;
f2(1)=0;
ezz1(1)=0;
ezz2(1)=0;
fporo(1)=0;
t(1)=0;
counter=1;
jij=1;

coef=(1+tow*(1+n0*ro_f/(ro_s*(1-n0))))*ro_f;
coef0=tow*ro_f/(ro_s*(1-n0));
p_wave=1.65e5;
lamdaf=-2*mu/3;
while time<6e-4
    %solving for vr,vz, wr & wz
```

170

```matlab
%1) r=rw
i=1;
for j=2:Nz-1
    z1_mid=(z(j)+z(j-1))/2;
    z2_mid=(z(j)+z(j+1))/2;
    r2_mid=(r(i)+r(i+1))/2;
    vr(i,j)=0; %1D flow

    vz(i,j)=vz_past(i,j)-
(dt/coef)*((1+coef0*alfa)*(p_past(i,j+1)-p_past(i,j-1))/(z(j+1)-
z(j-1))+n_past(i,j)*muf*(vz_past(i,j)-wz_past(i,j))/kz(i,j)-...
        ro_f*g+coef0*((srz_past(i+1,j)-
srz_past(i,j))/(r(i+1)-r(i))+(srz_past(i,j))/r2_mid+...
%r(1)=0==>r2_mid
        (szz_past(i,j+1)-szz_past(i,j-1)+Fdzz_past(i,j+1)-
Fdzz_past(i,j-1))/(z(j+1)-z(j-1))-ro*g+bu(i,j)*(n_past(i,j+1)-
n_past(i,j-1))/(z(j+1)-z(j-1)))-...
        mu*((1/(r(i+1)-r(i)))*((vz_past(i+2,j)-
vz_past(i+1,j))/(r(i+2)-r(i+1))-(vz_past(i+1,j)-
vz_past(i,j))/(r(i+1)-r(i)))+...
        (vz_past(i+1,j)-vz_past(i,j))/(r2_mid*(r(i+1)-
r(i)))+... %r(1)=0==>r2_mid
        (1/(z2_mid-z1_mid))*((vz_past(i,j+1)-
vz_past(i,j))/(z(j+1)-z(j))-(vz_past(i,j)-vz_past(i,j-1))/(z(j)-
z(j-1))))-...
        (mu+lamdaf)*((vr_past(i+1,j+1)-vr_past(i+1,j-1)-
vr_past(i,j+1)+vr_past(i,j-1))/((r(i+1)-r(i))*(z(j+1)-z(j-
1)))+(vr_past(i,j+1)-vr_past(i,j-1))/(r2_mid*(z(j+1)-z(j-1)))+...
%r(1)=0==>r2_mid
        (1/(z2_mid-z1_mid))*((vz_past(i,j+1)-
vz_past(i,j))/(z(j+1)-z(j))-(vz_past(i,j)-vz_past(i,j-1))/(z(j)-
z(j-1)))));

    wr(i,j)=0; %axisym
    wz(i,j)=wz_past(i,j)-dt*(n_past(i,j)*ro_f*(vz(i,j)-
vz_past(i,j))/dt+...
        (srz_past(i+1,j)-srz_past(i,j))/(r(i+1)-
r(i))+srz_past(i,j)/r2_mid+... %r(1)=0==>r2_mid
        (szz_past(i,j+1)-szz_past(i,j-1)+Fdzz_past(i,j+1)-
Fdzz_past(i,j-1))/(z(j+1)-z(j-1))+...
        alfa*(p_past(i,j+1)-p_past(i,j-1))/(z(j+1)-z(j-1))-
ro*g+bu(i,j)*(n_past(i,j+1)-n_past(i,j-1))/(z(j+1)-z(j-1)))/((1-
n_past(i,j))*ro_s);
end
%2) left bottom corner z=0 r=rw
j=1;
i=1;
r2_mid=(r(i)+r(i+1))/2;
vr(i,j)=0; %1D flow
vz(i,j)=0; %no flow @ bot
wr(i,j)=0; %axisym
wz(i,j)=0; %fix @bot
%3) left top corner z=h r=rw
```

```matlab
    j=Nz;
    i=1;
    r2_mid=(r(i)+r(i+1))/2;
    %BC
    p(i,j)=p_wave+p0(j);
    szz(i,j)=szz_0(j)+(1-alfa)*p_wave;
    vr(i,j)=0; %1D flow

    vz(i,j)=vz_past(i,j)-(dt/coef)*((1+coef0*alfa)*(p_past(i,j)-
p_past(i,j-1))/(z(j)-z(j-1))+n_past(i,j)*muf*(vz_past(i,j)-
wz_past(i,j))/kz(i,j)-...
        ro_f*g+coef0*((srz_past(i+1,j)-srz_past(i,j))/(r(i+1)-
r(i))+(srz_past(i,j))/r2_mid+... %r(1)=0==>r2_mid
        (szz_past(i,j)-szz_past(i,j-1)+Fdzz_past(i,j)-
Fdzz_past(i,j-1))/(z(j)-z(j-1))-ro*g+bu(i,j)*(n_past(i,j)-
n_past(i,j-1))/(z(j)-z(j-1)))-...
        mu*((1/(r(i+1)-r(i)))*((vz_past(i+2,j)-
vz_past(i+1,j))/(r(i+2)-r(i+1))-(vz_past(i+1,j)-
vz_past(i,j))/(r(i+1)-r(i)))+...
        (vz_past(i+1,j)-vz_past(i,j))/(r2_mid*(r(i+1)-r(i)))+...
%r(1)=0==>r2_mid
        (1/(z(j)-z(j-1)))*((vz_past(i,j)-vz_past(i,j-1))/(z(j)-
z(j-1))-(vz_past(i,j-1)-vz_past(i,j-2))/(z(j-1)-z(j-2))))-...
        (mu+lamdaf)*((vr_past(i+1,j)-vr_past(i+1,j-1)-
vr_past(i,j)+vr_past(i,j-1))/((r(i+1)-r(i))*(z(j)-z(j-
1)))+(vr_past(i,j)-vr_past(i,j-1))/(r2_mid*(z(j)-z(j-1)))+...
%r(1)=0==>r2_mid
        (1/((z(j)-z(j-1))))*((vz_past(i,j)-vz_past(i,j-1))/(z(j)-
z(j-1))-(vz_past(i,j-1)-vz_past(i,j-2))/(z(j-1)-z(j-2)))));
    wr(i,j)=0; %axisym
    wz(i,j)=wz_past(i,j)-dt*(n_past(i,j)*ro_f*(vz(i,j)-
vz_past(i,j))/dt+...
        (srz_past(i+1,j)-srz_past(i,j))/(r(i+1)-
r(i))+srz_past(i,j)/r2_mid+... %r(1)=0==>r2_mid
        (szz_past(i,j)-szz_past(i,j-1)+Fdzz_past(i,j)-
Fdzz_past(i,j-1))/(z(j)-z(j-1))+...
        alfa*(p_past(i,j)-p_past(i,j-1))/(z(j)-z(j-1))-
ro*g+bu(i,j)*(n_past(i,j)-n_past(i,j-1))/(z(j)-z(j-1)))/((1-
n_past(i,j))*ro_s);
    %4) middle points  corr
    for i=2:Nr-1
        for j=2:Nz-1
            r1_mid=(r(i)+r(i-1))/2;
            r2_mid=(r(i)+r(i+1))/2;
            z1_mid=(z(j)+z(j-1))/2;
            z2_mid=(z(j)+z(j+1))/2;

            vr(i,j)=vr_past(i,j)-
(dt/coef)*((coef0*alfa+1)*(p_past(i+1,j)-p_past(i-1,j))/(r(i+1)-
r(i-1))+n_past(i,j)*muf*(vr_past(i,j)-wr_past(i,j))/kr(i,j)-...
                mu*((1/(r2_mid-r1_mid))*((vr_past(i+1,j)-
vr_past(i,j))/(r(i+1)-r(i))-(vr_past(i,j)-vr_past(i-1,j))/(r(i)-
r(i-1)))+...
```

172

```
                (vr_past(i+1,j)-vr_past(i-1,j))/(r(i)*(r(i+1)-
r(i-1)))+(1/(z2_mid-z1_mid))*((vr_past(i,j+1)-
vr_past(i,j))/(z(j+1)-z(j))-...
                (vr_past(i,j)-vr_past(i,j-1))/(z(j)-z(j-1)))-
vr_past(i,j)/(r(i)^2))-(mu+lamdaf)*((vr_past(i+1,j)-vr_past(i-
1,j))/(r(i)*(r(i+1)-r(i-1)))+...
                (1/(r2_mid-r1_mid))*((vr_past(i+1,j)-
vr_past(i,j))/(r(i+1)-r(i))-(vr_past(i,j)-vr_past(i-1,j))/(r(i)-
r(i-1)))-vr_past(i,j)/(r(i)^2)+...
                (vz_past(i+1,j+1)-vz_past(i+1,j-1)-vz_past(i-
1,j+1)+vz_past(i-1,j-1))/((r(i+1)-r(i-1))*(z(j+1)-z(j-
1))))+coef0*...
                ((srr_past(i+1,j)-srr_past(i-
1,j)+Fdrr_past(i+1,j)-Fdrr_past(i-1,j))/(r(i+1)-r(i-1))+...
                (srz_past(i,j+1)-srz_past(i,j-1))/(z(j+1)-z(j-
1))+(srr_past(i,j)-
stt_past(i,j)+Fdrr_past(i,j))/r(i)+bu(i,j)*(n_past(i+1,j)-
n_past(i-1,j))/(r(i+1)-r(i-1))));
                vz(i,j)=vz_past(i,j)-
(dt/coef)*((1+coef0*alfa)*(p_past(i,j+1)-p_past(i,j-1))/(z(j+1)-
z(j-1))+n_past(i,j)*muf*(vz_past(i,j)-wz_past(i,j))/kz(i,j)-...
                ro_f*g+coef0*((srz_past(i+1,j)-srz_past(i-
1,j))/(r(i+1)-r(i-1))+(srz_past(i,j))/r(i)+...
                (szz_past(i,j+1)-szz_past(i,j-
1)+Fdzz_past(i,j+1)-Fdzz_past(i,j-1))/(z(j+1)-z(j-1))-
ro*g+bu(i,j)*(n_past(i,j+1)-n_past(i,j-1))/(z(j+1)-z(j-1)))-...
                mu*((1/(r2_mid-r1_mid))*((vz_past(i+1,j)-
vz_past(i,j))/(r(i+1)-r(i))-(vz_past(i,j)-vz_past(i-1,j))/(r(i)-
r(i-1)))+(vz_past(i+1,j)-vz_past(i-1,j))/(r(i)*(r(i+1)-r(i-
1)))+...
                (1/(z2_mid-z1_mid))*((vz_past(i,j+1)-
vz_past(i,j))/(z(j+1)-z(j))-(vz_past(i,j)-vz_past(i,j-1))/(z(j)-
z(j-1))))-...
                (mu+lamdaf)*((vr_past(i+1,j+1)-vr_past(i+1,j-1)-
vr_past(i-1,j+1)+vr_past(i-1,j-1))/((r(i+1)-r(i-1))*(z(j+1)-z(j-
1)))+(vr_past(i,j+1)-vr_past(i,j-1))/(r(i)*(z(j+1)-z(j-1)))+...
                (1/(z2_mid-z1_mid))*((vz_past(i,j+1)-
vz_past(i,j))/(z(j+1)-z(j))-(vz_past(i,j)-vz_past(i,j-1))/(z(j)-
z(j-1)))));


                wr(i,j)=wr_past(i,j)-dt*(n_past(i,j)*ro_f*(vr(i,j)-
vr_past(i,j))/dt+...
                (srr_past(i+1,j)-srr_past(i-
1,j)+Fdrr_past(i+1,j)-Fdrr_past(i-1,j))/((r(i+1)-r(i-1)))+...
                (srz_past(i,j+1)-srz_past(i,j-1))/(z(j+1)-z(j-
1))+(srr_past(i,j)+Fdrr_past(i,j)-stt_past(i,j))/r(i)+...
                alfa*(p_past(i+1,j)-p_past(i-1,j))/(r(i+1)-r(i-
1))+bu(i,j)*(n_past(i+1,j)-n_past(i-1,j))/(r(i+1)-r(i-1)))/((1-
n_past(i,j))*ro_s);
                wz(i,j)=wz_past(i,j)-dt*(n_past(i,j)*ro_f*(vz(i,j)-
vz_past(i,j))/dt+...
```

```
                (srz_past(i+1,j)-srz_past(i-1,j))/(r(i+1)-r(i-
1))+srz_past(i,j)/r(i)+...
                (szz_past(i,j+1)-szz_past(i,j-
1)+Fdzz_past(i,j+1)-Fdzz_past(i,j-1))/(z(j+1)-z(j-1))+...
                alfa*(p_past(i,j+1)-p_past(i,j-1))/(z(j+1)-z(j-
1))-ro*g+bu(i,j)*(n_past(i,j+1)-n_past(i,j-1))/(z(j+1)-z(j-
1)))/((1-n_past(i,j))*ro_s);
        end
    end

%%%%%%%%%%%%%%%%%%%%%%%%%%%%%%%%%%%%%%%%%%%%%%%%%%%%%%%%%%%%%%%%%%%%%
%%%%%
    %5)  z=0
    j=1;
    for i=2:Nr-1
        r1_mid=(r(i)+r(i-1))/2;
        r2_mid=(r(i)+r(i+1))/2;


        vr(i,j)=vr_past(i,j)-
(dt/coef)*((coef0*alfa+1)*(p_past(i+1,j)-p_past(i-1,j))/(r(i+1)-
r(i-1))+n_past(i,j)*muf*(vr_past(i,j)-wr_past(i,j))/kr(i,j)-...
            mu*((1/(r2_mid-r1_mid))*((vr_past(i+1,j)-
vr_past(i,j))/(r(i+1)-r(i))-(vr_past(i,j)-vr_past(i-1,j))/(r(i)-
r(i-1)))+...
            (vr_past(i+1,j)-vr_past(i-1,j))/(r(i)*(r(i+1)-r(i-
1)))+(1/(z(j+1)-z(j)))*((vr_past(i,j+2)-vr_past(i,j+1))/(z(j+2)-
z(j+1))-...
            (vr_past(i,j+1)-vr_past(i,j))/(z(j+1)-z(j)))-
vr_past(i,j)/(r(i)^2))-(mu+lamdaf)*((vr_past(i+1,j)-vr_past(i-
1,j))/(r(i)*(r(i+1)-r(i-1)))+...
            (1/(r2_mid-r1_mid))*((vr_past(i+1,j)-
vr_past(i,j))/(r(i+1)-r(i))-(vr_past(i,j)-vr_past(i-1,j))/(r(i)-
r(i-1)))-vr_past(i,j)/(r(i)^2)+...
            (vz_past(i+1,j+1)-vz_past(i+1,j)-vz_past(i-
1,j+1)+vz_past(i-1,j))/((r(i+1)-r(i-1))*(z(j+1)-z(j))))+coef0*...
            ((srr_past(i+1,j)-srr_past(i-1,j)+Fdrr_past(i+1,j)-
Fdrr_past(i-1,j))/(r(i+1)-r(i-1))+...
            (srz_past(i,j+1)-srz_past(i,j))/(z(j+1)-
z(j))+(srr_past(i,j)-
stt_past(i,j)+Fdrr_past(i,j))/r(i)+bu(i,j)*(n_past(i+1,j)-
n_past(i-1,j))/(r(i+1)-r(i-1))));
        vz(i,j)=0; %no flow @ bot


        wr(i,j)=wr_past(i,j)-dt*(n_past(i,j)*ro_f*(vr(i,j)-
vr_past(i,j))/dt+...
            (srr_past(i+1,j)-srr_past(i-1,j)+Fdrr_past(i+1,j)-
Fdrr_past(i-1,j))/((r(i+1)-r(i-1)))+...
            (srz_past(i,j+1)-srz_past(i,j))/(z(j+1)-
z(j))+(srr_past(i,j)+Fdrr_past(i,j)-stt_past(i,j))/r(i)+...
            alfa*(p_past(i+1,j)-p_past(i-1,j))/(r(i+1)-r(i-
1))+bu(i,j)*(n_past(i+1,j)-n_past(i-1,j))/(r(i+1)-r(i-1)))/((1-
n_past(i,j))*ro_s);
```

```matlab
        wz(i,j)=0; %fixed @ bot
    end
    %6) z=h  corr top
    j=Nz;
    for i=2:Nr-1
        %BC
        p(i,j)=p_wave+p0(j);
        szz(i,j)=szz_0(j)+(1-alfa)*p_wave;


        r1_mid=(r(i)+r(i-1))/2;
        r2_mid=(r(i)+r(i+1))/2;


        vr(i,j)=vr_past(i,j)-
(dt/coef)*((coef0*alfa+1)*(p_past(i+1,j)-p_past(i-1,j))/(r(i+1)-
r(i-1))+n_past(i,j)*muf*(vr_past(i,j)-wr_past(i,j))/kr(i,j)-...
            mu*((1/(r2_mid-r1_mid))*((vr_past(i+1,j)-
vr_past(i,j))/(r(i+1)-r(i))-(vr_past(i,j)-vr_past(i-1,j))/(r(i)-
r(i-1)))+...
            (vr_past(i+1,j)-vr_past(i-1,j))/(r(i)*(r(i+1)-r(i-
1)))+(1/(z(j)-z(j-1)))*((vr_past(i,j)-vr_past(i,j-1))/(z(j)-z(j-
1))-...
            (vr_past(i,j-1)-vr_past(i,j-2))/(z(j-1)-z(j-2)))-
vr_past(i,j)/(r(i)^2))-(mu+lamdaf)*((vr_past(i+1,j)-vr_past(i-
1,j))/(r(i)*(r(i+1)-r(i-1)))+...
            (1/(r2_mid-r1_mid))*((vr_past(i+1,j)-
vr_past(i,j))/(r(i+1)-r(i))-(vr_past(i,j)-vr_past(i-1,j))/(r(i)-
r(i-1)))-vr_past(i,j)/(r(i)^2)+...
            (vz_past(i+1,j)-vz_past(i+1,j-1)-vz_past(i-
1,j)+vz_past(i-1,j-1))/((r(i+1)-r(i-1))*(z(j)-z(j-1))))+coef0*...
            ((srr_past(i+1,j)-srr_past(i-1,j)+Fdrr_past(i+1,j)-
Fdrr_past(i-1,j))/(r(i+1)-r(i-1))+...
            (srz_past(i,j)-srz_past(i,j-1))/(z(j)-z(j-
1))+(srr_past(i,j)-
stt_past(i,j)+Fdrr_past(i,j))/r(i)+bu(i,j)*(n_past(i+1,j)-
n_past(i-1,j))/(r(i+1)-r(i-1))));


        vz(i,j)=vz_past(i,j)-
(dt/coef)*((1+coef0*alfa)*(p_past(i,j)-p_past(i,j-1))/(z(j)-z(j-
1))+n_past(i,j)*muf*(vz_past(i,j)-wz_past(i,j))/kz(i,j)-...
            ro_f*g+coef0*((srz_past(i+1,j)-srz_past(i-
1,j))/(r(i+1)-r(i-1))+(srz_past(i,j))/r(i)+...
            (szz_past(i,j)-szz_past(i,j-1)+Fdzz_past(i,j)-
Fdzz_past(i,j-1))/(z(j)-z(j-1))-ro*g+bu(i,j)*(n_past(i,j)-
n_past(i,j-1))/(z(j)-z(j-1)))-...
            mu*((1/(r2_mid-r1_mid))*((vz_past(i+1,j)-
vz_past(i,j))/(r(i+1)-r(i))-(vz_past(i,j)-vz_past(i-1,j))/(r(i)-
r(i-1)))+(vz_past(i+1,j)-vz_past(i-1,j))/(r(i)*(r(i+1)-r(i-
1)))+...
            (1/(z(j)-z(j-1)))*((vz_past(i,j)-vz_past(i,j-
1))/(z(j)-z(j-1))-(vz_past(i,j-1)-vz_past(i,j-2))/(z(j-1)-z(j-
2))))-...
```

175

```matlab
            (mu+lamdaf)*((vr_past(i+1,j)-vr_past(i+1,j-1)-
vr_past(i-1,j)+vr_past(i-1,j-1))/((r(i+1)-r(i-1))*(z(j)-z(j-
1)))+(vr_past(i,j)-vr_past(i,j-1))/(r(i)*(z(j)-z(j-1))))+...
            (1/(z(j)-z(j-1)))*((vz_past(i,j)-vz_past(i,j-
1))/(z(j)-z(j-1))-(vz_past(i,j-1)-vz_past(i,j-2))/(z(j-1)-z(j-
2))))));

        wr(i,j)=wr_past(i,j)-dt*(n_past(i,j)*ro_f*(vr(i,j)-
vr_past(i,j))/dt+...
            (srr_past(i+1,j)-srr_past(i-1,j)+Fdrr_past(i+1,j)-
Fdrr_past(i-1,j))/((r(i+1)-r(i-1)))+...
            (srz_past(i,j)-srz_past(i,j-1))/(z(j)-z(j-
1))+(srr_past(i,j)+Fdrr_past(i,j)-stt_past(i,j))/r(i)+...
            alfa*(p_past(i+1,j)-p_past(i-1,j))/(r(i+1)-r(i-
1))+bu(i,j)*(n_past(i+1,j)-n_past(i-1,j))/(r(i+1)-r(i-1)))/((1-
n_past(i,j))*ro_s);
        wz(i,j)=wz_past(i,j)-dt*(n_past(i,j)*ro_f*(vz(i,j)-
vz_past(i,j))/dt+...
            (srz_past(i+1,j)-srz_past(i-1,j))/(r(i+1)-r(i-
1))+srz_past(i,j)/r(i)+...
            (szz_past(i,j)-szz_past(i,j-1)+Fdzz_past(i,j)-
Fdzz_past(i,j-1))/(z(j)-z(j-1))+...
            alfa*(p_past(i,j)-p_past(i,j-1))/(z(j)-z(j-1))-
ro*g+bu(i,j)*(n_past(i,j)-n_past(i,j-1))/(z(j)-z(j-1)))/((1-
n_past(i,j))*ro_s);
    end

    %7) right r=re   corr
    i=Nr;
    for j=2:Nz-1
        z1_mid=(z(j)+z(j-1))/2;
        z2_mid=(z(j)+z(j+1))/2;
        vr(i,j)=0; %no flow B/sealed

        vz(i,j)=vz_past(i,j)-
(dt/coef)*((1+coef0*alfa)*(p_past(i,j+1)-p_past(i,j-1))/(z(j+1)-
z(j-1))+n_past(i,j)*muf*(vz_past(i,j)-wz_past(i,j))/kz(i,j)-...
            ro_f*g+coef0*((srz_past(i,j)-srz_past(i-1,j))/(r(i)-
r(i-1))+(srz_past(i,j))/r(i)+...
            (szz_past(i,j+1)-szz_past(i,j-1)+Fdzz_past(i,j+1)-
Fdzz_past(i,j-1))/(z(j+1)-z(j-1))-ro*g+bu(i,j)*(n_past(i,j+1)-
n_past(i,j-1))/(z(j+1)-z(j-1)))-...
            mu*((1/(r(i)-r(i-1)))*((vz_past(i,j)-vz_past(i-
1,j))/(r(i)-r(i-1))-(vz_past(i-1,j)-vz_past(i-2,j))/(r(i-1)-r(i-
2)))+(vz_past(i,j)-vz_past(i-1,j))/(r(i)*(r(i)-r(i-1)))+...
            (1/(z2_mid-z1_mid))*((vz_past(i,j+1)-
vz_past(i,j))/(z(j+1)-z(j))-(vz_past(i,j)-vz_past(i,j-1))/(z(j)-
z(j-1))))-...
            (mu+lamdaf)*((vr_past(i,j+1)-vr_past(i,j-1)-
vr_past(i-1,j+1)+vr_past(i-1,j-1))/((r(i)-r(i-1))*(z(j+1)-z(j-
1)))+(vr_past(i,j+1)-vr_past(i,j-1))/(r(i)*(z(j+1)-z(j-1)))+...
```

```
            (1/(z2_mid-z1_mid))*((vz_past(i,j+1)-
vz_past(i,j))/(z(j+1)-z(j))-(vz_past(i,j)-vz_past(i,j-1))/(z(j)-
z(j-1)))));


        wr(i,j)=wr_past(i,j)-dt*(n_past(i,j)*ro_f*(vr(i,j)-
vr_past(i,j))/dt+...
            (srr_past(i,j)-srr_past(i-1,j)+Fdrr_past(i,j)-
Fdrr_past(i-1,j))/((r(i)-r(i-1)))+...
            (srz_past(i,j+1)-srz_past(i,j-1))/(z(j+1)-z(j-
1))+(srr_past(i,j)+Fdrr_past(i,j)-stt_past(i,j))/r(i)+...
            alfa*(p_past(i,j)-p_past(i-1,j))/(r(i)-r(i-
1))+bu(i,j)*(n_past(i,j)-n_past(i-1,j))/(r(i)-r(i-1)))/((1-
n_past(i,j))*ro_s);
        wz(i,j)=wz_past(i,j)-dt*(n_past(i,j)*ro_f*(vz(i,j)-
vz_past(i,j))/dt+...
            (srz_past(i,j)-srz_past(i-1,j))/(r(i)-r(i-
1))+srz_past(i,j)/r(i)+...
            (szz_past(i,j+1)-szz_past(i,j-1)+Fdzz_past(i,j+1)-
Fdzz_past(i,j-1))/(z(j+1)-z(j-1))+...
            alfa*(p_past(i,j+1)-p_past(i,j-1))/(z(j+1)-z(j-1))-
ro*g+bu(i,j)*(n_past(i,j+1)-n_past(i,j-1))/(z(j+1)-z(j-1)))/((1-
n_past(i,j))*ro_s);
    end


    %8) right bottom corner z=0 r=re    corr
    j=1;
    i=Nr;
    vr(i,j)=0;
    vz(i,j)=0;


    wr(i,j)=wr_past(i,j)-dt*(n_past(i,j)*ro_f*(vr(i,j)-
vr_past(i,j))/dt+...
        (srr_past(i,j)-srr_past(i-1,j)+Fdrr_past(i,j)-
Fdrr_past(i-1,j))/((r(i)-r(i-1)))+...
        (srz_past(i,j+1)-srz_past(i,j))/(z(j+1)-
z(j))+(srr_past(i,j)+Fdrr_past(i,j)-stt_past(i,j))/r(i)+...
        alfa*(p_past(i,j)-p_past(i-1,j))/(r(i)-r(i-
1))+bu(i,j)*(n_past(i,j)-n_past(i-1,j))/(r(i)-r(i-1)))/((1-
n_past(i,j))*ro_s);
    wz(i,j)=0;
    %9) right top corner z=h r=re   corr
    j=Nz;
    i=Nr;
    %BC
    p(i,j)=p_wave+p0(j);
    szz(i,j)=szz_0(j)+(1-alfa)*p_wave;
    vr(i,j)=0;
    vz(i,j)=vz_past(i,j)-(dt/coef)*((1+coef0*alfa)*(p_past(i,j)-
p_past(i,j-1))/(z(j)-z(j-1))+n_past(i,j)*muf*(vz_past(i,j)-
wz_past(i,j))/kz(i,j)-...
        ro_f*g+coef0*((srz_past(i,j)-srz_past(i-1,j))/(r(i)-r(i-
1))+(srz_past(i,j))/r(i)+...
```

```
        (szz_past(i,j)-szz_past(i,j-1)+Fdzz_past(i,j)-
Fdzz_past(i,j-1))/(z(j)-z(j-1))-ro*g+bu(i,j)*(n_past(i,j)-
n_past(i,j-1))/(z(j)-z(j-1)))-...
        mu*((1/(r(i)-r(i-1)))*((vz_past(i,j)-vz_past(i-
1,j))/(r(i)-r(i-1))-(vz_past(i-1,j)-vz_past(i-2,j))/(r(i-1)-r(i-
2)))+(vz_past(i,j)-vz_past(i-1,j))/(r(i)*(r(i)-r(i-1)))+...
        (1/(z(j)-z(j-1)))*((vz_past(i,j)-vz_past(i,j-1))/(z(j)-
z(j-1))-(vz_past(i,j-1)-vz_past(i,j-2))/(z(j-1)-z(j-2))))-...
        (mu+lamdaf)*((vr_past(i,j)-vr_past(i,j-1)-vr_past(i-
1,j)+vr_past(i-1,j-1))/((r(i)-r(i-1))*(z(j)-z(j-
1)))+(vr_past(i,j)-vr_past(i,j-1))/(r(i)*(z(j)-z(j-1)))+...
        (1/(z(j)-z(j-1)))*((vz_past(i,j)-vz_past(i,j-1))/(z(j)-
z(j-1))-(vz_past(i,j-1)-vz_past(i,j-2))/(z(j-1)-z(j-2)))));

    wr(i,j)=wr_past(i,j)-dt*(n_past(i,j)*ro_f*(vr(i,j)-
vr_past(i,j))/dt+...
        (srr_past(i,j)-srr_past(i-1,j)+Fdrr_past(i,j)-
Fdrr_past(i-1,j))/((r(i)-r(i-1)))+...
        (srz_past(i,j)-srz_past(i,j-1))/(z(j)-z(j-
1))+(srr_past(i,j)+Fdrr_past(i,j)-stt_past(i,j))/r(i)+...
        alfa*(p_past(i,j)-p_past(i-1,j))/(r(i)-r(i-
1))+bu(i,j)*(n_past(i,j)-n_past(i-1,j))/(r(i)-r(i-1)))/((1-
n_past(i,j))*ro_s);
    wz(i,j)=wz_past(i,j)-dt*(n_past(i,j)*ro_f*(vz(i,j)-
vz_past(i,j))/dt+...
        (srz_past(i,j)-srz_past(i-1,j))/(r(i)-r(i-
1))+srz_past(i,j)/r(i)+...
        (szz_past(i,j)-szz_past(i,j-1)+Fdzz_past(i,j)-
Fdzz_past(i,j-1))/(z(j)-z(j-1))+...
        alfa*(p_past(i,j)-p_past(i,j-1))/(z(j)-z(j-1))-
ro*g+bu(i,j)*(n_past(i,j)-n_past(i,j-1))/(z(j)-z(j-1)))/((1-
n_past(i,j))*ro_s);

%%%%%%%%%%%%%%%%%%%%%%%%%%%%%%%%%%%%%%%%%%%%%%%%%%%%%%%%%%%%%%%%%%%
%%%%%
    %solving for p,srr,szz,srz,stt
    %1) r=rw    Corr
    i=1;
    for j=2:Nz-1
        r2_mid=(r(i)+r(i+1))/2;

        err=(wr(i+1,j)-wr(i,j))/(r(i+1)-r(i));
        ett=wr(i,j)/r2_mid;
        ezz=(wz(i,j+1)-wz(i,j-1))/(z(j+1)-z(j-1));
        erz=.5*((wz(i+1,j)-wz(i,j))/(r(i+1)-r(i))+(wr(i,j+1)-
wr(i,j-1))/(z(j+1)-z(j-1)));
        vol=err+ett+ezz;
        volf=(vr(i+1,j)-vr(i,j))/(r(i+1)-
r(i))+vr(i,j)/r2_mid+(vz(i,j+1)-vz(i,j-1))/(z(j+1)-z(j-1));
%r(i); ==>r2_mid
        dr=(r(i+1)-r(i))/2;
        dz=(z(j+1)-z(j-1))/2;
        q1=-sign(err)*4*ro*(dr*err)^2;
```

```matlab
        q2=-sign(err)*1*ro*cc*(dr)*abs(err);
        Fdrr(i,j)=q2+q1;
        q1=-sign(ezz)*4*ro*(dz*ezz)^2;
        q2=-sign(ezz)*1*ro*cc*(dz)*abs(ezz);
        Fdzz(i,j)=q2+q1;

        lamda=bu(i,j)-2*sh(i,j)/3;
        Mu=sh(i,j);

        p(i,j)=p_past(i,j)-dt*((alfa-n_past(i,j))*vol+...
            (vr(i,j)-wr(i,j))*(n_past(i+1,j)-
n_past(i,j))/(r(i+1)-r(i))+...
            (vz(i,j)-wz(i,j))*(n_past(i,j+1)-n_past(i,j-
1))/(z(j+1)-z(j-1))+...
            n_past(i,j)*(volf)+n_past(i,j)*cf*((vr(i,j)-
wr(i,j))*(p_past(i+1,j)-p_past(i,j))/(r(i+1)-r(i))+(vz(i,j)-
wz(i,j))*(p_past(i,j+1)-p_past(i,j-1))/(z(j+1)-z(j-1))))/Sp;
        srr(i,j)=srr_past(i,j)-dt*(lamda*(err+ett+ezz)+2*Mu*err);
        szz(i,j)=szz_past(i,j)-dt*(lamda*(err+ett+ezz)+2*Mu*ezz);
        stt(i,j)=stt_past(i,j)-dt*(lamda*(err+ett+ezz)+2*Mu*ett);
        srz(i,j)=srz_past(i,j)-dt*2*Mu*erz;
        n(i,j)=n_past(i,j)+dt*(ds*vol-df*volf);

    end
    %2) left bottom corner z=0 r=rw
    j=1;
    i=1;
    r2_mid=(r(i)+r(i+1))/2;
    err=(wr(i+1,j)-wr(i,j))/(r(i+1)-r(i));
    ett=wr(i,j)/r2_mid;
    ezz=(wz(i,j+1)-wz(i,j))/(z(j+1)-z(j));
    erz=.5*((wz(i+1,j)-wz(i,j))/(r(i+1)-r(i))+(wr(i,j+1)-
wr(i,j))/(z(j+1)-z(j)));
    vol=err+ett+ezz;
    volf=(vr(i+1,j)-vr(i,j))/(r(i+1)-
r(i))+vr(i,j)/r2_mid+(vz(i,j+1)-vz(i,j))/(z(j+1)-z(j));
%r(i);==>r2_mid
    dr=(r(i+1)-r(i))/2;
    dz=(z(j+1)-z(j))/2;

    q1=-sign(err)*4*ro*(dr*err)^2;
    q2=-sign(err)*1*ro*cc*(dr)*abs(err);
    Fdrr(i,j)=q2+q1;
    q1=-sign(ezz)*4*ro*(dz*ezz)^2;
    q2=-sign(ezz)*1*ro*cc*(dz)*abs(ezz);
    Fdzz(i,j)=q2+q1;
    p(i,j)=p_past(i,j)-dt*((alfa-n_past(i,j))*(vol)+...
        (vr(i,j)-wr(i,j))*(n_past(i+1,j)-n_past(i,j))/(r(i+1)-
r(i))+...
        (vz(i,j)-wz(i,j))*(n_past(i,j+1)-n_past(i,j))/(z(j+1)-
z(j))+...
```

```
        n_past(i,j)*(volf)+n_past(i,j)*cf*((vr(i,j)-
wr(i,j))*(p_past(i+1,j)-p_past(i,j))/(r(i+1)-r(i))+(vz(i,j)-
wz(i,j))*(p_past(i,j+1)-p_past(i,j))/(z(j+1)-z(j))))/Sp;


    lamda=bu(i,j)-2*sh(i,j)/3;
    Mu=sh(i,j);
    srr(i,j)=srr_past(i,j)-dt*(lamda*(err+ett+ezz)+2*Mu*err);
    szz(i,j)=szz_past(i,j)-dt*(lamda*(err+ett+ezz)+2*Mu*ezz);
    stt(i,j)=stt_past(i,j)-dt*(lamda*(err+ett+ezz)+2*Mu*ett);
    srz(i,j)=srz_past(i,j)-dt*2*Mu*erz;

    n(i,j)=n_past(i,j)+dt*(ds*vol-df*volf);

    %3) left top corner z=h r=rw    Corr
    j=Nz;
    i=1;
    r2_mid=(r(i)+r(i+1))/2;
    err=(wr(i+1,j)-wr(i,j))/(r(i+1)-r(i));
    ett=wr(i,j)/r2_mid;
    ezz=(wz(i,j)-wz(i,j-1))/(z(j)-z(j-1));
    erz=.5*((wz(i+1,j)-wz(i,j))/(r(i+1)-r(i))+(wr(i,j)-wr(i,j-
1))/(z(j)-z(j-1)));
    vol=err+ett+ezz;
    volf=(vr(i+1,j)-vr(i,j))/(r(i+1)-
r(i))+vr(i,j)/r2_mid+(vz(i,j)-vz(i,j-1))/(z(j)-z(j-1));
%r(i);==r2_mid
    dr=(r(i+1)-r(i))/2;
    dz=(z(j)-z(j-1))/2;

    q1=-sign(err)*4*ro*(dr*err)^2;
    q2=-sign(err)*1*ro*cc*(dr)*abs(err);
    Fdrr(i,j)=q2+q1;
    q1=-sign(ezz)*4*ro*(dz*ezz)^2;
    q2=-sign(ezz)*1*ro*cc*(dz)*abs(ezz);
    Fdzz(i,j)=q2+q1;
    p(i,j)=p_wave+p0(j);
    lamda=bu(i,j)-2*sh(i,j)/3;
    Mu=sh(i,j);
    srr(i,j)=srr_past(i,j)-dt*(lamda*(err+ett+ezz)+2*Mu*err);
    szz(i,j)=szz_0(j)+(1-alfa)*p_wave;
    stt(i,j)=stt_past(i,j)-dt*(lamda*(err+ett+ezz)+2*Mu*ett);
    srz(i,j)=srz_past(i,j)-dt*2*Mu*erz;
    n(i,j)=n_past(i,j)+dt*(ds*vol-df*volf);
    %4) middle points
    for i=2:Nr-1
        for j=2:Nz-1
            err=(wr(i+1,j)-wr(i-1,j))/(r(i+1)-r(i-1));
            ett=wr(i,j)/r(i);
            ezz=(wz(i,j+1)-wz(i,j-1))/(z(j+1)-z(j-1));
            erz=.5*((wz(i+1,j)-wz(i-1,j))/(r(i+1)-r(i-
1))+(wr(i,j+1)-wr(i,j-1))/(z(j+1)-z(j-1)));
            vol=err+ett+ezz;
```

```
            volf=(vr(i+1,j)-vr(i-1,j))/(r(i+1)-r(i-
1))+vr(i,j)/r(i)+(vz(i,j+1)-vz(i,j-1))/(z(j+1)-z(j-1));
            dr=(r(i+1)-r(i-1))/2;
            dz=(z(j+1)-z(j-1))/2;

            q1=-sign(err)*4*ro*(dr*err)^2;
            q2=-sign(err)*1*ro*cc*(dr)*abs(err);
            Fdrr(i,j)=q2+q1;
            q1=-sign(ezz)*4*ro*(dz*ezz)^2;
            q2=-sign(ezz)*1*ro*cc*(dz)*abs(ezz);
            Fdzz(i,j)=q2+q1;
            p(i,j)=p_past(i,j)-dt*((alfa-n_past(i,j))*(vol)+...
                (vr(i,j)-wr(i,j))*(n_past(i+1,j)-n_past(i-
1,j))/(r(i+1)-r(i-1))+...
                (vz(i,j)-wz(i,j))*(n_past(i,j+1)-n_past(i,j-
1))/(z(j+1)-z(j-1))+...
                n_past(i,j)*(volf)+n_past(i,j)*cf*((vr(i,j)-
wr(i,j))*(p_past(i+1,j)-p_past(i-1,j))/(r(i+1)-r(i-1))+(vz(i,j)-
wz(i,j))*(p_past(i,j+1)-p_past(i,j-1))/(z(j+1)-z(j-1))))/Sp;

            lamda=bu(i,j)-2*sh(i,j)/3;
            Mu=sh(i,j);
            srr(i,j)=srr_past(i,j)-
dt*(lamda*(err+ett+ezz)+2*Mu*err);
            szz(i,j)=szz_past(i,j)-
dt*(lamda*(err+ett+ezz)+2*Mu*ezz);
            stt(i,j)=stt_past(i,j)-
dt*(lamda*(err+ett+ezz)+2*Mu*ett);
            srz(i,j)=srz_past(i,j)-dt*2*Mu*erz;
            n(i,j)=n_past(i,j)+dt*(ds*vol-df*volf);
        end
    end
    %5) z=0
    j=1;
    for i=2:Nr-1
        err=(wr(i+1,j)-wr(i-1,j))/(r(i+1)-r(i-1));
        ett=wr(i,j)/r(i);
        ezz=(wz(i,j+1)-wz(i,j))/(z(j+1)-z(j));
        erz=.5*((wz(i+1,j)-wz(i-1,j))/(r(i+1)-r(i-1))+(wr(i,j+1)-
wr(i,j))/(z(j+1)-z(j)));
        vol=err+ett+ezz;
        volf=(vr(i+1,j)-vr(i-1,j))/(r(i+1)-r(i-
1))+vr(i,j)/r(i)+(vz(i,j+1)-vz(i,j))/(z(j+1)-z(j));
        dr=(r(i+1)-r(i-1))/2;
        dz=(z(j+1)-z(j))/2;

        q1=-sign(err)*4*ro*(dr*err)^2;
        q2=-sign(err)*1*ro*cc*(dr)*abs(err);
        Fdrr(i,j)=q2+q1;
        q1=-sign(ezz)*4*ro*(dz*ezz)^2;
        q2=-sign(ezz)*1*ro*cc*(dz)*abs(ezz);
        Fdzz(i,j)=q2+q1;
        p(i,j)=p_past(i,j)-dt*((alfa-n_past(i,j))*(vol)+...
```

```matlab
                (vr(i,j)-wr(i,j))*(n_past(i+1,j)-n_past(i-
1,j))/(r(i+1)-r(i-1))+...
                (vz(i,j)-wz(i,j))*(n_past(i,j+1)-
n_past(i,j))/(z(j+1)-z(j))+...
                n_past(i,j)*(volf)+n_past(i,j)*cf*((vr(i,j)-
wr(i,j))*(p_past(i+1,j)-p_past(i-1,j))/(r(i+1)-r(i-1))+(vz(i,j)-
wz(i,j))*(p_past(i,j+1)-p_past(i,j))/(z(j+1)-z(j))))/Sp;

        lamda=bu(i,j)-2*sh(i,j)/3;
        Mu=sh(i,j);
        srr(i,j)=srr_past(i,j)-dt*(lamda*(err+ett+ezz)+2*Mu*err);
        szz(i,j)=szz_past(i,j)-dt*(lamda*(err+ett+ezz)+2*Mu*ezz);
        stt(i,j)=stt_past(i,j)-dt*(lamda*(err+ett+ezz)+2*Mu*ett);
        srz(i,j)=srz_past(i,j)-dt*2*Mu*erz;
        n(i,j)=n_past(i,j)+dt*(ds*vol-df*volf);
    end
    %6) z=h
    j=Nz;
    for i=2:Nr-1
        err=(wr(i+1,j)-wr(i-1,j))/(r(i+1)-r(i-1));
        ett=wr(i,j)/r(i);
        ezz=(wz(i,j)-wz(i,j-1))/(z(j)-z(j-1));
        erz=.5*((wz(i+1,j)-wz(i-1,j))/(r(i+1)-r(i-1))+(wr(i,j)-
wr(i,j-1))/(z(j)-z(j-1)));
        vol=err+ett+ezz;
        dr=(r(i+1)-r(i-1))/2;
        dz=(z(j)-z(j-1))/2;

        q1=-sign(err)*4*ro*(dr*err)^2;
        q2=-sign(err)*1*ro*cc*(dr)*abs(err);
        Fdrr(i,j)=q2+q1;
        q1=-sign(ezz)*4*ro*(dz*ezz)^2;
        q2=-sign(ezz)*1*ro*cc*(dz)*abs(ezz);
        Fdzz(i,j)=q2+q1;

        p(i,j)=p_wave+p0(j);
        lamda=bu(i,j)-2*sh(i,j)/3;
        Mu=sh(i,j);
        srr(i,j)=srr_past(i,j)-dt*(lamda*(err+ett+ezz)+2*Mu*err);
        szz(i,j)=szz_0(j)+(1-alfa)*p_wave;
        stt(i,j)=stt_past(i,j)-dt*(lamda*(err+ett+ezz)+2*Mu*ett);
        srz(i,j)=srz_past(i,j)-dt*2*Mu*erz;
        volf=(vr(i+1,j)-vr(i-1,j))/(r(i+1)-r(i-
1))+vr(i,j)/r(i)+(vz(i,j)-vz(i,j-1))/(z(j)-z(j-1));
        n(i,j)=n_past(i,j)+dt*(ds*vol-df*volf);
    end
    %7) r=re
    i=Nr;
    for j=2:Nz-1
        err=(wr(i,j)-wr(i-1,j))/(r(i)-r(i-1));
        ett=wr(i,j)/r(i);
        ezz=(wz(i,j+1)-wz(i,j-1))/(z(j+1)-z(j-1));
```

```matlab
        erz=.5*((wz(i,j)-wz(i-1,j))/(r(i)-r(i-1))+(wr(i,j+1)-
wr(i,j-1))/(z(j+1)-z(j-1)));
        vol=err+ett+ezz;
        volf=(vr(i,j)-vr(i-1,j))/(r(i)-r(i-
1))+vr(i,j)/r(i)+(vz(i,j+1)-vz(i,j-1))/(z(j+1)-z(j-1));
        dr=(r(i)-r(i-1))/2;
        dz=(z(j+1)-z(j-1))/2;

        q1=-sign(err)*4*ro*(dr*err)^2;
        q2=-sign(err)*1*ro*cc*(dr)*abs(err);
        Fdrr(i,j)=q2+q1;
        q1=-sign(ezz)*4*ro*(dz*ezz)^2;
        q2=-sign(ezz)*1*ro*cc*(dz)*abs(ezz);
        Fdzz(i,j)=q2+q1;

        p(i,j)=p_past(i,j)-dt*((alfa-n_past(i,j))*(vol)+...
            (vr(i,j)-wr(i,j))*(n_past(i,j)-n_past(i-1,j))/(r(i)-
r(i-1))+...
            (vz(i,j)-wz(i,j))*(n_past(i,j+1)-n_past(i,j-
1))/(z(j+1)-z(j-1))+...
            n_past(i,j)*(volf)+n_past(i,j)*cf*((vr(i,j)-
wr(i,j))*(p_past(i,j)-p_past(i-1,j))/(r(i)-r(i-1))+(vz(i,j)-
wz(i,j))*(p_past(i,j+1)-p_past(i,j-1))/(z(j+1)-z(j-1))))/Sp;

        lamda=bu(i,j)-2*sh(i,j)/3;
        Mu=sh(i,j);
        srr(i,j)=srr_past(i,j)-dt*(lamda*(err+ett+ezz)+2*Mu*err);
        szz(i,j)=szz_past(i,j)-dt*(lamda*(err+ett+ezz)+2*Mu*ezz);
        stt(i,j)=stt_past(i,j)-dt*(lamda*(err+ett+ezz)+2*Mu*ett);
        srz(i,j)=srz_past(i,j)-dt*2*Mu*erz;
        n(i,j)=n_past(i,j)+dt*(ds*vol-df*volf);

    end
    %8) right bottom corner z=0 r=re
    j=1;
    i=Nr;
    err=(wr(i,j)-wr(i-1,j))/(r(i)-r(i-1));
    ett=wr(i,j)/r(i);
    ezz=(wz(i,j+1)-wz(i,j))/(z(j+1)-z(j));
    erz=.5*((wz(i,j)-wz(i-1,j))/(r(i)-r(i-1))+(wr(i,j+1)-
wr(i,j))/(z(j+1)-z(j)));
    vol=err+ett+ezz;
    volf=(vr(i,j)-vr(i-1,j))/(r(i)-r(i-
1))+vr(i,j)/r(i)+(vz(i,j+1)-vz(i,j))/(z(j+1)-z(j));
    dr=(r(i)-r(i-1))/2;
    dz=(z(j+1)-z(j))/2;

    q1=-sign(err)*4*ro*(dr*err)^2;
    q2=-sign(err)*1*ro*cc*(dr)*abs(err);
    Fdrr(i,j)=q2+q1;
    q1=-sign(ezz)*4*ro*(dz*ezz)^2;
    q2=-sign(ezz)*1*ro*cc*(dz)*abs(ezz);
    Fdzz(i,j)=q2+q1;
```

```matlab
    p(i,j)=p_past(i,j)-dt*((alfa-n_past(i,j))*(vol)+...
        (vr(i,j)-wr(i,j))*(n_past(i,j)-n_past(i-1,j))/(r(i)-r(i-
1))+...
        (vz(i,j)-wz(i,j))*(n_past(i,j+1)-n_past(i,j))/(z(j+1)-
z(j))+...
        n_past(i,j)*(volf)+n_past(i,j)*cf*((vr(i,j)-
wr(i,j))*(p_past(i,j)-p_past(i-1,j))/(r(i)-r(i-1))+(vz(i,j)-
wz(i,j))*(p_past(i,j+1)-p_past(i,j))/(z(j+1)-z(j)))))/Sp;
    lamda=bu(i,j)-2*sh(i,j)/3;
    Mu=sh(i,j);
    srr(i,j)=srr_past(i,j)-dt*(lamda*(err+ett+ezz)+2*Mu*err);
    szz(i,j)=szz_past(i,j)-dt*(lamda*(err+ett+ezz)+2*Mu*ezz);
    stt(i,j)=stt_past(i,j)-dt*(lamda*(err+ett+ezz)+2*Mu*ett);
    srz(i,j)=srz_past(i,j)-dt*2*Mu*erz;
    n(i,j)=n_past(i,j)+dt*(ds*vol-df*volf);

    %9) right top corner z=h r=re
    j=Nz;
    i=Nr;
    err=(wr(i,j)-wr(i-1,j))/(r(i)-r(i-1));
    ett=wr(i,j)/r(i);
    ezz=(wz(i,j)-wz(i,j-1))/(z(j)-z(j-1));
    erz=.5*((wz(i,j)-wz(i-1,j))/(r(i)-r(i-1))+(wr(i,j)-wr(i,j-
1))/(z(j)-z(j-1)));
    vol=err+ett+ezz;
    volf=(vr(i,j)-vr(i-1,j))/(r(i)-r(i-1))+vr(i,j)/r(i)+(vz(i,j)-
vz(i,j-1))/(z(j)-z(j-1));

    dr=(r(i)-r(i-1))/2;
    dz=(z(j)-z(j-1))/2;

    q1=-sign(err)*4*ro*(dr*err)^2;
    q2=-sign(err)*1*ro*cc*(dr)*abs(err);
    Fdrr(i,j)=q2+q1;
    q1=-sign(ezz)*4*ro*(dz*ezz)^2;
    q2=-sign(ezz)*1*ro*cc*(dz)*abs(ezz);
    Fdzz(i,j)=q2+q1;

    %BC
    p(i,j)=p_wave+p0(j);
    lamda=bu(i,j)-2*sh(i,j)/3;
    Mu=sh(i,j);
    srr(i,j)=srr_past(i,j)-dt*(lamda*(err+ett+ezz)+2*Mu*err);
    szz(i,j)=szz_0(j)+(1-alfa)*p_wave;
    stt(i,j)=stt_past(i,j)-dt*(lamda*(err+ett+ezz)+2*Mu*ett);
    srz(i,j)=srz_past(i,j)-dt*2*Mu*erz;
    n(i,j)=n_past(i,j)+dt*(ds*vol-df*volf);

    time=time+dt;
    jj2=jj2+1;
    t(jj2)=time;
    f1(jj2)=p(Nr_mid,Ip1+1)-p0(Ip1+1);
    f2(jj2)=p(Nr_mid,Ip2+1)-p0(Ip2+1);
```

184

```matlab
        ezz1(jj2)=ezz1(jj2-1)+dt*(wz(Nr,Ip1+2)-wz(Nr,Ip1))/(z(Ip1+1)-
z(Ip1-1));
        ezz2(jj2)=ezz2(jj2-1)+dt*(wz(Nr,Ip2+2)-wz(Nr,Ip2))/(z(Ip2+1)-
z(Ip2-1));
        fvz(jj2)=vz(Nr_mid,Ip1+1);
        fvr(jj2)=vr(Nr_mid,Ip1+1);
        fwz(jj2)=wz(Nr_mid,Ip1+1);
        fwr(jj2)=wr(Nr_mid,Ip1+1);
        favz(jj2)=(vz(Nr_mid,Ip1+1)-vz_past(Nr_mid,Ip1+1))/(dt);
        fawz(jj2)=(wz(Nr_mid,Ip1+1)-wz_past(Nr_mid,Ip1+1))/(dt);
        favr(jj2)=(vr(Nr_mid,Ip1+1)-vr_past(Nr_mid,Ip1+1))/(dt);
        fawr(jj2)=(wr(Nr_mid,Ip1+1)-wr_past(Nr_mid,Ip1+1))/(dt);
        fvz2(jj2)=vz(Nr_mid,Ip2+1);
        fvr2(jj2)=vr(Nr_mid,Ip2+1);
        fwz2(jj2)=wz(Nr_mid,Ip2+1);
        fwr2(jj2)=wr(Nr_mid,Ip2+1);
        favz2(jj2)=(vz(Nr_mid,Ip2+1)-vz_past(Nr_mid,Ip2+1))/(dt);
        fawz2(jj2)=(wz(Nr_mid,Ip2+1)-wz_past(Nr_mid,Ip2+1))/(dt);
        favr2(jj2)=(vr(Nr_mid,Ip2+1)-vr_past(Nr_mid,Ip2+1))/(dt);
        fawr2(jj2)=(wr(Nr_mid,Ip2+1)-wr_past(Nr_mid,Ip2+1))/(dt);
        fporo(jj2)=(n(Nr_mid,Ip2+1)-n0)/n0;
        %giving current values as the past ones
        p_past=p;
        vr_past=vr;
        vz_past=vz;
        wr_past=wr;
        wz_past=wz;
        ur=ur+wr.*dt;
        uz=uz+wz.*dt;
        n_past=n;
        srr_past=srr;
        szz_past=szz;
        stt_past=stt;
        srz_past=srz;

        Fdrr_past=Fdrr;
        Fdzz_past=Fdzz;

        jj=jj+1;
end
```

Appendix B: Sequential-Coupled Dynamic Code Developed

B.1 FLAC Code

```
new
set pl jpg
set overwrite on
config gwflow dy axi ex 5;
 grid 100,30
set grav 10 ;positive means downward
set dy_damp avisc 1 1   ;Artificial viscosity damping
set dy off flow on

def para
 Nr=igp
 Nz=jgp
 Nz_1=Nz-1
 N=Nz*Nr
 N_stres=(Nr-1)*(Nz-1)
 z_length=0.3000
 r_length=1.0000
 well_rad=.09525  ;dia=7.5"
 _dr=r_length/(Nr-1)
 _dz=z_length/(Nz-1)

 r_length2=r_length+well_rad
 Nz_mid=int(Nz/2)
 perf1=Nz_mid
 perf1_2=perf1+1
 perf2=Nz_mid+2

 _nhis1=2;int(0.2000/_dr)  ;history points indices
 _nhis2=5;int(1.0000/_dr)
 _nhis3=10;int(5.0000/_dr)

 pA=8000000.00             ;applied wave bc
 _freq=17.0000             ;applied wave bc frequency

  _k0=9.867e-10  ;k=1000mD
 n0=0.22

 ro_f=1000
 ro_s=2650
 ro=ro_f*n0+(1-n0)*ro_s
 _g=10 ;gravity
 counter5=0  ;for saving
 alfa=0.999606973
```

```
end
para

gen well_rad,0 well_rad,z_length r_length2,z_length, r_length2,0

;Constitutive model
call Sand_fin_ten.txt
;call sand_santarelli.txt

;total density=2287; dry density must be given
prop den 2067 ;bu 2.1836e8 sh 1.31e8
nu=.2857
prop por n0 perm _k0
water bu 2.0e9 den 1000

set biot on
prop biot_c alfa ;1.0

fix y j 1 ;fixed @ bottom
fix x i Nr ;fixed @ right

def _variation
 _p0=27.8e6
 _sy0=-50.5e6
 _sx0=-39.4e6
 _sx50m=-40.15e6  ;srr at 1m when a 50m model is run
 _p50m=29.07e6    ;gpp at 1m when a 50m model is run
 _pinj=-1*_sx0
 p_var=-ro_f*_g*(y(1,Nz)-y(1,1))
 sy_var=ro*_g*(y(1,Nz)-y(1,1))
 p_bot=ro_f*_g*z_length+_p50m
 sy_bot=-ro*_g*(y(1,Nz)-y(1,1))+_sy0
 _sxx_ini=-1*p_bot
 syy_ap=-1*_sy0
 sxx_ap=-1*_sx50m
 sxx_var=-1*p_var
end
_variation

ini sat 1
ini pp p_bot var 0 p_var
ini syy sy_bot var 0 sy_var
ini sxx _sx50m var 0 sxx_var
ini szz _sx50m var 0 sxx_var

;Top Boundary
fix y j Nz

;Right Boundary
fix pp i Nr
fix x i Nr ;fixed @ right

;Left Boundary
```

```
app pp p_bot var 0 p_var i 1
app press sxx_ap var 0 p_var i 1



def abc
ii=0
 array ww_r(N) ww_z(N) ww_r_ini(N) ww_z_ini(N) acc_r(N) acc_z(N)
_zer(N)
 array vv_z_ini(N) vv_r_ini(N) _poro(N_stres)
 array _Ev(N) _Ev_str(N) x_coor(Nr) y_coor(Nz)
 array ww_r_str(N) ww_z_str(N)
 array _ppp(N) _pp_no(Nr,Nz) pp_str(N) _aaa(8) del_n(N)
 array flacend1(1)  ;to know when the flac file finishes running
 array p_ini(N) p0(Nz) p00(Nz_1) _aaa2(Nz) p_star_1D(N)
 array sxx_ini(N_stres) syy_ini(N_stres)
 array szz_ini(N_stres) sxy_ini(N_stres)
loop ii (1,N_stres)
 sxx_ini(ii)='0.00'
 syy_ini(ii)='0.00'
 szz_ini(ii)='0.00'
 sxy_ini(ii)='0.00'
end_loop
counter=0
end
abc

def p_res  ;BC pressure will be added to this
loop jj(1,Nz-1)
 j2=jj+1
 p0(jj)=gpp(1,jj)
 p00(jj)=(gpp(1,jj)+gpp(1,j2))/2
end_loop
p0(Nz)=gpp(1,Nz)
end
p_res

set sratio 1e-3
solve            ;before applying the dynamic load there should
be equilibrium

;must read pp as an input for flac
;;;;;;;;;;;;;;;;;;;;;;;;;;;;;;;;;;;;;;;;;;;;;;;;;;
def _input2D

status=open('_pp.txt',0,1)
status=read(_ppp,N)
status=close

status=open('por.txt',0,1)
status=read(del_n,N_stres)
status=close

status=open('wr_co.txt',0,1)
```

```
status=read(ww_r,N)
status=close

status=open('wz_co.txt',0,1)
status=read(ww_z,N)
status=close

loop ii (1,Nr)
 loop jj (1,Nz)
   NN=(jj-1)*Nr+ii

  aa_r=parse(ww_r(NN),1)
  aa_z=parse(ww_z(NN),1)

 xvel(ii,jj)=xvel(ii,jj)+aa_r
 yvel(ii,jj)=yvel(ii,jj)+aa_z

 xdisp(ii,jj)=xdisp(ii,jj)+aa_r*dydt
 ydisp(ii,jj)=ydisp(ii,jj)+aa_z*dydt

  _pp_no(ii,jj)=parse(_ppp(NN),1)
  gpp(ii,jj)=_pp_no(ii,jj)

 end_loop
end_loop
end
;;;;;;;;;;;;;;;;;;;;;;;;;;;;;;;;;;;;;;;;;;;;;;;;;;;;;
;must write  Ev, wr, wz & stresses as an output for input to
matlab
;;;;;;;;;;;;;;;;;;;;;;;;;;;;;;;;;;;;;;;;;;;;;;;;;;;;;
def _output
loop ii (1,Nr)
 loop jj (1,Nz)
  bbb=xvel(ii,jj)
  ccc=yvel(ii,jj)
  if abs(bbb)<1e-20 then
   bbb=0.00
  end_if
  if abs(ccc)<1e-20 then
   ccc=0.00
  end_if

  NN=(jj-1)*Nr+ii
  ww_r_str(NN)=string(bbb)  ;xvel

  ww_z_str(NN)=string(ccc)  ;yvel
end_loop
end_loop

status=open('_wr.txt',1,1)
status=write(ww_r_str,N)  ;N=igp
status=close

status=open('_wz.txt',1,1)
```

```
status=write(ww_z_str,N)   ;N=igp
status=close




end
;;;;;;;;;;;;;;;;;;;;;;;;;;;;;;;;;;;;;;;;;;
def endflac
flacend1(1)=string(1)
status=open('Z_End.txt',1,1)
status=write(flacend1,1)
status=close
end
;;;;;;;;;;;;;;;;;;;;;;;;;;;;;;;;;;;;;;;;;;

def casing ;
command
  app rem i 1 j 1,perf1
  app rem i 1 j perf2, Nz
  ;;free x i 1
  fix x i 1 j 1,perf1
  fix x i 1 j perf2,Nz
end_command

loop jjj(perf1,perf2-1)
 _aa2=p00(jjj)  ;initial pp
 j2=jjj+1
 command
  app pp _aa2 i 1 j jjj,j2
  app press _aa2 i 1 j jjj,j2
 end_command
end_loop
end

casing

set sratio 5e-4  ;must be in equilibrium before dynamics starts;
solve

def injection
 command
  app pp _pinj i 1 j perf1,perf2
  app press _pinj i 1 j perf1,perf2
  set sratio 1e-4  ;must be in equilibrium before dynamics
  solve
 set ste 1000000 sratio 1e-20
 solve age 3
 end_command
end
injection

save b4_dynamic.sav
```

```
set flow off
water bu 2e9
set dyn on

app nq i Nr
app sq i Nr

p_res

def p_wave
  p_wave0=pA*sin(2*pi*_freq*dytime)
  p_var2=-ro_f*_g*(y(1,perf2)-y(1,perf1));
_pperf1= pinitial1+p_wave0
_pperf2= pinitial2+p_wave0
command
 app pp _pperf1 i 1 j perf1,perf1_2
 app pp _pperf2 i 1 j perf1_2,perf2
 app pres _pperf1 i 1 j perf1,perf1_2
 app pres _pperf2 i 1 j perf1_2,perf2
end_command

end

p_wave

set dy_dam combined .8
set dy_damp avisc 1 1   ;Artificial viscosity damping
ini xdisp 0
ini ydisp 0


def _dt1     ;writes dt Nx Nz & coordinates to text
_aa=1.0e-6; 3.4e-7
_aaa(1)=string(_aa)
_aaa(2)=string(Nr)
_aaa(3)=string(Nz)
_aaa(4)=string(well_rad)
_aaa(5)=string(perf1)
_aaa(6)=string(perf2)
_aaa(7)=string(pinitial1)
_aaa(8)=string(_p50m)
_aaa(p)=string(pA)

status=open('dt.txt',1,1)      ;write dt Nr & Nz
status=write(_aaa,8)
status=close
end
_dt1
;;;;;;;;;;;;;;;;;;;;;;;;;;;;;;;;;;;;;;;;;;;;;;;;;;;;
set dydt _aa
save cont.sav
;;;;;;;;;;;;;;;;;;;;;;;;;;;;;;;;;;;;;;;;;;;;;;;;;;;;;
call Qratio.fis
set flow on  ;so that xflow & yflow r nonzero
```

```
def _dt2
loop ii (1,Nr)
 x_coor(ii)=string(x(ii,1))
end_loop
loop jj (1,Nz)
 y_coor(jj)=string(y(Nr,jj))
end_loop

status=open('r.txt',1,1)      ;write x coordinates
status=write(x_coor,Nr)
status=close

status=open('z.txt',1,1)      ;write y coordinates
status=write(y_coor,Nz)
status=close

loop ii (1,Nr)
 loop jj (1,Nz)
  NN=(jj-1)*Nr+ii
  p_ini(NN)=gpp(ii,jj)  ;not string to export accurately

  ww_r_ini(NN)=string(xvel(ii,jj))
  ww_z_ini(NN)=string(yvel(ii,jj))
  _zer(NN)=string(0.0000)
  p_star_1D(NN)=string(gpp(ii,jj))
 end_loop
end_loop


loop ii (1,Nr-1)
 loop jj (1,Nz-1)
   NN=(jj-1)*(Nr-1)+ii
   sxx_ini(NN)=string(sxx(ii,jj))   ;not string to export
accurately
   syy_ini(NN)=string(syy(ii,jj))   ;not string to export
accurately
   szz_ini(NN)=string(szz(ii,jj))   ;not string to export
accurately
   sxy_ini(NN)=string(sxy(ii,jj))   ;not string to export
accurately

   vv_z_ini(NN)=string(yflow(ii,jj))
   vv_r_ini(NN)=string(xflow(ii,jj))
   _poro(NN)=string(n0)
 end_loop
end_loop

loop iji(1,N)
 last='0'
 nn=1;
 no=int(p_ini(iji))
 no2=int((p_ini(iji)-no)*10000)  ;kepping 4 decimal points
```

```
 loop while no-10.0^nn>0
   nn=nn+1;
 end_loop
 loop ii (1,nn)
   _ii=nn-ii
   aa=int(no/10.0^_ii);
   no=no-aa*10.0^_ii;
   last=last+string(aa);
 end_loop
 last=last+'.'+string(no2)
 p_ini(iji)=last
end_loop

status=open('p_ini.txt',1,1)          ;write initial p
status=write(p_ini,N)
status=close

status=open('sxx_ini.txt',1,1)   ;write initial sxx
status=write(sxx_ini,N_stres)
status=close

status=open('syy_ini.txt',1,1)   ;write initial syy
status=write(syy_ini,N_stres)
status=close

status=open('szz_ini.txt',1,1)   ;write initial szz
status=write(szz_ini,N_stres)
status=close

status=open('sxy_ini.txt',1,1)   ;write initial sxy
status=write(sxy_ini,N_stres)
status=close

status=open('wz_ini.txt',1,1)   ;write initial sxy
status=write(ww_z_ini,N)
status=close

status=open('wr_ini.txt',1,1)   ;write initial sxy
status=write(ww_r_ini,N)
status=close

status=open('vz_ini.txt',1,1)   ;write initial sxy
status=write(vv_z_ini,N_stres)
status=close

status=open('vr_ini.txt',1,1)   ;write initial sxy
status=write(vv_r_ini,N_stres)
status=close

; These are for the first time step so that input runs but
doesn't change anything

status=open('_pp.txt',1,1)     ;write initial p
status=write(p_ini,N)
```

```
status=close

status=open('wr_co.txt',1,1)        ;write initial p
status=write(_zer,N)
status=close

status=open('wz_co.txt',1,1)        ;write initial p
status=write(_zer,N)
status=close

status=open('por.txt',1,1)     ;write initial p
status=write(_poro,N_stres)
status=close

status=open('p_star.txt',1,1)       ;write initial p
status=write(p_star_1D,N)
status=close
end
_dt2
```

B.2 MATLAB Code

```
clear
clc
Time2Run=0.085;
z_length=.3;
r_length=1.0000;
fid = fopen('dt.txt');
ttt=textscan(fid,'%f');
fclose(fid);
parameters=ttt{1};
dt=parameters(1);
Nr=parameters(2); %i index
Nz=parameters(3); %j index
well_rad=parameters(4);   %Well radius
perf1=parameters(5);   %perforation bottom j
perf2=parameters(6);   %perforation top j
p0_original=parameters(7); %In Flac this is pressure before
dynamics
P_res=parameters(8);    %for right-hand boundary
pA=parameters(9);   %WH amplitude

clear parameters
N=Nz*Nr;
N_stres=(Nz-1)*(Nr-1);
Nr_mid=floor(Nr/2);
Nz_mid=floor(Nz/2);
%Fluid properties
ro_f=1000; %kg/m3
mu=1*.001; %cp to kg/(m.Sec) water viscosity
muf=mu;
```

```matlab
lamdaf=-2*muf/3;
ro_s=2650;
k0=9.867e-10*mu; %1D
kr=k0*ones(Nr,Nz);
kz=k0*ones(Nr,Nz);
n0=0.22; %initial porosity
n=n0*ones(Nr,Nz);
tow=0; %Tortuosity
g=-10;
bu=ones(Nr,Nz)*2.1836e8;
sh=ones(Nr,Nz)*1.31e8;
nu=(3*bu(1,1)-2*sh(1,1))/(2*(3*bu(1,1)+sh(1,1)));
mv=1/(bu(1,1)+4*sh(1,1)/3); %2e-10
cf=.0005*1e-6; %m2/MN fluid compressibility to 1/Pa
cm=mv;
ro=ro_f*n0+(1-n0)*ro_s;
cs=1e-12; %1/(4e9); %1/Pa
alfa=1-cs/cm; %Biot Coeff
Sp=n0*cf+(alfa-n0)*cs;
cc1=sqrt(1/(ro*mv)+alfa^2/(ro*(Sp)));
cc2=sqrt((1-alfa+Sp/mv)*n0/(Sp*ro_f*(alfa-
n0+tow+(1+tow)*Sp/mv)));
ds=cf*n0*(1-n0)/(n0*cf+(1-n0)*cs);
df=cs*n0*(1-n0)/(n0*cf+(1-n0)*cs);

cc=sqrt(1/(ro*mv));  %p_wave speed
% wave properties
freq=17;%frequency 1/s
period=1/freq; %sec
%mesh properties
fid = fopen('r.txt');
www=textscan(fid,'%f');
fclose(fid);
r=www{1};
clear www
fid = fopen('z.txt');
www=textscan(fid,'%f');
fclose(fid);
z=www{1};
clear www

ratio=1;
sum=0;
for i=1:Nr-1
    sum=sum+ratio^(i-1);
end
r(1)=well_rad;
r(2)=r(1)+(r_length/sum);

for i=3:Nr-1
    r(i)=r(i-1)+(r(i-1)-r(i-2))*ratio;
end
rw=r(1);
```

195

```matlab
r(Nr)=r_length+rw;
re=r(Nr);

dr=r(2)-r(1);
dz=z(2)-z(1);

drmin=min(dr,dz);

%Defining matrices
wr_past=zeros(Nr,Nz);
wz_past=zeros(Nr,Nz);
wr=wr_past;
wr_1D=zeros(N,1);
wz=wz_past;
wz_1D=zeros(N,1);
p_past=zeros(Nr,Nz);
p=p_past;
p_1D=zeros(N,1);
del_poro=zeros(N_stres,1);
wr_cor=zeros(N,1);
wz_cor=zeros(N,1);
del_wr=zeros(Nr,Nz);
del_wz=zeros(Nr,Nz);
vr=zeros(Nr,Nz);
vz=zeros(Nr,Nz);
vr_past=zeros(Nr,Nz);
vz_past=zeros(Nr,Nz);
n_past=n;
Ev=zeros(Nr,Nz);   %total volumetric strain
srr=0*ones(Nr,Nz);
szz=0*ones(Nr,Nz);
stt=0*ones(Nr,Nz);
srz=0*ones(Nr,Nz);
Fdrr_past=zeros(Nr,Nz);
Fdzz_past=zeros(Nr,Nz);
Fdrr=zeros(Nr,Nz);
Fd=zeros(Nr,Nz);

%initialization
time=0;
jj=0;
h = actxserver('WScript.Shell'); %creates a COM automation server
h.Run('"flac500.exe.lnk"'); %Invokes flac.exe
pause(.08); %Waits for the application to load.
h.AppActivate('"flac500.exe.lnk"'); %Brings notepad to focus
h.SendKeys('re cont.sav~'); %Sends keystrokes
pause(1) %to run the file
h.SendKeys('set echo off~');
h.SendKeys('set message off~');
h.SendKeys('set dy_da avisc 0 0~');
h.SendKeys('set dy_dam combined .8~');
h.SendKeys('set pl jpg~');
h.SendKeys('w well_rad,.2 -.01,.31~');
```

```matlab
h.SendKeys('ca history.txt~');
h.SendKeys('set dydt 1.000E-06~');
counter=0;

fid = fopen('p_ini.txt');
www=textscan(fid,'%f');
fclose(fid);
p_1D=www{1};
clear www

fid = fopen('wr_ini.txt');
www=textscan(fid,'%f');
fclose(fid);
wr_1D=www{1};
clear www

fid = fopen('wz_ini.txt');
www=textscan(fid,'%f');
fclose(fid);
wz_1D=www{1};
clear www

for Num_count=1:N
    i=rem(Num_count,Nr);
    if i==0
        i=Nr;
    end
    j=(Num_count-i)/Nr+1;
    p_past(i,j)=p_1D(Num_count);
    wr_past(i,j)=wr_1D(Num_count);
    wz_past(i,j)=wz_1D(Num_count);
end
p0=zeros(Nr,Nz);
szz_0=zeros(Nr,Nz);

p=p_past;
fid = fopen('sxx_ini.txt');
www=textscan(fid,'%f');
fclose(fid);
srr_1D=-www{1};
clear www
fid = fopen('syy_ini.txt');
www=textscan(fid,'%f');
fclose(fid);
szz_1D=-www{1};
clear www
fid = fopen('sxy_ini.txt');
www=textscan(fid,'%f');
fclose(fid);
srz_1D=-www{1};
clear www
fid = fopen('szz_ini.txt');
www=textscan(fid,'%f');
```

```matlab
fclose(fid);
stt_1D=-www{1};
clear www
fid = fopen('vr_ini.txt');
www=textscan(fid,'%f');
fclose(fid);
vr_1D=www{1};
clear www
fid = fopen('vz_ini.txt');
www=textscan(fid,'%f');
fclose(fid);
vz_1D=www{1};
clear www
srr_flac=zeros(Nr-1,Nz-1);
srz_flac=zeros(Nr-1,Nz-1);
szz_flac=zeros(Nr-1,Nz-1);
stt_flac=zeros(Nr-1,Nz-1);
vr_flac=zeros(Nr-1,Nz-1);
vz_flac=zeros(Nr-1,Nz-1);
for Num_count=1:N_stres  %syy==szz  szz==stt
    i=rem(Num_count,Nr-1);
    if i==0
        i=Nr-1;
    end
    j=(Num_count-i)/(Nr-1)+1;
    srr_flac(i,j)=srr_1D(Num_count);
    srz_flac(i,j)=srz_1D(Num_count);
    szz_flac(i,j)=szz_1D(Num_count);
    stt_flac(i,j)=stt_1D(Num_count);
    vr_flac(i,j)=vr_1D(Num_count);
    vz_flac(i,j)=vz_1D(Num_count);
end
%extropolation

rmid=zeros(Nr-1,1);
for i=1:Nr-1 %coordinate of middle points
    rmid(i)=(r(i)+r(i+1))/2;
end
zmid=zeros(Nz-1,1);
for i=1:Nz-1 %coordinate of middle points
    zmid(i)=(z(i)+z(i+1))/2;
end
[X,Y]=meshgrid(zmid,rmid);
[X1,Y1]=meshgrid(z,r);
%if linera==on the boundaries =NAN
srr_past=griddata(X,Y,srr_flac,X1,Y1,'nearest')-alfa.*p;
szz_past=griddata(X,Y,szz_flac,X1,Y1,'nearest')-alfa.*p;
srz_past=griddata(X,Y,srz_flac,X1,Y1,'nearest');
stt_past=griddata(X,Y,stt_flac,X1,Y1,'nearest')-alfa.*p;

vz_past=griddata(X,Y,vz_flac,X1,Y1,'nearest');
vr_past=griddata(X,Y,vr_flac,X1,Y1,'nearest');
%imposing BCs
```

```
vr_past(1,1:perf1-1)=0;   %no flow behnid casing
vr_past(1,perf2+1:Nz)=0;
vz_past(:,1)=0;
vz_past(:,Nz)=0;

for i=1:Nr
for j=1:Nz
    p0(i,j)=p_past(i,j);
    szz_0(j)=szz_past(i,j);
end
end

%history
nhis1=2;%floor(.2/dr);   %history points indices
nhis2=5;%floor(1/dr);
nhis3=10;%floor(5/dr);
HisSiz=floor(Time2Run/(dt*30));
tt=zeros(HisSiz,1);
pp1=zeros(HisSiz,1);
pp2=zeros(HisSiz,1);
pp3=zeros(HisSiz,1);
bc=zeros(HisSiz,1);
coef=(1+tow*(1+n0*ro_f/(ro_s*(1-n0))))*ro_f;
coef0=tow*ro_f/(ro_s*(1-n0));

vz=vz_past;
vr=vr_past;
p=p_past;
wr=wr_past;
wz=wz_past;
p_star=zeros(Nr,Nz);
p_inter=zeros(Nr,Nz);
volu=zeros(Nr,Nz);
FLACendFileDel ='Z_End.txt';
del_wr1=zeros(Nr,Nz);
del_wz1=zeros(Nr,Nz);
ro_12=0;
while time<Time2Run

    jj=jj+1;

    p_wave=pA*sin(2*pi*freq*time);   %make sure the same is used
in Flac file

    %%%%%%%%%%%1 solving for w and
s%%%%%%%%%%%%%%%%%%%%%%%%%%%%%%%%%%%
    %disp('Running FLAC file')
    delete(FLACendFileDel)  %The command deletes the file left
from the previous solution
    h.AppActivate('"flac500.exe.lnk"'); %Brings notepad to focus
    h.SendKeys('ca run_ex.txt~'); %Sends keystrokes
    %This will run flac for 1 step
```

199

```matlab
    fid=-1;   %-1 means file not found
    % Open text file to see if FLAC is ended
    while fid==-1
        pause(.005)
        fid = fopen(FLACendFileDel);
    end
    fclose('all');
    %extract w & p*
    fid = fopen('_wr.txt');
    www=textscan(fid,'%f');
    fclose(fid);
    wr_1D=www{1};
    clear www

    fid = fopen('_wz.txt');
    www=textscan(fid,'%f');
    fclose(fid);
    wz_1D=www{1};
    clear www

    for i=1:Nr  %changing vector of velocities to matrix of
velocities
        for j=1:Nz
            Num_count=(j-1)*Nr+i;
            wr(i,j)=wr_1D(Num_count);    %reading
            wz(i,j)=wz_1D(Num_count);
        end
    end
%    Calculate p_star
    %1)r=rw
    i=1;
    for j=2:Nz-1

        err=(wr(i+1,j)-wr(i,j))/(r(i+1)-r(i));
        ett=wr(i,j)/r(i);
        ezz=(wz(i,j+1)-wz(i,j-1))/(z(j+1)-z(j-1));
        volu(i,j)=err+ett+ezz;
        dr=(r(i+1)-r(i))/2;
        dz=(z(j+1)-z(j-1))/2;
        LL=sqrt(dr*dz);
        q1=-sign(volu(i,j))*4*ro*(LL*volu(i,j))^2;
        q2=-sign(volu(i,j))*1*ro*cc*(LL)*abs(volu(i,j));
        Fd(i,j)=q2+q1;

    end
    %2)
    j=1;
    i=1;

    err=(wr(i+1,j)-wr(i,j))/(r(i+1)-r(i));
    ett=wr(i,j)/r(i);
    ezz=(wz(i,j+1)-wz(i,j))/(z(j+1)-z(j));
    volu(i,j)=err+ett+ezz;
```

```matlab
dr=(r(i+1)-r(i))/2;
dz=(z(j+1)-z(j))/2;
LL=sqrt(dr*dz);
q1=-sign(volu(i,j))*4*ro*(LL*volu(i,j))^2;
q2=-sign(volu(i,j))*1*ro*cc*(LL)*abs(volu(i,j));
Fd(i,j)=q2+q1;

%3)
j=Nz;
i=1;

err=(wr(i+1,j)-wr(i,j))/(r(i+1)-r(i));
ett=wr(i,j)/r(i);
ezz=(wz(i,j)-wz(i,j-1))/(z(j)-z(j-1));
volu(i,j)=err+ett+ezz;
dr=(r(i+1)-r(i))/2;
dz=(z(j)-z(j-1))/2;
LL=sqrt(dr*dz);
q1=-sign(volu(i,j))*4*ro*(LL*volu(i,j))^2;
q2=-sign(volu(i,j))*1*ro*cc*(LL)*abs(volu(i,j));
Fd(i,j)=q2+q1;

%4)
for i=2:Nr-1
    for j=2:Nz-1   %assuming zero tow
        err=(wr(i+1,j)-wr(i-1,j))/(r(i+1)-r(i-1));
        ett=wr(i,j)/r(i);
        ezz=(wz(i,j+1)-wz(i,j-1))/(z(j+1)-z(j-1));
        volu(i,j)=err+ett+ezz;
        dr=(r(i+1)-r(i-1))/2;
        dz=(z(j+1)-z(j-1))/2;
        LL=sqrt(dr*dz);
        q1=-sign(volu(i,j))*4*ro*(LL*volu(i,j))^2;
        q2=-sign(volu(i,j))*1*ro*cc*(LL)*abs(volu(i,j));
        Fd(i,j)=q2+q1;

    end
end
%5)
j=1;
for i=2:Nr-1
    err=(wr(i+1,j)-wr(i-1,j))/(r(i+1)-r(i-1));
    ett=wr(i,j)/r(i);
    ezz=(wz(i,j+1)-wz(i,j))/(z(j+1)-z(j));
    volu(i,j)=err+ett+ezz;
    dr=(r(i+1)-r(i-1))/2;
    dz=(z(j+1)-z(j))/2;
    LL=sqrt(dr*dz);
    q1=-sign(volu(i,j))*4*ro*(LL*volu(i,j))^2;
    q2=-sign(volu(i,j))*1*ro*cc*(LL)*abs(volu(i,j));
    Fd(i,j)=q2+q1;

end
```

```matlab
%6)
j=Nz;
for i=2:Nr-1
    err=(wr(i+1,j)-wr(i-1,j))/(r(i+1)-r(i-1));
    ett=wr(i,j)/r(i);
    ezz=(wz(i,j)-wz(i,j-1))/(z(j)-z(j-1));
    volu(i,j)=err+ett+ezz;
    dr=(r(i+1)-r(i-1))/2;
    dz=(z(j)-z(j-1))/2;
    LL=sqrt(dr*dz);
    q1=-sign(volu(i,j))*4*ro*(LL*volu(i,j))^2;
    q2=-sign(volu(i,j))*1*ro*cc*(LL)*abs(volu(i,j));
    Fd(i,j)=q2+q1;

end
%7)
i=Nr;
for j=2:Nz-1
    err=(wr(i,j)-wr(i-1,j))/(r(i)-r(i-1));
    ett=wr(i,j)/r(i);
    ezz=(wz(i,j+1)-wz(i,j-1))/(z(j+1)-z(j-1));
    volu(i,j)=err+ett+ezz;
    dr=(r(i)-r(i-1))/2;
    dz=(z(j+1)-z(j-1))/2;
    LL=sqrt(dr*dz);
    q1=-sign(volu(i,j))*4*ro*(LL*volu(i,j))^2;
    q2=-sign(volu(i,j))*1*ro*cc*(LL)*abs(volu(i,j));
    Fd(i,j)=q2+q1;

end
%8)
j=1;
i=Nr;
err=(wr(i,j)-wr(i-1,j))/(r(i)-r(i-1));
ett=wr(i,j)/r(i);
ezz=(wz(i,j+1)-wz(i,j))/(z(j+1)-z(j));
volu(i,j)=err+ett+ezz;
dr=(r(i)-r(i-1))/2;
dz=(z(j+1)-z(j))/2;
LL=sqrt(dr*dz);
q1=-sign(volu(i,j))*4*ro*(LL*volu(i,j))^2;
q2=-sign(volu(i,j))*1*ro*cc*(LL)*abs(volu(i,j));
Fd(i,j)=q2+q1;

%9)
j=Nz;
i=Nr;
err=(wr(i,j)-wr(i-1,j))/(r(i)-r(i-1));
ett=wr(i,j)/r(i);
ezz=(wz(i,j)-wz(i,j-1))/(z(j)-z(j-1));
volu(i,j)=err+ett+ezz;
dr=(r(i)-r(i-1))/2;
dz=(z(j)-z(j-1))/2;
```

```
LL=sqrt(dr*dz);
q1=-sign(volu(i,j))*4*ro*(LL*volu(i,j))^2;
q2=-sign(volu(i,j))*1*ro*cc*(LL)*abs(volu(i,j));
Fd(i,j)=q2+q1;

for i=1:Nr
    for j=1:Nz
        p_star(i,j)=p_past(i,j)-alfa*dt*volu(i,j)/Sp;
        p_inter(i,j)=(p_star(i,j)+p_past(i,j))/2;
    end
end
%solving for vr,vz
%1) r=rw       corr
i=1;
for j=2:Nz-1
    z1_mid=(z(j)+z(j-1))/2;
    z2_mid=(z(j)+z(j+1))/2;
    r2_mid=(r(i)+r(i+1))/2;
    if j>=perf1 && j<=perf2
        p(i,j)=p0_original+p_wave;
        vr(i,j)=vr_past(i,j)-(dt/(ro_f-
ro_12/n_past(i,j)))*((p_inter(i+1,j)+Fd(i+1,j)-p_inter(i,j)-
Fd(i,j))/(r(i+1)-r(i))+n_past(i,j)*mu*(vr_past(i,j)-
wr_past(i,j))/kr(i,j)-...
            muf*((1/(r(i+1)-r(i)))*((vr_past(i+2,j)-
vr_past(i+1,j))/(r(i+2)-r(i+1))-(vr_past(i+1,j)-
vr_past(i,j))/(r(i+1)-r(i)))+...
            (vr_past(i+1,j)-vr_past(i,j))/(r(i)*(r(i+1)-
r(i)))+(1/(z2_mid-z1_mid))*((vr_past(i,j+1)-
vr_past(i,j))/(z(j+1)-z(j))-...
            (vr_past(i,j)-vr_past(i,j-1))/(z(j)-z(j-1)))-
vr_past(i,j)/(r(i)^2))-(muf+lamdaf)*((vr_past(i+1,j)-
vr_past(i,j))/(r(i)*(r(i+1)-r(i)))+...
            (1/(r(i+1)-r(i)))*((vr_past(i+2,j)-
vr_past(i+1,j))/(r(i+2)-r(i+1))-(vr_past(i+1,j)-
vr_past(i,j))/(r(i+1)-r(i)))-vr_past(i,j)/(r(i)^2)+...
            (vz_past(i+1,j+1)-vz_past(i+1,j-1)-
vz_past(i,j+1)+vz_past(i,j-1))/((r(i+1)-r(i))*(z(j+1)-z(j-1))))-
ro_12*(vr_past(i,j)+wr(i,j)-wr_past(i,j))/(n_past(i,j)*dt));
    else
        vr(i,j)=0; %no flow behind casing
    end
    vz(i,j)=vz_past(i,j)-(dt/ro_f-
ro_12/n_past(i,j))*((p_inter(i,j+1)+Fd(i,j+1)-p_inter(i,j-1)-
Fd(i,j-1))/(z(j+1)-z(j-1))+n_past(i,j)*mu*(vz_past(i,j)-
wz_past(i,j))/kz(i,j)-...
        ro_f*g-muf*((1/(r(i+1)-r(i)))*((vz_past(i+2,j)-
vz_past(i+1,j))/(r(i+2)-r(i+1))-(vz_past(i+1,j)-
vz_past(i,j))/(r(i+1)-r(i)))+...
        (vz_past(i+1,j)-vz_past(i,j))/(r(i)*(r(i+1)-
r(i)))+...
```

```matlab
            (1/(z2_mid-z1_mid))*((vz_past(i,j+1)-
vz_past(i,j))/(z(j+1)-z(j))-(vz_past(i,j)-vz_past(i,j-1))/(z(j)-
z(j-1)))))-...
            (muf+lamdaf)*((vr_past(i+1,j+1)-vr_past(i+1,j-1)-
vr_past(i,j+1)+vr_past(i,j-1))/((r(i+1)-r(i))*(z(j+1)-z(j-
1)))+(vr_past(i,j+1)-vr_past(i,j-1))/(r(i)*(z(j+1)-z(j-1)))+...
            (1/(z2_mid-z1_mid))*((vz_past(i,j+1)-
vz_past(i,j))/(z(j+1)-z(j))-(vz_past(i,j)-vz_past(i,j-1))/(z(j)-
z(j-1)))))));
        if j>perf1 && j<perf2
            del_wr1(i,j)=-(n_past(i,j)*ro_f*(vr(i,j)-vr_past(i,j)-
wr(i,j)+wr_past(i,j)))/ro;
        else
            del_wr1(i,j)=0;
        end
        del_wz1(i,j)=-(n_past(i,j)*ro_f*(vz(i,j)-vz_past(i,j)-
wz(i,j)+wz_past(i,j)))/ro;

    end

    %2) left bottom corner z=0 r=rw
    j=1;
    i=1;
    r2_mid=(r(i)+r(i+1))/2;
    p(i,j)=p0_original+p_wave;
    vr(i,j)=0; %no flow behind casing
    vz(i,j)=0; %no flow @ bot
    del_wr1(i,j)=0;
    del_wz1(i,j)=0;

    %3) left top corner z=h r=rw
    j=Nz;
    i=1;
    r2_mid=(r(i)+r(i+1))/2;
    p(i,j)=p0_original+p_wave;
    vr(i,j)=0; %%no flow behind casing
    vz(i,j)=0; %no flow to upper layer (shale)

    del_wz1(i,j)=-(n_past(i,j)*ro_f*(vz(i,j)-vz_past(i,j)-
wz(i,j)+wz_past(i,j)))/ro;
    del_wr1(i,j)=0;

    %4) middle points
    for i=2:Nr-1
        for j=2:Nz-1  %assuming zero tow
            r1_mid=(r(i)+r(i-1))/2;
            r2_mid=(r(i)+r(i+1))/2;
            z1_mid=(z(j)+z(j-1))/2;
            z2_mid=(z(j)+z(j+1))/2;

            vr(i,j)=vr_past(i,j)-(dt/(ro_f-
ro_12/n_past(i,j)))*((p_inter(i+1,j)+Fd(i+1,j)-p_inter(i-1,j)-
```

```matlab
Fd(i-1,j))/(r(i+1)-r(i-1))+n_past(i,j)*mu*(vr_past(i,j)-
wr_past(i,j))/kr(i,j)-...
            muf*((1/(r2_mid-r1_mid))*((vr_past(i+1,j)-
vr_past(i,j))/(r(i+1)-r(i))-(vr_past(i,j)-vr_past(i-1,j))/(r(i)-
r(i-1)))+...
            (vr_past(i+1,j)-vr_past(i-1,j))/(r(i)*(r(i+1)-
r(i-1)))+(1/(z2_mid-z1_mid))*((vr_past(i,j+1)-
vr_past(i,j))/(z(j+1)-z(j))-...
            (vr_past(i,j)-vr_past(i,j-1))/(z(j)-z(j-1)))-
vr_past(i,j)/(r(i)^2))-(muf+lamdaf)*((vr_past(i+1,j)-vr_past(i-
1,j))/(r(i)*(r(i+1)-r(i-1)))+...
            (1/(r2_mid-r1_mid))*((vr_past(i+1,j)-
vr_past(i,j))/(r(i+1)-r(i))-(vr_past(i,j)-vr_past(i-1,j))/(r(i)-
r(i-1)))-vr_past(i,j)/(r(i)^2)+...
            (vz_past(i+1,j+1)-vz_past(i+1,j-1)-vz_past(i-
1,j+1)+vz_past(i-1,j-1))/((r(i+1)-r(i-1))*(z(j+1)-z(j-1))))-
ro_12*(-vr_past(i,j)-wr(i,j)+wr_past(i,j))/(n_past(i,j)*dt));

        vz(i,j)=vz_past(i,j)-(dt/(ro_f-
ro_12/n_past(i,j)))*((p_inter(i,j+1)+Fd(i,j+1)-p_inter(i,j-1)-
Fd(i,j-1))/(z(j+1)-z(j-1))+n_past(i,j)*mu*(vz_past(i,j)-
wz_past(i,j))/kz(i,j)-...
            ro_f*g-muf*((1/(r2_mid-r1_mid))*((vz_past(i+1,j)-
vz_past(i,j))/(r(i+1)-r(i))-(vz_past(i,j)-vz_past(i-1,j))/(r(i)-
r(i-1)))+(vz_past(i+1,j)-vz_past(i-1,j))/(r(i)*(r(i+1)-r(i-
1)))+...
            (1/(z2_mid-z1_mid))*((vz_past(i,j+1)-
vz_past(i,j))/(z(j+1)-z(j))-(vz_past(i,j)-vz_past(i,j-1))/(z(j)-
z(j-1))))-...
            (muf+lamdaf)*((vr_past(i+1,j+1)-vr_past(i+1,j-1)-
vr_past(i-1,j+1)+vr_past(i-1,j-1))/((r(i+1)-r(i-1))*(z(j+1)-z(j-
1)))+(vr_past(i,j+1)-vr_past(i,j-1))/(r(i)*(z(j+1)-z(j-1)))+...
            (1/(z2_mid-z1_mid))*((vz_past(i,j+1)-
vz_past(i,j))/(z(j+1)-z(j))-(vz_past(i,j)-vz_past(i,j-1))/(z(j)-
z(j-1))))-ro_12*(-vz_past(i,j)-
wz(i,j)+wz_past(i,j))/(n_past(i,j)*dt));

            del_wr1(i,j)=-(n_past(i,j)*ro_f*(vr(i,j)-
vr_past(i,j)-wr(i,j)+wr_past(i,j)))/ro;
            del_wz1(i,j)=-(n_past(i,j)*ro_f*(vz(i,j)-
vz_past(i,j)-wz(i,j)+wz_past(i,j)))/ro;
        end
    end

%%%%%%%%%%%%%%%%%%%%%%%%%%%%%%%%%%%%%%%%%%%%%%%%%%%%%%%%%%%%%%%%%
    %5) z=0
    j=1;
    for i=2:Nr-1
        r1_mid=(r(i)+r(i-1))/2;
        r2_mid=(r(i)+r(i+1))/2;
        vr(i,j)=vr_past(i,j)-(dt/(ro_f-
ro_12/n_past(i,j)))*((p_inter(i+1,j)+Fd(i+1,j)-p_inter(i-1,j)-
```

```
Fd(i-1,j))/(r(i+1)-r(i-1))+n_past(i,j)*mu*(vr_past(i,j)-
wr_past(i,j))/kr(i,j)-...
            muf*((1/(r2_mid-r1_mid))*((vr_past(i+1,j)-
vr_past(i,j))/(r(i+1)-r(i))-(vr_past(i,j)-vr_past(i-1,j))/(r(i)-
r(i-1)))+...
            (vr_past(i+1,j)-vr_past(i-1,j))/(r(i)*(r(i+1)-r(i-
1)))+(1/(z(j+1)-z(j)))*((vr_past(i,j+2)-vr_past(i,j+1))/(z(j+2)-
z(j+1))-...
            (vr_past(i,j+1)-vr_past(i,j))/(z(j+1)-z(j)))-
vr_past(i,j)/(r(i)^2))-(muf+lamdaf)*((vr_past(i+1,j)-vr_past(i-
1,j))/(r(i)*(r(i+1)-r(i-1)))+...
            (1/(r2_mid-r1_mid))*((vr_past(i+1,j)-
vr_past(i,j))/(r(i+1)-r(i))-(vr_past(i,j)-vr_past(i-1,j))/(r(i)-
r(i-1)))-vr_past(i,j)/(r(i)^2)+...
            (vz_past(i+1,j+1)-vz_past(i+1,j)-vz_past(i-
1,j+1)+vz_past(i-1,j))/((r(i+1)-r(i-1))*(z(j+1)-z(j))))-ro_12*(-
vr_past(i,j)-wr(i,j)+wr_past(i,j))/(n_past(i,j)*dt));
        vz(i,j)=0; %no flow @ bot

        del_wr1(i,j)=-(n_past(i,j)*ro_f*(vr(i,j)-vr_past(i,j)-
wr(i,j)+wr_past(i,j)))/ro;
        del_wz1(i,j)=0;


    end
    %6) z=h
    j=Nz;
    for i=2:Nr-1
        r1_mid=(r(i)+r(i-1))/2;
        r2_mid=(r(i)+r(i+1))/2;
        vr(i,j)=vr_past(i,j)-(dt/(ro_f-
ro_12/n_past(i,j)))*((p_inter(i+1,j)+Fd(i+1,j)-p_inter(i-1,j)-
Fd(i-1,j))/(r(i+1)-r(i-1))+n_past(i,j)*mu*(vr_past(i,j)-
wr_past(i,j))/kr(i,j)-...
            muf*((1/(r2_mid-r1_mid))*((vr_past(i+1,j)-
vr_past(i,j))/(r(i+1)-r(i))-(vr_past(i,j)-vr_past(i-1,j))/(r(i)-
r(i-1)))+...
            (vr_past(i+1,j)-vr_past(i-1,j))/(r(i)*(r(i+1)-r(i-
1)))+(1/(z(j)-z(j-1)))*((vr_past(i,j)-vr_past(i,j-1))/(z(j)-z(j-
1))-...
            (vr_past(i,j-1)-vr_past(i,j-2))/(z(j-1)-z(j-2)))-
vr_past(i,j)/(r(i)^2))-(muf+lamdaf)*((vr_past(i+1,j)-vr_past(i-
1,j))/(r(i)*(r(i+1)-r(i-1)))+...
            (1/(r2_mid-r1_mid))*((vr_past(i+1,j)-
vr_past(i,j))/(r(i+1)-r(i))-(vr_past(i,j)-vr_past(i-1,j))/(r(i)-
r(i-1)))-vr_past(i,j)/(r(i)^2)+...
            (vz_past(i+1,j)-vz_past(i+1,j-1)-vz_past(i-
1,j)+vz_past(i-1,j-1))/((r(i+1)-r(i-1))*(z(j)-z(j-1))))-ro_12*(-
vr_past(i,j)-wr(i,j)+wr_past(i,j))/(n_past(i,j)*dt));
        vz(i,j)=0; %no flow to upper layer (shale)
        del_wr1(i,j)=-(n_past(i,j)*ro_f*(vr(i,j)-vr_past(i,j)-
wr(i,j)+wr_past(i,j)))/ro;
        del_wz1(i,j)=-(n_past(i,j)*ro_f*(vz(i,j)-vz_past(i,j)-
wz(i,j)+wz_past(i,j)))/ro;
```

```matlab
    end

    %7) r=re
    i=Nr;
    for j=2:Nz-1
        z1_mid=(z(j)+z(j-1))/2;
        z2_mid=(z(j)+z(j+1))/2;


        p(i,j)=P_res;    %Res Pres.
        vr(i,j)=vr_past(i,j)-(dt/(ro_f-
ro_12/n_past(i,j)))*((p_inter(i,j)+Fd(i,j)-p_inter(i-1,j)-Fd(i-
1,j))/(r(i)-r(i-1))+n_past(i,j)*mu*(vr_past(i,j)-
wr_past(i,j))/kr(i,j)-...
            muf*((1/(r(i)-r(i-1)))*((vr_past(i,j)-vr_past(i-
1,j))/(r(i)-r(i-1))-(vr_past(i-1,j)-vr_past(i-2,j))/(r(i-1)-r(i-
2)))+...
            (vr_past(i,j)-vr_past(i-1,j))/(r(i)*(r(i)-r(i-
1)))+(1/(z2_mid-z1_mid))*((vr_past(i,j+1)-vr_past(i,j))/(z(j+1)-
z(j))-...
            (vr_past(i,j)-vr_past(i,j-1))/(z(j)-z(j-1)))-
vr_past(i,j)/(r(i)^2))-(muf+lamdaf)*((vr_past(i,j)-vr_past(i-
1,j))/(r(i)*(r(i)-r(i-1)))+...
            (1/(r(i)-r(i-1)))*((vr_past(i,j)-vr_past(i-
1,j))/(r(i)-r(i-1))-(vr_past(i-1,j)-vr_past(i-2,j))/(r(i-1)-r(i-
2)))-vr_past(i,j)/(r(i)^2)+...
            (vz_past(i,j+1)-vz_past(i,j-1)-vz_past(i-
1,j+1)+vz_past(i-1,j-1))/((r(i)-r(i-1))*(z(j+1)-z(j-1))))-
ro_12*(-vr_past(i,j)-wr(i,j)+wr_past(i,j))/(n_past(i,j)*dt));


        vz(i,j)=vz_past(i,j)-
(dt/coef)*((1+coef0*alfa)*(p_inter(i,j+1)+Fd(i,j+1)-p_inter(i,j-
1)-Fd(i,j-1))/(z(j+1)-z(j-1))+n_past(i,j)*mu*(vz_past(i,j)-
wz_past(i,j))/kz(i,j)-...
            ro_f*g+coef0*((srz_past(i,j)-srz_past(i-1,j))/(r(i)-
r(i-1))+(srz_past(i,j))/r(i)+...
            (szz_past(i,j+1)-szz_past(i,j-1)+Fdzz_past(i,j+1)-
Fdzz_past(i,j-1))/(z(j+1)-z(j-1))-ro*g+bu(i,j)*(n_past(i,j+1)-
n_past(i,j-1))/(z(j+1)-z(j-1)))-...
            muf*((1/(r(i)-r(i-1)))*((vz_past(i,j)-vz_past(i-
1,j))/(r(i)-r(i-1))-(vz_past(i-1,j)-vz_past(i-2,j))/(r(i-1)-r(i-
2)))+(vz_past(i,j)-vz_past(i-1,j))/(r(i)*(r(i)-r(i-1)))+...
            (1/(z2_mid-z1_mid))*((vz_past(i,j+1)-
vz_past(i,j))/(z(j+1)-z(j))-(vz_past(i,j)-vz_past(i,j-1))/(z(j)-
z(j-1))))-...
            (muf+lamdaf)*((vr_past(i,j+1)-vr_past(i,j-1)-
vr_past(i-1,j+1)+vr_past(i-1,j-1))/((r(i)-r(i-1))*(z(j+1)-z(j-
1)))+(vr_past(i,j+1)-vr_past(i,j-1))/(r(i)*(z(j+1)-z(j-1)))+...
            (1/(z2_mid-z1_mid))*((vz_past(i,j+1)-
vz_past(i,j))/(z(j+1)-z(j))-(vz_past(i,j)-vz_past(i,j-1))/(z(j)-
z(j-1)))));

        del_wr1(i,j)=-(n_past(i,j)*ro_f*(vr(i,j)-vr_past(i,j)-
wr(i,j)+wr_past(i,j)))/ro;
```

```matlab
        del_wz1(i,j)=-(n_past(i,j)*ro_f*(vz(i,j)-vz_past(i,j)-
wz(i,j)+wz_past(i,j)))/ro;

    end
    %8) right bottom corner z=0 r=re
    j=1;
    i=Nr;
    p(i,j)=P_res;   %Res Pres.
     vr(i,j)=vr_past(i,j)-(dt/(ro_f-
ro_12/n_past(i,j)))*((p_inter(i,j)+Fd(i,j)-p_inter(i-1,j)-Fd(i-
1,j))/(r(i)-r(i-1))+n_past(i,j)*mu*(vr_past(i,j)-
wr_past(i,j))/kr(i,j)-...
            muf*((1/(r(i)-r(i-1)))*((vr_past(i,j)-vr_past(i-
1,j))/(r(i)-r(i-1))-(vr_past(i-1,j)-vr_past(i-2,j))/(r(i-1)-r(i-
2)))+...
            (vr_past(i,j)-vr_past(i-1,j))/(r(i)*(r(i)-r(i-
1)))+(1/(z(j+1)-z(j)))*((vr_past(i,j+2)-vr_past(i,j+1))/(z(j+2)-
z(j+1))-...
            (vr_past(i,j+1)-vr_past(i,j))/(z(j+1)-z(j)))-
vr_past(i,j)/(r(i)^2))-(muf+lamdaf)*((vr_past(i,j)-vr_past(i-
1,j))/(r(i)*(r(i)-r(i-1)))+...
            (1/(r(i)-r(i-1)))*((vr_past(i,j)-vr_past(i-
1,j))/(r(i)-r(i-1))-(vr_past(i-1,j)-vr_past(i-2,j))/(r(i-1)-r(i-
2)))-vr_past(i,j)/(r(i)^2)+...
            (vz_past(i,j+1)-vz_past(i,j)-vz_past(i-
1,j+1)+vz_past(i-1,j))/((r(i)-r(i-1))*(z(j+1)-z(j))))-ro_12*(-
vr_past(i,j)-wr(i,j)+wr_past(i,j))/(n_past(i,j)*dt));
    vz(i,j)=0;
    del_wr1(i,j)=-(n_past(i,j)*ro_f*(vr(i,j)-vr_past(i,j)-
wr(i,j)+wr_past(i,j)))/ro;
    del_wz1(i,j)=-(n_past(i,j)*ro_f*(vz(i,j)-vz_past(i,j)-
wz(i,j)+wz_past(i,j)))/ro;
    %9) right top corner z=h r=re
    j=Nz;
    i=Nr;
    %BC
    p(i,j)=P_res;   %Res Pres.

    vr(i,j)=vr_past(i,j)-(dt/(ro_f-
ro_12/n_past(i,j)))*((p_inter(i,j)+Fd(i,j)-p_inter(i-1,j)-Fd(i-
1,j))/(r(i)-r(i-1))+n_past(i,j)*mu*(vr_past(i,j)-
wr_past(i,j))/kr(i,j)-...
        muf*((1/(r(i)-r(i-1)))*((vr_past(i,j)-vr_past(i-
1,j))/(r(i)-r(i-1))-(vr_past(i-1,j)-vr_past(i-2,j))/(r(i-1)-r(i-
2)))+...
        (vr_past(i,j)-vr_past(i-1,j))/(r(i)*(r(i)-r(i-
1)))+(1/(z(j)-z(j-1)))*((vr_past(i,j)-vr_past(i,j-1))/(z(j)-z(j-
1))-...
        (vr_past(i,j-1)-vr_past(i,j-2))/(z(j-1)-z(j-2)))-
vr_past(i,j)/(r(i)^2))-(muf+lamdaf)*((vr_past(i,j)-vr_past(i-
1,j))/(r(i)*(r(i)-r(i-1)))+...
```

```matlab
        (1/(r(i)-r(i-1)))*((vr_past(i,j)-vr_past(i-1,j))/(r(i)-
r(i-1))-(vr_past(i-1,j)-vr_past(i-2,j))/(r(i-1)-r(i-2)))-
vr_past(i,j)/(r(i)^2)+...
        (vz_past(i,j)-vz_past(i,j-1)-vz_past(i-1,j)+vz_past(i-
1,j-1))/((r(i)-r(i-1))*(z(j)-z(j-1))))-ro_12*(-vr_past(i,j)-
wr(i,j)+wr_past(i,j))/(n_past(i,j)*dt));
    vz(i,j)=0;

    del_wr1(i,j)=-(n_past(i,j)*ro_f*(vr(i,j)-vr_past(i,j)-
wr(i,j)+wr_past(i,j)))/ro;
    del_wz1(i,j)=-(n_past(i,j)*ro_f*(vz(i,j)-vz_past(i,j)-
wz(i,j)+wz_past(i,j)))/ro;


    for j=1:Nz
        for i=1:Nr
            Num_count=(j-1)*Nr+i;
            wr_cor(Num_count)=del_wr1(i,j);
            wz_cor(Num_count)=del_wz1(i,j);


        end
    end

dlmwrite('wr_co.txt',wr_cor,'newline','pc','delimiter','\t','prec
ision','%2.14f');

dlmwrite('wz_co.txt',wz_cor,'newline','pc','delimiter','\t','prec
ision','%2.14f');

%%%%%%%%%%%%%%%%%%%%%%%%%%%%%%%%%%%%%%%%%%%%%%%%%%%%%%%%%%%%%%%%%%%
    wr=wr+del_wr1;
    wz=wz+del_wz1;

%%%%%%%%%%%%%%%%%%%%%%%%%%%%%%%%%%%%%%%%%%%%%%%%%%%%%%%%%%%%%%%%%%%
    %solving for p & n
    %1) r=rw
    i=1;
    for j=2:Nz-1

        err=(wr(i+1,j)-wr(i,j))/(r(i+1)-r(i));
        ett=wr(i,j)/r(i);
        ezz=(wz(i,j+1)-wz(i,j-1))/(z(j+1)-z(j-1));
        vol=err+ett+ezz;
        volf=(vr(i+1,j)-vr(i,j))/(r(i+1)-
r(i))+vr(i,j)/r(i)+(vz(i,j+1)-vz(i,j-1))/(z(j+1)-z(j-1));
        Ev(i,j)=Ev(i,j)+vol*dt;
        if Ev(i,j)<-(n0-.05)
            Ev(i,j)=-(n0-.05);
        end

        if j>=perf1 && j<=perf2
            p(i,j)=p0_original+p_wave;
        else
            %EV_based
```

```matlab
            p(i,j)=p_past(i,j)-dt*(n_past(i,j)*(volf)+(1-
n0)*(vol)/(1+Ev(i,j))^2+...
                (vr(i,j)-wr(i,j))*(n_past(i+1,j)-
n_past(i,j))/(r(i+1)-r(i))+...
                (vz(i,j)-wz(i,j))*(n_past(i,j+1)-n_past(i,j-
1))/(z(j+1)-z(j-1))+...
                n_past(i,j)*cf*((vr(i,j)-wr(i,j))*(p_past(i+1,j)-
p_past(i,j))/(r(i+1)-r(i))+(vz(i,j)-wz(i,j))*(p_past(i,j+1)-
p_past(i,j-1))/(z(j+1)-z(j-1))))/(cf*n(i,j));


        end
        n(i,j)=1-(1-n0)/(1+Ev(i,j));
    end
    %2) left bottom corner z=0 r=rw
    j=1;
    i=1;

    err=(wr(i+1,j)-wr(i,j))/(r(i+1)-r(i));
    ett=wr(i,j)/r(i);
    ezz=(wz(i,j+1)-wz(i,j))/(z(j+1)-z(j));
    vol=err+ett+ezz;
    volf=(vr(i+1,j)-vr(i,j))/(r(i+1)-
r(i))+vr(i,j)/r(i)+(vz(i,j+1)-vz(i,j))/(z(j+1)-z(j));
    Ev(i,j)=Ev(i,j)+vol*dt;
    if Ev(i,j)<-(n0-.05)
        Ev(i,j)=-(n0-.05);
    end
    %EV_based
    p(i,j)=p_past(i,j)-dt*(n_past(i,j)*(volf)+(1-
n0)*(vol)/(1+Ev(i,j))^2+...
        (vr(i,j)-wr(i,j))*(n_past(i+1,j)-n_past(i,j))/(r(i+1)-
r(i))+...
        (vz(i,j)-wz(i,j))*(n_past(i,j+1)-n_past(i,j))/(z(j+1)-
z(j))+...
        n_past(i,j)*cf*((vr(i,j)-wr(i,j))*(p_past(i+1,j)-
p_past(i,j))/(r(i+1)-r(i))+(vz(i,j)-wz(i,j))*(p_past(i,j+1)-
p_past(i,j))/(z(j+1)-z(j))))/(cf*n(i,j));

    n(i,j)=1-(1-n0)/(1+Ev(i,j));
    %3) left top corner z=h r=rw
    j=Nz;
    i=1;
    r2_mid=(r(i)+r(i+1))/2;

    err=(wr(i+1,j)-wr(i,j))/(r(i+1)-r(i));
    ett=wr(i,j)/r(i);
    ezz=(wz(i,j)-wz(i,j-1))/(z(j)-z(j-1));
%     erz=.5*((wz(i+1,j)-wz(i,j))/(r(i+1)-r(i))+(wr(i,j)-wr(i,j-
1))/(z(j)-z(j-1)));
    vol=err+ett+ezz;
    volf=(vr(i+1,j)-vr(i,j))/(r(i+1)-r(i))+vr(i,j)/r(i)+(vz(i,j)-
vz(i,j-1))/(z(j)-z(j-1));
    Ev(i,j)=Ev(i,j)+vol*dt;
```

```matlab
    if Ev(i,j)<-(n0-.05)
        Ev(i,j)=-(n0-.05);
    end
    %Ev based
     p(i,j)=p_past(i,j)-dt*(n_past(i,j)*(volf)+(1-
n0)*(vol)/(1+Ev(i,j))^2+...
        (vr(i,j)-wr(i,j))*(n_past(i+1,j)-n_past(i,j))/(r(i+1)-
r(i))+...
        (vz(i,j)-wz(i,j))*(n_past(i,j)-n_past(i,j-1))/(z(j)-z(j-
1))+...
        n_past(i,j)*cf*((vr(i,j)-wr(i,j))*(p_past(i+1,j)-
p_past(i,j))/(r(i+1)-r(i))+(vz(i,j)-wz(i,j))*(p_past(i,j)-
p_past(i,j-1))/(z(j)-z(j-1))))/(cf*n(i,j));

    n(i,j)=1-(1-n0)/(1+Ev(i,j));
    %%%%%%%%%%%%%%%
    %4) middle points
    %%%%%%%%%%%%%%%%
    for i=2:Nr-1
        for j=2:Nz-1  %assuming zero tow
            err=(wr(i+1,j)-wr(i-1,j))/(r(i+1)-r(i-1));
            ett=wr(i,j)/r(i);
            ezz=(wz(i,j+1)-wz(i,j-1))/(z(j+1)-z(j-1));
            vol=err+ett+ezz;
            volf=(vr(i+1,j)-vr(i-1,j))/(r(i+1)-r(i-
1))+vr(i,j)/r(i)+(vz(i,j+1)-vz(i,j-1))/(z(j+1)-z(j-1));
            Ev(i,j)=Ev(i,j)+vol*dt;
            if Ev(i,j)<-(n0-.05)
                Ev(i,j)=-(n0-.05);
            end
            %Ev based
             p(i,j)=p_past(i,j)-dt*(n_past(i,j)*(volf)+(1-
n0)*(vol)/(1+Ev(i,j))^2+...
                (vr(i,j)-wr(i,j))*(n_past(i+1,j)-n_past(i-
1,j))/(r(i+1)-r(i-1))+...
                (vz(i,j)-wz(i,j))*(n_past(i,j+1)-n_past(i,j-
1))/(z(j+1)-z(j-1))+...
                n_past(i,j)*cf*((vr(i,j)-wr(i,j))*(p_past(i+1,j)-
p_past(i-1,j))/(r(i+1)-r(i-1))+(vz(i,j)-wz(i,j))*(p_past(i,j+1)-
p_past(i,j-1))/(z(j+1)-z(j-1))))/(cf*n(i,j));

            n(i,j)=1-(1-n0)/(1+Ev(i,j));
        end
    end
    %5) z=0
    j=1;
    for i=2:Nr-1
        err=(wr(i+1,j)-wr(i-1,j))/(r(i+1)-r(i-1));
        ett=wr(i,j)/r(i);
        ezz=(wz(i,j+1)-wz(i,j))/(z(j+1)-z(j));
        vol=err+ett+ezz;
        volf=(vr(i+1,j)-vr(i-1,j))/(r(i+1)-r(i-
1))+vr(i,j)/r(i)+(vz(i,j+1)-vz(i,j))/(z(j+1)-z(j));
```

```matlab
        Ev(i,j)=Ev(i,j)+vol*dt;
        if Ev(i,j)<-(n0-.05)
            Ev(i,j)=-(n0-.05);
        end
        p(i,j)=p_past(i,j)-dt*(n_past(i,j)*(volf)+(1-
n0)*(vol)/(1+Ev(i,j))^2+...
            (vr(i,j)-wr(i,j))*(n_past(i+1,j)-n_past(i-
1,j))/(r(i+1)-r(i-1))+...
            (vz(i,j)-wz(i,j))*(n_past(i,j+1)-
n_past(i,j))/(z(j+1)-z(j))+...
            n_past(i,j)*cf*((vr(i,j)-wr(i,j))*(p_past(i+1,j)-
p_past(i-1,j))/(r(i+1)-r(i-1))+(vz(i,j)-wz(i,j))*(p_past(i,j+1)-
p_past(i,j))/(z(j+1)-z(j))))/(cf*n(i,j));
        n(i,j)=1-(1-n0)/(1+Ev(i,j));
    end
    %6) z=h
    j=Nz;
    for i=2:Nr-1
        err=(wr(i+1,j)-wr(i-1,j))/(r(i+1)-r(i-1));
        ett=wr(i,j)/r(i);
        ezz=(wz(i,j)-wz(i,j-1))/(z(j)-z(j-1));
        vol=err+ett+ezz;
        volf=(vr(i+1,j)-vr(i-1,j))/(r(i+1)-r(i-
1))+vr(i,j)/r(i)+(vz(i,j)-vz(i,j-1))/(z(j)-z(j-1));
        Ev(i,j)=Ev(i,j)+vol*dt;
        if Ev(i,j)<-(n0-.05)
            Ev(i,j)=-(n0-.05);
        end
        p(i,j)=p_past(i,j)-dt*(n_past(i,j)*(volf)+(1-
n0)*(vol)/(1+Ev(i,j))^2+...
            (vr(i,j)-wr(i,j))*(n_past(i+1,j)-n_past(i-
1,j))/(r(i+1)-r(i-1))+...
            (vz(i,j)-wz(i,j))*(n_past(i,j)-n_past(i,j-1))/(z(j)-
z(j-1))+...
            n_past(i,j)*cf*((vr(i,j)-wr(i,j))*(p_past(i+1,j)-
p_past(i-1,j))/(r(i+1)-r(i-1))+(vz(i,j)-wz(i,j))*(p_past(i,j)-
p_past(i,j-1))/(z(j)-z(j-1))))/(cf*n(i,j));
%           n(i,j)=n_past(i,j)+dt*(ds*vol-df*volf);
        n(i,j)=1-(1-n0)/(1+Ev(i,j));
    end

    %7) r=re   Corr
    i=Nr;
    for j=2:Nz-1
        err=(wr(i,j)-wr(i-1,j))/(r(i)-r(i-1));
        ett=wr(i,j)/r(i);
        ezz=(wz(i,j+1)-wz(i,j-1))/(z(j+1)-z(j-1));
        vol=err+ett+ezz;
        volf=(vr(i,j)-vr(i-1,j))/(r(i)-r(i-
1))+vr(i,j)/r(i)+(vz(i,j+1)-vz(i,j-1))/(z(j+1)-z(j-1));
        Ev(i,j)=Ev(i,j)+vol*dt;
        if Ev(i,j)<-(n0-.05)
            Ev(i,j)=-(n0-.05);
```

```matlab
        end
        p(i,j)=P_res; % Res. Press.
%          n(i,j)=n_past(i,j)+dt*(ds*vol-df*volf);
        n(i,j)=1-(1-n0)/(1+Ev(i,j));
    end
    %8) right bottom corner z=0 r=re   Corr
    j=1;
    i=Nr;
    err=(wr(i,j)-wr(i-1,j))/(r(i)-r(i-1));
    ett=wr(i,j)/r(i);
    ezz=(wz(i,j+1)-wz(i,j))/(z(j+1)-z(j));
    vol=err+ett+ezz;
    volf=(vr(i,j)-vr(i-1,j))/(r(i)-r(i-
1))+vr(i,j)/r(i)+(vz(i,j+1)-vz(i,j))/(z(j+1)-z(j));
    Ev(i,j)=Ev(i,j)+vol*dt;
    if Ev(i,j)<-(n0-.05)
        Ev(i,j)=-(n0-.05);
    end

    p(i,j)=P_res; % Res. Press.
    n(i,j)=1-(1-n0)/(1+Ev(i,j));

    %9) right top corner z=h r=re Corr
    j=Nz;
    i=Nr;
    err=(wr(i,j)-wr(i-1,j))/(r(i)-r(i-1));
    ett=wr(i,j)/r(i);
    ezz=(wz(i,j)-wz(i,j-1))/(z(j)-z(j-1));
    erz=.5*((wz(i,j)-wz(i-1,j))/(r(i)-r(i-1))+(wr(i,j)-wr(i,j-
1))/(z(j)-z(j-1)));
    vol=err+ett+ezz;
    volf=(vr(i,j)-vr(i-1,j))/(r(i)-r(i-1))+vr(i,j)/r(i)+(vz(i,j)-
vz(i,j-1))/(z(j)-z(j-1));
    Ev(i,j)=Ev(i,j)+vol*dt;
    if Ev(i,j)<-(n0-.05)
        Ev(i,j)=-(n0-.05);
    end
    %BC
    p(i,j)=P_res; % Res. Press.
%     n(i,j)=n_past(i,j)+dt*(ds*vol-df*volf);
    n(i,j)=1-(1-n0)/(1+Ev(i,j));
    %%%%%%%%% Extract p & n for Flac
%%%%%%%%%%%%%%%%%%%%%%%%%%%%%%%%%%%
    for j=1:Nz
        for i=1:Nr
            Num_count=(j-1)*Nr+i;
            p_1D(Num_count)=p(i,j);
        end
    end
    for j=1:Nz-1
        for i=1:Nr-1
            Num_count=(j-1)*(Nr-1)+i;
```

```matlab
del_poro(Num_count,1)=(n(i,j)+n(i+1,j)+n(i,j+1)+n(i+1,j+1))/4;
%n_flac(i,j)
        end
    end


dlmwrite('_pp.txt',p_1D,'newline','pc','delimiter','\t','precisio
n','%8.10f');

dlmwrite('por.txt',del_poro,'newline','pc','delimiter','\t','prec
ision','%2.10f');

%%%%%%%%%%%%%%%%%%%%%%%%%%%%%%%%%%%%%%%%%%%%%%%%%%%%%%%%%%%%%%%%%%%
    %giving current values as the past ones
    p_past=p;
    vr_past=vr;
    vz_past=vz;
    wr_past=wr;
    wz_past=wz;
    n_past=n;
    time=time+dt;
    tt(jj)=time;
    pp1(jj)=(p(nhis1,Nz_mid)-p0(nhis1,Nz_mid));
    pp2(jj)=(p(nhis2,Nz_mid)-p0(nhis2,Nz_mid));
    pp3(jj)=(p(nhis3,Nz_mid)-p0(nhis3,Nz_mid));
    nn1(jj)=n(1,16);
    nn2(jj)=n(2,16);
    nn3(jj)=n(5,16);
    nn4(jj)=n(15,16);
    bc(jj)=p_wave;
end
```

B.3 FLAC Code (run_ex.txt)

```
_input2D
p_wave
step 1
_output
endflac
```